Young stellar clusters throughout the Galaxy and the interaction with their molecular environment

Dissertation
zur
Erlangung des Doktorgrades (Dr. rer. nat.)
der
Mathematisch-Naturwissenschaftlichen Fakultät
der
Rheinischen Friedrich-Wilhelms-Universität Bonn

vorgelegt von
Esteban Félix Eduardo Morales Häfelin
aus Santiago, Chile

Bonn Oktober 2012

Angefertigt mit Genehmigung der
Mathematisch-Naturwissenschaftlichen Fakultät der Rheinischen
Friedrich-Wilhelms-Universität Bonn

1. Referent: Prof. Dr. Karl M. Menten

2. Referent: Prof. Dr. Pavel Kroupa

Tag der Promotion: 12.03.2013
Erscheinungsjahr: 2014

a Denise

Abstract

Stars are born within dense clumps of giant molecular clouds, constituting young stellar agglomerates known as embedded clusters. Once the parental gas is expelled through stellar feedback, they evolve into bound open clusters only under special conditions. In this thesis, we study observationally all embedded clusters (ECs) and open clusters (OCs) known so far in the inner Galaxy, investigating particularly their interaction with the surrounding molecular environment. We first compiled a merged list of 3904 clusters from optical and infrared clusters catalogs in the literature, including 71 new embedded clusters discovered by us in the GLIMPSE mid-infrared data after applying a red-color criterion. From this list, 695 clusters are within the Galactic range $|l| \leq 60^\circ$ and $|b| \leq 1.5^\circ$ covered by the ATLASGAL survey, which was used to search for correlations with submm dust continuum emission tracing dense molecular gas. Based on the morphology of this emission, we defined an evolutionary sequence of five morphological types: deeply embedded cluster (EC1), partially embedded cluster (EC2), emerging open cluster (OC0), open cluster still associated with a submm clump in the vicinity (OC1), and open cluster without correlation with ATLASGAL (OC2). We found that this sequence correlates well with other observational indicators of evolution, such as UV-excited PAH emission and H II regions tracing stellar feedback in the first four evolutionary stages, and infrared dark clouds probing a very early phase within the EC1 type. We also found that an OC defined observationally in this way (clusters with types OC0, OC1 and OC2 and confirmed as real clusters) is equivalent to the physical concept of open cluster (a bound exposed cluster) for ages in excess of ~ 16 Myr; some observed OCs younger than this limit can be actually unbound associations.

We found that our OC and EC samples are roughly complete up to ~ 1 kpc and ~ 1.8 kpc from the Sun, respectively, after which the completeness decays exponentially. Using available age estimates for a few ECs, we derived an upper limit of 3 Myr for the duration of the embedded phase. Combined with the OC age distribution within 3 kpc from the Sun, we computed formation rates of 0.54, 1.18, and 6.50 Myr^{-1} kpc^{-2} for bound open clusters, all observed young exposed clusters, and embedded clusters, respectively, implying an EC dissolution fraction of $88 \pm 8\%$.

We carried out follow-up ^{13}CO(2−1) and C^{18}O(2−1) mapping observations towards a subsample of 14 clusters showing evidence of ongoing stellar feedback in our previous analysis, and we indeed found kinematic signatures of enhanced turbulence and expanding motions. A more detailed study towards the IR bubble G10.31−0.14, including a comparison with simple geometrical models of the velocity field, reveals that this source is more likely an expanding molecular ring inclined with respect to the plane of the sky, rather than a 3D shell seen in projection.

Contents

1 Introduction **1**
- 1.1 Observational tools: Galactic surveys . . . 3
  - 1.1.1 ATLASGAL . . . 5
  - 1.1.2 2MASS . . . 5
  - 1.1.3 GLIMPSE . . . 6
- 1.2 This Thesis . . . 7

2 The current understanding of embedded cluster formation and early evolution **11**
- 2.1 Formation of embedded clusters . . . 11
  - 2.1.1 Theories . . . 11
  - 2.1.2 Spatial distribution and clustering . . . 15
- 2.2 Gas disruption . . . 22
  - 2.2.1 Stellar feedback in young clusters . . . 22
  - 2.2.2 Early dynamical evolution . . . 27
  - 2.2.3 Triggered star formation . . . 31
- 2.3 Cluster definition revisited . . . 33

3 Compilation of all-sky cluster catalogs **35**
- 3.1 Optical clusters . . . 36
- 3.2 Near-infrared clusters . . . 37
- 3.3 Mid-infrared clusters . . . 39
- 3.4 New GLIMPSE search for embedded clusters . . . 39
- 3.5 Cross-identifications . . . 46
- 3.6 Spurious cluster candidates . . . 47

4 Stellar clusters in the inner Galaxy and their correlation with ATLASGAL **53**
- 4.1 Construction of the Catalog . . . 54
  - 4.1.1 Designations, position and angular size . . . 54
  - 4.1.2 ATLASGAL emission . . . 54
  - 4.1.3 Mid-IR morphology and association with known objects 57

4.1.4 Kinematic distance . . . 59
4.1.5 Stellar distance and age . . . 64
4.1.6 Adopted distance, complexes and subclusters . . . 67
4.1.7 Additional comments . . . 69
4.2 Analysis . . . 70
4.2.1 Morphological evolutionary sequence . . . 70
4.2.2 Spatial distribution . . . 76
4.2.3 Completeness and definition of a representative sample . . . 86
4.2.4 Age distribution and young cluster dissolution . . . 88
4.2.5 Correlations . . . 94

5 Follow-up ^{13}CO(2−1) and C^{18}O(2−1) mapping observations 97
5.1 Observations . . . 97
5.1.1 APEX . . . 99
5.1.2 IRAM 30-m . . . 101
5.2 General Results . . . 102
5.3 The infrared bubble G10.31−0.14 . . . 120
5.3.1 Description of the region . . . 120
5.3.2 Kinematics . . . 124
5.3.3 Discussion . . . 134

6 Conclusions 139

A Cluster Classical Evolution 145

B Catalog of stellar clusters in the inner Galaxy 153

Bibliography 193

Acknowledgements 207

List of Figures

1.1 Infrared and optical images of the embedded cluster RCW 38 . 4

2.1 Hydrodynamic simulations of star formation in a Giant Molecular Cloud 13
2.2 Zoomed-in image of star formation hydrodynamic simulations . 14
2.3 Young stellar objects in the Orion A molecular cloud 17
2.4 Cumulative fraction of YSO surface densities in the solar neighborhood 18
2.5 Spatial distributions of sink particles in a star formation simulation 20
2.6 Schematic representation of a wind-blown H II region 25
2.7 Comparison of feedback mechanisms in protoclusters on the (Σ, M) plane 26

3.1 Examples of new GLIMPSE embedded cluster candidates . . . 43

4.1 Comparison of kinematic and stellar distances 70
4.2 Examples of the two morphological types of embedded clusters 72
4.3 Examples of the three morphological types of open clusters . . 73
4.4 Crossing time vs. age in an solar neighborhood open cluster sample 77
4.5 Galactic distribution of the star cluster sample 78
4.6 Zoomed-in Galactic distribution of the star cluster sample . . . 79
4.7 Distribution of heights from the Galactic plane 81
4.8 Distribution of heliocentric distances 82
4.9 Age distribution of open clusters 91

5.1 ^{13}CO(2−1)integrated maps of the observed sample 103
5.2 CO analysis for G305.26+0.22 108
5.3 CO analysis for G305.27−0.01 109
5.4 CO analysis for G320.17+0.80 110
5.5 CO analysis for G332.54−0.14 111
5.6 CO analysis for G348.25−0.97 112

5.7 CO analysis for G350.51+0.95 113
5.8 CO analysis for G353.41−0.37 114
5.9 CO analysis for G1.12−0.11 115
5.10 CO analysis for G5.90−0.44 116
5.11 CO analysis for G10.31−0.14 117
5.12 CO analysis for G18.15−0.30 118
5.13 CO analysis for G25.39−0.16 119
5.14 ATLASGAL image of the W31 complex 122
5.15 Multiwavelength view of the G10.31−0.14 bubble 123
5.16 ^{13}CO(2−1) integrated spectrum of the G10.31−0.14 bubble . . 125
5.17 ^{13}CO(2−1) channel maps of G10.31−0.14, from 0 to 29 km s^{-1} 126
5.18 ^{13}CO(2−1) integrated spectrum of the outflow in G10.31−0.14 127
5.19 ^{13}CO(2−1) channel maps of G10.31−0.14, from 5 to 20 km s^{-1} 128
5.20 C^{18}O(2−1) channel maps of G10.31−0.14, from 5 to 20 km s^{-1} 129
5.21 Schematic description of the expanding ring geometrical model 130
5.22 Channel maps of expanding shell model with the back face missing. 131
5.23 Channel maps of expanding shell model with front face missing. 132
5.24 Channel maps of expanding ring model (asymmetrical case) . . 134
5.25 Channel maps of expanding ring model (symmetrical case) . . . 135

List of Tables

3.1 New GLIMPSE stellar cluster candidates. 44
3.2 Number of clusters for every catalog used in this work. 47
3.3 List of spurious clusters, duplicated entries, and globular clusters within the catalogs used in this work. 50

4.1 Number of clusters in each morphological type. 74
4.2 Best-fit parameters from the Z- and D-distributions. 85
4.3 Statistics for each morphological type. 95

5.1 The sample of regions mapped in ^{13}CO(2−1) and C^{18}O(2−1). . 100
5.2 Summary of the ^{13}CO(2−1) and C^{18}O(2−1) mapping observations. 101

B.1 Catalog of embedded and open clusters in the inner Galaxy (main information) 155
B.2 Catalog of embedded and open clusters in the inner Galaxy (additional information) 173
B.3 References for Tables B.1 and B.2. 191

1 Introduction

Stars form by gravitational collapse of high-density fluctuations in the interstellar molecular gas, which are generated by supersonic turbulent motions (Klessen 2011). Most of the mass of the molecular gas in the interstellar medium (ISM) is in the form of giant molecular clouds (GMCs), large structures with sizes from ~ 20 to ~ 100 pc, masses in the range $\sim [10^4, 10^6]\, M_\odot$, and average densities of $n \sim 100$ cm^{-3} (Williams et al. 2000; Beuther et al. 2007). Observations of GMCs in the Milky Way reveal their extremely complex hierarchical configuration, with densities varying by several orders of magnitude, as the result of turbulence. Following the nomenclature of Williams et al. (2000), star formation takes place in dense ($n \gtrsim 10^4$ cm^{-3}) *clumps* which are, in turn, fragmented into denser ($n \gtrsim 10^5$ cm^{-3}) *cores*, where individual stars or small multiple systems are born.

Given this nature of the star formation process, stars are born correlated in space and time, with typical scales of 1 pc and 1 Myr, respectively (see Kroupa 2011), which are much more restricted than those characterizing the field population of the Galaxy. Therefore, recently formed (or forming) stars are found in young stellar agglomerates, still embedded in their parent molecular clumps, referred to as *embedded clusters*. Bressert et al. (2010) studied the spatial distribution of star formation within 500 pc from the Sun and found that, in fact, nearly all stars in their sample are formed in regions with number densities greater than $\sim 2\,\mathrm{pc}^{-3}$, that is more than an order of magnitude higher than the density of field stars in the Galactic disk, $0.13\,\mathrm{pc}^{-3}$ (Chabrier

2001).

Many of the embedded clusters defined in this way, however, are not gravitationally bound and do not become classical open clusters, i.e., bound stellar agglomerates that are free of gas and evolve in timescales of the order of 100 Myr. It is very important to make the distinction from the start because there is often some confusion about this in the literature. In our definition described above and explained in more detail in Section § 2.3, embedded clusters are *not* necessarily the direct progenitors of bound open clusters, but just the natural outcome of the star formation process, which is "clustered" with respect to the field stars. Some embedded clusters could be unbound from birth even considering the gas potential, and disperse into the field, while others, within a giant molecular complex, might merge and form a few merged large entities (Maschberger et al. 2010, see also § 2.1.1). A bound embedded cluster can still be disrupted due to collisional N-body dynamics, tidal shocks from the surrounding gas, or fast gas expulsion driven by stellar feedback (c.f. § 2.2.2). Bound exposed clusters are therefore the few survivors of all these processes (which effect is dominant depends on the physical conditions of the system and the environment) and correspond to the remnants of originally more massive embedded clusters.

Embedded clusters have a strong influence on their parent molecular clouds by injecting energy and momentum through various mechanisms, leading to the expulsion of the residual gas out of the cluster volume and halting the general star formation process. These feedback mechanisms include protostellar outflows, evaporation driven by non-ionizing ultraviolet radiation, photoionization and subsequent H II region expansion, stellar winds, radiation pressure and, eventually, supernovae. Again, as we will see in Section § 2.2.1, the relative importance of a certain dissipation process is determined by both the characteristics of the recently born stellar population and the physical properties of the molecular cloud. Under certain conditions, stellar feedback may also trigger the formation of a new generation of stars in the surrounding molecular material (see § 2.2.3). Therefore, embedded clusters themselves help to regulate star formation in the Galaxy, apart from magnetic fields and large-scale interstellar turbulence.

The observational study of embedded clusters is thus fundamental to account for most of the newly formed stellar population in the Galaxy, and to investigate the interaction with its birth-giving interstellar material through the different feedback mechanisms mentioned above. At the same time, such studies are crucial to understand better the dynamical evolution of embedded clusters towards the production of field stars (through early dissolution) and, in some cases, of bound open clusters, especially when combined with

observations of the latter (as in this thesis).

Nevertheless, there is an observational limitation that impeded the study of embedded clusters till a few decades ago. During their formation and early evolution, embedded clusters are located in regions with high column densities of gas. Since in the ISM there is also cosmic dust, which is well mixed with the gas in a roughly constant mass proportion of $\sim 1\%$, a high column density of gas translates in a relatively high column density of dust too. Dust is composed of solid grains of typical sizes of 0.1 μm that efficiently extinguish starlight at optical wavelengths, making embedded clusters heavily obscured from optical observations and practically impossible to study at these wavelengths. Fortunately, during the past three decades, the development of infrared (IR) astronomy including, more recently, near-infrared ($1-3$ μm) imaging cameras and spectrometers on ground-based telescopes, and mid-infrared ($3-25$ μm) cameras on space telescopes, has provided astronomers the ability to survey and systematically study embedded clusters within molecular clouds, thanks to the fact that IR radiation is much less affected by dust extinction than visible light. An example of the power of infrared imaging for revealing the stellar population of embedded clusters is presented in Figure 1.1, which shows the southern young cluster RCW 38. While the optical image (*top*) is able to detect only the brightest (most massive) members, the IR image (*bottom*) clearly probes a rich cluster embedded in nebulosity.

In the last decade, thanks to the development of all-sky infrared imaging surveys like 2MASS and GLIMPSE (c.f. § 1.1), many new embedded clusters have been discovered in the Galaxy (e.g., Dutra et al. 2003a; Bica et al. 2003b; Mercer et al. 2005; Borissova et al. 2011), increasing significantly the number of known systems. In this thesis, we study systematically all embedded clusters and open clusters known so far in the inner Galaxy, investigating particularly their interaction with the surrounding molecular environment. We take advantage of the recently completed ATLASGAL survey, which provides us a completely unbiased view of the distribution of the dense molecular material in the Milky Way. The main observational data used in this work is described in the next Section, and at the end of this chapter we outline the scientific goals of this thesis and the content of the following chapters.

1.1 Observational tools: Galactic surveys

Throughout this work, me make extensive use of three surveys of continuum emission that cover practically the whole inner Galactic plane: ATLASGAL in the submillimeter regime, 2MASS in the near-infrared (NIR), and GLIMPSE in the mid-infrared (MIR).

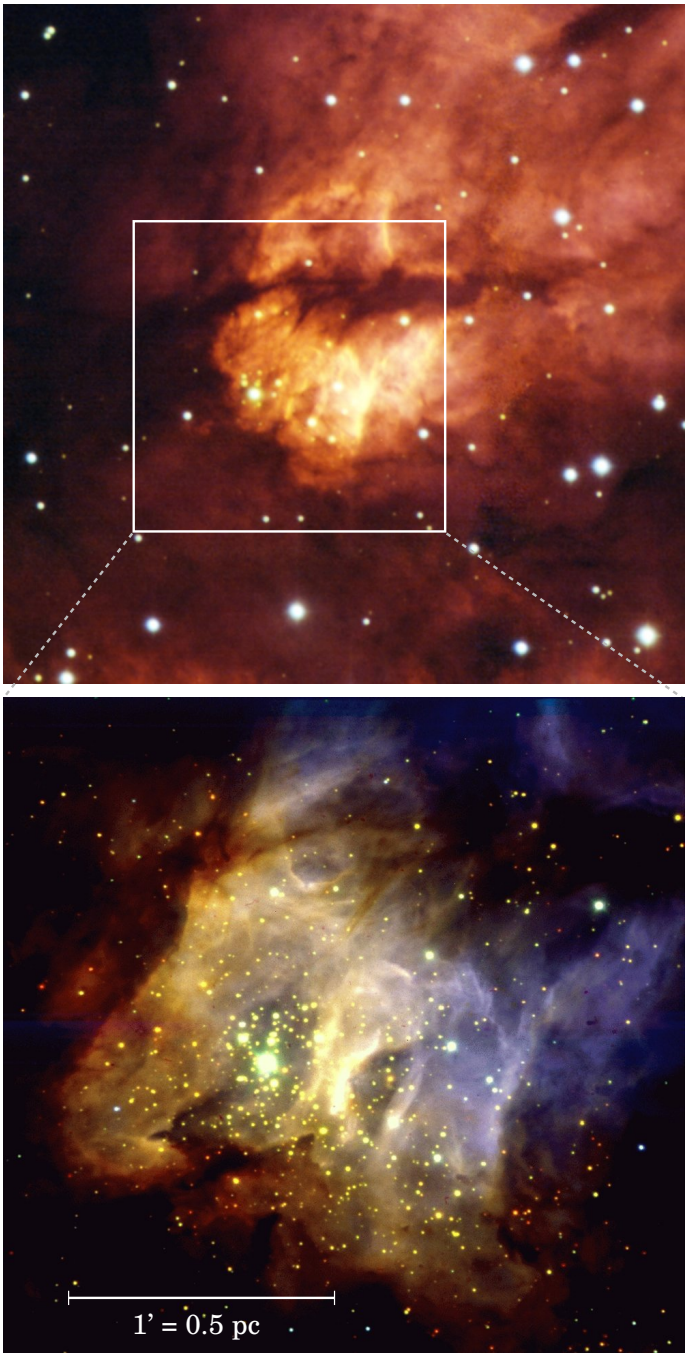

Figure 1.1: The southern embedded cluster RCW 38. *Top:* Optical 4-color image made with the B, R, and Hα filters at the MPG/ESO 2.2m Telescope. Credit: ESO. *Bottom:* Near-infrared JHK image obtained with the ESO Very Large Telescope. The field of view is about 2.5′ ($\sim$ 1.2 pc). Credit: ESO.

1.1.1 ATLASGAL

The APEX Telescope Large Area Survey of the Galaxy (ATLASGAL, Schuller et al. 2009) is the first unbiased submm continuum survey of the whole inner Galactic disk, covering a total of 360 square degrees of the sky with Galactic coordinates in the range $|l| \leq 60°$ and $|b| \leq 1.5°$. The observations were carried out at 870 μm using the Large APEX Bolometer Camera (LABOCA; Siringo et al. 2009) of the the APEX telescope (Güsten et al. 2006), located on Llano de Chajnantor, Chile, at 5100 m of altitude. With an antenna diameter of 12 m, the observations reach an angular resolution of $19.2''$ at this wavelength.

The submm continuum emission primarily corresponds to gray-body radiation from cold dust located in regions of relatively dense molecular gas (see Figure 5.14 for an example image of ATLASGAL). The emitting dust grains are at typical temperatures $T_{\rm d}$ in the range $[10, 30]$ K, and are generally in equilibrium with the gas molecules. In the submm regime, this dust emission is optically thin (see Schuller et al. 2009), so that the received flux is directly proportional to the total amount of dust, and hence of total cloud's material (assuming a constant gas/dust mass ratio), on the line of sight. Simple relations can be derived for the column density as a function of flux per beam, and for the mass as a function of the total flux of a source (see appendix A by Kauffmann et al. 2008, and Eq. (5.5)). The ATLASGAL survey reaches an average rms noise level of ~ 50 mJy/beam, which translates in a 3σ detection limit of $\sim 4\ M_{\odot}$ of total molecular mass (for a nominal distance of 2 kpc and a dust temperature of $T_{\rm d} = 20$ K).

1.1.2 2MASS

The Two Micron All Sky Survey (2MASS, Skrutskie et al. 2006) provides near-infrared images of the whole sky, in the J (1.25 μm), H (1.65 μm), and K_s (2.16 μm) filters, taken from two dedicated 1.3 m diameter telescopes located at Mount Hopkins, Arizona, and Cerro Tololo, Chile. The angular resolution is $\sim 2.5''$ or slightly higher (depending on the seeing conditions) and the reached 10σ detection levels for point sources were typically 15.8, 15.1, and 14.3 magnitudes for J, H, and K_s, respectively. These wavelengths trace primarily starlight, but in young clusters there is usually a contribution from nebular extended emission from ionized gas, and radiation from warm circumstellar dust in the immediate vicinity of individual protostars, generally distributed in disks and not resolved by these observations. The 2MASS images and point source catalog are publicly available.

1.1.3 GLIMPSE

The Galactic Legacy Infrared Mid-Plane Survey Extraordinaire (GLIMPSE, Benjamin et al. 2003; Churchwell et al. 2009) is a set of various surveys of the Galactic plane carried out with the InfraRed Array Camera (IRAC, Fazio et al. 2004), on board of the *Spitzer Space Telescope* (Werner et al. 2004). Here we use the GLIMPSE I and II surveys which cover the (l, b) ranges: $5° < |l| \leq 65°$ and $|b| \leq 1°$; $2° < |l| \leq 5°$ and $|b| \leq 1.5°$; $|l| \leq 2°$ and $|b| \leq 2°$, comprising a total of 274 square degrees. The IRAC camera provides images at four filters centered at wavelengths 3.6, 4.5, 5.6, and 8.0 μm, with an angular resolution of $\sim 2''$. The GLIMPSE products are publicly available and consist of mosaic images, a highly reliable point source catalog, and the slightly lower reliability but more complete point source "archive".

In star-forming regions, the four *Spitzer*-IRAC filters are dominated by different emission mechanisms. One of the most relevant features is the mid-infrared emission from polycyclic aromatic hydrocarbons (PAHs), which are large organic molecules containing tens or hundreds of C atoms. Exposure to ultraviolet (UV) radiation excites various vibrational modes of the PAHs causing them to radiate strongly as emission features in the infrared. While UV photons of sufficiently low energy excite PAH emission, harder UV photons, as those above the Lyman limit, destroy these molecules. Therefore, PAH emission is strong in photo-dissociation regions (PDRs), that lie just outside ionized gas regions.

The main emission processes for each IRAC band are the following (see introduction of Watson et al. 2008):

- 3.6 μm: Brightest objects are stars, while faint diffuse emission traces a weak PAH feature at 3.3 μm and possibly some scattered starlight.
- 4.5 μm: Brightest objects are stars, and localized diffuse emission might be tracing shocked H_2 and/or CO lines; when present, this emission is usually interpreted as the activity of protostellar outflows crashing into the ambient interstellar medium (see Cyganowski et al. 2008, and references therein). The 4.5 μm filter contains no PAH features.
- 5.8 μm: This filter contains a strong PAH feature at 6.2 μm, which can dominate the diffuse emission except close to ionizing stars, where PAHs are destroyed and radiation from thermal dust is probably the main emission mechanism.
- 8.0 μm: This filter contains two very strong PAH features at 7.7 and 8.6 μm which dominate the diffuse emission in this band; again, close to ionizing stars, this filter mainly traces warm dust.

The GLIMPSE surveys have revealed very peculiar structures in star-forming regions (a summary is provided in § 2 of Churchwell et al. 2009). In particular, *infrared dark clouds* (IRDCs), already found in previous MIR surveys, are seen as extinction features against the bright and diffuse mid-infrared Galactic background, specially at 8.0 μm. They represent the densest and coldest condensations within giant molecular clouds and are the most likely sites of future star formation. On the other hand, bright PAH emission is often confined to ring-like structures known as *IR bubbles*, which in most cases are tracing the molecular material swept up by the expansion of H II regions created by the ionizing UV radiation from massive stars (Deharveng et al. 2010). Specifically, the bright rims of the bubbles are likely tracing the inner surface of the swept-up neutral gas, just outside the ionization front (see § 2.2.1), where the UV field is strong enough to highly excite PAHs but below the destruction limit of these molecules.

1.2 This Thesis

Although the current sample of embedded clusters in the Galaxy has considerably improved over the last years, so far there has not been any systematic analysis in the literature dealing with the whole sample; in particular there is no study combining all observed embedded and open clusters in an important fraction of the Galaxy. The first goal of this thesis is thus the construction of a merged list of all embedded and open cluster catalogs from the literature, dealing properly with cross-identifications and placing particular emphasis in the part of the Galactic plane covered by ATLASGAL ($|l| \leq 60°$ and $|b| \leq 1.5°$), where all further analysis is done.

While the distinction of embedded clusters from open clusters in these catalogs has been made primarily via correlations with known H II regions or nebulae seen in the IR, the ATLASGAL survey allows us to objectively discriminate[1] whether or not these objects are associated with dense molecular material, in an unbiased and uniform way. This redefinition is important since we have seen that embedded and open clusters are different astrophysical objects. On the other hand, the distribution of the ATLASGAL emission towards each one of the clusters of our sample, if present, tells us how embedded is the cluster and gives us some clues about the importance of the stellar feedback, allowing us to delineate possible evolutionary stages. As mentioned before, with proper statistics of these different stages, mainly of embedded clusters relative to open clusters, we can test the different disruption mechanisms that

[1] In combination with velocity information for cases of ambiguous physical relation.

are dominant at different stages of evolution and understand better how embedded clusters evolve into the production of field stars or bound open clusters. For embedded clusters (and young open clusters also), further clues about the relative evolutionary differences are provided by the characteristics of the mid-infrared emission available from the GLIMPSE survey, via identification of IRDCs, and IR bubbles or more irregular PAH emission. In this work, we aim at addressing all these issues through careful inspection of each individual cluster within the ATLASGAL range, and subsequent statistics with an appropriate treatment of the incompleteness.

The work presented in this thesis is organized in the following chapters:

- Chapter 2 gives a review of the current understanding of embedded cluster formation and early evolution, presenting the results of recent observational and theoretical investigations. The covered topics include the theories of embedded cluster formation, the observed spatial distribution of newly formed stars, stellar feedback mechanisms, the early dynamical evolution of an embedded cluster, and triggered star formation. A companion appendix (Appendix A) presents some basic concepts of the classical evolution of an open cluster, some of which are still useful when studying embedded clusters.

- In Chapter 3, we describe the literature compilation of all embedded and open clusters known so far in the Galaxy, including a new search for embedded cluster we conducted on the GLIMPSE survey. We explain how we constructed our final all-sky list after cross-identification, and discuss about spurious detections.

- Chapter 4 presents a thoughtful study of the cluster sample within the ATLASGAL Galactic range. We first constructed a big catalog with many pieces of information regarding the characteristics of the ATLASGAL and mid-infrared emission; correlation with IRDCs, IR bubbles, and H II regions; distances (kinematic and/or stellar) and ages; and membership in big molecular complexes. We then delineate a possible evolutionary sequence and define embedded and open cluster types based on ATLASGAL emission; study the spatial distribution and completeness; and analyze the age distribution of open clusters in combination with the statistics and typical ages of embedded clusters. The whole list of clusters within the ATLASGAL range is given in Appendix B, together with an important fraction of the compiled information in our catalog.

- In Chapter 5, we describe a follow-up study of the gas kinematics of a subsample of 14 clusters exhibiting signposts of stellar feedback, via ded-

icated ^{13}CO(2−1) and C^{18}O(2−1) mapping observations. In particular, we present a detailed analysis of the IR bubble G10.31−0.14.

- Finally, Chapter 6 summarizes the main conclusions of this thesis.

2

The current understanding of embedded cluster formation and early evolution

2.1 Formation of embedded clusters

2.1.1 Theories

Galactic molecular clouds have ubiquitously presented observational evidence of supersonic turbulence (e.g., McKee & Ostriker 2007). On large scales, turbulence is highly supersonic and support the cloud against global gravitational collapse. At the same time, however, supersonic turbulence creates a highly transient and inhomogeneous molecular cloud structure which is characterized by large density contrasts produced by shocked layers of gas. Under the right conditions, high-density fluctuations can become gravitationally unstable and decouple from the overall turbulent flow. The largest and most massive of these fragments, or *clumps*, are potential sites of cluster formation. It is known that the density contrast for isothermal gas scales with the Mach number $\mathcal{M}$ to the second power (Klessen 2011), which means that for a typical $\mathcal{M} \sim 10$ we expect density contrasts of roughly 100, consistent with the observed ratio between clump (10^4 cm^{-3}) and global (100 cm^{-3}) average densities in GMCs. When zooming in on cluster-forming clumps, one still observes supersonic Mach numbers of $\mathcal{M} \sim 5$, still leading to localized density fluctuations of a factor of 25

on average, which may exceed the critical mass for gravitational collapse to set in. The presence of turbulence, therefore, makes the massive clump to break apart into smaller units, or *cores*, and build up a cluster of stars with a wide range of masses. This process is called gravoturbulent fragmentation, because turbulence generates the distribution of clumps/cores initially and then gravity selects a subset of them for star formation (Klessen 2011).

While now it is quite accepted that the density fluctuations that allow local gravitational collapse in molecular clouds are produced by supersonic turbulent motions, the exact mechanism through which the clump gas is accreted onto the forming stars is not clear. Currently, there are two main possible models regarding the formation itself of a stellar cluster that would explain the origin of the so-called initial mass function (IMF), the distribution of stellar masses at birth. This is now a key prerequisite to any theory of star formation given that the IMF derived from observations presents strong evidences of universality in diverse environments (e.g., Kroupa 2002; Bastian et al. 2010). In the *core accretion* model, collapses that produce individual stars or small multiple systems within a massive clump are local, so that different protostars are for the most part not accreting from the same mass reservoir. The mass distribution of the stars is set by the mass distribution of the regions of localized collapse, the *cores* (e.g., Padoan & Nordlund 2002; Hennebelle & Chabrier 2008, 2009). In contrast, in the *competitive accretion* model, collapses that produce star clusters are global in nature, so all stars accrete from the same mass reservoir. In this case, the stellar mass distribution is determined by a competition between formation of new, small fragments and growth of existing fragments that continue accreting gas, specially at the center of the proto-cluster potential (e.g., Bonnell et al. 2001; Bonnell & Bate 2006). One of the critical differences between these two models is the formation of high-mass stars, which would require, in the case of core accretion, the existence of single collapsing massive cores that must not fragment during the star formation process in order to be able to build up a single or binary massive star. Whereas some hydrodynamic simulations have indeed shown massive core fragmentation (e.g., Dobbs et al. 2005), this can be reduced by considering the influence of protostellar radiation on the gas heating (Krumholz et al. 2007), under the assumption that the internal sources are formed before the core becomes susceptible to fragmentation.

Figures 2.1 and 2.2 show different snapshots of a smoothed particle hydrodynamics (SPH) simulation of star formation in a GMC, performed by Bonnell et al. (2011). The initial conditions consist of a $10^4 M_\odot$ cylindrical molecular cloud of 10 pc length and 1.5 pc radius, a turbulent velocity field, and a linear density gradient along the major axis making the top region grav-

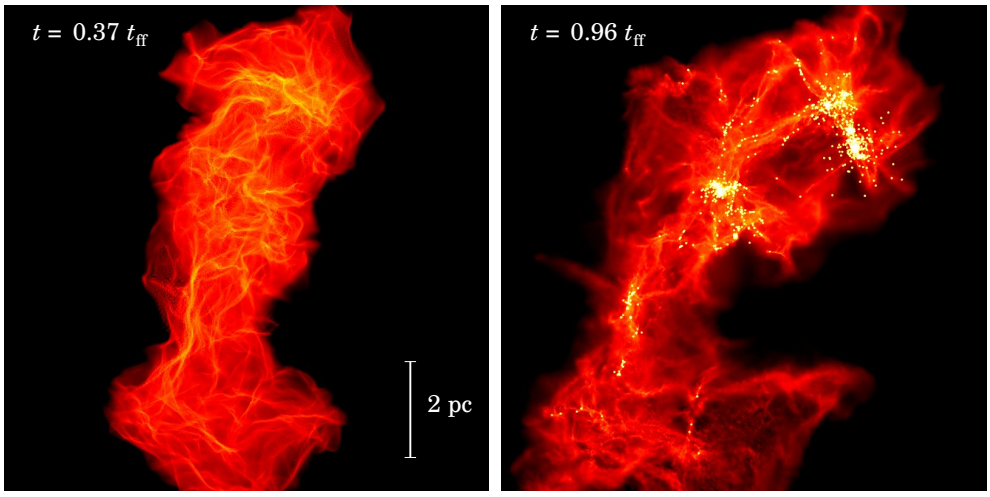

Figure 2.1: Hydrodynamic simulations of star formation in a Giant Molecular Cloud, shown at times $0.365\,t_{\rm ff}$ (*left*) and $0.961\,t_{\rm ff}$ (*right*), with $t_{\rm ff} \simeq 0.66$ Myr. The size scale of each panel is 10 pc on a side. The gas column densities are plotted on a logarithmic scale from 0.01 g cm^{-2} (black) to 100 g cm^{-2} (white). Yellow and white dots are sink particles representing forming stars. (From Bonnell et al. 2011).

itationally bound, while keeping the lower region slightly unbound. It can be seen on the left panel of Fig. 2.1, which shows the simulation at $0.365\,t_{\rm ff}$ (with $t_{\rm ff} \simeq 0.66$ Myr), how turbulence and self-gravity establishes a complex network of overdense filamentary structures from an initially smooth density distribution. Subsequent fragmentation lead to the formation of dense cores, specially at the intersection of such filaments, where further gravitational collapse gives birth to the first protostars, at a time of about $0.4\,t_{\rm ff}$ in this simulation. The right panel presents a snapshot at $0.961\,t_{\rm ff}$, close to the final computation time, and shows the formed stars as white and yellow dots, represented numerically as "sink particles" (point masses with the ability to accrete further gas). The majority of the stars have formed in the upper gravitationally bound part of the molecular cloud, mostly in a clustered mode, whereas a smaller fraction have formed in the lower, gravitationally unbound regions, in a more distributed way (see also § 2.1.2). If we zoom in on the top region around the highest stellar densities and display different simulation times (Fig. 2.2), we can have a better idea of the assembly history of the formed star clusters there. Newly born stars fall into local potential wells and form small-N subclusters which quickly grow by accreting other stars (and gas) that flow along the filaments into the subcluster potential. Maschberger et al. (2010) carried out a detailed analysis of the evolution of clustering in these simulations, following the track of individual stars over the time, and found that the system in this region undergoes a process of hierarchical merging of small-N subclusters and evolves

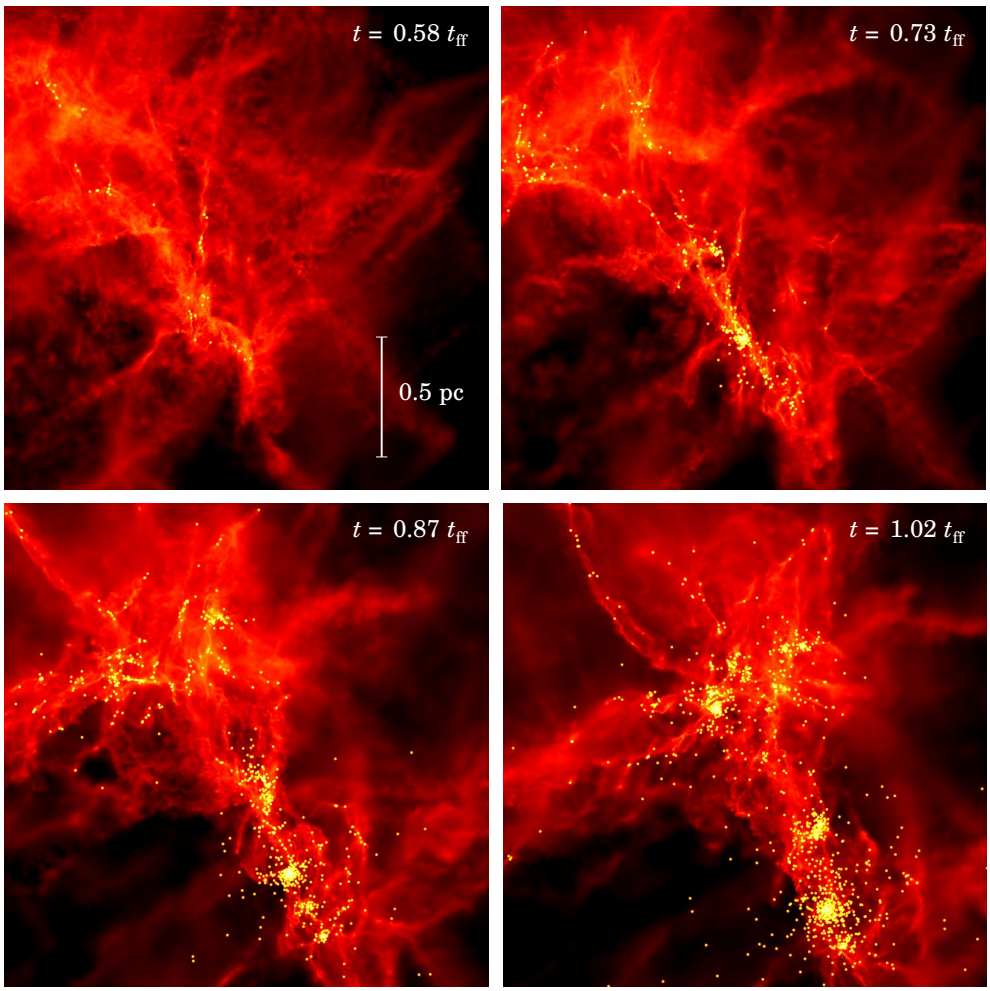

Figure 2.2: Zoomed-in image of the star formation hydrodynamic simulations presented in Fig. 2.1, shown at times 0.58, 0.73, 0.87 and 1.02 $t_{\rm ff}$ ($t_{\rm ff} \simeq 0.66$ Myr) from left to right, and top to bottom. The size scale of each panel is 2 pc on a side. The gas column densities are plotted on a logarithmic scale from 0.01 g cm^{-2} (black) to 100 g cm^{-2} (white). Yellow and white dots are sink particles representing forming stars. (From Bonnell et al. 2011).

into a few merged large entities.

It is worth noting that similar simulations to the ones presented by Bonnell et al. (2011) have been analyzed in the framework of competitive accretion (Smith et al. 2009), but also as statistically consistent with the core accretion scenario (Chabrier & Hennebelle 2010). In this kind of simulations, however, the overall gravitational collapse of a bound cluster-forming clump is fast and efficient, as Krumholz et al. (2011) claim is required by the competitive accretion model. These authors challenged the applicability of these simulations to interpret observed properties, particularly regarding the resulting stellar mass distribution. They conducted their own hydrodynamic simulations of a $1000\,M_{\odot}$ molecular clump centrally condensed and initially turbulent, but adding also a detailed treatment of stellar radiative feedback. The found that, once the first $\sim 10\% - 20\%$ of the gas mass is incorporated into stars, their radiative feedback raises the gas temperature high enough to suppress any further fragmentation. However, gas continues to accrete onto existing stars, and, as a result, the stellar mass distribution becomes top-heavy, which is incompatible with the observed IMF. More recently, additional simulations by Krumholz et al. (2012), including now protostellar outflows and starting from self-consistently turbulent initial conditions (density and velocity fields embedded in a realistic surrounding turbulent molecular cloud), have solved the clump overheating problem and reproduce the observed IMF, because the external turbulent driving and the internal mechanical feedback slow star formation down and decrease the artificially high accretion luminosity of the former simulations. This example illustrates the importance of including all the possible pieces of physics in future star formation simulations, as a high variety of ingredients can interplay at the same time. In fact, Krumholz et al. (2012) claim that the star formation rate in their simulations is still high compared to the observed, and that a possible solution is the inclusion of magnetic fields, and other stellar feedback mechanisms in addition to protostellar outflows (see § 2.2.1).

For more details about the current star formation models and simulations briefly described here, and how they match the observed properties in star-forming regions, in particular the IMF, we refer to the reviews by Clarke (2010) and Klessen (2011), and the recent works by Krumholz et al. (2011, 2012).

2.1.2 Spatial distribution and clustering

It is often stated that most stars, if not all, form in clusters (e.g., Lada & Lada 2003). Nevertheless, the veracity of this premise as well as any quantitative estimate of the fraction of stars actually formed in clusters is highly dependent

on the actual definition of a *stellar cluster*.

The notion that most stars form in clusters has been based primarily on systematic, large-scale near-infrared surveys of individual GMCs within the solar neighborhood (e.g., Carpenter 2000), aimed at placing constraints on the spatial distribution of young stellar objects (YSOs) by using star counts methods[1], i.e., identifying overdensities in the whole set of detected sources, typically in the K-band (2.2 μm). These techniques were excellent in picking up the dense inner structures of clusters, but largely missed the lower density regions where the distinction of YSOs from foreground and background stars is extremely difficult and uncertain.

With the advent of the *Spitzer Space Telescope*, YSOs could be identified based on the mid-infrared colors, and hence their spatial distribution could be studied independently of the surface densities. Large field-of-view *Spitzer* observations of nearby star-forming regions (see Allen et al. 2007) found that YSOs extend well beyond the densest groups in their environment and continue throughout. As an example of this, we illustrate in Figure 2.3 the distribution of *Spitzer*-identified YSOs in the Orion A cloud (Megeath et al. 2005), the most active star forming cloud within 450 pc of the Sun. The observed distribution exhibits structure on a range of spatial scales and stellar densities. A significant fraction of YSOs is found within the well-known massive cluster in the Orion Nebula (ONC), which is easily distinguished in the figure as a large and centrally condensed cluster of sources to the northern edge of the cloud. However, numerous YSOs are also located in smaller groups, as the known L1641 North, V380, L1641 Center and L1641 South, and in a distributed population of relatively isolated sources which fills in much of the space between the groups.

Bressert et al. (2010) further explored the spatial distribution of star formation by studying several *Spitzer* surveys that cover nearly all the star-forming regions within 500 pc of the Sun. They found a smooth distribution of YSO surface densities (number of sources per pc^2) without evidence for multiple discrete modes of star formation, i.e., there is not a clear way to distinguish between clusters, associations, or distributed star formation. The resulting cumulative surface density distribution plots are presented in Figure 2.4. If there were discrete modes of star formation, then we would expect to see a bi-modal or multi-modal profile instead of the obtained smooth and featureless distributions from the low to high stellar surface densities. They showed that the YSO surface density distribution is well described by a lognormal function, which is consistent with predictions of hierarchically structured star formation, where

[1] A description and comparison of different cluster finding algorithms is recently given by Schmeja (2011).

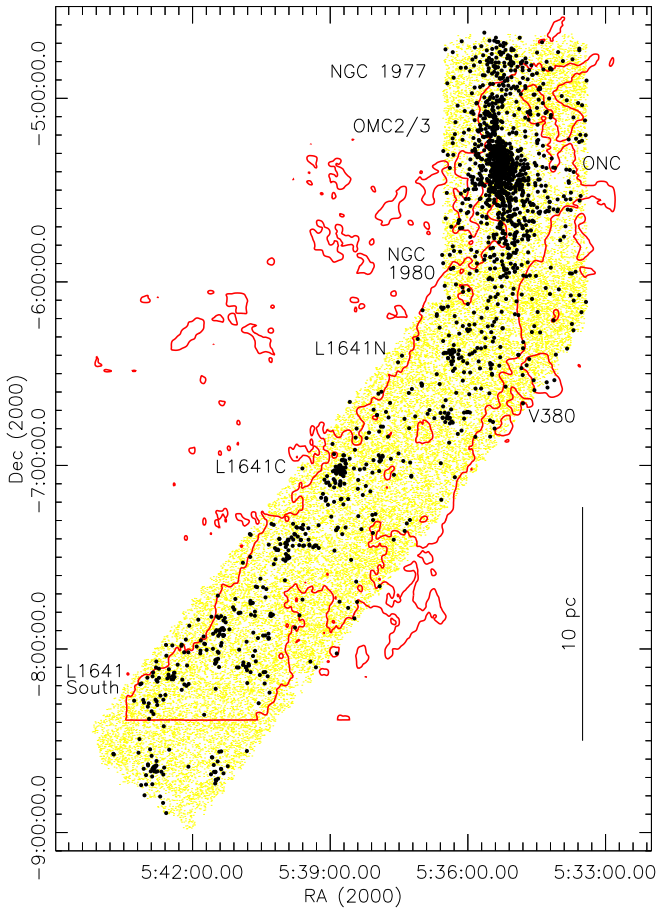

Figure 2.3: Distribution of young stars in the Orion A molecular cloud. The red contour outlines the 5 K km s^{-1} level of the velocity integrated ^{13}CO$(1-0)$ emission from the Bell Labs maps. The yellow dots mark all point sources detected in the 3.6 μm and 4.5 μm bands (which of course includes foreground and background stars), while the black circles indicate the positions of the identified YSOs based on mid-infrared colors. Labels mark the the locations of known regions, nebulae or stellar groups. (From Megeath et al. 2005).

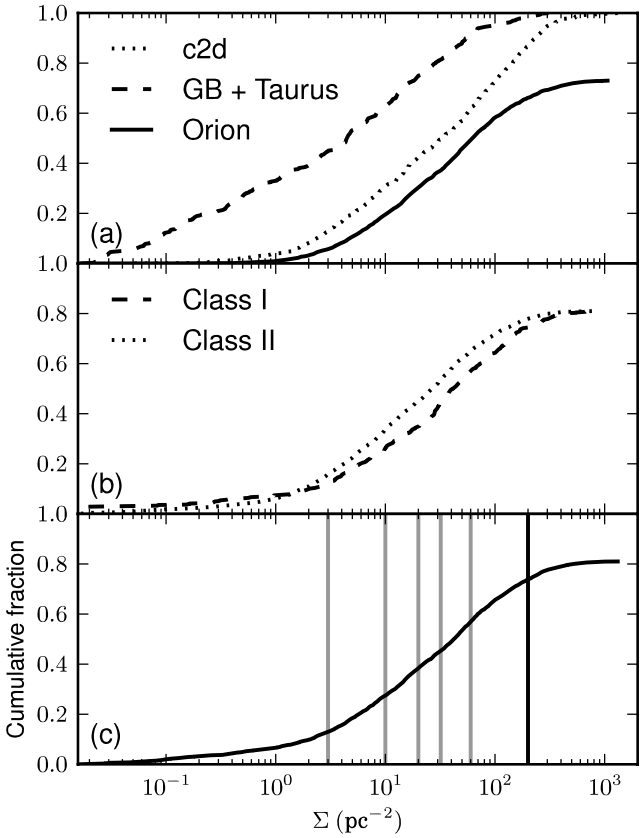

Figure 2.4: Cumulative fraction of YSO surface densities (Σ) in the solar neighborhood. (a) Distributions for the GB+Taurus, c2d and Orion *Spitzer* surveys. The Orion survey stops at 80% for the cumulative fraction since the ONC is excluded. (b) Class I & II distributions for all the surveys combined. The similarity shows that we are likely seeing the primordial distribution of the YSOs. (c) Combined distribution compared with different cluster definitions. The vertical gray lines from left to right are Lada & Lada (2003), Megeath et al. (in preparation), Jørgensen et al. (2008), Carpenter (2000) and Gutermuth et al. (2009) stellar density requirements for *cluster* definition, corresponding to Σ = 3, 10, 20, 32 and 60 YSOs pc^{-2}, and implying that 87, 73, 62, 55 and 43 per cent of stars form in clusters, respectively. The black vertical line is for a dense cluster with $\Sigma \geq 200$ YSOs pc^{-2}, corresponding to a fraction of $< 26\%$ of the YSOs. (From Bressert et al. 2010).

the structure comes from the hierarchical ISM (see discussion by Bressert et al. 2010, and references therein). They conclude that stars form in a broad and continuous spectrum of surface densities.

Similar results were reached by Kruijssen et al. (2012), who analyzed the outcome of SPH simulations performed by Bonnell and coworkers[2], extending the work by Maschberger et al. (2010). The obtained spatial distribution of sink particles at the end of the simulation (at about one $t_{\rm ff}$) is shown in Figure 2.5, where we can see a wide range of substructure and stellar density, nicely resembling the appearance of a typical distribution of observed YSOs within a molecular cloud (Fig. 2.3). In fact, Kruijssen et al. (2012) also found a smooth surface density distribution for the sink particles, following an approximately lognormal distribution similar to that observed by Bressert et al. (2010). The stellar surface densities at the end of the simulation are, however, several orders of magnitude higher than the observed YSO densities. According to Kruijssen et al. (2012), two reasons would explain this discrepancy: 1) crowding obstructs the observation of the densest parts of star-forming regions, which are therefore not included in the Bressert et al. (2010) sample; and 2) the high densities that are achieved in the simulation are likely the result of the initial conditions. Indeed, Moeckel et al. (2012, see § 2.2.2) took the outcome of the Bonnell et al. hydrodynamic simulations and evolved its sink particles forward using a N-body code, and found that the system expands significantly within a short timescale, so that the surface stellar densities match the observed YSO densities after only 2 Myr. If we add the total time of the hydrodynamic simulation since the first stars are born, this translates into ~ 2.4 Myr, which agrees well with the typical ages of young stellar clusters.

The smooth distribution of surface densities of recently born stars in molecular clouds makes any definition of a *stellar cluster*, and hence the estimation of the fraction of star formed in clusters, somewhat arbitrary. Usually, the criteria are based on "by-eye" perceptions or are empirically derived from the data being considered. For example, the works by Maschberger et al. (2010) and Kruijssen et al. (2012) employed a minimum spanning tree (MST) clustering algorithm[1] to detect subclusters of sink particles in the simulations (see Fig. 2.5), and adjusted the free parameter, the so-called break distance, to match the type of subclusters which would be identified by the human eye. They found that at the end of the simulation by Bonnell et al. (2011), about 60% of the stars are located in such clusters, but as acknowledged by Maschberger et al. (2010), this identification does not imply a priori that the clusters are bound or long

[2]The simulations analyzed there are the same presented by Bonnell et al. (2011), see § 2.1.1

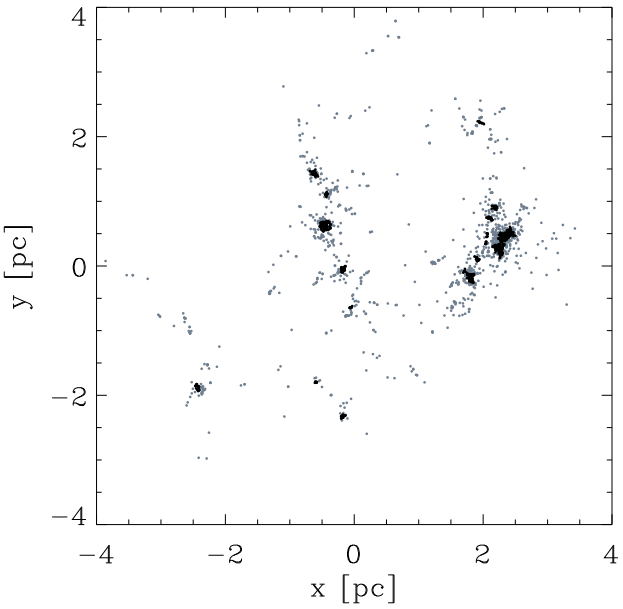

Figure 2.5: Spatial distribution of sink particles present at the end of the SPH simulation by Bonnell et al. (2011), projected on the x-y plane. Black particles constitute subclusters identified by a MST algorithm, the remaining population is represented by dark gray particles. Since the spatial extent of the simulation in the z-direction is larger than in the x-y plane, some of the apparent clustering is the result of the projection. (From Kruijssen et al. 2012).

lived[3]. Bressert et al. (2010) investigated different cluster definitions from the literature and what they mean in terms of stellar surface density (vertical gray lines in Fig. 2.4(c)), resulting in a wide range of estimates for the fraction of star formation in clusters. Considering the empirically derived definitions from observations, this fraction ranges from 43% to 73%.

An attempt of physically motivated definition of a stellar cluster was done by Lada & Lada (2003), who considered the dependence of the typical cluster dissolution times (by different disruptive agents), required to be ≥ 100 Myr, on the stellar density and on the number of member stars, N. The minimum stellar-mass volume density needed for the cluster to survive encounters with interstellar molecular clouds is $\sim 1\,M_\odot$ pc^{-3} (see equation (A.9)), equivalent to a number surface density of 3 pc^{-2} (Bressert et al. 2010). The constraints on N imposed by Lada & Lada (2003) are, however, based on analytical approximations of the dissolution times, which are only valid for N sufficiently

[3]Interestingly, as we describe in § 2.2.2, these identified subclusters were found to be bound and close to virial equilibrium (Kruijssen et al. 2012), but not necessarily long lived (Moeckel et al. 2012).

large to treat the system statistically, and are highly dependent on the specific equations that are used. Indeed, if we assume $t_{\rm diss} \simeq 100\, t_{\rm relax}$ as Lada & Lada (2003), but the more accurate expression for the relaxation time given in the appendix (equation (A.15)), we would obtain no constraint at all on N, i.e., $t_{\rm diss} \geq 100$ Myr always, even for a small group of $N \simeq 7$ stars[4]. We would still get the same result if we use the more realistic dissolution timescale of a cluster within the Galactic tidal field (equation (A.8)), for which a smaller number of members would decrease its lifetime by a fraction of at most ~ 0.4 with respect to the lifetime for $N \simeq 100$ (~ 144 Myr in the solar neighborhood). This would not represent a real restriction on N to define a stellar cluster.

Applying only the surface density criterion of Lada & Lada (2003), Bressert et al. (2010) found that nearly all stars in their sample ($\sim 90\%$) are formed in clusters defined in such way. But what about the remaining 10%? Recently, Kroupa (2011) introduced the concept of *Correlated Star Formation Event* (CSFE), which means a group of stars formed over a spatial scale of about one pc within about one Myr. CSFEs would account for the totality of the star formation in the Galaxy, because it is known to be confined to the dense cores of molecular clouds. Kroupa (2011) claims that even a gravitationally self bound structure (i.e., a classical star cluster) has always a certain fraction of its stars below a density threshold in its outer regions, so that an observer who applies a density threshold to define "clustered star formation" would always find some stars formed in "isolation". This is consistent with the idea presented above that stars form in a smooth distribution of surface densities.

In conclusion, we can say that all star formation occurs in groups or "clusters" correlated in time and space (the CSFEs), keeping in mind that only a part of those groups are gravitationally bound and will be the direct progenitors of the classical open clusters. Observations and simulations have shown that stars are born in a broad and continuous spectrum of surface densities, with an important fraction of them forming within more dense clusters. However, any quantitative estimate of this fraction, given the nature of the surface density distribution, is very dependent on the threshold used to define these denser stellar systems. Empirically derived definitions used so far imply a fraction around $\sim 50\%$.

[4]The computation is limited to $N > 6$, where the Coulomb logarithm, $\ln \Lambda \simeq 0.15N$, becomes unphysical.

2.2 Gas disruption

Currently, it is unclear if the star formation process occurs fast, on a free-fall timescale[5] (Elmegreen 2007; Klessen 2011), or more slowly on a timescale covering many free-fall times (Krumholz & Tan 2007). Whatever regime takes place in reality, the observed values for the *star formation efficiency* (SFE) imply that feedback from the recently born stars should halt the star formation at some point by removing the residual gas, as explained in the following. The SFE is defined throughout this work as

$$\epsilon \equiv \frac{M_\star}{M_\star + M_{\rm gas}} \ , \tag{2.1}$$

where $M_\star$ and $M_{\rm gas}$ are, respectively, the stellar and gas mass associated with the cluster.[6] Observational studies of embedded clusters (Lada & Lada 2003; Evans et al. 2009; Higuchi et al. 2010) have shown that the measured SFE ranges from a few percent ($\epsilon \simeq 3\%$) to about 30%, and suggest that ϵ is an increasing function of time, as expected for a finite gas reservoir. Whether all clusters can reach SFEs as high as 30% is not clear; however, it does seem apparent that embedded clusters rarely achieve $\epsilon \geq 30\%$. This limit is relatively low compared to the final SFEs that would be obtained if most of the gas were consumed to form stars ($\epsilon \simeq 100\%$), implying that stellar feedback quenches further star formation after only a small fraction ($\leq 1/3$) of the initial mass has been converted to stars. This is likely done through the quick expulsion of the remaining gas by the energy and momentum injected by young stars. Indeed, clusters with ages greater than ~ 5 Myr are rarely associated with molecular gas (Leisawitz et al. 1989), and this timescale corresponds to a few crossing times of a typical star cluster (about 1 Myr).

2.2.1 Stellar feedback in young clusters

There are several possible sources of internal energy and momentum that may drive the disruption of the residual molecular gas within a stellar cluster, depending on the physical properties of the system. For star-forming clouds that were not able to form an O star or an early B star, the ionizing flux is not sufficiently strong to cause the expulsion of the totality of the gas out of the cluster boundaries (see below). In these regions, protostellar outflows

[5] The free-fall time satisfies $t_{\rm ff} \simeq t_{\rm cross}$, where the latter is the crossing time defined in equation (A.1)

[6] The SFE as defined here should not be confused with the SFE *per free-fall time*, $\epsilon_{\rm ff} = \dot{M}_\star t_{\rm ff}/M_{\rm gas}$ (Krumholz & McKee 2005), which measures the rate of star formation and therefore depends on whether it is fast or slow.

may be the predominant mechanism for gas disruption, as studied analytically by Matzner & McKee (2000). Observational support of this theory has been provided by, e.g., Quillen et al. (2005), who found evidence of wind-blown cavities in the molecular gas of the young low-mass cluster NGC 1333. Based on *Spitzer* observations of nearby embedded clusters, Allen et al. (2007) suggested an additional dissipation process that might be occurring on clusters containing (not early) B stars. They noted that some of such clusters are located within cavities filled with emission from PAH molecules (see § 1.1.3), which are excited by non-ionizing ultraviolet (UV) radiation, in this case from B type stars. The corresponding gas disruption mechanism would consist of the heating of the molecular cloud surfaces by this kind of radiation, and subsequent evaporative flows. However, the importance of this effect has not been studied quantitatively yet.

For systems with high-mass (O and early B) stars, which emit copious Lyman continuum photons that rapidly ionize the neutral medium, the gas disruption can be driven by the evolution of the H II regions. In the classical model (Spitzer 1978), which assumes that the ambient medium is homogeneous, a very short H II region formation phase of a few years is followed by its expansion due to the high over-pressure of the warm ionized gas ($T_e \simeq 10^4$ K) with respect to the cold neutral surrounding medium (T_0 in the range $[10, 100]$ K). The expansion velocity can exceed the (significantly lower) sound speed in the ambient medium, hence the ionization front is preceded by a shock front on the neutral side. Formally, the expansion stalls at some radius $R_{\rm f}$, where pressure equilibrium is reached between the ionized and neutral sides. We can roughly estimate the minimum mass of a star needed to potentially remove the whole residual molecular gas through the H II region expansion, by imposing the condition $R_{\rm f} = R$, where R is the star-forming clump radius. Using the expression for $R_{\rm f}$ given in Garay & Lizano (1999), and assuming a clump temperature of $T_0 \simeq 20$ K, we obtain the following restriction for the ionizing flux Q_0:

$$Q_0 \geq Q_{\rm crit} = 3 \times 10^{47} \left(\frac{R}{\rm pc}\right)^3 \left(\frac{n_0}{10^5\,{\rm cm}^{-3}}\right)^2 {\rm s}^{-1}, \tag{2.2}$$

where n_0 is the clump density ($= 2n({\rm H}_2)$). We are interested in finding the minimum $Q_{\rm crit}$ to really have a lower limit for Q_0, over which the ionizing flux *might* be able to disrupt the clump. Based on the mass-radius plot of the compilation of star-forming clumps by Fall et al. (2010), we estimate[7] that the minimum $Q_{\rm crit}$ in those data is achieved for $n_0 \simeq 10^4$ cm^{-3} and $R \simeq 0.7$ pc,

[7] Each value of $Q_{\rm crit}$ defines a line in the $(\log R, \log M)$ plane, with slope 2/3 and position depending on $Q_{\rm crit}$.

resulting in $Q_{\rm crit} \simeq 10^{45}$ s^{-1}. This ionizing flux corresponds to a young star of spectral type earlier than B2 (Panagia 1973), which implies a minimum star mass of $\sim 10\ M_\odot$ (for a B1–B1.5 star; Mottram et al. 2011). The total stellar mass of an embedded cluster needed to contain at least one 10 $M_\odot$ star is $M_\star \geq 115\ M_\odot$ (Weidner et al. 2010)[8], which translates in an initial star-forming clump mass of $M = M_\star/\epsilon \gtrsim 400\ M_\odot$ (using a final SFE of $\epsilon \simeq 0.3$).

Early O stars and OB giants drive powerful winds that fundamentally alter the structure of more luminous H II regions, creating an "onion-layer" configuration (Weaver et al. 1977). The structure of a wind-blown ionized bubble is shown in Figure 2.6 and consists of: an inner cavity cleared rapidly by freely flowing hypersonic ($1000 - 2000$ km s^{-1}) stellar winds; a high-temperature ($T > 10^6$ K) region of shocked stellar wind material; a shell of shocked, photoionized gas; and the "classical" H II region which is now confined within a shell of non-shocked photoionized gas. The outer boundary is the same as in the classical case: an ionization front, a shell of shocked neutral gas, a shock front, and finally the ambient neutral medium. While late-O and early B dwarfs give rise to classical H II regions powered by UV photons alone (e.g., Watson et al. 2008, 2009), in early O stars and massive OB clusters there is observational evidence of the existence of winds shocks (see Povich 2012), directly through the X-ray emission of the hot plasma in the central cavity (as in M17), or indirectly by the presence of central holes in the warm dust and ionized gas emission (as in the bubble N49). However, whether in such cases the effect of the stellar winds can be dynamically more important than the radiation pressure or the classical expansion due to thermal pressure difference between the ionized and neutral gas, is not fully understood yet, and some controversial results are found in the recent literature (Povich 2012). Due to leakage through pores in the shell, Krumholz & Matzner (2009) estimate that stellar winds simply provide an order-unity enhancement to radiation pressure.

An order-of-magnitude comparison of different stellar feedback mechanisms for initial star-forming clump masses $M = M_\star/\epsilon \geq 1000\ M_\odot$ was provided by Fall et al. (2010), and is shown in Figure 2.7. The same authors compiled a sample of massive star-forming clumps with physical properties determined observationally, and their typical mean surface densities Σ are concentrated in the range $[0.1, 1]$ g cm^{-2}. Consequently, the plot reveals that the dominant feedback mechanism in most protoclusters with $M \gtrsim 10^4\ M_\odot$ is radiation pressure[9]. On the other hand, gas dissipation in most protoclusters with

[8] In practice, we used the linear regime of the analytical formula provided by Pflamm-Altenburg et al. (2007): $\log m_{\rm max} \simeq a/b \log M_\star + c$, with a, b, c constants given there.

[9] Note that, however, in that work the effect of stellar winds was included *within* the estimated radiation pressure, through a very uncertain parameter $f_{\rm trap,w}$ which can be of

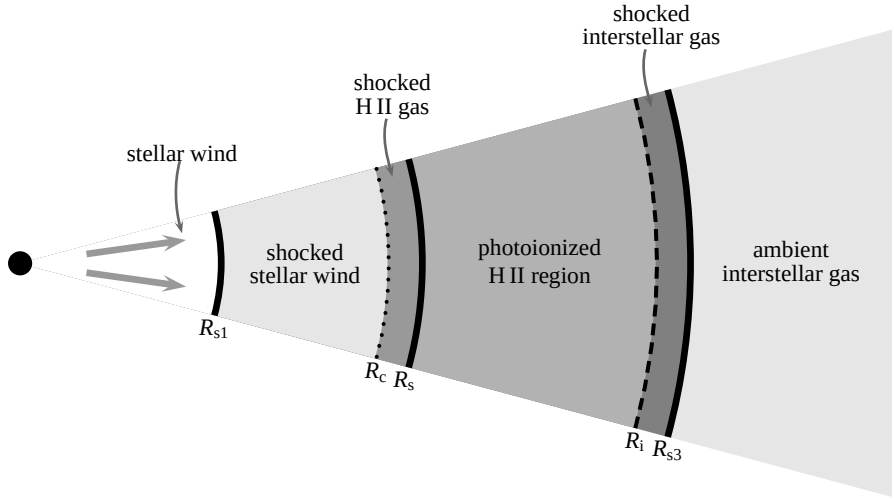

Figure 2.6: Schematic representation of the components of a wind-blown H II region. The different boundary radii are indicated: R_{s1} is the stellar wind shock, R_c is a contact discontinuity separating shocked stellar wind material from swept-up photoionized gas, R_s is the shock front on the ionized gas, and R_i, R_{s3} correspond to the "classical" H II region outer border, the ionization front and shock front on the ambient medium, respectively. (From Arthur 2007).

$M \lesssim 2000\ M_\odot$ is driven by photoionization (classical H II region expansion) or protostellar outflows. According to the above discussion, this regime can be extrapolated to $M \gtrsim 400\ M_\odot$.

The effect of ionization feedback in a protocluster with a realistically inhomogeneous gas distribution was studied numerically by Dale et al. (2005), who performed SPH simulations, coupled with a photoionization algorithm, of a $M \simeq 750\ M_\odot$ star-forming clump. They took as initial conditions the outcome of the cluster-formation SPH simulations by Bonnell & Bate (2002), in which a stellar cluster with a mass of $M_\star \simeq 220\ M_\odot$ has been formed after about one free-fall time (~ 1 Myr). At the cluster center, which lies at the intersection of several high-density filaments that channel an accretion flow into the core (see § 2.1.1), they introduced a single ionization source equivalent to an O5−O6 star. The results of these computations for the case of relatively "low" gas density ($n \simeq 10^6$ cm^{-3} within the core) indicate that, although the presence of high-density substructures protects some of the gas in the system, at least temporarily, from the ionizing radiation, the disruption of the accretion flows is achieved. At the end of the simulation (~ 0.5 Myr after source ignition), gas expulsion is already ongoing: $\sim 35\%$ of the gas is unbound at this point, and the core of the stellar protocluster appears nearly cleared out. The authors

order unity; in such case, stellar winds are as important as radiation pressure.

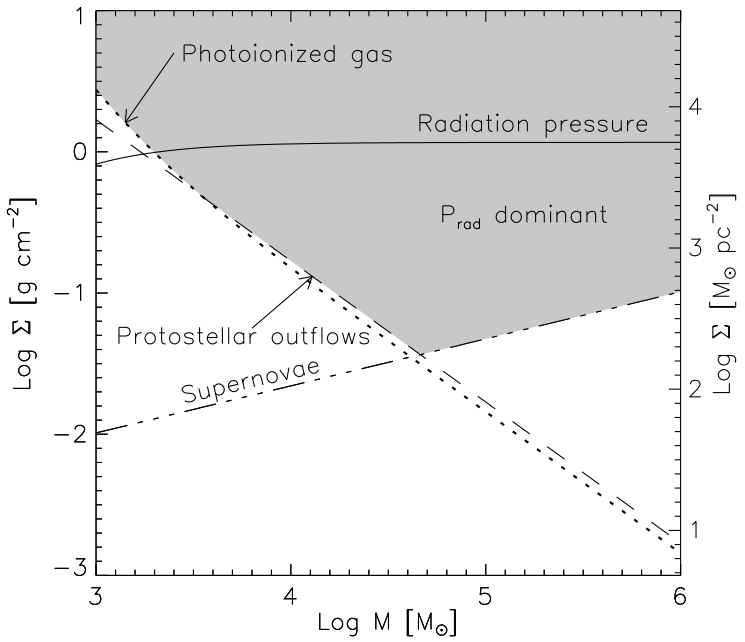

Figure 2.7: Feedback mechanisms in protoclusters of mean surface density Σ and mass M (gas + stars). Radiation pressure is the dominant mechanism throughout the shaded region. For the radiation pressure and protostellar outflows, the lines show where each mechanism alone achieves a SFE of $\epsilon \simeq 0.5$; the area below each line is where each mechanism alone is even more compelling ($\epsilon < 0.5$). For supernovae, the line delimits the zone where they can dominate (below the line), based on timescale estimates. The line for photoionized gas indicate where the H II region pressure equals the radiation pressure (i.e, below the line, classical H II region expansion dominates over radiation pressure). (From Fall et al. 2010).

found that ionization feedback quickly brings global accretion to an almost complete halt, leaving the SFE little changed from its initial value ($\epsilon \simeq 0.3$, see their Figure 18).

Dale et al. (2005) carried out also simulations with a higher gas density ($n \simeq 10^8$ cm^{-3} within the core), in which case the ionizing radiation is able to escape in only a few directions of lower local density, and accretion is delayed but never halted. However, as the same authors show, in an azimuthally averaged rendition of such gas distribution, the ionized region would be completely trapped within the cluster core due to the gravitational potential (escape velocity higher than the H II region expansion velocity). The Dale et al. (2005) high-density run corresponds therefore to a regime (probably rare at this clump mass) where photoionization feedback is not important, and other mechanism(s) regulates the star formation, like stellar winds or radiation pres-

sure: indeed, it can be shown that the area in Figure 2.7 where the escape velocity exceeds the sound speed of the ionized gas ($\sim$ 10 km s^{-1}) is within the radiation pressure domain. Similarly, the simulations of ionization feedback performed by Dale & Bonnell (2011) in a 10^6 $M_\odot$ molecular cloud are also in the radiation pressure regime, and hence their result that the ionized gas only fills pre-existing voids and bubbles originally created by the turbulent velocity field and that photoionizing radiation has little impact on the evolution of the protocluster, is expected and consistent with the simple theory presented here. It is worth mentioning that this dependence of the impact of the ionization feedback on the physical properties of the star-forming clouds (disruption by ionization is more difficult for clouds with larger escape velocities, corresponding roughly to the more massive ones) has been recently confirmed by Dale et al. (2012), who conducted similar simulations to the ones described before, but now covering a wider range of cloud masses and sizes.

2.2.2 Early dynamical evolution

The dynamical response of a cluster to the loss of the residual gas depends partially on the gas expulsion timescale $\Delta t_{\rm gas}$ relative to the crossing time $t_{\rm cross}$ of the cluster. For most young stellar clusters, gas expulsion is very fast ($\Delta t_{\rm gas} \ll t_{\rm cross}$). For instance, a classical H II region expands into the surrounding medium at a typical velocity of the order of the sound speed of the ionized gas, $C_{\rm II} \simeq 10$ km s^{-1}; for a protocluster of radius $R \simeq 1$ pc, this translates in a timescale $\Delta t_{\rm gas} \simeq R/C_{\rm II} = 0.1$ Myr, which is shorter than the crossing time of protoclusters with total masses $M \leq 10^4$ $M_\odot$ (see Table 8.1 of Kroupa 2008). More massive clusters are associated with H II regions dominated by radiation pressure (recall Fig. 2.7), whose expansion velocities can be much higher (Krumholz & Matzner 2009) and might still lead to gas evacuation timescales shorter than $t_{\rm cross}$.

For $\Delta t_{\rm gas} \ll t_{\rm cross}$, the positions and velocities of the stars remain fixed during the gas expulsion phase and the cluster's response can be calculated under the assumption that the mass loss is *instantaneous*. In a self-gravitating system, such a mass loss implies a decrease of the absolute value of the gravitational potential, and thus a decrease of the escape velocity. A fraction of stars that were originally bound to the cluster will then be released and escape away from the remaining cluster population, which is still bound in a central gas-free core. When this core reaches virial equilibrium, it will adjust its size according to the following expression (Kruijssen et al. 2012):

$$2(1-Q_{\star,1})\, r_{\rm h,2} = f_{\rm b}[f_{\rm b} - (1-f_{\rm b})\bar{\beta}^2]\, r_{\rm h,1} \ , \tag{2.3}$$

where the subindexes 1 and 2 denote, respectively, the time of instantaneous gas removal and the time at which the remaining bound cluster core attains virial equilibrium; $r_{\rm h}$ represents the corresponding half-mass radii, $f_{\rm b} = M_{\star,2}/M_{\star,1}$ is the mass fraction of stars that stay bound, and $\bar{\beta}$ is the average velocity[10] of the escaping stars after they leave the influence of the potential (formally at infinity), in units of the velocity dispersion of the virialized bound population ($\sigma_2 = \sqrt{0.4GM_{\star,2}/r_{\rm h,2}}$, see equation (A.10)). The parameter $Q_{\star,1}$ is the virial ratio (cf. equation (A.4)) of the stellar cluster at the moment of instantaneous gas removal:

$$Q_{\star,1} = \frac{K_{\star,1}}{-W_{\star,1}} = \frac{f_v^2}{2\epsilon} \ . \tag{2.4}$$

In the last equality, obtained by Goodwin (2009), ϵ is the SFE and f_v is a velocity fraction defined by $f_v = \sqrt{\langle v_1^2 \rangle}/\sigma_0$, where σ_0 is the velocity dispersion that the whole system (stars + gas) would have if it were in virial equilibrium before gas expulsion, and $\langle v_1^2 \rangle$ is the actual mean square speed of the stars.

It follows from equation (2.3) that, as long as $f_{\rm b} - (1 - f_{\rm b})\bar{\beta}^2 > 0$, in the limit of a system marginally unbound at the time of instantaneous gas expulsion ($Q_{\star,1} \longrightarrow 1^-$), the totality of the cluster dissolves ($r_{\rm h,2} \longrightarrow \infty$). According to equation (2.4), this would imply that, if the gas and stars were in virial equilibrium before gas removal ($f_v = 1$), the SFE has necessarily to be $\epsilon > 0.5$ in order to leave some fraction of the stars bound, which is the classical condition for cluster survival found in early works (e.g., Hills 1980). However, we can also see from equation (2.3) that if $Q_{\star,1} \geq 1$, formally it is still possible to find a combination for the parameters $f_{\rm b}$ and $\bar{\beta}$ to obtain a valid solution for $r_{\rm h,2}$. The condition in this case can be written as

$$\bar{\beta} \geq \sqrt{\frac{f_{\rm b}}{1 - f_{\rm b}}} \ . \tag{2.5}$$

For example, for a bound mass fraction of $f_{\rm b} = 1/3$, the mean velocity of the unbound stars at infinity has to be $v = \bar{\beta}\sigma_2 \geq 0.71\sigma_2$. Physically, this means that the excess of energy might be carried away by high-velocity escaping stars, leaving a fraction of the stars bound. Indeed, N-body simulations (e.g., Baumgardt & Kroupa 2007) have shown that for clusters in virial equilibrium with the gas before its instantaneous expulsion ($f_v = 1$), a SFE of $\epsilon \gtrsim 0.33$ is required for survival, i.e., clusters with virial ratios up to $Q_{\star,1} \simeq 1.5$ can leave a bound remnant. These simulations also showed that if $\Delta t_{\rm gas}$ is short relative

[10] Strictly, it is the square root of the mean square speed: for clarity, we define $\bar{\beta} = \sqrt{\beta}$, where β is the parameter originally used by Kruijssen et al. (2012), so that $\bar{\beta}$ is a velocity fraction instead of a square velocity fraction.

to $t_{\rm cross}$ but finite (not instantaneous), the needed SFE for survival can be even lower (e.g., $\epsilon \gtrsim 0.25$ if $\Delta t_{\rm gas}/t_{\rm cross} = 1/3$, for the simulations of Baumgardt & Kroupa 2007).

The last identity in equation (2.4), with ϵ the global SFE in the star-forming cloud, holds only if the stars and gas have the same spatial distribution (Goodwin 2009). If this condition is not satisfied, the local gas content inside the cluster, and hence the effect of gas expulsion, can be lower. To illustrate that, let us consider an idealized situation in which the stars and gas spatial distributions are spherically symmetric and centered at the same position, but the gas covers a larger length scale. Due to the Newton's first theorem (cf. § 2.2.1 of Binney & Tremaine 2008), the stars only feel the gas gravitational potential due to the gas mass *within* the cluster volume. Therefore, in equation (2.4), instead of the global SFE, ϵ, the parameter which determines the dynamical state of such a cluster at the moment of instantaneous gas expulsion is the *local stellar fraction* (LSF; Smith et al. 2011),

$$\epsilon_{\rm h} \equiv \frac{M_\star}{M_\star + 2M_{\rm gas}(r < r_{\rm h,1})} \ , \tag{2.6}$$

where $M_\star$ is the total mass in stars, and $M_{\rm gas}(r < r_{\rm h,1})$ is the gas mass contained within the *stellar* half-mass radius. The LSF can be considerably larger than the global SFE, reducing the actual virial ratio $Q_{\star,1}$ of the cluster and thus raising its survivability. For example, Smith et al. (2011) showed through N-body simulations that mergers of stellar substructures can generate a merged object with a high LSF ($\epsilon_{\rm h} \simeq 0.4$) relative to a low global SFE ($\epsilon \simeq 0.2$), and that the cluster actually survives instantaneous gas expulsion.

Another way to reach a lower $Q_{\star,1}$ is if the stellar velocities are subvirial ($f_v < 1$) at the time of gas expulsion. Offner et al. (2009) found that the velocity dispersions of the stars in hydrodynamic simulations of star formation are smaller than that of the gas by about a factor of 5, suggesting that the assumption of equilibrium between both components indeed does not hold. The fact that this behavior is seen since the first stars form in the simulations (see their Figure 1) suggests that the stars are already born decoupled from the overall gas dynamics, and the subsequent formation of small and growing agglomerates or subclusters of protostars is expected. Kruijssen et al. (2012) studied the dynamical state of the subclusters arising from the simulations of Bonnell and coworkers (recall § 2.1.1, in particular Figure 2.2) and found that the subclusters are close to virial equilibrium when considering the stars only, with a mean virial ratio over all the simulation snapshots of $Q_{\star,1} = 0.59$, which is well into the regime of surviving gas expulsion (see equation (2.3)). The estimated mean expansion factor after instantaneous gas expulsion is of

only $r_{\rm h,2}/r_{\rm h,1} \simeq 1.08$, and more than 90% of the identified subclusters would survive this process. They concluded that the virialization of the subclusters is a consequence of their low gas fractions ($\lesssim 0.2$, which translates in LSFs of $\epsilon_{\rm h} \gtrsim 1 - 0.2 = 0.8$), caused by the accretion of gas on to the stars and the accretion-induced shrinkage (see Bonnell et al. 1998) of the subclusters. Kruijssen et al. (2012) argue that although most of the identified subclusters survive an eventual gas removal, they could be disrupted by another mechanism: tidal shocks from the natal dense environment. On the other hand, they claim that the protostellar population with lower densities can be affected by gas expulsion.

The above discussion shows that the response to gas expulsion is not easily parameterized[11], due to the high complexity of the star formation process and the fact that protostar subclusters undergo N-body evolution from very early. In fact, Moeckel et al. (2012) argue that, for N sufficiently low ($\sim$ few times 100), the dynamical evolution of a young cluster can become collisional within a timescale of a few Myr, and therefore might represent an alternative early disruptive agent. They took the end result of the Bonnell et al. hydrodynamic simulations and evolved its sink particles forward for 10 Myr using a N-body code, i.e., after removing the gas entirely. They found that the overall system expands considerably due to two effects: the unbinding of the individual subclusters from each other as a result of gas expulsion, and the expansion and mass-loss of the individual subclusters driven uniquely by internal stellar dynamics and stellar evolution. These young subclusters might therefore dissipate (observationally, their masses fall below the detection limit) in a < 10 Myr timescale, without need of gas expulsion as a disruption mechanism.

In order to obtain observational constraints to these theories, it is needed to trace the kinematics of the individual member stars of a young cluster by high-resolution spectroscopy or proper motion studies, which is very difficult and time-consuming. A few of such studies have been carried out so far towards young massive clusters (see Bastian 2011, and references therein), and they have found that the stellar velocity dispersions are indeed low ($Q_{\star,1} < 1$). An exception to this trend is the Orion Nebula Cluster (ONC), whose high velocity dispersion was interpreted previously as an indication of cluster expansion (Kroupa 2005), and therefore as being consistent with ongoing cluster disruption due to gas expulsion. We remark that an expansion would be also consistent with the dissipation mechanism proposed recently by Moeckel et al. (2012, see above), in which individual low-N subclusters constituting the ONC would evolve dynamically and dissolve in a short timescale. On the other hand,

[11] For example, the variables involved in equation (2.4), f_v and ϵ (or $\epsilon_{\rm h}$), are not independent of each other, and evolve significantly over time.

Proszkow et al. (2009), using N-body simulations, were able to reproduce the velocity dispersion and other kinematic signatures of the ONC, provided that the cluster is nonspherical and is undergoing a radial collapse due to subvirial initial conditions after it was born. We note that, however, whereas the ONC is observed mostly free of residual gas, in the computations of Proszkow et al. (2009) a background gas potential is included, and in particular the matching simulation has a high gas content ($\epsilon = 0.17$). This would mean that the simulated collapse velocity might be artificially enhanced by the presence of gas, unless at the present time we are observing the ONC *just after* a practically instantaneous gas expulsion phase. Again, this example shows that the dynamics of a young cluster and its interaction with its natal environment is highly dependent on time, making the interpretation of the observations very challenging, specially for a small sample of clusters or an unique object.

2.2.3 Triggered star formation

Although the ionization feedback from young massive stars can be a compelling mechanism in removing the residual gas and halting star formation in system with masses up to a few thousand $M_{\odot}$ (see § 2.2.1), under certain conditions, the H II region expansion may also trigger the formation of a new generation of stars in the surrounding molecular material. From a theoretical point of view, two main triggering scenarios have been proposed: Collect and Collapse (C&C), and Radiation Driven Implosion (RDI).

The C&C model (Elmegreen & Lada 1977) is based on the fact that, in the classical H II region expansion, the initially uniform ambient neutral medium is swept up by the pressure of the ionized gas, provoking the accumulation of a shell of dense molecular gas between the ionization and shock fronts (the "shocked interstellar gas" layer in Figure 2.6). At some point, the shell cools down, becomes gravitationally unstable and fragments into dense clumps which eventually collapse to form stars.

In contrast, RDI (Bertoldi 1989) triggers star formation by externally compressing pre-existing cold molecular condensations which would be gravitationally stable without the influence of the H II region. Since the ionized gas pushes away the lower density material faster than the higher density cloud structures, bright rims and pillars are formed and distort the shape of the ionization front. In the RDI model, triggered star formation is predicted in the dense heads of pillars.

Multi-wavelength observational studies towards bright-rimmed globules and fragmented dense gas shells on the edges of H II regions have shown different signatures which are consistent with the RDI and/or the C&C mechanism tak-

ing place (e.g., Urquhart et al. 2009; Deharveng et al. 2010; Elmegreen 2011, and references therein). Nevertheless, one difficulty with most of these studies is that their methods are often phenomenological, based on the visual identification of YSOs or star formation signposts in regions where one might have a prior expectation that they may have been triggered. When detecting star formation on the boundaries of an H II region, we cannot exclude the possibility that it would have happened spontaneously, without the influence of the trigger. The statistical study by Thompson et al. (2012) has addressed this issue: by cross-correlating the catalog of bubble-like H II regions of Churchwell et al. (2006) with the sample of massive YSOs from the RMS survey (Urquhart et al. 2008), they found a statistically significant overdensity of YSOs towards the bubbles, with a clear peak in the surface density of YSOs projected against the border of the bubbles. A similar result has been obtained recently by Kendrew et al. (2012) using a considerably larger sample of bubbles. The correlation between bubbles and YSOs is expected without invoking triggered star formation, if we accept that the former are indeed star-forming regions where more stars can be born spontaneously in addition to the one(s) producing the H II region; but in this case the distribution of YSOs throughout the bubble should be roughly uniform. Hence, the YSOs surface density peak on the bubbles edge favors the triggered nature of the formation of the protostars located there.

However, this morphological approach has been recently challenged by Walch et al. (2011), who performed SPH simulations of a fractal 10^4 $M_\odot$ molecular cloud, including photoionization feedback from a central source. They showed that the presence of massive clumps and newly born protostars within an expanding shell formed around an H II region simply reflects the pre-existing, non-uniform cloud density structure, whose contrast is enhanced by the ionizing radiation. Therefore, this kind of observed configuration would not necessarily support triggering scenarios like C&C. Indeed, at no time in the simulations they found the formation of a coherent shell, which grows to become gravitationally unstable and then fragments. Elmegreen (2011) argues that this kind of simulations run for too short a time to generate an expanding coherent shell and form stars by the C&C mechanism; the timescale has to be several dynamical times in the pre-shock material. A possible scenario may be that, whereas dense clumps arising from initial density inhomogeneities form stars anyway, without need of triggering, the swept-up lower density material at some point is accumulated in a layer which does undergo the C&C process. Further numerical computations are required to explore this possibility. As already mentioned in § 2.2.1, we note that the simulations by Dale & Bonnell (2011) are in a regime where photoionization is not a dominant feedback mechanism, and thus their result of minimal triggered star formation is totally

expected, as they do not include other forms of feedback.

The discussion presented above leads us to keep in mind that finding massive clumps (bright-rimmed or distributed along a shell) and star-formation signposts around an H II region does not represent a proof of triggered star formation. These regions are instead *candidates* of triggering. The importance of this scenario in the overall star formation process is still uncertain.

2.3 Cluster definition revisited

The observed cluster population in the Milky Way has revealed that the number of embedded clusters is too high with respect to the number of gas-free clusters: Lada & Lada (2003) found that they would expect ~ 10 times more open clusters than observed if all embedded clusters evolve into open clusters. The explanation provided by these authors is that $\sim 90\%$ of embedded clusters are disrupted after they quickly remove the residual gas (this process is often referred to as "infant mortality"). However, the discussion presented in this chapter leads to substantial changes in this paradigm, mainly due to three points:

1. Since stars form in a continuous spectrum of surface densities, a particular population of recently born stars in the more dispersed part of the distribution might be already born unbound even considering the gas potential, and would quickly disperse in the field. Such dissolving young stellar associations, which probably arise from gravitationally unbound regions within a GMC (see, e.g., § 2.1.1), could still be identified observationally as (part of) "embedded clusters", as their star members are correlated in space and time (they constitute CSFEs, see § 2.1.2) in more restricted scales (of the order of 1 pc and 1 Myr) than those characterizing the field stars, given the nature of the star formation process. If we were able to exclude these young associations, which potentially cannot become classical open clusters, the required fraction of embedded clusters that have to disrupted to explain the observed number of open clusters could be significantly lower than 90% (Bastian 2011).

2. As shown by numerical simulations of clustered star formation (Maschberger et al. 2010, see also § 2.1.1), in regions with higher overall stellar densities, several small subclusters of protostars might undergo a process of hierarchical merging, resulting in a few merged large clusters as output. This scenario has also been suggested by observational studies of big star-forming complexes, where many embedded clusters have been

found in close proximity, within a scale of a few parsecs (e.g., in W49A, Homeier & Alves 2005). If in a given sample of embedded clusters, some of them are or will be involved in a merging, such mechanism would also produce a high observed embedded cluster/open clusters fraction with respect to that expected from a simple one-to-one relation, reducing the need of early cluster disruption.

3. Stellar agglomerates that are formed bound (from birth or after a merging) can be disrupted totally in the field, or only partially, giving rise to bound exposed clusters with a lower mass than the original stellar mass. The cause of this disruption can be either the fast gas expulsion (probably only important in low density regions), tidal shocks from the surrounding gas (dominant in dense regions; Kruijssen et al. 2012), or collisional dynamical evolution (for small-N systems or larger clusters with a hierarchical substructure; Moeckel et al. 2012).

Because the relative contributions of each effect (dissolving associations from birth, merging of subclusters, gas expulsion, tidal shocks from environment, and collisional dynamical evolution of subclusters) causing the high observed embedded clusters/open clusters fraction are so far unknown, we simply define an *embedded cluster* as any stellar group recently born and still containing an important fraction of residual gas within its volume, keeping in mind that maybe it was never able to become a classical open cluster on its own. Since star formation takes place in molecular clouds, this definition is equivalent to the concept of CSFE introduced by Kroupa (2011); we keep the term "cluster" in order to match older designations in the literature. On the other hand, we define a *physical open cluster* as a bound stellar agglomerate relatively free of the remaining gas (a classical open cluster). Unbound, exposed stellar agglomerates are called *associations*, and can be easily distinguished from physical open clusters using the empirical definition provided by Gieles & Portegies Zwart (2011), whenever estimates for masses, characteristic radii and ages are available. In this work, we sometimes use the term "star clusters" generically for both embedded and physical open clusters, especially when concerning observations. Bound, exposed star clusters, however, will be always be referred to explicitly as *physical open clusters*.

3

Compilation of all-sky cluster catalogs

The ATLASGAL survey (see § 1.1.1) provides an unbiased (only flux-limited) sample of sources emitting at 870 μm in the inner Galactic plane. In order to obtain statistically meaningful results in a general Galactic context, we would have to use in this study a star cluster sample which were also unbiased. Even though the development of outstanding infrared surveys (e.g., 2MASS and GLIMPSE) allows us to count with an enormous sample of stars within the ATLASGAL Galactic range, the difficulty in cluster identification, and the presence of dust extinction, which at IR wavelengths prevents us to probe deeply embedded or very distant regions, makes the task of obtaining an unbiased catalog of Galactic stellar clusters practically impossible with the current observational capabilities (see § 4.2.3).

However, we can aim at possessing the most complete star cluster sample as possible, representative enough to look for some general trends (but always keeping in mind the biases). We thus performed a huge compilation of all Galactic star clusters catalogs from the literature, including some individual infrared studies not present in these catalogs, and complemented the sample with a new search for clusters in the GLIMPSE survey, since the only work using these data (Mercer et al. 2005) misses some embedded objects, as discussed in § 3.4. For completeness, the compilation was not initially restricted to the ATLASGAL Galactic range; we only did it afterwards for the comparison with ATLASGAL emission. This literature compilation is updated till August, 2011.

In the following Sections we describe the diverse cluster catalogs and references we used for our compilation, separated in three categories according to the wavelength in which they are detected: *optical*, *near-infrared* and *mid-infrared* clusters. We then describe our new search for clusters in the GLIMPSE data; and finally we present the overall cluster sample after cross-identifications, including later a discussion about the contamination by false cluster candidates. A summary of the cluster sample can be found in Table 3.2. We warn that the number of clusters given there and within the text are after removing a few spurious objects and globular clusters (listed in Table 3.3), unless explicitly mentioned.

3.1 Optical clusters

Dias et al. (2002) provide the most complete catalog of optically visible open clusters and candidates, containing revised data compiled from old catalogs and from isolated papers recently published. The list is regularly updated on a dedicated webpage[1], with additional clusters seen in the optical and revised fundamental parameters from new references. We used the version 3.1 (from November, 2010), which contains 2117 objects, of which 99.7% have estimated angular diameters, and 59.4% have simultaneous reddening, distance and age determinations. Kinematic information is also given for a fraction of clusters, 22.9% of the list have both radial velocity and proper motion data. It should be noted that this catalog aims at collecting not only the open clusters first *detected* in the optical, but also most of (ideally, all) the clusters which were detected in the infrared and are *visible* in the optical. For example, 293 objects from the 998 2MASS-detected clusters of Froebrich et al. (2007b) were included in the last version of the catalog, based on by-eye inspection of the Digitized Sky Survey (DSS) images.

We also included in our compilation the list of new galactic open cluster candidates by Kronberger et al. (2006), who did a visual inspection of DSS and 2MASS images towards selected regions, and a subsequent analysis of the 2MASS color-magnitude diagrams of the candidates. The clusters were divided in different lists, some of them with fundamental parameters determined, and are all included in the Dias et al. (2002, ver. 3.1) catalog, except most of the stellar fields classified as *suspected* open cluster candidates (their Table 2e), which adds 130 objects to the optical cluster sample.

[1] http://www.astro.iag.usp.br/~wilton/

3.2 Near-infrared clusters

Stellar clusters detected by near-infrared imaging, mainly from surveys of individual star-forming regions, are compiled from the literature by Bica et al. (2003a), Porras et al. (2003) and Lada & Lada (2003). The first two catalogs include also stellar groups, whereas Lada & Lada (2003) restricted the compilation to objects with more than 35 members, in order to match their definition of an *embedded cluster*. The Porras et al. (2003) and Lada & Lada (2003) catalogs are limited exclusively to nearby regions (distances less than 1 kpc and $\simeq 2$ kpc, respectively); Bica et al. (2003a) did not use that restriction, but their list is representative only for nearby distances too ($\lesssim 2$ kpc). It is not surprising that the three compilations overlap considerably, as is shown in Table 3.2. All together, these catalogs contribute 297 additional objects with respect to the optical cluster sample.

However, most of the near-infrared clusters correspond to recent discoveries using the 2MASS survey. More than 300 new clusters were found by visual inspection of a huge number of 2MASS J, H, and specially K_s images (Dutra & Bica 2000, 2001; Bica et al. 2003b; Dutra et al. 2003a). In the pioneer work of Dutra & Bica (2000), 58 star clusters and candidates were originally detected by doing a systematic visual search on a field of $5^\circ \times 5^\circ$ centered close to the Galactic Center, and towards the directions of H II regions and dark clouds for $|l| \leq 4^\circ$; though most of them were observed later at higher angular resolution, and 36 turned out to be spurious detections mainly due to the high contamination from field stars in this area (see § 3.6). Additional 42 objects were discovered by Dutra & Bica (2001), who searched for embedded clusters and stellar groups around the central positions of optical and radio nebulae in the Cygnus X area and other specific regions of the sky (they are included in the literature compilation by Bica et al. 2003a). They extended the method for the whole Milky Way (Dutra et al. 2003a; Bica et al. 2003b, southern and equatorial/northern Galaxy, respectively), inspecting a sample of 4450 nebulae collected from the literature, and they found a total of 337 new clusters, stellar groups and candidates.

In addition to the visual inspection technique, a large number of 2MASS star clusters have been discovered by automated searches, which are based on the selection of enhancements on stellar surface density maps constructed with the point source catalog. The early works of Ivanov et al. (2002) and Borissova et al. (2003) led to 14 detections (the ones not present in any of the catalogs mentioned above are counted in the "Not cataloged (NIR)" row of Table 3.2); similarly, Kumar et al. (2006) found 54 embedded clusters of which 20 are new detections, focusing the search around the positions of massive protostellar can-

didates. More recently, Froebrich et al. (2007b) searched for 2MASS clusters along the entire Galactic Plane with $|b| \leq 20°$, looking automatically for star density enhancements, and selecting manually all remaining objects possessing the same visual appearance in the star density maps as known star clusters. They identified a total of 1788 star cluster candidates, 1021 of which resulted to be originally new discoveries and were given as a catalog; an estimate of the contamination suggested that about half of these new candidates are real star clusters. A considerable number of objects from the Froebrich et al. (2007b) list have been analyzed in more detail by a variety of authors, and they were compiled by Froebrich et al. (2008). For these objects and the ones studied recently by Froebrich et al. (2010) (comprising a total of 68 clusters), we use the refined coordinates and diameters instead of the original ones. The follow-up studies compiled by Froebrich et al. (2008) also unveil 22 spurious clusters and one globular cluster (see Table 3.3). A similar automatic 2MASS search done by Glushkova et al. (2010) in the $|b| < 24°$ range, which includes the verification of the obtained star density enhancements by the analysis of color-magnitude diagrams and radial density distributions, produced a list of ~ 100 new clusters (most of them included in the last version of the catalog by Dias et al. 2002), providing physical parameters for a total of 168 new and previously discovered objects.

Expectations for the near future are that the new generation of all-sky NIR surveys, such as the United Kingdom Infrared Deep Sky Survey (UKIDSS) and VISTA Variables in the Vía Láctea (VVV), will give rise to the discovery of many more stellar clusters, thanks to their improved limiting magnitude and angular resolution compared to 2MASS. A cluster search using these data has already been performed by Borissova et al. (2011), who found 96 previously unknown stellar clusters and groups by visually inspecting multiwavelength NIR images of the VVV survey in the covered disk area ($295° \leq l \leq 350°$ and $|b| \leq 2°$), towards directions of star formation signposts (masers, radio, and infrared sources). The objects listed in their catalog were required to present distinguishable sequences on the color-color and color-magnitude diagrams, after applying a field-star decontamination algorithm, in order to minimize the presence of false detections. Automated cluster searches in the UKIDSS and VVV surveys are being done by the corresponding teams.[2]

In our star cluster compilation, we also included recent near-infrared studies

[2] According to unpublished data, there seem to be more than 300 new clusters detected so far by the UKIDSS team. An independent automated search on UKIDSS, leading to the discovery of 167 additional clusters and multiple star forming regions, has already been published by Solin et al. (2012), but after the last update of our cluster compilation was done.

towards specific star-forming regions, or individual star clusters, which are not listed in the previous catalogs. In their near-infrared survey of 26 high-mass star-forming regions, Faustini et al. (2009) identified the presence of 23 clusters, 16 of which are new discoveries. Additional individual new objects are counted as "Not cataloged clusters (NIR)" in Table 3.2.

3.3 Mid-infrared clusters

As a result of the high sensitivity of the GLIMPSE mid-infrared survey, Mercer et al. (2005) managed to find 92 new star clusters (2 of which are globular clusters) using an automated algorithm applied to the GLIMPSE point source catalog and archive, and a visual inspection of the image mosaics to search for embedded clusters (the GLIMPSE Galactic range at that time was $10^\circ \leq |l| \leq 65^\circ$ and $|b| \leq 1^\circ$, excluding the inner part of the GLIMPSE II survey). The automatic detection method consisted of the construction of a renormalized star density map, which accounts for the varying background, the estimation of the clusters spatial parameters by fitting 2D Gaussians to the point sources with an expectation-maximization algorithm, and finally the removal of false detections by using a Bayesian criterion. This technique yielded 91 cluster candidates, 59 of which were new discoveries. Most of the clusters were detected applying a bright magnitude cut at 3.6 μm before the construction of the stellar density map. Additional 33 new embedded clusters were identified by the visual inspection, which were missed by the automated method.

However, simple by-eye examination of some GLIMPSE color images led us to conclude that there are still some embedded cluster candidates missing in the Mercer et al. (2005) list. Because of this (and also to cover the GLIMPSE II area) we performed a new semi-automatic search in the whole GLIMPSE data, focused in the embedded clusters, which resulted in increasing the number of mid-infrared clusters, stellar groups and candidates to a total of 164 objects[3]. The search is described in § 3.4.

3.4 New GLIMPSE search for embedded clusters

The GLIMPSE on-line viewer[4] from the Space Science Institute represents a very useful tool to quickly examine color images constructed using the four 3.6, 4.5, 5.8 and 8.0 μm IRAC filters, of the whole survey. By inspecting some

[3] including 3 additional GLIMPSE clusters from the literature counted as 'Not cataloged clusters (MIR)" in Table 3.2

[4] http://www.alienearths.org/glimpse/glimpse.php

specific regions with this viewer, we noticed that some heavily embedded cluster candidates are still missing in the Mercer et al. (2005) list. An embedded cluster consists mostly of young stellar objects (YSOs), which are intrinsically redder than field stars due to thermal emission from circumstellar dust, so that it is distinguished from background/foreground stars mainly by its population's red colors. Such a cluster would therefore produce a clearer spatial overdensity of stars in a point source catalog previously filtered by a red-color criterion, and would be more likely missed in a search of overdensities considering the totality of point sources, due the high number of field stars. We believe that this is the principal reason which would explain the lack of embedded clusters in the Mercer et al. (2005) catalog.

We then implemented a very simple automated algorithm using the GLIMPSE point source catalog to find the locations of embedded cluster candidates. First, we selected all point sources satisfying a red-color criterion: $[4.5]-[8.0] \geq 1$, following Robitaille et al. (2008), who applied this condition to create their catalog of GLIMPSE intrinsically red sources. As already explained in that work, the use of these specific IRAC bands is supported by the fact that the interstellar extinction law is approximately flat between 4.5 and 8.0 μm, and therefore the contamination by extinguished field stars in this selection is reduced compared to other red-color criteria. Applying this condition to the entire GLIMPSE catalog, 268 513 sources were selected. We did not impose the additional brightness and quality restrictions used by Robitaille et al. (2008) because we favor the number of sources (and therefore higher sensitivity to possible YSO overdensities) rather than strict completeness and photometric reliability, which are not needed to only detect the locations of potential embedded clusters. With the 268 513 selected sources, a stellar surface density map was constructed by counting the number of sources within boxes of 0.01° ($= 36''$), in steps of 0.002° ($= 7.2''$). This significant oversampling was adopted in order to detect density enhancements that would have fallen into two or more boxes if we had used not overlapping bins. The bin size correspond to the typical angular dimension of some embedded cluster candidates found serendipitously using the on-line GLIMPSE viewer. To account for larger overdensities, a second stellar density map was produced with a bin size of 0.018° ($= 64.8''$).

The red-source density maps were checked in a test field, and we found that conservative thresholds (i.e., allowing over-detection) of 5 sources for the small bin, and 7 sources for the large bin, are enough to detect the positions of all cluster candidates which can be identified by-eye using the GLIMPSE on-line viewer within that area. It was also noticed that using the GLIMPSE point source archive instead of the catalog is roughly equivalent to utilize the

catalog with a lower threshold, so as long as we choose a correct threshold, the use of the more reliable GLIMPSE catalog (with respect to the archive) is justified. Within the whole GLIMPSE area, we detected 702 independent positions (bins containing not-intersecting subsets of red sources) with densities larger or equal to 5 sources/bin for the 36″ bin or 7 sources/bin for the 64.8″ bin. It should be noted that since the red-color criterion produced density maps with low crowding and therefore the local background density is always close to zero, a more sophisticated algorithm is not needed. We also emphasize that, as mentioned before, the automated search was only used to find possible locations of embedded clusters; we did not intend to catch the complete YSO population for a given cluster in this process.

However, since we allow for significant over-detection in the automated method, many of the 702 positions are spurious detections and do not contain cluster candidates; thus, a subsequent visual selection was performed by examining the GLIMPSE images, based on a series of criteria which are explained below. Because the GLIMPSE on-line viewer has limited angular resolution and is not efficient to inspect a high number of specific locations, we downloaded original GLIMPSE cutouts around these 702 positions and constructed by ourselves three-color images using the 3.6 (blue), 4.5 (green) and 8.0 μm (red) IRAC bands. This by-eye inspection led us to finally select 88 overdensities as locations of embedded cluster candidates, 17 of which are identified as known clusters from our literature compilation presented before. The remaining 71 new objects are listed in Table 3.1. The adopted identification is a record number (column 1) preceded by the acronym "G3CC" (GLIMPSE 3-color Cluster Candidate[5]). The final coordinates and the angular diameter (column 6) were estimated by eye on the GLIMPSE three-color images fitting circles interactively with the display software *SAO Image DS9*[6]. The selection of the 88 overdensities was based on a series of visual criteria which are identified for each new object as flags in the last column of Table 3.1. Figure 3.1 shows GLIMPSE three-color images of 6 cluster candidates, illustrating these different criteria. An almost ubiquitous characteristic of the selected candidates (present in 82 cases) is their association with typical mid-infrared star formation signposts, namely: extended 8.0 μm emission in the immediate surroundings (flag E8, see Fig. 3.1(a,b,d,e,f)), likely corresponding to radiation from UV-excited PAHs or warm dust; more localized extended 4.5 μm emission within the cluster area (flag E4, Fig. 3.1(b)), which might trace shocked gas by outflowing activity from protostars; and presence of an infrared dark

[5] referring to the fact that the cluster candidates were finally selected on the GLIMPSE three-color images

[6] http://hea-www.harvard.edu/RD/ds9/

cloud in which the cluster candidate is embedded (flag DC, Fig. 3.1(b,c)). We also indicate whether a cluster candidate appears to have more stellar members than those identified by the red-color criterion, including the following situations: cluster composed of red sources and additional bright normal (not reddened) stars (flag BR, Fig. 3.1(d)), suggesting that the cluster is in a more evolved phase, probably emerging from the molecular cloud; cluster composed exclusively of bright normal stars (flag B, but only two cases, in conjunction with flag V2, see below); and presence of additional probable YSOs within the cluster, identified as sources detected uniquely at 8.0 μm (flag U8, representing extreme cases of red color), or compact 8.0 μm objects not listed in the point source catalog or archive (flag C8, Fig. 3.1(a,d,e,f)), due to the bright and variable extended emission at this wavelength, saturation for bright sources, or localized diffuse emission around a particular source which makes its apparent size larger than a point-source. The other flags indicate when the cluster candidate shows up as a sparse, not centrally condensed star-forming region (flag S, Fig. 3.1(f)), or if the candidate was noticed by-eye on the GLIMPSE images in a nearby location of an automatically detected overdensity, but not exactly at the same position (flag V2).

The remaining positions were rejected as cluster candidates, and correspond typically to background stars extinguished by dark clouds or seen behind foreground 8.0 μm diffuse emission, producing a red-source density enhancement by chance, sometimes together in the same line of sight with a couple of intrinsically red sources (YSOs) which however do not represent a cluster by their own. Quantitatively, we found that, in general, most of the rejected positions correspond to overdensities with fewer elements than the ones selected as cluster candidates. In fact, if we choose stricter thresholds of 8 sources for the small bin, and 10 sources for the large bin, instead of the originally used 5 and 7, respectively, the total set of overdensities decrease from 702 to just 87 independent positions, 37 of which correspond to our cluster candidates. This would mean an improved "success" rate of $37/87 = 43\%$ for the automated method rather than the original $88/702 = 13\%$. Furthermore, if we consider the *effective* number of elements in the 88 bins selected originally as being locations of cluster candidates, i.e., summing possible additional stellar members (flags BR,C8,U8) within the bins, we obtain that 61 of our candidates satisfy the new threshold. We emphasize, however, that the additional stellar members of each candidate were recognized after detailed inspection of the GLIMPSE images, so that the use of low star density thresholds and the consequent over-detection in the automated method were necessary to identify the initial cluster locations. If we had used from the beginning the stricter threshold, we would have missed $88-37 = 51$ candidates. Column 7 of Table 3.1 lists

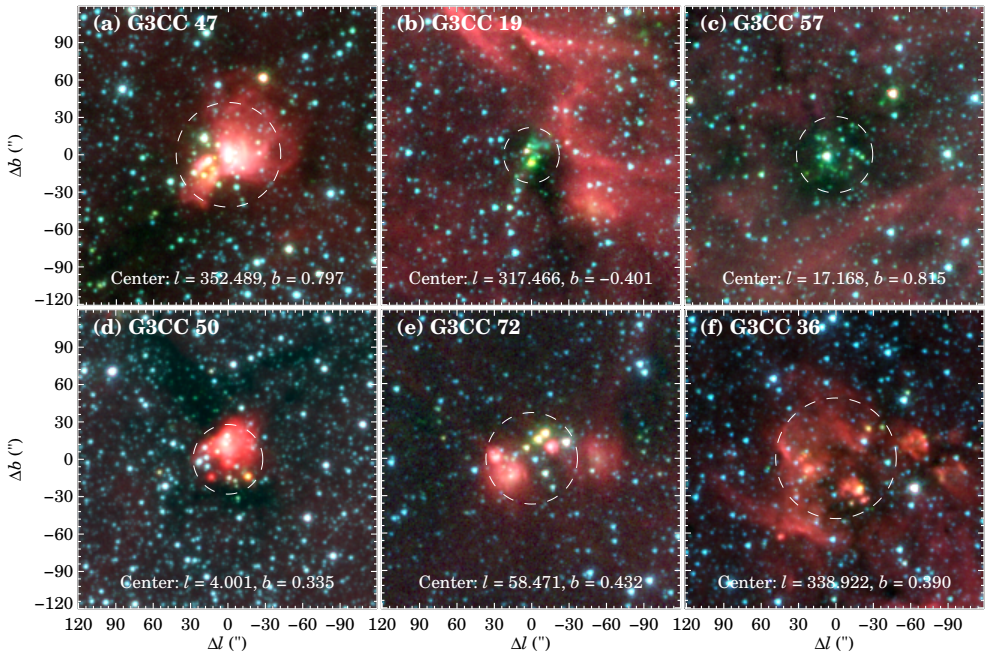

Figure 3.1: *Spitzer*-IRAC three-color images made with the 3.6 (blue), 4.5 (green) and 8.0 μm (red) bands, of six (out of 75) new embedded cluster candidates discovered in this work, using the GLIMPSE survey. The dashed circles represent the estimated angular sizes. The images are in Galactic coordinates and the given offsets are with respect to the cluster center, indicated at the bottom of each panel.

for every cluster candidate the estimated number of stellar members within the assumed radius, $N_{\rm circ}$, counting the YSOs selected by the red-color criterion and the additional members identified in the images (flags BR,C8,U8). Note that this number corresponds to a lower limit, since lower mass members could still be undetected due to the limited angular resolution and sensitivity for long distances.

Finally, we tried to complete our list of new cluster candidates by doing a systematic visual inspection with the on-line viewer in the entire GLIMPSE surveyed area, including also fully exposed clusters that appear bright at 3.6 μm (equivalent to flag 'B'). We found from this process 23 additional clusters, of which, however, only 4 are new discoveries with respect to our literature compilation. They are marked in column 8 of Table 3.1 with a 'V', while the ones detected by the automated method are indicated with an 'A'. We note that, of the 17 known clusters we rediscovered from the red-source overdensities, only 3 are from the Mercer et al. (2005) list. This practically null overlap between the two detection methods demonstrates that our search is fully complementary and particularly useful to detect embedded cluster can-

didates, confirming the ideas we presented at the beginning of this Section.

Table 3.1: New GLIMPSE stellar cluster candidates.

G3CC	l	b	α	δ	Diam.	$N_{\rm circ}$	Det.	Flags
	(°)	(°)	(J2000)	(J2000)	(″)			
(1)	(2)	(3)	(4)	(5)	(6)	(7)	(8)	(9)
1	295.151	−0.587	11:43:24.9	−62:25:36	98	16	A	C8,E8,S
2	299.014	0.128	12:17:24.9	−62:29:04	60	4	V	B,E8
3	299.051	0.181	12:17:47.9	−62:26:12	81	14	A	C8
4	299.337	−0.319	12:19:43.1	−62:58:08	51	9	A	BR,E8
5	300.913	0.887	12:34:16.2	−61:55:04	76	10	A	C8,E8
6	301.643	−0.240	12:40:02.6	−63:05:01	67	9	A	DC,E8,S
7	301.947	0.313	12:42:53.7	−62:32:32	65	12	A	E8
8	303.927	−0.687	13:00:22.2	−63:32:30	107	14	A	C8,E8
9	304.002	0.464	13:00:40.3	−62:23:17	82	···	A	BR,E8,S
10	304.887	0.635	13:08:12.3	−62:10:23	41	7	A	DC,E4
11	307.083	0.528	13:26:58.8	−62:03:25	71	8	A	C8,DC,E8,S
12	309.421	−0.621	13:48:38.1	−62:46:11	48	10	A	DC
13	309.537	−0.742	13:49:51.6	−62:51:42	38	7	A	C8,DC,E8
14	309.968	0.302	13:51:25.6	−61:44:51	40	6	A	DC,E8
15	309.996	0.507	13:51:15.8	−61:32:30	88	8	A	E8,DC
16	313.762	−0.860	14:24:58.6	−61:44:56	80	15	A	BR,C8,DC,E4,E8,U8
17	314.203	0.213	14:25:15.4	−60:35:22	86	12	A	C8,E8,U8
18	314.269	0.092	14:26:06.6	−60:40:43	87	8	A	C8,DC,E8,S,V2
19	317.466	−0.401	14:51:19.3	−59:50:46	45	7	A	DC,E4,E8
20	317.884	−0.253	14:53:45.6	−59:31:34	74	15	A	DC,E4,E8
21	318.049	0.088	14:53:42.2	−59:08:49	88	20	A	C8,DC,U8
22	318.777	−0.144	14:59:33.5	−59:00:59	105	8	A	B,E8,V2
23	319.336	0.912	14:59:31.0	−57:49:18	65	12	A	
24	321.937	−0.006	15:19:43.2	−57:18:04	33	9	A	C8,DC,E8
25	321.952	0.014	15:19:44.6	−57:16:35	37	10	A	E8
26	326.476	0.699	15:43:18.0	−54:07:23	81	12	A	C8,DC,E4,U8
27	326.796	0.385	15:46:20.3	−54:10:35	54	10	A	DC,E4
28	328.165	0.587	15:52:42.6	−53:09:48	31	6	A	E4,U8
29	328.252	−0.531	15:57:58.9	−53:58:02	58	9	A	C8,DC,E4,E8
30	328.809	0.635	15:55:48.4	−52:43:00	82	9	V	C8,DC,E4
31	329.184	−0.313	16:01:47.0	−53:11:40	73	8	A	DC,E4,U8
32	330.031	1.043	16:00:09.4	−51:36:52	56	6	A	DC,E8,S
33	335.061	−0.428	16:29:23.5	−49:12:25	63	6	A	C8,DC,E4
34	337.153	−0.393	16:37:48.5	−47:38:53	49	4	A	DC,U8,V2
35	338.396	−0.406	16:42:43.2	−46:43:36	65	8	A	C8,DC,E4
36	338.922	0.390	16:41:15.7	−45:48:23	97	11	A	C8,E8,S
37	338.930	−0.495	16:45:08.6	−46:22:50	80	11	A	C8,DC,E8,U8
38	339.584	−0.127	16:45:59.1	−45:38:44	53	9	A	DC,E4,E8
39	344.221	−0.569	17:04:06.6	−42:18:57	51	11	A	BR,E4,E8
40	344.996	−0.224	17:05:09.7	−41:29:26	75	15	A	DC,E4,U8
41	347.883	−0.291	17:14:27.3	−39:12:35	62	6	V	C8,E8
42	348.180	0.483	17:12:08.1	−38:30:54	38	7	A	E8
43	348.584	−0.920	17:19:11.6	−39:00:08	52	10	A	C8,E4
44	350.105	0.085	17:19:26.7	−37:10:48	167	25	A	C8,E8,V2
45	350.930	0.753	17:19:04.7	−36:07:16	90	14	A	C8,DC,E8,S
46	351.776	−0.538	17:26:43.1	−36:09:18	93	14	A	C8,DC,E4,E8
47	352.489	0.797	17:23:15.6	−34:48:53	84	7	A	C8,E8
48	358.386	−0.482	17:43:37.5	−30:33:51	57	5	A	C8,DC,E4,E8,V2
49	0.675	−0.046	17:47:23.7	−28:22:59	140	23	A	C8,E8,S

Table 3.1: continued.

G3CC	l	b	α	δ	Diam.	$N_{\rm circ}$	Det.	Flags
	(°)	(°)	(J2000)	(J2000)	(″)			
(1)	(2)	(3)	(4)	(5)	(6)	(7)	(8)	(9)
50	4.001	0.335	17:53:34.5	−25:19:57	56	12	A	BR,C8,E8
51	5.636	0.239	17:57:33.9	−23:58:05	65	7	A	C8,DC,E8
52	6.797	−0.256	18:01:57.6	−23:12:26	50	11	A	C8,DC,E4,U8
53	8.492	−0.633	18:06:59.3	−21:54:55	126	28	A	DC,S
54	9.221	0.166	18:05:31.3	−20:53:21	42	7	A	DC,E8
55	14.113	−0.571	18:18:12.4	−16:57:18	57	9	A	DC,E8
56	14.341	−0.642	18:18:55.2	−16:47:15	124	15	A	C8,DC,E4,E8
57	17.168	0.815	18:19:08.4	−13:36:29	61	12	A	DC
58	25.297	0.309	18:36:20.5	−06:38:57	39	8	A	E8
59	26.507	0.284	18:38:40.0	−05:35:06	49	7	A	C8,DC
60	31.158	0.047	18:48:02.1	−01:33:26	50	8	A	E8
61	34.403	0.229	18:53:18.4	01:24:47	91	8	A	DC,E4
62	39.497	−0.993	19:06:60.0	05:23:05	53	7	A	C8,V2
63	43.040	−0.451	19:11:38.7	08:46:40	52	6	A	C8,E4,E8
64	43.893	−0.785	19:14:26.8	09:22:44	63	7	A	C8,E8
65	47.874	0.309	19:18:04.1	13:24:41	68	11	A	C8,E8
66	49.912	0.369	19:21:47.7	15:14:20	55	11	V	BR,C8,E8
67	50.053	0.064	19:23:11.3	15:13:10	107	14	A	DC,S
68	52.570	−0.955	19:31:54.7	16:56:44	44	9	A	E4,E8
69	53.147	0.071	19:29:18.0	17:56:41	119	13	A	C8,DC,S
70	53.237	0.056	19:29:32.3	18:00:57	76	19	A	DC,S
71	56.961	−0.234	19:38:16.7	21:08:02	58	8	A	C8,E8
72	58.471	0.432	19:38:58.4	22:46:32	73	10	A	C8,E8
73	59.783	0.071	19:43:09.9	23:44:14	120	11	A	C8,E4,E8,V2
74	62.379	0.298	19:48:02.4	26:05:51	47	7	A	
75	64.272	−0.425	19:55:09.4	27:21:18	55	10	A	BR

Notes. Units of right ascension are hours, minutes, and seconds, and units of declination are degrees, arcminutes, and arcseconds. Column 6 gives the estimated angular diameter. Column 7 gives the estimated number of stellar members within the assumed radius, considered as a lower limit due to possible non-detection of low mass stars. Column 8 indicates the detection method: automated search (A), or on-line viewer (V). Column 9 lists different flags determined after visual inspection of the GLIMPSE three-color images, indicating: association with extended 8.0 μm emission (E8) or localized diffuse 4.5 μm emission (E4); cluster embedded in an infrared dark cloud (DC); cluster composed of red sources and additional bright normal stars (BR); cluster composed of bright normal stars only (B); presence of additional probable YSOs, identified as sources detected uniquely at 8.0 μm (U8), or compact 8.0 μm objects not listed in the point source catalog or archive (C8); sparse, not centrally condensed morphology (S); cluster identified by-eye in a nearby location of an automatically detected overdensity, but not exactly at the same position (V2).

3.5 Cross-identifications

Since we are dealing with cluster catalogs coming from different compilations and searches, a specific object can be present in more than one list, as was already shown in the previous Sections. We therefore implemented a simple merging procedure to have finally an unique sample of stellar clusters. The first condition to identify one repetition, i.e., the same object in two different catalogs, was that the angular distance between the two given center positions were less than both listed angular diameters. We checked all merged objects under this criterion looking for the corresponding cluster names, when available, and confirmed a repetition when the names coincided. Otherwise (names not available or different), two clusters were considered the same object when the angular distance was less than both angular radius, which were also required to agree within a factor of 5. The last condition was imposed to account for the case when a compact infrared cluster shares the same field of view of a (different) optical cluster with a large angular size. This cross-identification process was not intended to be perfect, but good enough to not affect the statistical results of the whole cluster sample. Within the ATLASGAL Galactic range, a much more thoughtful revision was done (see § 4.1), further refining the cross-identifications, and even recognizing a few duplications and spurious clusters which were excluded from the final sample, as described in Section § 3.6.

A repeated cluster was moved to the previous list, following the sequence presented in Table 3.2. The optical catalogs were put first, so that any cluster visible in the optical is considered an *optical* cluster. The infrared lists (including the *near-infrared* and *mid-infrared* clusters) were positioned afterwards in chronological order, and therefore following roughly the discovery time. Table 3.2 summarizes the final cluster sample. In the first three columns we list the specific cluster catalogs with an ID used throughout this work, and their category according to the previous Sections. For a given reference, we represent as $N_{\rm cl}$ the absolute (original) number of objects in the catalog, whereas $N^*_{\rm cl}$ is the number of different entries with respect to all catalog listed before it. Absolute and after-merging numbers are presented for the total sky range of every list, the ATLASGAL Galactic range ($|l| \leq 60^\circ$ and $|b| \leq 1.5^\circ$), and finally for only those associated with ATLASGAL emission according to the criterion explained in § 4.2.1.

After cross-identifications, we ended up with a final sample of 3904 stellar clusters, groups and candidates, of which 2247 are *optical*, 1493 *near-infrared*, and 164 *mid-infrared* clusters. Taking into account the repetitions within each category, but not between them, the numbers of objects are 2247 for *optical*,

Table 3.2: Number of clusters for every catalog used in this work.

Catalog		Type	Total		ATLASGAL range[a]		ATLASGAL emission[b]	
ID	Reference		$N_{\rm cl}$	$N^*_{\rm cl}$	$N_{\rm cl}$	$N^*_{\rm cl}$	$N_{\rm cl}$	$N^*_{\rm cl}$
01	Dias et al. (2002, ver. 3.1)[c]	*Optical*	2117	2117	216	216	29	29
02	Kronberger et al. (2006)	*Optical*	239	130	29	11	5	4
03	Dutra & Bica (2000)	*NIR*	22	8	18	8	8	2
04	Bica et al. (2003a)[d]	*NIR*	275	264	30	28	28	26
05	Dutra et al. (2003a)	*NIR*	174	167	81	80	78	77
06	Bica et al. (2003b)	*NIR*	163	155	69	68	63	62
07	Lada & Lada (2003)	*NIR*	76	12	4	0	4	0
08	Porras et al. (2003)	*NIR*	73	21	0	0	0	0
09	Mercer et al. (2005)	*MIR*	90	86	83	81	55	54
10	Kumar et al. (2006)	*NIR*	54	20	0	0	0	0
11	Froebrich et al. (2007b)	*NIR*	998	676	44	21	2	0
12	Faustini et al. (2009)	*NIR*	23	16	9	9	9	9
13	Glushkova et al. (2010)	*NIR*	194	32	12	4	1	0
14	Borissova et al. (2011)	*NIR*	96	96	85	85	65	65
15	Not cataloged (NIR)	*NIR*	26	26	12	12	10	10
16	Not cataloged (MIR)	*MIR*	3	3	3	3	0	0
17	New GLIMPSE (this work)	*MIR*	111	75	103	69	94	67
	Total *Optical*		2247	2247	227	227	33	33
	Total *NIR*		1950	1493	356	315	265	251
	Total *MIR*		197	164	182	153	144	121

Notes. $N_{\rm cl}$ is the absolute number of entries in every catalog, whereas $N^*_{\rm cl}$, for a given reference, is the number of objects not present in any of the catalogs listed before it (see § 3.5 for details). Absolute numbers for whole categories ($N_{\rm cl}$ for last three lines) take into account repetitions inside the category, naturally. All numbers in this table are after removing a few spurious objects (listed in Table 3.3).
[(a)] Clusters with galactic coordinates within the ATLASGAL range: $|l| \leq 60°$ and $|b| \leq 1.5°$. [(b)] Clusters associated with ATLASGAL emission (see § 4.2.1). [(c)] Version 3.1 is from November, 2010. [(d)] Includes clusters from Dutra & Bica (2001).

1950 for *near-infrared*, and 197 for *mid-infrared*. Note that the low number of *mid-infrared* clusters is due to the confined Galactic range of the GLIMPSE survey; actually, when considering the ATLASGAL range only, which is similar to the GLIMPSE range, the numbers of objects are of the same order for the different categories: 227 *optical*, 315 *near-infrared*, and 153 *mid-infrared* clusters, after merging.

3.6 Spurious cluster candidates

The majority of the new IR star cluster catalogs compiled here are based on algorithmic or by-eye detections of stellar density enhancements on images of

IR Galactic surveys, and do not provide information whether the identified objects are really composed of physically related stars, or are instead produced by chance alignments on the same line of sight. Due to the patchy interstellar extinction, an apparent stellar overdensity can simply correspond to a low extinction region with high extinction surroundings. In addition, bright spatially extended emission might be incorrectly classified as unresolved star clusters embedded in nebulae. Confirmation of a real cluster can be achieved through deeper, high-resolution IR photometry or through spectroscopic observations of the candidate stellar members (e.g., Dutra et al. 2003b; Borissova et al. 2005, 2006; Messineo et al. 2009; Hanson et al. 2010; Davies et al. 2012b), which in some cases make also possible the estimation of physical parameters. Though an important number of such studies have been carried out during the last decade, they still cover a small fraction of the total sample of cluster candidates to be confirmed, mainly because these objects correspond to relatively new discoveries, and the observations needed for a more detailed analysis are very time-consuming.

Nevertheless, we can roughly estimate the contamination by spurious detections in our sample of cluster candidates in a statistical way. For example, by comparison of the basic characteristics (Galactic distribution, detection method and morphology) of the cluster candidates with that of known clusters rediscovered by their method, Froebrich et al. (2007b) found that about 50% of their catalog correspond to false clusters. Detailed follow-up studies of unbiased subsets of objects from this catalog, only restricted to certain areas, have determined similar contamination rates (Froebrich et al. 2008, and references therein). Another example is the Dutra & Bica (2000) catalog, where 52 (out of 58) candidates have been observed using higher resolution NIR imaging (Dutra et al. 2003b; Borissova et al. 2005), resulting in 36 previously unresolved alignments of few bright stars (probably in most cases unrelated) which resemble compact cluster at the 2MASS resolution. This would imply a $\sim 70\%$ contamination by spurious detections, but we note that, since this catalog is based on a systematic search for sources projected close to the Galactic center, it is particularly affected by a higher number of background/foreground stars and more intervening dust, which all help to mimic star clusters.

The subsequent 2MASS by-eye searches performed by this team (Dutra & Bica 2001; Dutra et al. 2003a; Bica et al. 2003b) cover the whole Galactic plane and, furthermore, they are focused on radio/optical nebulae which generally correspond to H II regions, increasing the chance to find real stellar clusters and related groups. Typical spurious clusters associated with radio/optical nebulae correspond to one or few bright stars plus extended emission (e.g., Borissova et al. 2005). We caution that, however, as the number of stars in

these embedded multiple systems is larger, under the assumption that the stars are physically related, the consideration of a particular candidate as spurious or possible cluster is more dependent on how we define an *embedded cluster*. Under the definition used throughout this work (see § 2.3), since we do not impose any constraint on the number of members, we expect a minimal contamination by false detections for clusters associated with molecular gas[7]. For exposed clusters, on the contrary, the probability of that a cluster candidate consists of only unrelated stars on the same line of sight is much higher. Based on the above discussion, we estimate an overall spurious contamination rate of $\sim 50\%$ for exposed clusters that have not been confirmed by follow-up studies.

We list in Table 3.3 the spurious candidates within the compiled cluster catalogs, which were not included in our final sample. This table is composed by the false detections found by Dutra et al. (2003b) and Borissova et al. (2005), and the candidates from the Froebrich et al. (2007b) catalog listed as "not a cluster" by the literature compilation of follow-up studies by Froebrich et al. (2008). The other objects correspond to a few globular clusters, and false clusters or duplications found in this work, primarily from the literature revision of the cluster sample in the ATLASGAL range (§ 4.1).

[7]For consistency with earlier studies, however, we anyway excluded from our sample a few embedded cluster candidates that have been considered spurious in the literature.

Table 3.3: List of spurious clusters, duplicated entries, and globular clusters within the catalogs used in this work.

Name	Flag[a]	Catalog[b]	Ref.	Comments
[DB2000] 2	S	03	1	
[DB2000] 3	S	03	1	
[DB2000] 4	S	03	1	
[DB2000] 7	S	01,03	2	
[DB2000] 8	S	03	1,2	
[DB2000] 9	S	03	1	
[DB2000] 13	S	03	1	
[DB2000] 14	S	03	1	
[DB2000] 15	S	03	1	
[DB2000] 16	S	03	1	
[DB2000] 19	S	03	1	
[DB2000] 20	S	03	1	
[DB2000] 21	S	03	1	
[DB2000] 22	S	03	1	
[DB2000] 23	S	03	1	
[DB2000] 24	S	03	1	
[DB2000] 29	S	03	1	
[DB2000] 30	S	03	1	
[DB2000] 33	S	03	1	
[DB2000] 34	S	03	1	
[DB2000] 36	S	03	1	
[DB2000] 37	S	03	1	
[DB2000] 38	S	03	1	
[DB2000] 39	S	03	1	
[DB2000] 40	S	01,03	2	
[DB2000] 41	S	03	2	
[DB2000] 43	S	03	1	
[DB2000] 44	S	03	1	
[DB2000] 46	S	03	1	
[DB2000] 47	S	03	1	
[DB2000] 48	S	03	1	
[DB2000] 53	S	03	1	
[DB2000] 54	S	03	1	
[DB2000] 56	S	03	2	
[DB2000] 57	S	03	1	
[DB2000] 58	S	01,03	2	
NGC 6334 VI	S	04	3	
[DBS2003] 83	S	05	2	
[DBS2003] 84	S	05	2	
[DBS2003] 95	D	05	4	[d]
[DBS2003] 170	S	05	2	
[DBS2003] 172	S	05	5	
[BDS2003] 101	S	06	2	
[BDS2003] 103	GC	06	2	
[BDS2003] 105	S	06	2	
[BDS2003] 150	D	06	4	[e]
[MCM2005b] 3	GC	09	6,7	
[MCM2005b] 5	GC	09	8	
[FSR2007] 2	S	11	9	
[FSR2007] 23	S	01,11	9	
[FSR2007] 41	S	11	10	
[FSR2007] 91	S	11	10	

Table 3.3: continued.

Name	Flag[a]	Catalog[b]	Ref.	Comments
[FSR2007] 94	S	01,11	9	
[FSR2007] 114	S	11	10	
[FSR2007] 128	S	11	10	
[FSR2007] 744	S	01,11	11	
[FSR2007] 776	S	11	11	
[FSR2007] 801	S	11	11	
[FSR2007] 841	S	11	11	
[FSR2007] 894	S	01,11	11	
[FSR2007] 927	S	01,11	11	
[FSR2007] 956	S	01,11	11	
[FSR2007] 1527	S	11	9	
[FSR2007] 1635	S	11	10	
[FSR2007] 1647	S	11	10	
[FSR2007] 1659	S	11	9	
[FSR2007] 1685	S	11	10	
[FSR2007] 1695	S	11	10	
[FSR2007] 1754	S	11	10,9	
[FSR2007] 1767	S	01,11	9	
[FSR2007] 1735	GC	11	12,9	
Ruprecht 166	S	01	13	
Lynga 3	S	01	14	
NGC 6334	S	01	4	*f*
NGC 6357	D	01	4	*g*
SAI 24[c]	D	01	4	*h*
[FSR2007] 101[c]	D	01	4	*i*
[FSR2007] 124[c]	S	01	4	*j*
[FSR2007] 178[c]	D	01	4	*i*
[FSR2007] 198[c]	D	01	4	*i*
[FSR2007] 869[c]	D	01	4	*k*
[FSR2007] 923[c]	D	01	4	*i*
[FSR2007] 974[c]	D	01	4	*i*
[FSR2007] 1471[c]	D	01	4	*i*

Notes. We exclude in this list: [FSR2007] 119 and [FSR2007] 584 from the Froebrich et al. (2008) list, reconsidered by Froebrich et al. (2010) as possible very old cluster and embedded young cluster, respectively; [DBS2003] 174 from Borissova et al. (2005), since we discovered an associated compact cluster of YSOs in the GLIMPSE images.
[(a)] Flag indicates if the cluster is spurious (S), a duplicated entry in the corresponding catalog (D), or a globular cluster (GC). [(b)] Catalog ID as given in Table 3.2. [(c)] Affects the corresponding entry in Dias et al. (2002, ver. 3.1) catalog only.
Comments: [(d)] Significantly overlaps [DBS2003] 96. [(e)] Significantly overlaps [BDS2003] 151, and does not show an independent overdensity. [(f)] NGC 6334 is not a single cluster but a molecular complex containing many young star clusters (already included in our sample). [(g)] = Pismis 24. [(h)] = Collinder 34. [(i)] Duplicated name. [(j)] Wrong coordinates with respect to the original catalog. [(k)] = Koposov 63.

References. (1) Dutra et al. (2003b); (2) Borissova et al. (2005); (3) Straw et al. (1989); (4) This work; (5) Borissova et al. (2006); (6) Strader & Kobulnicky (2008); (7) Kurtev et al. (2008); (8) Longmore et al. (2011); (9) Froebrich et al. (2008); (10) Bica et al. (2008a); (11) Bonatto & Bica (2008); (12) Froebrich et al. (2007a); (13) Piatti & Clariá (2001); (14) Carraro et al. (2006).

4

Stellar clusters in the inner Galaxy and their correlation with ATLASGAL

The next step of this work was to characterize the ATLASGAL emission, if present, at the positions of the star clusters compiled before, and to compare this emission with near-infrared and mid-infrared images. Hereafter, our study is naturally restricted to the ATLASGAL Galactic range ($|l| \leq 60°$ and $|b| \leq 1.5°$), and we refer to the list of the 695 stellar clusters within that range as the "whole cluster sample" (or simply as the "cluster sample"), unless noted. Together with this process, we performed a thoughtful literature revision in order to add and update distances and ages for an important fraction of the sample, as well as to look for connections with known H II regions, IRDCs, and IR bubbles. We organize all this information in an unique catalog, which in the near future will be available electronically to the community at the VizieR service[1]. In Appendix B, we list the whole sample of clusters with the most relevant columns of our catalog (Tables B.1 and B.2), as well as the used references with their corresponding identification numbers (Table B.3). In this chapter, we describe the construction of the catalog (§ 4.1) and a subsequent statistical analysis (§ 4.2).

[1] http://vizier.u-strasbg.fr/viz-bin/VizieR

4.1 Construction of the Catalog

4.1.1 Designations, position and angular size

The basic information of each cluster is obtained directly from the original cluster catalogs compiled in § 2. The column `ID` is a record number from 1 to 695 with the clusters sorted by Galactic longitude. The cluster designation, based on the original catalog, is listed in the column `Name`, which was chosen, in general, to be consistent with the SIMBAD database identifier. Other common names, or designations from other catalog(s) (for clusters originally present in more than one catalog), are given in the column `OName`. In the column `Cat`, we provide the original cluster catalog(s) from which each object was extracted, using the reference ID defined in Table 3.2.

The position of each object is based on the equatorial coordinates listed in the original catalog(s). For multiple catalogs, we averaged the listed positions and angular sizes to obtain the final values given here, ignoring in some cases certain references that were considered less accurate or redundant (which are listed between parentheses in the column `Cat`). The galactic coordinates are given in `GLON` and `GLAT`, whereas the equatorial coordinates (J2000.0) are listed in `RAJ2000` and `DECJ2000`. The column `Diam` is the angular diameter in arcseconds.

4.1.2 ATLASGAL emission

From the ATLASGAL survey images, we extracted submaps centered at the cluster locations and with a field of view of $\max\{30', 2 * \texttt{Diam}\}$ to search for submm dust continuum emission tracing molecular gas likely associated with the clusters, and to then characterize its morphology. The first computation needed to determine the presence of real emission in those fields is a proper estimation of the local rms noise level, σ, for which we used an iterative sigma-clipping procedure[2] with a threshold of 2σ and a convergence criterion of 1% (iteration stops when the non-sky pixels are a fraction lower than 1% of the total of sky pixels of the previous iteration). With these chosen parameters, the computed values of σ agree well with quick estimations of the noise over emission-free regions identified by eye in some test fields. The average noise level is $\sigma = 45$ mJy/beam, and 95% of the total of fields have σ in the range $[30, 60]$ mJy/beam.

Using the computed rms noise level of each field, we identified clumps of emission by applying the decomposition algorithm *Clumpfind* (Williams et al.

[2]We use the routine `meanclip` from the the IDL Astronomy User's Library.

1994) in its IDL implementation for 2D data, `clfind2d`. This routine requires only two input parameters: 1) the intensity threshold, which determines the minimum emission to be included in the decomposition; and 2) the stepsize which sets the contrast needed between two contiguous features to be identified as different clumps. We chose threshold = stepsize = 3σ, after visualizing the decomposition on some test fields and requiring that the obtained clumps were roughly similar to those that would be identified by the human eye. We slightly modified the IDL code of `clfind2d` to improve the clump decomposition and to avoid false detections. Originally, the code described by Williams et al. (1994) deals with blended emission by splitting it into its corresponding clumps using a simple friends-of-friends method, but instead the current implementation breaks up the emission by assigning the blended pixels to the clump with the nearest peak, which produces some disconnected clumps, i.e., pixels of the same clump not connected by a continuous path. We thus changed the peak distance criterion by the *minimum distance to a clump* to assign blended emission to the existing clumps, which noticeably minimizes the effect of disconnected clumps and resembles the friends-of-friends method. A second modification to the code was to require that the clumps have angular sizes larger than the beam in both image directions, in order to reject "snake"-shaped clumps marginally above the threshold which correspond to minor image artifacts rather than real astronomical emission.

The employed algorithm assigns into clumps all the emission above the given threshold and with an extension larger than the beam. We computed the angular distance from the cluster center of the nearest detected ATLASGAL emission pixel to have a quick first impression of the presence of molecular gas. Such values are listed in the column `Clump_sep`, normalized to the cluster angular radius (when no emission is detected in the whole ATLASGAL submap, a lower limit is given).

We also performed a careful visual inspection of every ATLASGAL submap, using an IDL script to overplot there the positions of all star clusters of our sample within the field, and the submm clumps detected before, as well as any interesting object, like the positions of measured molecular line velocities (see § 4.1.4). In another window, the script displays a smaller field of view ($\sim 10'$) with the cluster itself seen by whole set of IR images (2MASS and GLIMPSE, including three-color images) overlaid with ATLASGAL contours, in order to compare morphologically the IR and the submm emissions. The column `Clump_flag` is a two-digit flag which synthesizes whether or not the cluster appears physically related to the nearest submm clump detected by *Clumpfind*, as seen by the inspection of these images. The first digit of `Clump_flag` can take the values: 0, when the nearest ATLASGAL clump does

not seem to be associated with the cluster; 1, when it does seem to be clearly associated, specially for the cases of star clusters deeply embedded within centrally condensed ATLASGAL clumps; and 2, when the physical connection is less clear but still likely, in most cases when the clump appears to belong to the same star-forming region than the stellar cluster, connected by some diffuse mid-IR emission. The second digit of `Clump_flag` provides information about the line velocity available for each object and will be described in § 4.1.4.

The column `Morph` is a text flag that gives further information about the morphology of the detected ATLASGAL emission versus the IR emission, after the visual inspection explained above. It is composed of two parts separated by a period. The second part indicates the mid-IR morphology and will be described in § 4.1.3. The first part tells about how the ATLASGAL emission is distributed throughout the immediate star cluster area, including the following cases:

- `emb`: cluster fully embedded, with its center matching the submm clump peak (Fig. 4.2, *top*).
- `p-emb`: cluster partially embedded, whose area is not completely covered, or the submm clump peak is significantly shifted from the (proto-) stars locations (Fig. 4.2, *bottom*).
- `surr`: possibly associated submm emission surrounding the cluster or close to its boundaries (Fig. 4.3, *top*).
- `few`: one or few ATLASGAL clumps within the cluster area (mostly for optical clusters having a large angular size), not necessarily physically related with the cluster.
- `few*`: the same morphology than before, but now the clump(s) is (are) likely associated with the star cluster according to previous studies in the literature, or because the kinematic distance from the gas (see § 4.1.4) agrees with the stellar distance.
- `exp`: exposed cluster, without ATLASGAL emission in the immediate surroundings (Fig. 4.3, *middle* and *bottom*).
- `exp*`: cluster which is physically exposed, but presents submm emission within the cluster area which appears in the same line of sight, but with a kinematic distance discrepant from the stellar distance (the cluster would be categorized as `few` or `surr` if no distance information were available).

4.1.3 Mid-IR morphology and association with known objects

The mid-infrared morphology of a stellar cluster can also provide some clues about its evolutionary stage and presence of feedback, in particular the intensity and distribution of the 8.0 μm emission. We indicate in the second part of the column `Morph` (after the period) details about the 8.0 μm morphology of each cluster, after visually inspecting GLIMPSE three-color images made with the 3.6 (blue), 4.5 (green) and 8.0 μm (red) bands, as part of the process described in the previous Section. This flag includes the following cases:

- `bub-cen`: presence of an IR bubble which seems to be produced by the cluster through stellar feedback, and appears in the images centered near the cluster position (Fig. 4.3, *top*).
- `bub-cen-trig`: the same situation than before, together with the presence of possible YSOs at the periphery of the bubble identified by their reddened appearance in the images, suggesting triggered star formation generated by the cluster (see also Fig. 4.3, *top*).
- `bub-edge`: in this case, the cluster itself appears at the edge of an IR bubble, suggesting that it was probably formed by triggering from an independent cluster or massive star.
- `pah`: presence of bright and irregular emission at 8.0 μm which seems to be produced by the cluster through stellar feedback (Fig. 4.2, *bottom*); it is attributed also to radiation from UV excited PAHs or warm dust, but is not clearly identified as an IR bubble (though it sometimes shows bubble-like borders)[3].

All IR bubbles associated with star clusters and recognized in this work are identified in the table column `Bub`. We give the bubble names from the catalogs by Churchwell et al. (2006, 2007) when the objects are listed there, otherwise an identifier based on the cluster `ID` is provided. We also list in this column IR bubbles that are located in the neighborhood of the clusters but that do not appear clearly associated with them or do not represent any of the scenarios defined above (e.g., bubble in the same star-forming region but not interacting directly with the cluster). Similarly, we identified on the GLIMPSE three-color images and on the 8.0 μm images the presence of an infrared dark

[3]This situation is conceptually different from the one indicated by the flag E8 for G3CC objects (see § 3.4), where any extended 8.0 μm emission in the vicinity of the cluster is flagged. Here, the emission has to be located throughout most of the cluster area and appears as produced by the whole cluster.

cloud in which the cluster appears to be embedded (see Fig. 4.2, *top*). These objects are listed in the column `IRDC` using a name based on the cluster `ID` when the IRDC has not been cataloged so far, or the designations from the catalogs by Simon et al. (2006) and Peretto & Fuller (2009) if it was identified there before. Unlike the IR bubbles, since we do not provide information of the IRDCs within the `Morph` flag, we only list in the column `IRDC` those objects that exhibit possible physical connection with the cluster. Many of the IRDCs reported by Peretto & Fuller (2009) are only small dark fluctuations over a bright background and do not constitute cluster-forming clumps. In any case, in this work what we really use to study the star cluster maternities is the ATLASGAL emission, that represents a much more unbiased and objective tracer of the dense molecular material of which they are composed. We note that all these features were distinguished on the GLIMPSE images, so that we are limited to the coverage of the survey which is more restricted in the Galactic plane than the ATLASGAL range. The table column `no_GL` indicates when a particular cluster has no GLIMPSE data available (`no_GL` = 1, otherwise `no_GL` = 0). GLIMPSE images are available for 93% of the cluster sample.

In addition, we searched in the literature for the presence of H II regions associated with the clusters, and they are listed in the column `HII_reg` with designations compatible with SIMBAD or common names used in the literature for large molecular complexes (see the references for complexes, `ref_Complex`, explained in § 4.1.6). Particular designations used here which do not exist in SIMBAD and do not belong to complexes are those starting with: "HRDS", indicating the H II regions discovered recently by Anderson et al. (2011) using radio recombination line (RRL) observations; and "RMS", which represent possible H II regions corresponding to radio continuum sources found by the RMS survey (see § 4.1.4 for a description of the on-line search we performed in such database; the objects listed here were taken from the "Radio Catalogue Search Results" section of the webpage of each individual RMS source investigated). It is worth noting that, for the H II regions found primarily using SIMBAD, we carefully checked their nature in the literature by requiring the presence of radio continuum emission or RRLs, since some sources are misclassified as H II regions in SIMBAD. Two important consulted references of RRL observations were Caswell & Haynes (1987) (sources with prefix [CH87]) and Lockman (1989) (sources with prefix [L89b]). We also specified two flags at the end of some names to indicate two particular situations: the flag "(UC)", when the source is classified as an ultra compact H II region in the literature; and the flag "(bub)", when the H II region appears associated with the listed IR bubble, but not directly with the star cluster. However, we note that the UC classification is just an estimation, considering that detailed interferometric and large-scale

observations are needed to really unveil the spatial distribution of a particular H II region.

4.1.4 Kinematic distance

An important effort of this work was to assign distances to the most number of clusters as possible. In this regard, we took advantage of the fact that many of the ATLASGAL clumps which were assumed to be physically associated with the stellar clusters have measurements of molecular line LSR velocities. By assuming a Galactic rotation model, we can transform these velocities in kinematic distance estimates for the clumps and, hence, for the associated clusters. We used four main references of line velocities, which were searched systematically on the ATLASGAL submaps (positions overlaid there), in the following priority order: 1) follow-up $NH_3\,(1,1)$ observations towards bright ATLASGAL sources (Wienen et al. 2012, for northern sources; and Wienen et al., in preparation, for southern ones); 2) similar targets observed in the $N_2H^+\,(1-0)$ line (Wyrowski et al., in preparation); 3) the CS $(2-1)$ Galactic survey by Bronfman et al. (1996) towards *IRAS* sources with colors typical of compact H II regions; and 4) velocities of massive YSO candidates from the Red MSX Source (RMS) survey (Urquhart et al. 2008) available on-line[4], corresponding mainly to targeted observations in the $(1-0)$ and $(2-1)$ transitions of ^{13}CO, or literature velocities compiled there. The priority sequence was based primarily on the number of ATLASGAL clumps available in each of the lists, in order to make more uniform the velocity sample; the RMS survey was put at the end because the ^{13}CO traces less dense gas than the other three molecules, which are unambiguously linked to the ATLASGAL emission. We note that, however, when the same clump is found in more than one list, the velocity differences are negligible compared to the error assumed for the computation of the kinematic distance (7 km s^{-1}, see below). The adopted LSR velocity is listed in the table column `Vlsr` (in km s^{-1}). We give the corresponding reference in the column `ref_Vlsr`, and the source name in `name_Vlsr` (SIMBAD compatible or the one used in the original paper). If no velocity was available from any of the four main lists mentioned before, additional velocity references were found by doing a coordinate query in SIMBAD.

In some cases, we did not find any velocity for the closest detected ATLASGAL clump, but we did for another possibly associated clump or for the H II region. This information is indicated in the second digit of the flag `Clump_flag`, which can take the values: 0, when no velocity is available; 1, when the listed velocity is from the nearest ATLASGAL clump or from a clump directly adja-

[4] http://www.ast.leeds.ac.uk/cgi-bin/RMS/RMS_SUMMARY_PAGE.cgi

cent to it; 2, when the clump with the velocity is not the nearest but is within the cluster area (used in cases of optical clusters with large angular size); 3, when the velocity is from an ATLASGAL clump which is apparently associated with the cluster as seen in the images, but is independent from the nearest one; and 4, when we list the RRL velocity of the related H II region. Considering the value of `Clump_flag` as an unique integer number, i.e., combining the first digit which gives information about the closest ATLASGAL clump (see § 4.1.2) with the second digit explained here, the kinematic distance computed from `Vlsr` can be assigned to the star cluster if `Clump_flag` ≥ 03.

Once collected all the available LSR velocities, the kinematic distances were calculated using a Galactic rotation curve. The widely employed rotation curve fitted by Brand & Blitz (1993) was based on a sample of H II regions and reflection nebulae with known stellar distances, and their associated molecular clouds, which have the velocity information. Most of these sources are located in the outer Galaxy, out to a Galactocentric radius R of about 17 kpc. They added to the sample the H I tangent point velocities available at that time to cover the inner Galaxy, (i.e., for $R < R_0$, where $R_0 \sim 8$ kpc is the distance from the Sun of the Galactic center). However, since they used a global functional form to fit simultaneously the inner and the outer Galaxy, this curve does not properly match the data for $R < R_0$, as is shown, e.g., in Figures 6 and 7 of Levine et al. (2008). These authors constructed an updated rotation curve for the inner Galaxy using recent high-resolution H I tangent point data. The linear function fitted by them to $R \leq 8$ kpc resulted to be steeper than the Brand & Blitz (1993) curve in that range, and better reproduces the increasing behavior of the rotation velocity with increasing R. Given that most of our studied sources are within the solar circle ($R < R_0$), we decided to adopt the Levine et al. (2008)[5] rotation curve for $R/R_0 \leq 0.78$, which is the point where it intersects the Brand & Blitz (1993) curve. For $R/R_0 > 0.78$, we adopted the Brand & Blitz (1993) curve to cover large Galactocentric radii. We used this intersection point instead of the whole range available in Levine et al. (2008) to ensure continuity of the overall rotation curve assumed.

It is worth mentioning that the fourth quadrant part of the same H I data used by Levine et al. (2008) were previously analyzed by McClure-Griffiths & Dickey (2007) who fitted their own rotation curve. As already suspected by Levine et al. (2008), the systematic shift of ~ 7 km s^{-1} between the two curves (see their Figure 7) is due to the differences in determining the terminal velocities from the data. We note that the erfc fitting method (used by

[5]Levine et al. (2008) provide a rotation curve as a function of both Galactocentric radius, R, and height off the Galactic plane, z. Here we z-averaged their rotation curve, so that it depends on R only.

McClure-Griffiths & Dickey 2007) is conceptually equivalent to consider the half-power point of the tangent velocity profile. Fitting instead the theoretical function derived by Celnik et al. (1979), which is a better approximation of the tangent velocity profile, it is found that the half-power point is shifted by $\sim 0.7\sigma_v$ from the real terminal velocity (where σ_v is the typical velocity dispersion; see the proof in that paper). We thus favor the rotation curve by Levine et al. (2008), since they fitted Celnik et al. (1979) profiles to derive the tangent point velocities.

We did not use the more recent rotation curve by Reid et al. (2009) mainly because it is based on a maser parallax on in 18 star-forming regions only, which cover just the first and second quadrant, so that the obtained rotation curve is not fully representative of our Galactic range and, as the authors acknowledge, cannot be conclusively distinguished from a flat curve (which is the assumed form at the end). In addition, their recommended fit assumes that the massive star-forming gas orbits slower the Galaxy than expected for circular rotation, which has been questioned by some subsequent studies (Baba et al. 2009; McMillan & Binney 2010).

Both rotation curves used here (Brand & Blitz 1993; Levine et al. 2008) were originally constructed assuming the standard IAU values for the Galactocentric radius and the orbital velocity of the Sun, $R_0 = 8.5$ kpc and $\Theta_0 = 220$ km s^{-1}, respectively. Nevertheless, it can be easily shown that the solution for $x = R/R_0$ derived by applying these curves and a particular LSR velocity is practically independent of the choice of (R_0, Θ_0) (fully independent for the case of a linear rotation curve constructed from tangent point velocities, as for Levine et al. 2008), and that any scaling of the curve parameters to match updates values of (R_0, Θ_0) is equivalent to adopt the original parameters in all the parts of the equations. The only thing we need afterwards is an accurate value for R_0, to transform from the dimensionless solution x to the physical Galactocentric radius R. Moreover, it can be also shown that the solution does not depend on the exact definition of the LSR, provided that the rotation curves and the input data use the same solar motion (generally standard in radiotelescopes), and that any possible correction would be only important in direction of the Galactic rotation, $V_\odot$ (which is also true; see Table 5 by Reid et al. 2009, and Schönrich et al. 2010), so that if applied it would be canceled out in the equations. We then applied the original rotation curves and the velocities `Vlsr` with no correction, to solve for $x = R/R_0$. To finally obtain R, we adopted $R_0 = 8.23$ (± 0.20) kpc from Genzel et al. (2010), who computed the weighted mean of all recent *direct* estimations of the Galactic center distance from the Sun. We exclude from the kinematic distance estimation those sources with $R < 2.4$ kpc (only 2% of the cases), which is the point were the

approaching and receding parts of the rotation curve constructed by Marasco & Fraternali (2012, using coarser resolution H I data, but covering smaller R) start to show significant differences likely due to non-circular motions in the region of the Galactic bar. The Levine et al. (2008) curve covers radii $R \geq 3$ kpc, which means that we implicitly extrapolated it to $R = 2.4$ kpc when we solved the equation for x.

There is a simple geometrical relation between the obtained Galactocentric radius R and the kinematic distance, but within the solar circle (in our sample, 99% of all kinematic distance estimations) an unique value of R results in two possible distances equally spaced on either side of the tangent point, which are referred to as the near and far distances. This is known as the kinematic distance ambiguity (KDA) problem. Fortunately, as discussed below, there exist a number of methods that have been applied in the literature for an important fraction of the sample to solve the KDA, which allowed us to assign an unique kinematic distance in the 92% of the cases. We list the 424 derived kinematic distances in the table column `KDist` (in kpc); when the KDA is not solved, both near and far distances are given separated by '/'. Uncertainties in these distances, provided in the column `e_KDist`, have been determined by shifting the LSR velocities by ± 7 km s^{-1} to account for random motions, following Reid et al. (2009), who suggest this value as the typical virial velocity dispersion of a massive star-forming region. We acknowledge, however, that the error in the kinematic distance can be larger due to randomly oriented peculiar motions of up to 20 or 30 km s^{-1} with respect to Galactic rotation, as shown, e.g., by the hydrodynamical simulations by Baba et al. (2009). Similarly, such large systematic velocities have been found from maser parallax observations (e.g., Kurayama et al. 2011), although is some cases it has been found also that the star-forming region does follow circular rotation (e.g., Sato et al. 2010b). With the assumed velocity dispersion of $\sigma_v = 7$ km s^{-1}, there are some critical cases where we can only assign an upper limit for the near distance ($|$`Vlsr`$| < \sigma_v$), or a lower limit for the far distance (`Vlsr` within σ_v from the forbidden velocity), and that are properly indicated in the table column `KDist`.

The solutions for the distance ambiguity found in the literature are given in the table column `KDA`, which informs whether the source with available velocity (listed in `name_Vlsr`) is located at the near (`KDA` = `N`) or far side (`KDA` = `F`), or just at the tangent point (`KDA` = `T`). A companion question mark indicates a doubtful assignation, e.g., from low-quality flags in the original reference, but this happens for only 2% of the solutions. The most common methods for resolution of the distance ambiguity are (examples of references are given below): 1) radio recombination lines in conjunction with H I absorption toward H II regions, called the H I Emission/Absorption method (H I E/A); and 2) H I

self-absorption (H I SA) and molecular line emission towards molecular clouds and massive YSOs. We considered any source with `Vlsr` within $\sigma_v = 7$ km s^{-1} of the terminal velocity as consistent with being at the tangent point, and in general we assigned a `KDA` = `T`. However, for some of these sources, there still exist reliable[6] KDA solutions that can further constrain the kinematic distance to a either side of the Galaxy, near (for which `KDA` = `NT`) or far (`KDA` = `FT`). The following references for resolved KDAs were checked systematically (positions overplotted on the ATLASGAL submaps) : Caswell & Haynes (1987, presence/absence of optical counterparts + H I E/A for a few sources), Faúndez et al. (2004, application of a spiral arms model of the IV quadrant), Anderson & Bania (2009, H I E/A + H I SA), Roman-Duval et al. (2009, H I SA), and the RMS survey (Urquhart et al. 2008). For the RMS survey, which is an ongoing project, we took the KDA solutions from an on-line search we performed for every possibly associated source on "The RMS Database Server"[7]; these solutions arise from dedicated application of H I absorption methods (Urquhart et al. 2011, 2012), from the literature, or from grouping of sources close in the phase space where there is at least one with resolved KDA. Additional KDA solutions were found through the SIMBAD coordinate query of each source, or from the reference from which the final cluster distance was adopted (e.g., a more accurate method like maser parallax, see § 4.1.6). All used references are listed as integer numbers in the column table `ref_KDA`. An '`*`' following the number means that the source in the corresponding reference with resolved KDA is not located at the same position of the source from which we took the velocity, but is nearby in the phase space (close position and similar velocity) indicating that is likely connected. A reference between parentheses means that it contradicts the KDA solution adopted in this work (see below). Non-numeric flags in the column `ref_KDA` indicate complementary criteria used here to solve the distance ambiguity:

- `C`: we adopt the KDA solution for the whole associated complex (see § 4.1.6), or from a particular source in the complex.
- `D`: source associated with an IRDC, favoring the near distance (see the arguments given by Jackson et al. 2008)
- `O`: out of the solar circle, i.e., no ambiguity in the kinematic distance.

[6] Considering that the source is near the tangent point and some method/solution combinations are not longer valid. Examples of reliable solutions are: an associated stellar distance, a far solution from the H I E/A method, or a near solution from the H I SA method.

[7] `http://www.ast.leeds.ac.uk/cgi-bin/RMS/RMS_DATABASE.cgi`; we did the search on August, 2011.

- `S`: adopted KDA solution consistent with the stellar distance (see § 4.1.5)
- `z`: near distance adopted, since if located at the far distance the source would be too high above the Galactic plane. We adopted a height value of $|z| = 200$ pc to exclude the far distance, following Blitz (1991).

For contradictory solutions of the KDA, in general we adopted the more recent, or the one using a more accurate method. Although this decision is somehow arbitrary, there are some reasonable guidelines that can be applied, e.g., we favor the consistency with stellar distance or with the complex (flags S and C), and we adopted the solution from the H I E/A method when conflicting with the H I SA method, since the first has been found to be more robust (Anderson & Bania 2009). In any case, the KDA solutions from different references usually agree; discrepant ones are only the 12% of the total of resolutions and should not affect the statistical results of this work.

4.1.5 Stellar distance and age

A direct estimation of the distance to a cluster, i.e., from the member stars, is particularly useful when the accuracy is better than that of the kinematic distance from the gas (e.g., when a large sample of stars is used), or when the cluster is fully exposed and there is no nebula that can be associated to it. Using data from the original cluster catalogs and new references found in SIMBAD for each object, we compiled values for the stellar distance (in kpc; table column `SDist`) and its uncertainty (column `e_SDist`), as well as the age and its error (in Myr; columns `Age` and `e_Age`, respectively) computed by studies of the cluster stellar population. The corresponding references of the adopted parameters are listed in the columns `ref_SDist` and `ref_Age`. For the optical clusters present in the Dias et al. (2002, see § 3.1) catalog, we generally used the original parameters provided there, unless there were new estimates based on a better method (or data), or represent a real improvement in accuracy. A more rigorous approach for multiple references of the same cluster would be similar to the statistical study by Paunzen & Netopil (2006), and is beyond the scope of this work. However, they concluded that their literature-averaged parameters have the same statistical significance as the data from the Dias et al. (2002) catalog, so that for the purposes of our work it is much more important a correct estimation of the uncertainties (see below) than a careful averaging. Out of the 216 clusters from the Dias et al. (2002) catalog present in our sample, 131 objects have originally determinations of both age and distance (+4 clusters with the distance only). We kept these parameters for most of them (110 with original values, and 21 with new ones),

and added parameters for 25 more clusters. To keep track of all these changes, the original references used in the Dias et al. (2002) catalog are listed in the column `ref_Dias`.

The uncertainties in the cluster fundamental parameters are often ignored or underestimated in the literature; in particular, they are not provided in the Dias et al. (2002) catalog. We therefore collected all available errors from the corresponding references and, to prevent underestimation, we imposed uniform *minimum* uncertainties in the derived parameters. We also assumed these values as errors when they were not given in the literature. For the stellar distance, the minimum uncertainty was carefully chosen depending on the method used to calculate it, in order to correctly compare it with the kinematic distance (e.g., to decide which of both distances is finally adopted, see § 4.1.6). All most common methods for cluster distance determination use stellar photometry, and hence the corresponding uncertainty is dominated by the errors from the absolute magnitude calibration and from the extinction estimation (e.g., Pinheiro et al. 2010). For the extinction, in addition to the statistical error intrinsic to the method, there is a systematic error produced by possible variations in the extinction law (e.g., Fritz et al. 2011; Moisés et al. 2011), which is often not considered in the literature and might be particularly relevant in the NIR regime. In the optical, we can consider that the typical extinction law assumed ($R_V \simeq 3.1$, appropriate for diffuse local gas) is not subject to important variations, since the observed stars are relatively close to the Sun and not heavily embedded in the associated molecular clouds (if any), otherwise they would not be visible at these wavelengths. In the NIR, the extinction law can be described by a power law, $A_\lambda \propto \lambda^{-\beta}$, and the variations can be accounted for with different values for the exponent β. Using the typical spread in β obtained by Fritz et al. (2011) in their compilation, we found that the corresponding uncertainty in the K-band extinction is $\sigma(A_K) \simeq 0.2\, A_K$.

In the following, we list the main methods for stellar distance determinations of the used references, and the corresponding minimum uncertainties adopted in this work:

- Optical main-sequence (MS) or isochrone fitting (e.g., Kharchenko et al. 2005b; Loktin et al. 2001): In this case, we follow Phelps & Janes (1994) who estimated an uncertainty in distance modulus of $\sigma(m - M) \sim 0.32$, from a detailed analysis of the typical error in fitting a template main sequence to the optical color-magnitude diagram. This is equivalent to an error of $\sim 15\%$ in distance. Due to the fact that, from the point of view of the distance uncertainty, fitting a MS is analogous to fitting an isochrone, we also adopted a minimum error of $\sim 15\%$ for the isochrone

method. Furthermore, this is consistent with the spread in distance modulus found by Grocholski & Sarajedini (2003, see their Table 2) in their comparison of different isochrone models.

- NIR isochrone fitting (e.g., Tadross 2008; Glushkova et al. 2010): We adopted the same minimum distance error as for optical isochrone fitting, 15%. Extinction law variations might be present, but since the type of clusters where isochrone fitting is possible are not severely extinguished (they are generally not young), the corresponding uncertainty in A_K due to these variations is also low (recall $\sigma(A_K) \simeq 0.2\,A_K$).

- Optical spectrophotometric distance (e.g., Herbst 1975): Here, we assumed an absolute magnitude calibration uncertainty of $\sigma(M_V) \simeq 0.5$, consistent with the typical spread of massive OB star calibration scales (e.g., Martins et al. 2005), and an error in spectral type determination of 1 subtype, equivalent to ± 0.3 magnitudes in M_V for the Martins et al. (2005) calibration. Adding both contributions in quadrature gives an overall uncertainty of ~ 0.58 magnitudes in distance modulus, or $\sim 27\%$ in distance.

- NIR spectrophotometric distance (e.g., Moisés et al. 2011): For calibration and spectral type errors, we adopted the same overall uncertainty of ~ 0.58 magnitudes in distance modulus as for the optical method (absolute magnitudes are usually converted from the optical to the NIR using tabulated intrinsic colors with little error). We added in quadrature an uncertainty to account for possible extinction law variations: assuming a typical extinction of $A_K \simeq 1.5$, $\sigma(A_K) \simeq 0.2\,A_K \simeq 0.3$. The final error in distance modulus is ~ 0.66 magnitudes, equivalent to $\sim 30\%$ in distance.

- Average of spectrophotometric distances from many stars (e.g., Moisés et al. 2011; Pinheiro et al. 2010): Redefining the errors here would mean a complete re-computation of the average distance, since the minimum errors should be imposed in every individual star. Fortunately, in general the uncertainty of the average is dominated by the variance of the sample rather than by the individual errors. We thus kept the original quoted uncertainty in this case.

- Kinematic distance from average stellar radial velocity (e.g., Davies et al. 2008): For consistency with gas kinematic distances, here we recomputed the stellar kinematic distance using the cluster LSR velocity, a velocity dispersion of 7 km s^{-1} and the rotation curve as described in § 4.1.4. This

special case is indicated with the flag '(K)' after the reference number in the column `ref_SDist`.

- 10^{th} brightest star method (Dutra et al. 2003b; Borissova et al. 2005): We do not use the stellar distances derived by applying this technique, because they are very uncertain. The errors can easily reach a factor 10 or more in distance (Borissova et al. 2005), which practically mean no constrain in the cluster location at Galactic scales.

For the cluster ages, we simply adopted uniform minimum errors based on the corresponding age range, following Bonatto & Bica (2011): 35% for `Age` $<$ 20 Myr, 30% for 20 Myr $\leq$ `Age` $<$ 100 Myr, 20% for 100 Myr $\leq$ `Age` $<$ 2 Gyr, and 50% for `Age` $\geq$ 2 Gyr. The most common method for age determination is isochrone fitting (e.g., Loktin et al. 2001). For a few clusters with stars studied spectroscopically, the age can be estimated using the evolutionary types of the identified stars and knowledge about their typical ages and lifetimes (e.g., Messineo et al. 2009). A total of 209 clusters have age estimations in the literature (30% of our sample).

For some clusters of our sample without determinations of fundamental parameters, there are still some studies in the literature that can be considered as *confirmations* of the star cluster nature of the objects, i.e., the possibility of being spurious can be practically discarded. These references are given in the table column `ref_Conf`, and usually correspond to higher resolution or/and sensitivity imaging NIR observations where the star cluster is undoubtedly revealed (e.g., Dutra et al. 2003b; Borissova et al. 2005; Kumar et al. 2004), or more detailed studies towards star-forming regions which are too young to really constrain the cluster physical parameters by isochrone fitting, but where it is still possible to recognize YSO candidates within the cluster as color excess sources in color-color and color-magnitude diagrams (e.g., Roman-Lopes & Abraham 2006a). The objects with both determined age and stellar distance can also be considered as confirmed stellar clusters, because the derivation of parameters usually requires the identification of the cluster sequence or stellar spectroscopy. We thus listed again the references for age and distance in the column `ref_Conf`, including in some cases additional references of further cluster analysis.

4.1.6 Adopted distance, complexes and subclusters

Young star clusters are normally not isolated but within bigger complexes of gas, stars and other clusters, as a result of the fact that star formation occurs in giant molecular clouds with a hierarchical structure. If a group of stellar

clusters in our sample was found to form a physically associated complex, we identified it in the table column `Complex`. We give there the corresponding name when the complex was identified in the literature and we found the cluster positions and radial velocities consistent with being part of it (e.g., the giant molecular cloud W51; Kang et al. 2010). References for complex identification and analysis are provided in the column `ref_Complex`. Small complexes of clusters not previously established in the literature but whose morphology in the IR images (field of view of $\sim 10'$) suggest that they belong to the same star-forming region are indicated by `Complex` = MC-i, where i is a record number. Bigger complexes of stellar clusters not found in the literature and identified visually within the ATLASGAL fields (of $\sim 30'$) through the proximity of their members in the phase-space are marked by `Complex` = KC-j, where j is another record number. We warn that, however, since the complexes were recognized as part of the visual inspection of the maps, or were found in the literature, not all possible physical groupings of star clusters are provided here. For that, a subsequent statistical analysis is needed, which will be presented in a forthcoming paper. We also identified in the IR images a few cases where there is a pair of star clusters even closer, usually sharing part of their population, which can be considered as subclusters of an unique merging (or merged) entity. Those subclusters are indicated in the table column `SubCl` with an identical record number.

For all the clusters of our sample, the final adopted distances with their corresponding errors are listed in the table columns `Dist` and `e_Dist` (in kpc), respectively, and were chosen from the available distance estimation with the lowest uncertainty. In some cases, we adopted independent distance estimations from the literature if they were more accurate than `SDist` and `KDist` (e.g., from maser parallax measurements; see Reid et al. 2009, and references therein). Clusters within a particular complex were assumed to be all located at the same distance, determined from the literature, or kinematically from an average position and velocity. The origin of the adopted distance is properly indicated in the column `ref_Dist`, and can be one of the following cases:

- `K`: kinematic distance adopted, `Dist` = `KDist`.
- `S`: stellar distance adopted, `Dist` = `SDist`.
- `Ref:`n: adopted distance from literature reference with identification number n.
- `KC`: complex distance computed kinematically from an average position and velocity, using the values compiled here for all the clusters within

the complex with available (and not repeated) `Vlsr`, and the rotation curve used in § 4.1.4.

- `SC`: complex distance computed by averaging the stellar distances (`SDist`) of the member clusters.
- `C(Ref:`n`)`: distance for the whole complex adopted from literature reference with identification number n.
- `CV(Ref:`n`)`: complex distance computed kinematically from an average position and velocity given by the reference with identification number n, and the rotation curve used in this work.
- `C(ID:`m`)`: adopted for the whole complex the distance given for the cluster with `ID` $= m$ (used when a particular cluster within a complex has a very accurate distance estimation).

Combining all these different methods, there are available distance determinations (`Dist`) for a total of 538 clusters, i.e., for 77% of our sample. Naturally, there is a dichotomy in the distance estimation method depending on whether or not the cluster is associated with an ATLASGAL source with available velocity, so that most exposed clusters have uniquely stellar distances, whereas the distances for embedded clusters are mainly kinematic or from identification of complexes. However, it is still possible to compare stellar and kinematic determinations for a subsample of 38 clusters (mostly embedded) which have distances available from both methods. This comparison is shown in Figure 4.1, where plus symbols mean agreement between stellar and kinematic distances within the corresponding uncertainties, and circles are the cases in which there is a discrepancy between both techniques; the color indicates which distance estimate was finally adopted in our catalog: stellar (*red*), kinematic (*blue*, including cases `KC` and `CV`), and other (*black*). The plot reveals that in our cluster sample, both methods are quite consistent with each other, with a 84% of agreement (32 out of 38 objects). We note that among the discrepant cases, there are two embedded clusters whose method for age and (stellar) distance estimation was found to be particularly inaccurate (see § 4.2.4).

4.1.7 Additional comments

Specific comments about the stellar cluster itself, or its compiled fundamental parameters (stellar distance and age) are provided in the column `Comments1`. We give additional remarks about the ATLASGAL emission, the associated complex or other objects, or about the finally adopted distance in the column

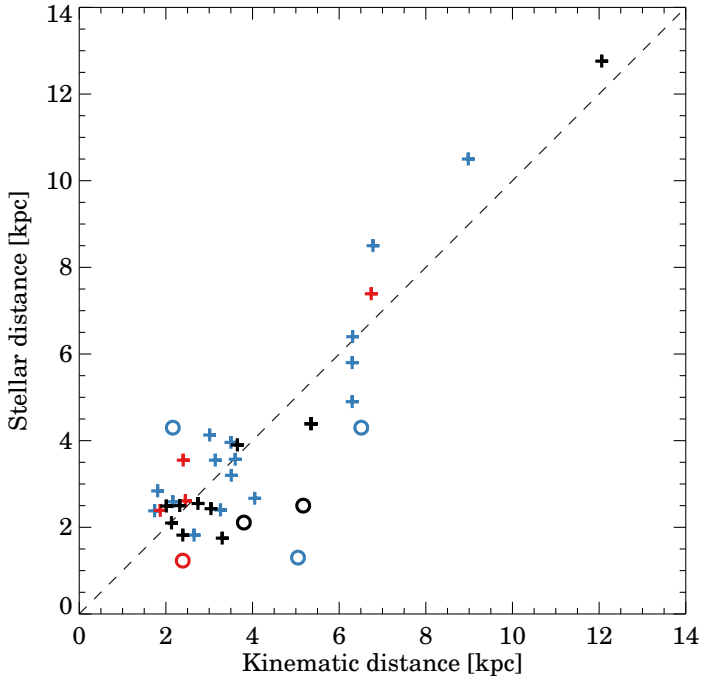

Figure 4.1: Comparison of kinematic and stellar distances for the 38 clusters of our sample with both estimations available. Plus signs (+) indicate agreement within the errors, and circles mark the discrepant cases. Colors indicate which distance estimate was finally adopted in our catalog: stellar (*red*), kinematic (*blue*), and other (*black*). The dashed line is the identity.

`Comments2`. Within the comments, the quoted literature is indicated by the code `Ref:`n, where n is the identification number of the used reference.

4.2 Analysis

4.2.1 Morphological evolutionary sequence

Here, we use the characterization of the ATLASGAL emission found throughout each cluster's area and/or environment (described in § 4.1.2) to define main morphological types and delineate an evolutionary sequence. First, in order to test our visual ATLASGAL morphological flags specified above (corresponding to the first part of the column `Morph`, and represented hereafter by $\mathtt{m}_0$), we compared them against the more quantitative parameter $s \equiv$ `Clump_sep`, which is the projected distance of the nearest ATLASGAL emission pixel, normalized to the cluster angular radius. We found a reasonable correlation: $s = 0$ for all deeply embedded clusters ($\mathtt{m}_0 =$ `emb`), $s < 0.42$ for partially embedded clusters

($\mathtt{m}_0$ = `p-emb`), $0.40 < s < 1.97$ for clusters surrounded by submm emission ($\mathtt{m}_0$ = `surr`), and $s > 0.94$ for exposed clusters ($\mathtt{m}_0$ = `exp`). Exposed clusters with $s < 1$ are only a few cases with a large angular size and very faint emission close to their borders. The remaining morphological flags are very specific and we do not expect any correlation with the quantity `Clump_sep`.

Denoting by $\mathtt{Cf}_0$ the first digit of the flag `Clump_flag` (a value > 0 means that the nearest ATLASGAL clump is likely associated with the cluster), and using the logical operators $\wedge$, $\vee$ and $\neg$ ('and', 'or', and 'not', respectively), we define five morphological types as follows:

- EC1: $\mathtt{m}_0 = \mathtt{emb}$
- EC2: $\mathtt{m}_0 = \mathtt{p\text{-}emb}$
- OC0: $\mathtt{m}_0 = \mathtt{surr} \vee \mathtt{m}_0 = \mathtt{few*} \vee (\mathtt{m}_0 = \mathtt{few} \wedge \mathtt{Cf}_0 > 0)$
- OC1: $\mathtt{m}_0 = \mathtt{exp} \wedge (\mathtt{Cf}_0 > 0 \vee \mathtt{KDist} \simeq \mathtt{SDist})$
- OC2: $(\mathtt{m}_0 = \mathtt{exp} \vee \mathtt{m}_0 = \mathtt{exp*} \vee \mathtt{m}_0 = \mathtt{few}) \wedge \neg(\mathrm{OC1} \vee \mathrm{OC2})$

The morphological type for each cluster is given in the column `Morph_type` of our catalog. Figures 4.2 and 4.3 present one example cluster for each morphological type, shown in GLIMPSE three-color images, and 2MASS three-color images overlaid with ATLASGAL contours. In simpler words, given that star clusters are expected to be less and less associated with molecular gas as time evolves, due to gas dispersal driven by stellar feedback, we have defined above a morphological evolutionary sequence, with decreasing correlation with ATLASGAL emission. EC1 are deeply embedded clusters (Fig. 4.2, *top*), EC2 are partially embedded clusters (Fig. 4.2, *bottom*), OC0 are emerging exposed clusters (Fig. 4.3, *top*), and finally there are two kinds of totally exposed clusters: OC1 are still physically associated with molecular gas in their surrounding neighborhood (an ATLASGAL clump at a projected distance of `Clump_sep` times the cluster radius, see Fig. 4.3, *middle*), whereas OC2 are all the remaining exposed clusters, which present no correlation with ATLASGAL emission (Fig. 4.3, *bottom*). Note that, however, this classification is not perfect. For example, although the gas velocity and stellar distance data are quite extensive, they are not complete to identify all the $\mathtt{m}_0 = \mathtt{few*}$, $\mathtt{m}_0 = \mathtt{exp*}$ and $\mathtt{KDist} \simeq \mathtt{SDist}$ cases, so that some misclassification might occur in the type OC2. Similarly, the physical link between the submm emission and the embedded clusters was based on the morphology seen in the images, and some chance alignments might still be present in a few cases. Therefore, the defined morphological types should be considered primarily in a statistical way, and for individual objects they must be treated with caution. Column 2 of Table 4.1

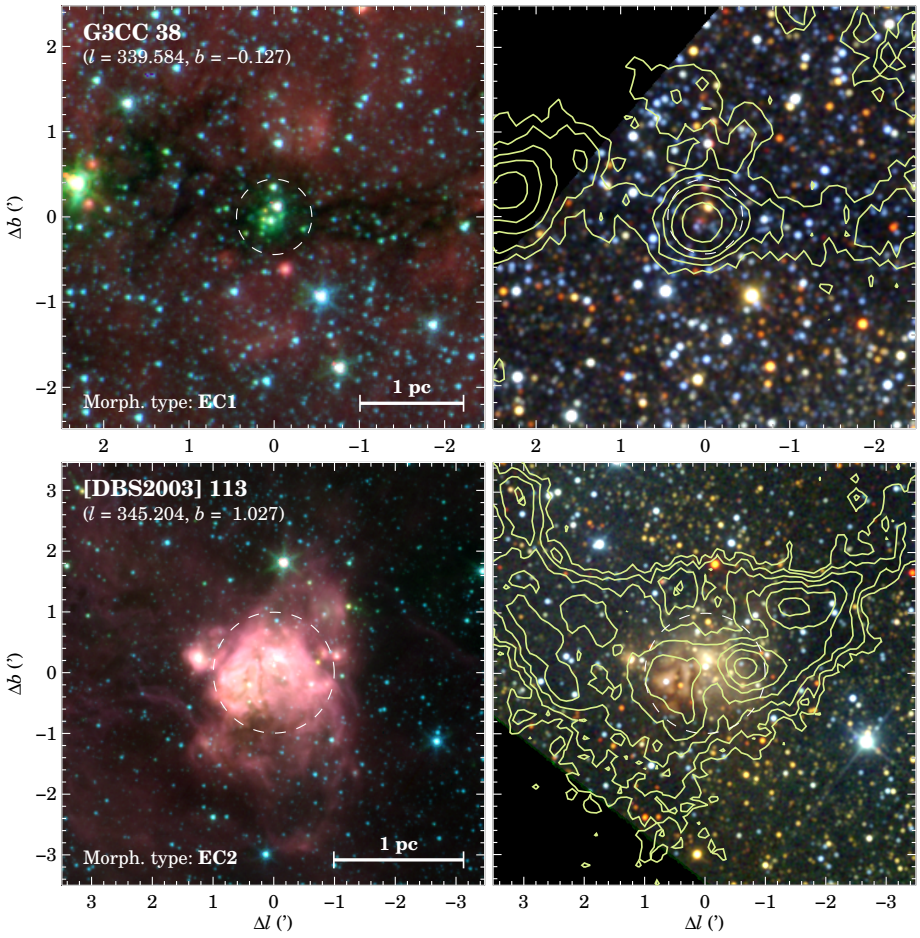

Figure 4.2: Examples of the two morphological types defined for embedded clusters: The cluster G3CC 38 of type EC1 (top panels), and the cluster [DBS2003] 113 of type EC2 (bottom panels). The left panels show *Spitzer*-IRAC three-color images made with the 3.6 (blue), 4.5 (green) and 8.0 μm (red) bands. The right panels present 2MASS three-color images of the same field of view, constructed with the J (blue), H (green), and K_s (red) bands. The overlaid contours on the 2MASS images correspond to ATLASGAL emission (870 μm); the contour levels are $\{5, 8.8, 15, 25, 46, 88, 170\} \times \sigma$, where σ is the local rms noise level (σ = 45 mJy/beam for G3CC 38, and σ = 42 mJy/beam for [DBS2003] 113). The images are in Galactic coordinates and the given offsets are with respect to the cluster center, indicated in the left panels below the cluster name. The dashed circles represent the estimated angular sizes from the original cluster catalogs (see § 4.1.1). The 1 pc scale-bar was estimated using the corresponding distance adopted in our catalog.

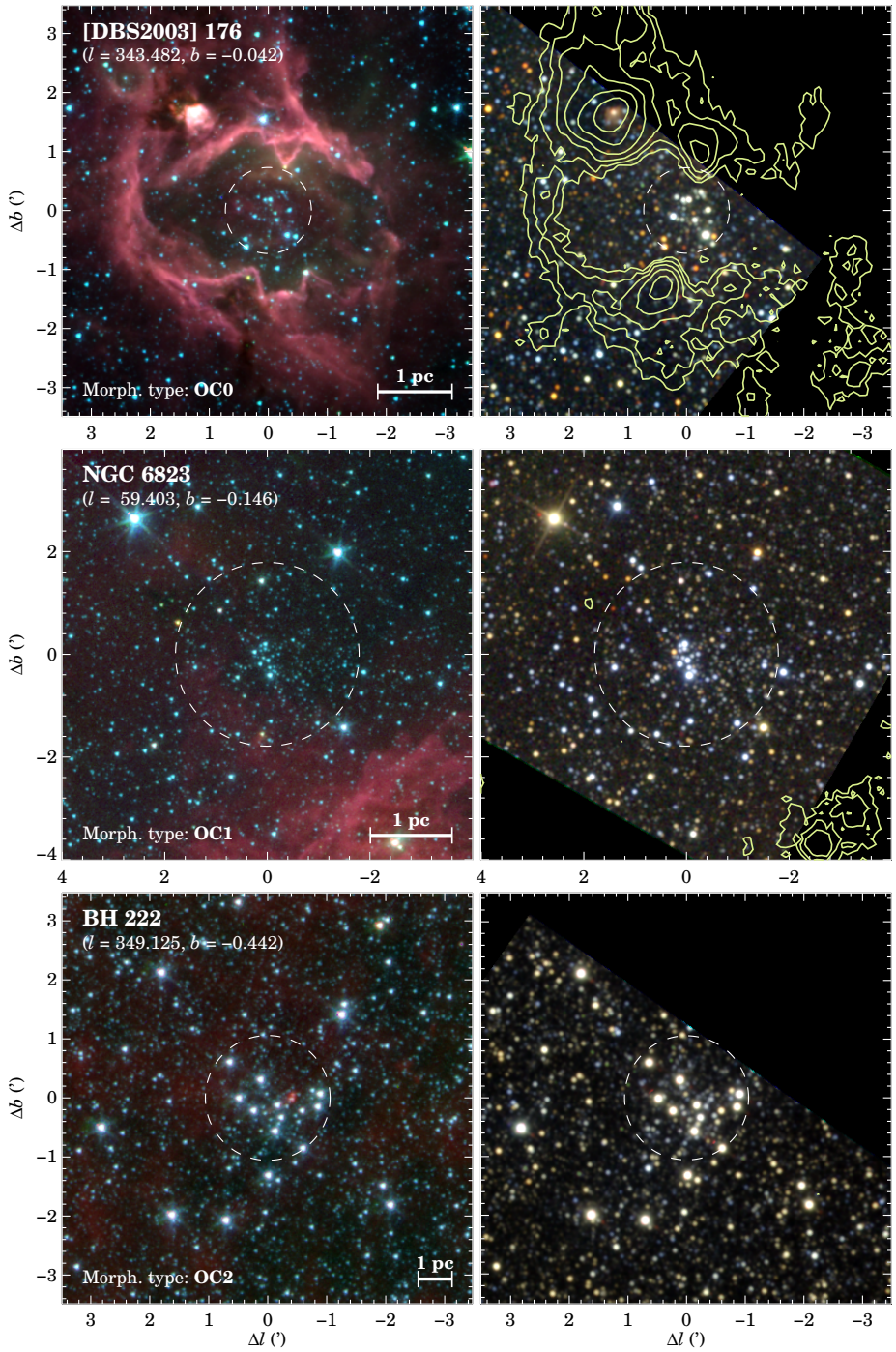

Figure 4.3: Examples of the three morphological types defined for open clusters: The cluster [DBS2003] 176 of type OC0 (top panels), the cluster NGC 6823 of type OC1 (middle panels), and the cluster BH 222 of type OC2 (bottom panels). The local rms noise level of the ATLASGAL emission is, respectively, 36, 46, and 29 mJy/beam. See caption of Figure 4.2 for more details of the images.

Table 4.1: Number of clusters in each morphological type.

Type	$N_{\rm cl}$	$N_{\rm cl}(D$ avail.)	$N_{\rm cl}(\leq D_{\rm rep})$	$N_{\rm cl}^{\rm conf}(\leq D_{\rm rep})$	$N_{\rm cl}^{\rm tot}(\leq D_{\rm rep})$
(1)	(2)	(3)	(4)	(5)	(6)
EC1	132	125	44	16	56
EC2	195	177	54	25	68
OC0	56	49	17	10	36
OC1	22	22	6	3	11
OC2	290	167	136	133	475

Notes. The given numbers are for the whole sample (Column 2), clusters with available distances (Column 3), clusters with distances $\leq D_{\rm rep}$ (Column 4), confirmed (`ref_Conf` not empty) clusters with $D \leq D_{\rm rep}$ (Column 5), and finally we give the estimated number of clusters with $D \leq D_{\rm rep}$ in an ideally complete sample (Column 6). The distance $D_{\rm rep} = 3.0$ kpc defines what we call the *representative* sample (see § 4.2.3 for details).

lists how many objects fall in each morphological type for the whole cluster sample. Note that the low number of OC1 clusters could be partially due to the observational difficulty in identifying an exposed cluster physically associated with molecular gas in their surroundings, as remarked before. Column 3 gives the number of clusters with available distances, and the remaining columns will be described in § 4.2.3.

With this morphological classification, it is easy to determine (again, statistically) which clusters are associated with ATLASGAL emission: simply as those with types EC1,EC2,OC0 or OC1. These clusters are counted for every catalog in the last two columns of Table 3.2, as absolute and after-merging numbers of objects ($N_{\rm cl}$ and $N_{\rm cl}^{*}$, respectively). As expected, *optical* clusters are rarely associated with ATLASGAL emission (only $\sim 15\%$ of them, most of which are of type OC0 or OC1), since otherwise they would be barely visible at optical wavelengths due to dust extinction. On the other hand, the majority of the *near-infrared* and *mid-infrared* clusters are physically related with submm dust radiation ($\sim 79\%$ and 74% of them, respectively). Although this is also expected because infrared emission is much less affected by dust extinction than visible light, these high percentages might be partially a consequence of the detection method of the infrared cluster catalogs, which in most cases tried to intentionally highlight the embedded cluster population. For example, the 2MASS by-eye searches by Dutra et al. (2003a) and Bica et al. (2003b) were done towards known radio/optical nebulae, and our new GLIMPSE cluster candidates were detected after applying a red-color criterion (see § 3.4). In these particular catalogs, almost the totality of objects are associated with ATLASGAL emission.

We can also use the morphological evolutionary sequence to define observationally in our sample the concepts of *embedded cluster* (EC) and *open cluster* (OC). Since any stellar agglomerate that appears deeply or partially embedded in ATLASGAL emission would satisfy our physical definition of *embedded cluster* presented in § 2.3, we simply use as observational definition the embedded morphological types: EC = EC1 ∨ EC2. We consider the remaining morphological types as open clusters, but excluding those objects that have not been confirmed by follow-up studies, since we expect for them a high contamination rate by spurious candidates (see § 3.6): OC = (OC0 ∨ OC1 ∨ OC2) ∧ (`ref_Conf` not empty).

However, this observational definition of open cluster does not necessarily mean that the cluster is bound by its own gravity, and hence, is not fully equivalent to the concept of *physical open cluster* defined in § 2.3. To investigate under which conditions both definitions agree, we can apply the empirical criterion proposed by Gieles & Portegies Zwart (2011) which distinguishes between physical open clusters and unbound associations by comparing the age of the object with its crossing time, $t_{\rm cross}$, computed as if it were in virial equilibrium. In useful physical units, Equation (1) of Gieles & Portegies Zwart (2011) becomes[8][9]

$$t_{\rm cross} = 9.33 \left(\frac{100\,M_\odot}{M}\right)^{1/2} \left(\frac{R_{\rm eff}}{\rm pc}\right)^{3/2} {\rm Myr}, \tag{4.1}$$

where M and $R_{\rm eff}$ are, respectively, the mass and the observed 2D projected half-light radius of the cluster. Unfortunately, mass estimates and accurate structural parameters are usually not directly available in the open cluster catalogs; in particular, there are no mass data in the Dias et al. (2002) catalog, and the given sizes come from individual studies compiled there and are mostly derived from visual inspection. We therefore used the masses and radii determined by Piskunov et al. (2007), who fitted a three-parameter King's profile (King 1962) to the observed stellar surface density distribution of 236 objects taken from an homogeneous sample of 650 optical clusters in the solar neighborhood (Kharchenko et al. 2005b,a), which is a subset of the current version of the Dias et al. (2002) catalog. Piskunov et al. (2007) estimated the masses

[8] Before converting to physical units, we corrected a mistake in the original equation by Gieles & Portegies Zwart (2011): the transformation from virial radius to projected half-light radius is just $16/(3\pi)$ for a Plummer model, so that the constant in their equation is $[32/(3\pi)]^{3/2} = 6.26$ instead of 10.

[9] This formula is equivalent to Equation (A.11), apart from a factor $\sim 1/0.8 = 1.25$ which arises from defining the crossing time in terms of the virial radius $r_{\rm vir} \equiv r_{\rm g}/2$ instead of the 3D half-mass radius $r_{\rm h}$.

from the tidal radii, and the effective radius $R_{\rm eff}$ entering in Equation (4.1) can be derived from both the core and tidal radius (we used Equation (B1) of Wolf et al. 2010). Because only 14 of the clusters analyzed by Piskunov et al. (2007) are within the ATLASGAL sky coverage, in order to improve the statistics we applied the Gieles & Portegies Zwart (2011) criterion to the 236 studied objects, under the assumption that they are all OCs as defined observationally by us. This supposition is quite acceptable since they are optically-detected clusters and indeed within the ATLASGAL range almost all of them (13 out of 14) are classified as OCs. We computed the crossing times using Equation (4.1), and in Figure 4.4 they are plotted versus the corresponding ages available from the Kharchenko et al. (2005b,a) catalogs. The dashed line is the identity $t_{\rm cross}$ = Age, which divides the physical open clusters ($t_{\rm cross} \leq$ Age) from associations ($t_{\rm cross} >$ Age). It can be seen in the plot that, because the resulting crossing times are relatively short ($\log(t_{\rm cross}/{\rm yr}) \lesssim 7.6$), the majority of the objects studied by Piskunov et al. (2007) are physical open clusters for ages in excess of 10 Myr. In fact, for $\log({\rm Age/yr}) > 7.2$, which is the threshold above which the age distribution can be explained through uniquely classical cluster disruption mechanisms (see § 4.2.4), only 2.6% of the objects are formally associations. We thus conclude that our observational definition of open cluster (OC) agrees with the physical one provided by Gieles & Portegies Zwart (2011, what we call a *physical open cluster*) for ages greater than $\sim$ 16 Myr, which corresponds to the 74% of our OC sample within the ATLASGAL range. Younger OCs can be either unbound associations, as a result of early dissolution, or already physical open clusters.

4.2.2 Spatial distribution

In this Section, we study the spatial distribution in the Galaxy, and with respect to the Sun, of the clusters in our sample with available distance estimates. Figure 4.5 shows the Galactic distribution of the clusters separated in the (a) open and (b) embedded cluster categories defined in the previous Section, on top of an artist's conception of the Milky Way viewed from the north Galactic pole (R. Hurt from the *Spitzer* Science Center, in consultation with R. Benjamin). The image was constructed based on multiwavelength data obtained from the literature, and we have scaled it to $R_0 = 8.23$ kpc (Genzel et al. 2010, see § 4.1.4). It is clear from the image that ECs probe deeper the inner Galaxy than the OC sample, which is concentrated within a few kpc from the Sun ($\lesssim 2$ kpc). This is of course an observational effect mainly produced by the difficulty in detecting exposed clusters against the Galactic background, compared to embedded clusters (see § 4.2.3), and enhanced by the fact that some

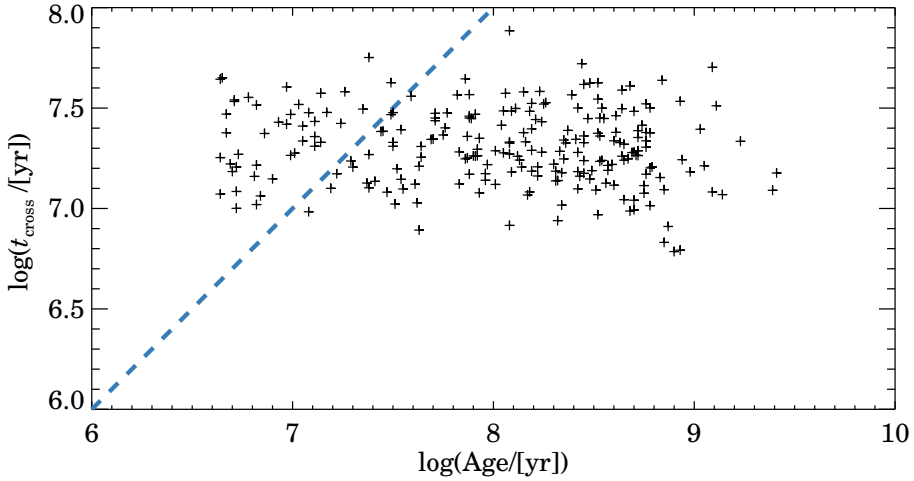

Figure 4.4: Crossing time vs. age for an all-sky sample of 236 clusters (Piskunov et al. 2006) taken from an homogeneous catalog of 650 optical clusters in the solar neighborhood (Kharchenko et al. 2005b,a). The dashed line is the identity $t_{\rm cross}$ = Age, which divides the physical open clusters ($t_{\rm cross} \leq$ Age) from unbound associations ($t_{\rm cross} >$ Age) according to the criterion proposed by Gieles & Portegies Zwart (2011).

genuine OCs have no distance estimates and therefore cannot be included in the spatial distribution analysis (e.g., there are 123 clusters of type OC2 without available distance, half of which might be real). Embedded clusters are spread over larger distances from the Sun ($\lesssim$ 6 kpc) and, although few of them can be detected beyond the Galactic center, a paucity of ECs is hinted within the Galactic bar, augmented by some apparent crowding close to both ends of the bar. The Galactic distribution of ECs is consistent with the spiral structure delineated on the background image; however, the large distance uncertainties ($\sim$ 0.5 kpc on average), and the limited distance coverage, prevent the ECs from defining the spiral arms by their own. The most clear correlation with an spiral arm can be seen in the zoomed-in version of the Galactic distribution around the solar neighborhood (Figure 4.6), where an overdensity of ECs is distinguished towards the Scutum-Centaurus arm in the IV quadrant.

To really quantify how deep are our OC and EC samples in the inner Galaxy, and to estimate the completeness fraction at a given distance, we need to study the observed heliocentric distance distribution of the clusters, and compare it to what is expected from making some basic assumptions. In the following, we denote by D the distance of the cluster from the Sun, projected on the Galactic plane[10], and by z the height of the cluster above the Galactic

[10]In practice, we did not distinguish between the distance d and the projected distance

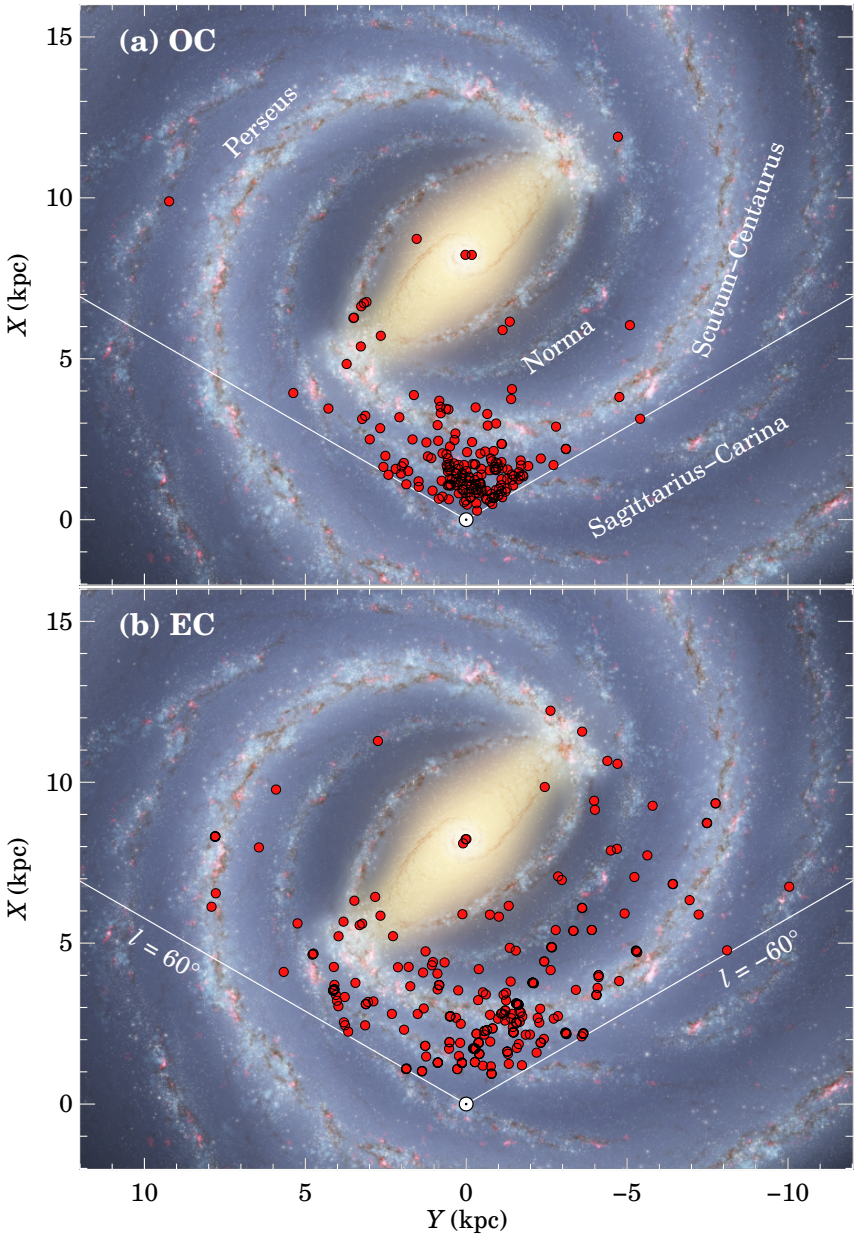

Figure 4.5: Galactic locations of (a) open and (b) embedded clusters within the ATLASGAL range, superimposed over an artist's conception of the Milky Way (R. Hurt from the *Spitzer* Science Center, in consultation with R. Benjamin), which was based on data obtained from the literature at radio, infrared, and visible wavelengths, and attempts to synthesize many of the key elements of the Galactic structure. The coordinate system is centered at the Sun position, indicated by the '⊙' symbol, and we have scaled the image such that $R_0 = 8.23$ kpc (Genzel et al. 2010). The two diagonal lines represent the ATLASGAL range in Galactic longitude ($|l| \leq 60°$). In panel (a), we indicate the names of the spiral arms.

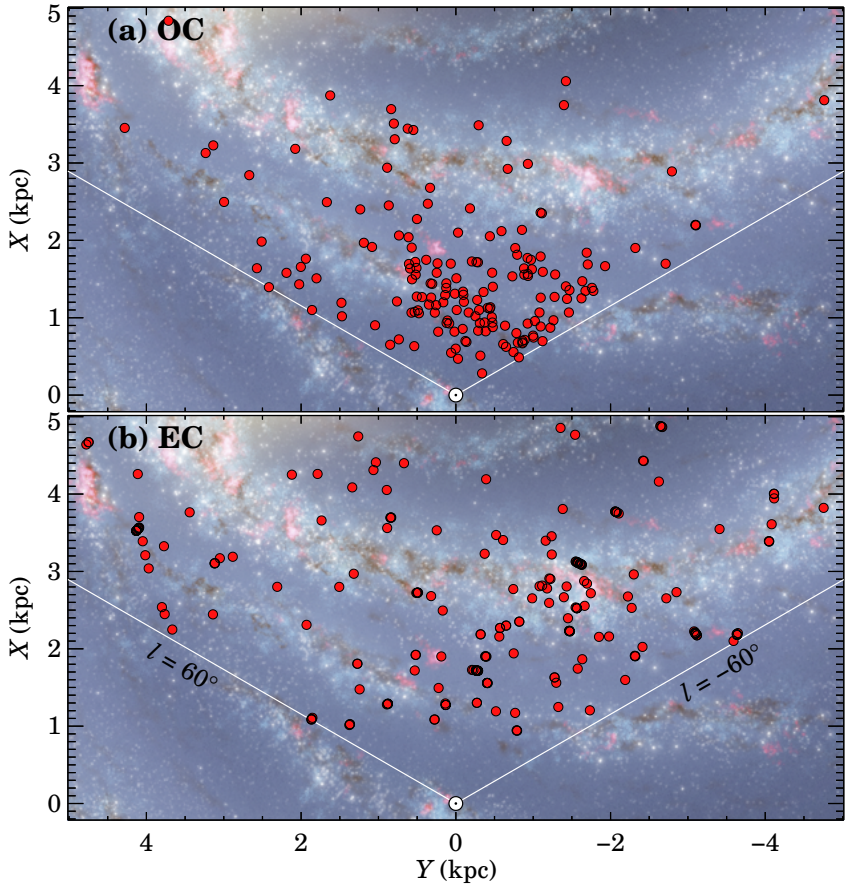

Figure 4.6: Zoomed-in version of Figure 4.5, showing the inner Galaxy in the solar neighborhood. (a) Open clusters. (b) Embedded clusters.

plane. For simplicity, we also define $Z \equiv z - z_0$, where z_0 is the displacement of the Sun above the plane; this is actually what we obtain directly from the cluster distance d and its Galactic latitude b, $Z = d \sin b$. The observed Z- and D-distributions are shown, respectively, in Figures 4.7 and 4.8, for our cluster sample separated in OC and EC categories. In the construction of the histograms, we used fixed bins of $\Delta D = 0.4$ kpc and $\Delta Z = 10$ pc, but since the distance uncertainties are quite nonuniform, we have fractionally spread every value of $D \pm \sigma_D$ and $Z \pm \sigma_Z$ over the covered bins.

In general, we can assume that the spatial number-density of open or embedded clusters in the Galaxy is described by a combination of two independent exponential-decay laws for the cylindrical coordinates z and R, centered

$D = d \cos b$. Since the maximum latitude within the ATLASGAL range is $|b| = 1.5°$, the difference is less than 0.03%, far below the distance uncertainties.

in the Galactic center: $\rho(R,z) = \rho_0\,\varphi_R(R)\,\varphi_z(z)$, with $\varphi_R(R) = e^{-R/R_\mathrm{D}}$ and $\varphi_z(z) = e^{-|z|/z_\mathrm{h}}$. This is a common functional form used to characterize the Galactic distribution of stars (see § 1.1.2 of Binney & Tremaine 2008), and has already been applied in previous open cluster studies (Bonatto et al. 2006a; Piskunov et al. 2006). One might want to include some spiral arm structure in the azimuthal distribution of ECs, since they are still embedded in molecular clouds, but here we are interested in the distance and height longitude-averaged distributions, for which azimuthal substructure is less important; furthermore, as noted above, our embedded cluster distances are not accurate enough to constrain the location of the spiral arms. If we transform the density $\rho(R,z)$ to a coordinate system centered at the Sun, and assuming that we are observing the *totality* of the clusters in the Galaxy within the ATLASGAL range ($|b| \leq b_1$ and $|l| \leq l_1$, with $b_1 \equiv 1.5°$ and $l_1 \equiv 60°$), the resulting density (not averaged in longitude l yet) can be written as

$$\rho_\mathrm{tot}(D,l,Z) = \begin{cases} \rho_0\,\varphi(D,l)\,\varphi_z(Z+Z_0) & \text{if } \; |Z| \leq D\tan b_1 \\ 0 & \text{else ,} \end{cases} \tag{4.2}$$

where

$$\varphi(D,l) \equiv \varphi_R\left(\sqrt{R_0^2 + D^2 - 2R_0 D\cos l}\right) \; . \tag{4.3}$$

Now we can derive an analytical expression for the D-distribution of an ideally complete sample:

$$\Phi_D^\mathrm{tot}(D) \equiv \int_{-\infty}^{\infty}\int_{-l_1}^{l_1} \rho_\mathrm{tot}(D,l,Z)\,D\,\mathrm{d}l\,\mathrm{d}Z \tag{4.4}$$

$$= \Sigma_0\,f_{b_1}(D)\,D\int_{-l_1}^{l_1}\varphi(D,l)\,\mathrm{d}l \; , \tag{4.5}$$

where $\Sigma_0 \equiv 2z_\mathrm{h}\rho_0$ is the surface number-density on the Galactic disk for $R = 0$, and we have defined the function $f_{b_1}(D)$ as

$$f_{b_1}(D) \equiv \begin{cases} e^{-z_0/z_\mathrm{h}}\,\sinh(D\tan b_1/z_\mathrm{h}) & \text{if } \; D \leq z_0/\tan b_1 \\ 1 - \cosh(z_0/z_\mathrm{h})\,e^{-D\tan b_1/z_\mathrm{h}} & \text{else ,} \end{cases} \tag{4.6}$$

which arises from the fact that the limited latitude coverage restricts the integration in Z at each distance.

In practice, however, as already mentioned before and discussed in § 4.2.3, we are unable to detect the totality of the clusters within the ATLASGAL range, due to the difficulty in star cluster identification towards the inner Galaxy. Indeed, the D-distributions that we really observe for OCs and ECs

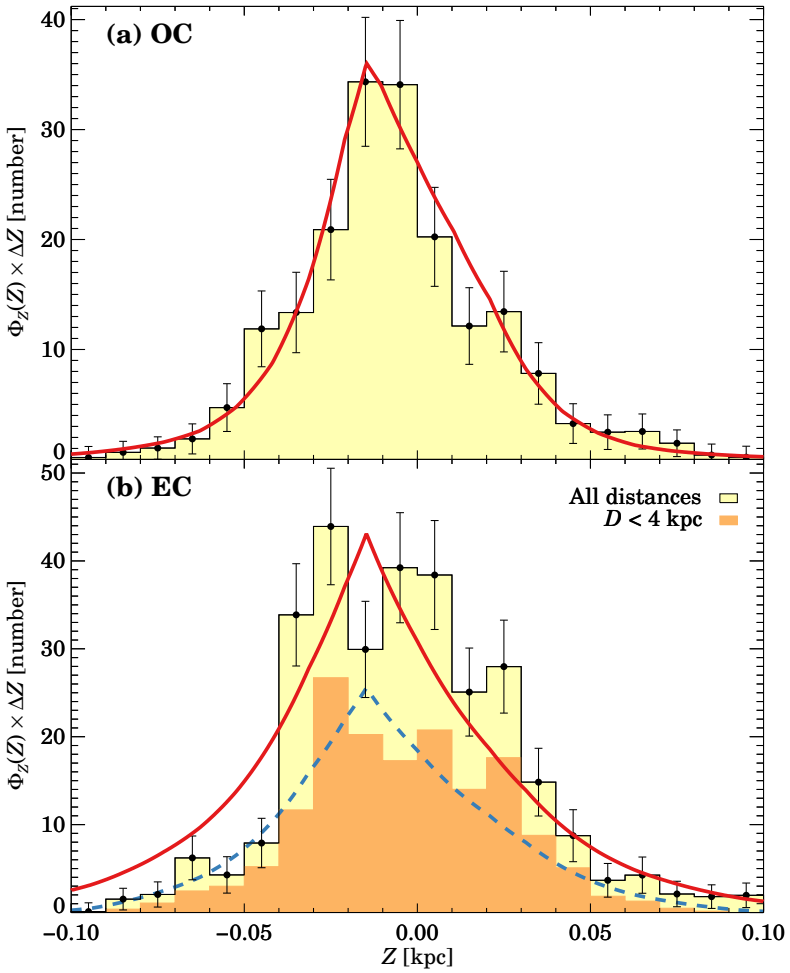

Figure 4.7: Histogram of heights from the Galactic plane, as measured from the Sun ($Z = z - z_0$), for (a) open and (b) embedded clusters, using a bin width of $\Delta Z = 10$ pc and Poisson uncertainties. The overplotted solid curve in each panel represents: (a) the fitted Z-distribution $\Phi_Z(Z)$ from Equation (4.10) with best-fit parameters $z_0 = 14.7 \pm 3.7$ pc and $z_\mathrm{h} = 42.5 \pm 9.9$ pc; (b) the predicted Z-distribution from Equation (4.10), using the parameters fitted for the OC sample. In panel (b), the darker shaded region is the Z-histogram for ECs with distances $D < 4$ kpc, whereas the dashed curve indicates the corresponding distribution as predicted from Equation (4.10) and the same parameters z_0 and z_h.

(see Figure 4.8) do not increase with distance up to the Galactic center ($D = R_0$), as we would expect from Equation (4.5); instead, they reach a maximum at a nearby distance and then decay considerably, especially for optical clusters. The observed D-distributions are dominated by the high incompleteness at larger distances from the Sun, and therefore, are insensitive to large scale structure on the Galactic disk such as the scale length R_D. Attempts to include

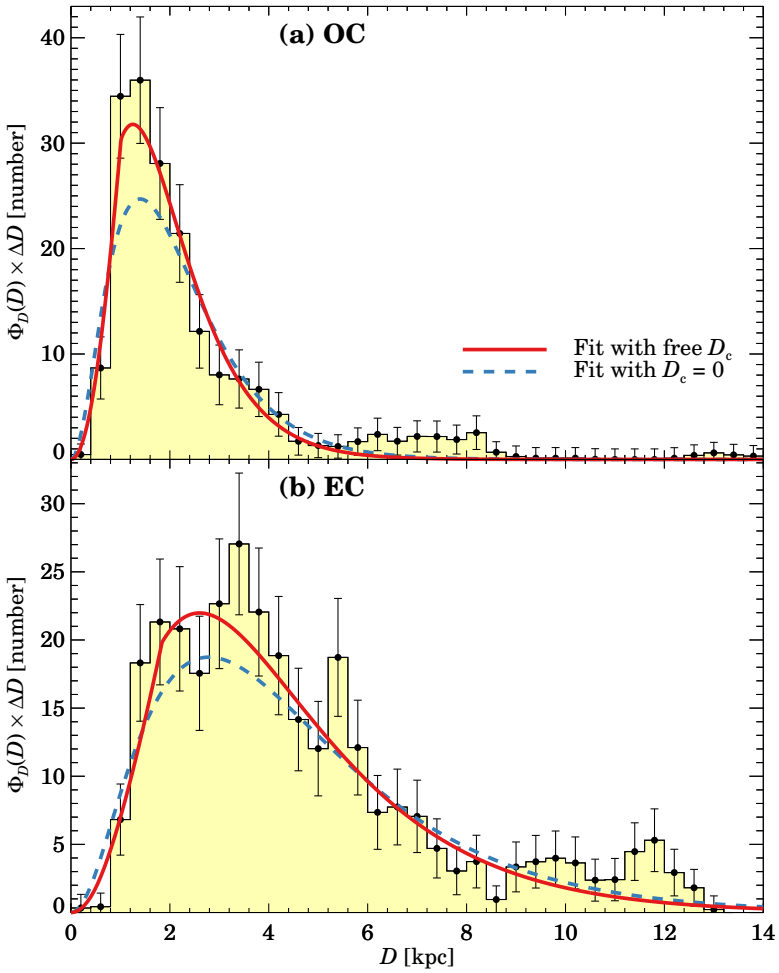

Figure 4.8: Histogram of heliocentric distances, D, for (a) open and (b) embedded clusters, using a bin width of $\Delta D = 0.4$ kpc and Poisson uncertainties. In each panel, the solid curve represents the fitted D-distribution $\Phi_D(D)$ from Equation (4.8), with the completeness distance D_c as free parameter (see Equation (4.9)); the dashed curve shows the fit with fixed $D_c = 0$ (see text for details). The best-fit parameters are given in Table 4.2.

R_D in the parametric fit to the distance distributions described below resulted in heavily degenerated output parameters and practically no constraint on their values. For this reason, and because the incompleteness produces that most clusters in our sample are within a few kpc from the Sun, we can make the rough approximation that cluster surface density on the Galactic disk is uniform, i.e., $\varphi_R(R) = 1$. The constants ρ_0 and Σ_0 must now be interpreted as Solar neighborhood values, and from Equation (4.5) the complete D-distribution

becomes

$$\Phi_D^{\rm tot}(D) = 2l_1\,\Sigma_0\,f_{b_1}(D)\,D\ , \tag{4.7}$$

which is a good approximation only within a few kpc from the Sun. On the other hand, defining a fractional factor $f_{\rm c}(D)$ that quantifies the completeness of the cluster sample as a function of distance, we can express the observed D-distribution $\Phi_D(D)$ as

$$\Phi_D(D) = 2l_1\,\Sigma_0\,f_{\rm c}(D)\,f_{b_1}(D)\,D\ . \tag{4.8}$$

In order to assign a particular parametric shape to the completeness fraction, we chose an ansatz for $f_{\rm c}(D)$ based on previous statistical works of open clusters in the whole sky. Bonatto et al. (2006a) studied the WEBDA database at that time and found, by completeness simulations, that their analyzed open cluster sample is highly incomplete in the inner Galaxy, even within what they called the "restricted zone", defined as an annulus segment with Galactocentric distances R in the range $[R_0-1.3$ kpc, $R_0+1.3$ kpc$]$. Their obtained completeness fraction decays almost immediately from $R = R_0$ to $R < R_0$ (see their Fig. 11; note that $R_0 = 8.0$ kpc in that work). However, Piskunov et al. (2006) claim that the Kharchenko et al. (2005b,a) open cluster catalogs constitute a complete sample up to about 0.85 kpc from the Sun. This is nicely illustrated in their Fig. 1, where a flat distribution of surface number-density of clusters is exhibited up to that distance, after which the distribution starts to decrease considerably. If the completeness fraction of their sample in the inner Galaxy were similar to that obtained by Bonatto et al. (2006a), the surface density distribution would be a decreasing function immediately from $D = 0$ kpc rather than from $D = 0.85$ kpc[11]. We think that this discrepancy is caused mainly by two effects: 1) the cluster sample studied by Bonatto et al. (2006a) (654 objects with known distances) is less complete than, e.g., the current version of the Dias et al. (2002) catalog used in this work (1309 clusters with available distances), which is equivalent to the Kharchenko et al. (2005b,a) sample within 0.85 kpc; and 2) the "restricted zone" considered by Bonatto et al. (2006a) covers a larger area than the circle defined by the completeness limit of Piskunov et al. (2006) (radius of 0.85 kpc centered at the Sun), and thus includes regions where the open cluster sample is indeed incomplete. In fact, we performed a quick test on the current Dias et al. (2002) catalog by constructing the Galactocentric radii distribution of clusters within 1 kpc from the

[11] We checked by numerical integration of $\Sigma(D) \propto \int_0^{2\pi} \varphi(D,l)\mathrm{d}l$ that the raising of the surface density distribution in the inner Galaxy due to an exponential Galactic disk is practically imperceptible for $D < 1$ kpc, and therefore, a flat distribution cannot be the combined result of incompleteness and exponential disk structure.

Sun, and we obtained a shape that is not incompatible with a exponential law in the whole range, as opposed to the distribution derived by Bonatto et al. (2006a, their Fig. 9).

Based on the above discussion, the completeness fraction for our open cluster sample is likely ~ 1 up to a close distance from the Sun, $D_{\rm c}$, and then starts to decay significantly. We assume that the decay is exponential:

$$f_{\rm c}(D) = \begin{cases} 1 & \text{if } D \leq D_{\rm c} \\ e^{-(D-D_{\rm c})/s_0} & \text{else .} \end{cases} \tag{4.9}$$

This parametrization allows us to investigate the possibility that the sample is always incomplete, as for Bonatto et al. (2006a), by just imposing $D_{\rm c} = 0$. We employ the same functional form for the completeness fraction of embedded clusters, but of course varying the parameters $D_{\rm c}$ and s_0.

Before proceeding to fit Equation (4.8) to the observed D-distributions, we need first some estimates for $z_{\rm h}$ and z_0 which are used to compute the factor $f_{b_1}(D)$. We obtain those estimates from the Z-distribution, that can be written analytically as

$$\Phi_Z(Z) = e^{-|Z+z_0|/z_{\rm h}} \int_{|Z|/\tan b_1}^{\infty} \frac{\Phi_D(D)}{2 z_{\rm h}\, f_{b_1}(D)}\, {\rm d}D \ . \tag{4.10}$$

The advantage in writing this equation explicitly in terms of $\Phi_D(D)$ is that we can use directly the observed D-distribution instead of its analytical expression (and compute the integral empirically), so that it is possible to fit the Z-distribution with only two free parameters, z_0 and $z_{\rm h}$, and independently from the fit of the distance distribution. All the fits were performed using the Levenberg-Marquardt least-squares minimization package `mpfit` (Markwardt 2009), implemented in IDL, and we have assumed Poisson uncertainties. The best fit of Equation (4.10) to the observed Z-distribution of OCs is shown in Figure 4.7(a) as a solid curve, and the corresponding fitted parameters are $z_0 = 14.7 \pm 3.7$ pc and $z_{\rm h} = 42.5 \pm 9.9$ pc. These values are in excellent agreement with the ones derived by Bonatto et al. (2006a), if we consider their scale height $z_{\rm h}$ within the Solar circle (which is the case for almost the totality of our OC sample). The observed Z-distribution of ECs (Figure 4.7(b)) is much more irregular than that of OCs, and hence a proper fit is not possible. This is likely produced by the fact that ECs are spread over a larger area than OCs, and therefore, present lower statistics in the Solar neighborhood and larger average errors in Z ($Z \propto D$). In addition, embedded clusters are usually grouped in complexes, as we will see in § 4.2.5 and can already be noted in Figure 4.6(b), where some particular locations appear crowded with many

Table 4.2: Best-fit parameters from the Z- and D-distributions of open clusters (OC) and embedded clusters (EC).

Parameter	OC	EC
z_0 (pc)	14.7(3.7)	... [a]
z_h (pc)	42.5(9.9)	... [a]
Σ_0 (kpc^{-2})	82.9(12.9)	19.5(3.1)
s_0 (kpc)	0.72(0.05)	1.81(0.10)
D_c (kpc)	1.01(0.16)	1.84(0.35)
Σ'_0 (kpc^{-2})	209.1(33.3)	40.3(5.0)
s'_0 (kpc)	0.82(0.04)	1.99(0.09)

Notes. z_0 is the displacement of the Sun above the plane, and z_h is the scale height; Σ_0 is the local surface number-density, s_0 is the length scale of the completeness, and D_c is the completeness distance (see Equation (4.9)); Σ'_0 and s'_0 represent values derived from an alternative fit with fixed $D_\mathrm{c} = 0$. Quantities between parentheses are the corresponding uncertainties.
[a] Fit not possible; assumed values from the OC sample.

close objects, enhancing the non-uniformity of their spatial distribution. However, if we adopt the same parameters z_0 and z_h derived from the OC sample and compute the predicted distribution from Equation (4.10) (naturally, using now the observed $\Phi_D(D)$ of ECs), the resulting curve is roughly consistent with the observed Z-distribution, as shown in Figure 4.7(b) (solid line). The most systematic discrepancy can be identified for $Z < -40$ pc, where there is a significant deficit of observed clusters with respect to the predicted distribution, probably due to the difficulty in detecting embedded clusters below the Galactic disk for large distances. In fact, Figure 4.7(b) also shows the observed Z-distribution for ECs with $D < 4$ kpc (darker inner histogram) and the corresponding prediction (dashed curve), and we can see that in this case the deficit of observed clusters below the Galactic plane is only marginal.

Using now z_0 and z_h obtained from the OC sample, which are also consistent with the EC height distribution, to compute the factor $f_{b_1}(D)$ defined in Equation (4.6), we fitted the analytical distribution $\Phi_D(D)$ from Equation (4.8) to the observed D-distributions of OCs and ECs, with free parameters Σ_0, D_c, s_0. The last two parameters appear inside the completeness factor $f_\mathrm{c}(D)$ defined in Equation (4.9). The best fits are overplotted as solid curves on the corresponding histograms of Figure 4.8, and the fitted parameters are given in Table 4.2. As can be already noted in the plots and confirmed by the reduced χ^2 values (0.90 for OCs, and 1.48 for ECs), the assumed form of the completeness fraction (Equation (4.9)) is a good representation of the overall detectability of star clusters in the inner Galaxy. The few outliers in the

observed distribution with respect to the fitted analytical function for OCs with distances $D \gtrsim 6$ kpc correspond mainly to exposed clusters recently discovered at infrared wavelengths. A similar tendency is hinted for ECs with $D \gtrsim 11$ kpc, although in this case these outliers are also consistent with being part of a general irregular distribution with small discrepancies with the fitted curve at some distance bins. It is remarkable that, despite the lower statistics within the ATLASGAL range, the fitted completeness limit of our OC sample, $D_c = 1.01 \pm 0.16$ kpc, is consistent with that derived by Piskunov et al. (2006) for their all-sky sample in the Solar neighborhood. For embedded clusters, both the completeness limit D_c and the completeness scale length s_0 are larger than the corresponding values of the OC distribution (see Table 4.2), confirming quantitatively that, from an observational point of view, ECs trace longer distances from the Sun than those probed by OCs.

The fitted completeness limits for OCs and ECs are significantly above zero, practically discarding the possibility that the cluster samples are always incomplete in the inner Galaxy, as suggested by Bonatto et al. (2006a) for open clusters. To further test this option, we performed an alternative fit of Equation (4.8) to the observed D-distributions, now fixing $D_c = 0$. For each distribution in Figure 4.8, the resulting best fit is shown as a dashed line, and we notice immediately that this alternative fit is poorer than the one with D_c as free parameter, specially for OCs. Indeed, we applied a Kolmogorov-Smirnov test to all the fitted distribution functions in a distance range free of far-distance outliers ($D \leq 6$ kpc for OCs, $D \leq 9$ kpc for ECs), and we found that the $D_c = 0$ fit can be rejected with a significance level of 5% for OCs, and 6.5% for ECs. We thus conclude that the OC and EC samples in the inner Galaxy are roughly complete up to a distance of ~ 1 kpc and ~ 1.8 kpc, respectively, as derived from the free-D_c fits.

4.2.3 Completeness and definition of a representative sample

In general, the existence of a stellar cluster is established observationally by an excess surface density of stars over the background, so that its detectability depends on its richness, its angular size, the number of resolved individual members and the apparent brightness of them (which is directly related to the distance), the surface density of field stars, and the amount of extinction on the line of sight (Lada & Lada 2003). Consequently, it is particularly difficult to identify a star cluster in the inner Galactic plane, where both the stellar background and the extinction are relatively high, or a very distant cluster, for which its members appear faint and could be confused as few single stars due to limited angular resolution of the observations. In fact, we have shown in

the previous Section that the current samples of open and embedded clusters in the inner Galaxy are complete up to only a close distance from the Sun, and then the completeness decreases heavily as distance increases.

We have also seen that the incompleteness affects more the OC sample than the ECs, i.e., the latter have a larger completeness limit and a less drastic decay in the completeness fraction. At first glance, this might seem contradictory since ECs are, by definition, embedded in molecular clouds and thus subject to the presence of high local dust extinction. However, at infrared wavelengths, embedded clusters become easier to detect than exposed clusters because it is less difficult to distinguish them from the field population. Since ECs are usually associated with illuminated interstellar material, they can be identified by eye towards the locations of known nebulae or star-forming regions (e.g., Dutra et al. 2003a; Bica et al. 2003b; Borissova et al. 2011), even if the clusters are partially resolved or highly contaminated by extended emission. Automated searches can also take advantage of some distinctive characteristic of ECs (like the red-color criterion of our GLIMPSE search, see § 3.4) to separate them from the background, which is in general not feasible for an evolved open cluster because its member stars present similar observational properties than the field population.

It is interesting to compare our distance distribution of embedded clusters (Figure 4.8(b)) with that of individual *Spitzer*-detected YSOs (Robitaille et al. 2008), as simulated by Robitaille & Whitney (2010) using a population synthesis model. They show that the synthetic YSOs that would have been detected by *Spitzer* and included in the Robitaille et al. (2008) catalog correspond to massive objects with a mass distribution that peaks at $\sim 8 M_{\odot}$. The corresponding distance distribution of this model is presented in Fig. 1 of Beuther et al. (2012) for the $10^{\circ} \leq l \leq 20^{\circ}$ range. The plot reveals a high number of far YSOs up to distances of ~ 14 kpc, showing that, despite the high extinction, individual (massive) YSOs can be detected deep into the Galactic plane, as opposed to embedded clusters. We therefore think that the low detectability of a far EC is mainly due to the faint apparent brightness of its low-mass population and confusion of its members, so that the whole cluster might be misidentified as an individual massive young star. At near-infrared wavelengths, however, extinction could still play an important role in hiding a far EC.

We can quantify how many OCs and ECs we are missing within a certain distance from the Sun, using the analytical expressions for the observed distance distribution, $\Phi_D(D)$ (Equation (4.8)), and for the distance distribution that would be observed if we detected the totality of the clusters in the inner Galaxy, $\Phi_D^{\rm tot}(D)$ (Equation (4.7)), together with the fitted parameters given

in Table 4.2. We define the cumulative completeness fraction, $F_{\rm c}(D)$, as the ratio of the number of observed clusters with distances $\leq D$ to the number that would result from a complete sample within D:

$$F_{\rm c}(D) \equiv \frac{N_{\rm cl}(\leq D)}{N_{\rm cl}^{\rm tot}(\leq D)} = \frac{\int_0^D \Phi_D(D')\,{\rm d}D'}{\int_0^D \Phi_D^{\rm tot}(D')\,{\rm d}D'} \ . \tag{4.11}$$

Now we can define a *representative* cluster sample as all objects with distances $D \leq D_{\rm rep}$ for which the fraction $F_{\rm c}(D_{\rm rep})$ is above a certain threshold in both the OC and EC samples (this naturally places the restriction on the OC sample only, since it is more incomplete). We chose a threshold of 0.25, for which the distance has to be $D \leq 3.15$ kpc. For simplicity, we just adopt $D_{\rm rep} = 3.0$ kpc, where $F_{\rm c}(D_{\rm rep}) = 0.28$ and $F_{\rm c}(D_{\rm rep}) = 0.79$ for the OC and EC samples, respectively. Note that although the selection of the threshold is somewhat arbitrary, if we keep in mind the above fractions, we only need a certain distance limit $D_{\rm rep}$ where the samples are not too incomplete and at the same time have a reasonable absolute number of objects to do statistics.

In Column 4 of Table 4.1, we list the number of clusters with $D \leq 3.0$ kpc for each morphological type; the total number of ECs in the representative sample is 98. To count the number of OCs, according to our definition we need that the clusters are also confirmed (`ref_Conf` not empty). The number of confirmed clusters with $D \leq 3.0$ kpc are given in Column 5 for each morphological type, from which we obtain a total number of 146 OCs in the representative sample. With the fractions $F_{\rm c}(D_{\rm rep})$ computed before, it is also possible to estimate the number of clusters, $N_{\rm cl}^{\rm tot}(\leq D_{\rm rep})$, that we would observe within 3 kpc if we had complete samples of OCs and ECs. The corresponding estimates are listed in Column 6, and were derived simply as $N_{\rm cl}(\leq D_{\rm rep})/0.79$ for EC types, and $N_{\rm cl}^{\rm conf}(\leq D_{\rm rep})/0.28$ for OC types. Note that the large number of OC2 clusters in this ideally complete sample is due to the fact that they cover a wide age range. The age distribution of our sample is analyzed in the next Section.

4.2.4 Age distribution and young cluster dissolution

We would expect that the ages of the stellar clusters increase along the morphological evolutionary sequence defined in § 4.2.1. If the cluster sample is separated in such morphological types, we indeed obtain an increasing tendency in the corresponding ages distributions, but we are unable to estimate an average age or age ranges for each individual type, given the low number of

clusters with available ages that fall within each category, except for OC2. In the whole sample, for types EC1, EC2, OC0 and OC1 there are, respectively, only 9, 16, 15 and 9 objects with age estimates, whereas for OC2 clusters there are 160. Note that for types OC0 and OC1, the total number of objects is also low (see Table 4.1), so that the main cause of the few age estimates for them is the low absolute statistics. The difficulty in determining the age of young and embedded clusters, on the other hand, would explain the lack of age estimates for the much more numerous EC1 and EC2 morphological types (this might also affect partially the OC0 type).

It is still possible, however, to derive an upper limit to the age of the ECs (EC1 and EC2 together), and also to study the age distribution of the whole OC population (OC0, OC1 and OC2 together), as described below. The embedded cluster ages compiled from the literature were estimated using a wide variety of methods, including: comparison with theoretical isochrones on a Hertzsprung-Russell diagram constructed after spectroscopic classification in the near-infrared (e.g., Furness et al. 2010), use of the relation between the circumstellar disk fraction in the cluster and its age (following Haisch et al. 2001), and comparison with synthetic clusters constructed by Monte Carlo simulations (Stead & Hoare 2011), among others. We remark that from the 25 ECs with available age estimates, there are two objects that seem to be artificial outliers, with too old ages to be embedded, namely 7.5 ± 2.6 Myr and 25 ± 7.5 Myr (respectively, clusters VVV CL100 and VVV CL059 from Borissova et al. 2011)[12]. These two objects are precisely the only embedded clusters in our sample whose age was determined simultaneously with the distance via isochrone fitting, and the high uncertainty of this method for very young clusters is indeed acknowledged by the authors (Borissova et al. 2011). In other few cases where isochrone fitting was used to derive the age of an EC, an independent measure of the distance was employed as input in order to reduce the uncertainty (e.g., Ojha et al. 2010). Excluding these two outliers from sample, we found that 90% (21 out of 23) of the ECs with available age estimates are younger than 3 Myr. Furthermore, given the high errors in this age range, even the remaining two clusters are consistent with being younger than 3 Myr, within the uncertainties: age of 3.3 ± 2.1 Myr for [BDS2003] 139 (Stead & Hoare 2011), and 4.2 ± 1.5 Myr for [DBS2003] 118 (Roman-Lopes 2007)[12]. We therefore adopt an upper limit of 3 Myr for the embedded phase, which represents a better constraint than the 5 Myr limit often quoted in the literature (from Leisawitz et al. 1989). Since practically all available EC ages in our sample are $\lesssim 3$ Myr, the same result is obtained if we consider the

[12]Note that the quoted uncertainties are from our catalog, which might be larger than the original paper because we adopted minimum errors for the age estimates (see § 4.1.5).

representative sample ($D \leq D_{\rm rep} = 3$ kpc), despite the low statistics (10 out of 11 embedded clusters are formally younger than 3 Myr, after removing one outlier).

The much higher number of open clusters with available age estimates allowed us to study their age distribution, which is shown in Figure 4.9 for the representative sample (a total of 143 OCs). Assuming a constant cluster formation rate (CFR), the decreasing number of open clusters as time evolves is due to the effect of different disruption processes. Lamers & Gieles (2006) provide a theoretical parameterization of the survival time of initially bound open clusters in the solar neighborhood, taking into account four main mechanisms: stellar evolution, tidal stripping from the Galactic field, shocking by spiral arms, and encounters with giant molecular clouds. They show that the observed age distribution $\Phi_a(a)$ for a constant CFR and a power-law cluster initial mass function with a slope of -2 can be written as

$$\Phi_a(a) = C \left[\left(\frac{M_{\rm lim}(a)}{M_\odot} \right)^{-1} - \left(\frac{M_{\rm max}}{M_\odot} \right)^{-1} \right] , \tag{4.12}$$

where a is the age, C is a constant, $M_{\rm lim}(a)$ is the initial mass of a cluster that, at an age a, reaches a mass equal to the detection limit (assumed to be 100 $M_\odot$), and $M_{\rm max}$ is the maximum initial mass of clusters that are formed. It can be shown that the cluster formation rate within the initial mass range $[100\,M_\odot, M_{\rm max}]$ is related with the factor C by

$$\mathrm{CFR} = C \left[\frac{1}{100} - \left(\frac{M_{\rm max}}{M_\odot} \right)^{-1} \right] . \tag{4.13}$$

We fitted $\Phi_a(a)$ from Equation (4.12) to the observed age distribution of OCs in the representative sample, with free parameters C and $M_{\rm max}$; the input function $M_{\rm lim}(a)$ was obtained by digitizing the dashed curve in Fig. 2 of Lamers & Gieles (2006). We plot the resulting best fit as a solid curve in Figure 4.9, corresponding to the parameters $\mathrm{CFR} = 0.93 \pm 0.09$ Myr^{-1} and $M_{\rm max} = (4.46 \pm 0.85) \times 10^4\ M_\odot$. It is clear from the figure that there is an excess of observed young open clusters with respect to the fitted theoretical distribution, whereas for older ages the fit is a pretty good representation of the data. The observed excess of young OCs could be the result of: 1) young OCs dominate at larger distances because they contain more luminous stars, so that within an incomplete sample the proportion of young OCs is relatively higher than that of older clusters (Piskunov et al. 2006), or 2) the over-population of young clusters correspond really to unbound associations

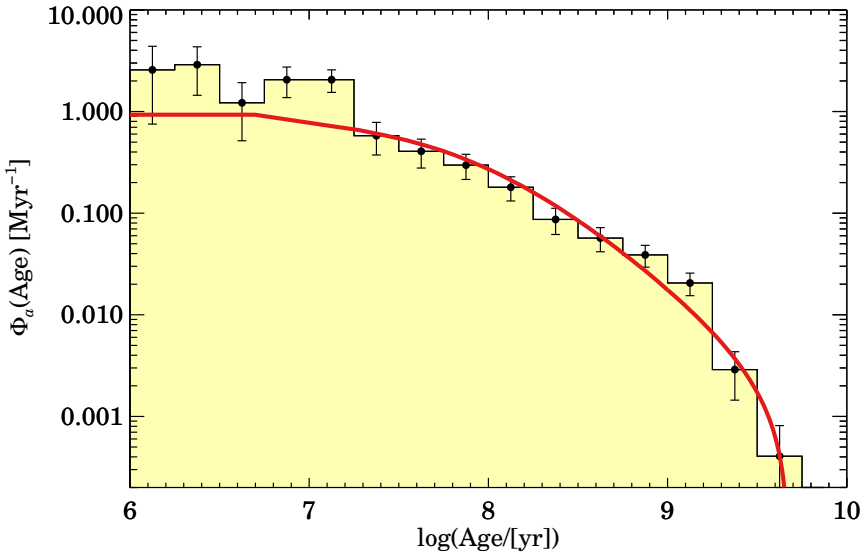

Figure 4.9: Age distribution of open clusters within the representative sample ($D \leq 3$ kpc), using a logarithmic bin width of $\Delta \log(\mathrm{Age/yr}) = 0.25$ and Poisson uncertainties. The solid curve corresponds to the fitted age distribution from Equation (4.12), following Lamers & Gieles (2006), with best-fit parameters CFR $= 0.93 \pm 0.09$ Myr^{-1} and $M_{\mathrm{max}} = (4.46 \pm 0.85) \times 10^4\ M_\odot$.

that will dissolve due to the star-formation process or the early dynamical evolution (not accounted for in the parameterization of Lamers & Gieles 2006). While the age-dependent incompleteness (first point) is likely playing a role within our $D_{\mathrm{rep}} = 3$ kpc limit, it is interesting to investigate whether or not there is also a contribution from the second effect. We found that the excess of observed young OCs still holds if we do the fit in a sample restricted to smaller distances, down to $D \leq 1.4$ kpc; nevertheless, the low statistics in the Solar neighborhood within the ATLASGAL range prevents us to perform this test on an even more restricted subsample of our catalog. We therefore fitted the model to all-sky samples of open clusters, namely, the Dias et al. (2002) catalog and the Kharchenko et al. (2005b,a) sample, restricted to a certain limit in projected distance, D. For clusters with $D \leq 0.6$ kpc, in both samples, we recovered the results from Lamers & Gieles (2006)[13], whose observed age distribution practically does not show the excess of young OCs

[13]This is totally expected for the Kharchenko et al. sample, since Lamers & Gieles (2006) used basically the same clusters. The only difference is that they do not included the new objects detected by Kharchenko et al. (2005a). On the other hand, the fact that for the Dias et al. (2002) sample we obtain the same result implies that there are no systematic effects arising from differences between both samples, in particular regarding the age estimates.

with respect to the fitted curve (see their Fig. 3). If we restrict the samples to $D \leq 1.4$ kpc, however, the age distribution for the Dias et al. (2002) catalog presents an statistically significant over-population of young OCs, whereas for the Kharchenko et al. (2005b,a) sample the excess is only marginal. Given that the Kharchenko et al. (2005b,a) sample is a subset of the Dias et al. (2002) catalog, this behavior means that the young excess cannot be due purely to the age-dependent incompleteness, since otherwise we would obtain a more noticeable effect in the more incomplete sample. The excess is less significant for the Kharchenko et al. catalog and hidden for clusters in both samples with $D \leq 0.6$ kpc probably because there is an observational limitation in detecting unbound associations at very close distances, due to their larger sizes. In summary, we think that the excess of young clusters in our representative OC sample with respect to the theoretical description of Lamers & Gieles (2006) is caused by a combination of age-dependent incompleteness and presence of unbound associations.

The age distribution shown in Figure 4.9 was constructed using a bin width large enough to have good statistics in whole age range, but we can refine the grid to constrain better a certain feature, as long as it remains statistically significant. By constructing the age distribution with smaller bin widths and doing the fitting again, we found that the transition after which the theoretical description fits well the data occurs at an age of $\log(a/\mathrm{yr}) \simeq 7.2$, i.e., ~ 16 Myr. Consistently, we have seen in § 4.2.1 that the ~ 16 Myr limit is roughly the age before which an observed open cluster might be either an unbound association or a physical open cluster, whereas observed OCs older than that are practically always bound and therefore are disrupted through "classical" mechanisms in a longer timescale.

Similarly to the estimation of the cumulative completeness fraction (see § 4.2.3), we can use the analytical expressions for the distance distributions from § 4.2.2 to transform the absolute CFR in the representative sample to an incompleteness-corrected cluster formation rate per unit area, $\dot{\Sigma}$, representative of the inner Galaxy close to the Sun. It can be easily shown that the conversion is

$$\dot{\Sigma} = \frac{\mathrm{CFR(D \leq D_{rep})}}{l_1 D_{\mathrm{eff}}^2(D_{\mathrm{rep}})} \ , \tag{4.14}$$

where

$$D_{\mathrm{eff}}^2(D) \equiv 2 \int_0^D f_{\mathrm{c}}(D')\, f_{b_1}(D')\, D'\, \mathrm{d}D' \ . \tag{4.15}$$

For the OC sample, $D_{\mathrm{eff}}(D_{\mathrm{rep}}) = 1.28$ kpc, which implies that the fitted cluster formation rate per unit area is $\dot{\Sigma}_{\mathrm{fit}} = 0.54 \pm 0.05$ Myr^{-1} kpc^{-2}. This value can now be compared with the analogous parameter in the Lamers & Gieles

(2006) fit for a complete all-sky sample within 0.6 kpc from the Sun, $\dot{\Sigma}_{\rm LG06} = 0.63$ Myr^{-1} kpc^{-2}. Together with their obtained maximum mass of $M_{\rm max} = 3 \times 10^4\ M_\odot$, we can see that both fits are consistent within the uncertainties, assuming that their errors are similar to ours (they are not provided). On the other hand, from the observed number of open clusters in our representative sample with ages $\log(a/{\rm yr}) < 7.2$, we derive $\dot{\Sigma}_{\rm obs} = 1.18 \pm 0.22$ Myr^{-1} kpc^{-2} (using Poisson errors), which sets an upper limit of ~ 0.5 to the fraction of observed young OCs that are actually unbound associations. The observed cluster formation rate corrected by age-dependent incompleteness is some value between $\dot{\Sigma}_{\rm fit}$ and $\dot{\Sigma}_{\rm obs}$ that can be parametrized as $\dot{\Sigma}^{\rm corr}_{\rm obs} = \dot{\Sigma}_{\rm obs} - f_{\rm adi}(\dot{\Sigma}_{\rm obs} - \dot{\Sigma}_{\rm fit})$, where $f_{\rm adi}$ is a factor in the range $[0, 1]$ ($f_{\rm adi} = 0$ for no age-dependent incompleteness, and $f_{\rm adi} = 1$ for no intrinsic young excess).

To really quantify the fraction of young clusters that will dissolve or merge with other(s) agglomerate(s), and therefore will not become physical open clusters by their own, we also need an equivalent estimate for the formation rate of embedded clusters. For that, we can simply take the local surface density Σ_0 obtained from fitting the distance distribution of embedded clusters (Table 4.2), and divide it by their upper limit age of 3 Myr, resulting in $\dot{\Sigma}_{\rm EC} = 6.50 \pm 1.03$ Myr^{-1} kpc^{-2}. This EC formation rate, however, is not directly comparable to that of OCs, since within 3 kpc from the Sun we are likely detecting embedded clusters with masses below the detection limit of 100 $M_\odot$ adopted by Lamers & Gieles (2006) for open clusters, as shown, e.g., by Lada & Lada (2003), whose EC catalog includes objects with masses down to 20 $M_\odot$, with a large number of clusters with masses in the range $[50, 100]\ M_\odot$. Fortunately, we found that the uncertainty in the fraction of ECs with masses above 100 $M_\odot$, $f_{>100\,M_\odot}$, is not dominant and does not prevent us to compute a good estimate of the young dissolution fraction. If we assume that $f_{>100\,M_\odot}$ is in the range $[0.1, 1]$, we obtain that the fraction of embedded clusters and young exposed clusters, $f_{\rm diss}$, that will not become physical open clusters is

$$f_{\rm diss} = 1 - \frac{\dot{\Sigma}_{\rm fit}}{\dot{\Sigma}_{\rm obs} - f_{\rm adi}(\dot{\Sigma}_{\rm obs} - \dot{\Sigma}_{\rm fit}) + f_{>100\,M_\odot}\dot{\Sigma}_{\rm EC}} = 88 \pm 8\% \ , \qquad (4.16)$$

where the uncertainty has been computed numerically assuming Gaussian random variables, except for $f_{>100\,M_\odot}$ and $f_{\rm adi}$ which were drawn from uniform probability distributions in the corresponding domains ($[0, 1]$ range for $f_{\rm adi}$, see above). The obtained value is in excellent agreement with that obtained by Lada & Lada (2003). However, the explanation proposed at that time for this high fraction has been changed (or extended) considerably in the recent years, as we review in § 2.3.

4.2.5 Correlations

In this Section, we look for correlations between the morphological types defined in § 4.2.1 and other information compiled in our cluster catalog, like the mid-infrared morphology and association with known objects. The percentages of clusters that satisfy the studied criteria within each morphological type are presented in Table 4.3. Column 2 gives the percentage of clusters that appear to be exciting PAH emission through UV radiation from their stars, as traced by bright diffuse 8 μm emission or the presence of IR bubbles (mid-infrared morphology `bub-cen`, `bub-cen-trig`, or `pah`, see § 4.1.3). Column 3 lists the fraction of clusters that seem to be triggering further star formation at the edge of the associated IR bubble (mid-infrared morphology `bub-cen-trig` only), whereas Column 4 indicates the fraction of clusters that are located at the edge of an IR bubble (mid-infrared morphology `bub-cen-edge`). Columns 5, 6 and 7 give, respectively, the percentage of objects that are associated with IRDCs, H II regions of any type, and UCH II regions only. Finally, Column 8 lists the fraction of clusters which are part of a complex of several clusters (see § 4.1.6). We present in this table the statistics calculated for the whole cluster sample, because we obtained the same results for the representative sample, within the uncertainties (assumed to be Poisson errors). The only exception is the association with infrared dark clouds, for which we give the fractions within the representative sample. This is expected since the identification of an IRDC requires that the source were located at a relatively near distance in order to manifest, with a detectable contrast, as a dark extinction feature in front of the Galactic diffuse background.

We note from the table that the presence of stellar feedback as traced by PAH emission and H II regions is very important in the first four stages of the evolutionary sequence. We found that both indicators of feedback are roughly equivalent, i.e., the same clusters present both tracers. The few clusters that have PAH emission but no H II region are probably due to the incompleteness of the current sample of H II regions, or in some cases might correspond to lower mass clusters whose UV radiation is strong enough to excite the PAH molecules, but not to produce a detectable region of ionized gas (Allen et al. 2007). On the other hand, the few H II regions without PAH emission are probably more evolved or misclassified UCH II regions. However, it is remarkable that although the identification of an ultra compact region was only based on the literature, their presence is indeed more important in the first morphological type, which presumably covers the youngest objects. The almost null correlation of OC2 clusters with indicators of stellar feedback is consistent with the fact that these clusters are mostly classical open clusters and already

Table 4.3: Statistics for each morphological type (in percentages).

Type	PAH or Bub.	Trigg.	Edge	IRDC[a]	H II	UCH II	Complex
(1)	(2)	(3)	(4)	(5)	(6)	(7)	(8)
EC1	58 (8)	0 (0.8)	3.1 (1.6)	55 (14)	62 (9)	18 (4)	52 (8)
EC2	87 (9)	8.5 (2.2)	0 (0.5)	12 (5)	69 (8)	5.6 (1.7)	63 (7)
OC0	48 (11)	13 (5)	0 (1.9)	0 (6.2)	55 (12)	0 (1.8)	52 (12)
OC1	52 (19)	9.5 (7)	0 (4.8)	0 (20)	59 (21)	0 (4.5)	45 (17)
OC2	1.2 (0.7)	0 (0.4)	0 (0.4)	0 (0.9)	0.7 (0.5)	0 (0.3)	1 (0.6)

Notes. Within each morphological type, the given number is the percentage in the whole sample of clusters associated with PAH emission or IR bubbles (Column 2), clusters with signposts of triggered star formation on the surroundings (Column 3), clusters located at the edge of an IR bubble (Column 4), clusters associated with IRDCs (Column 5), clusters associated with H II regions including ultra compact ones (Column 6), clusters associated with ultra compact H II regions only (Column 7), and finally clusters that are part of a complex of several clusters (Column 8). Numbers between parentheses are the corresponding Poisson uncertainties, with a minimum error of ± 1 clusters for null values.
[a] Percentages are from the representative sample (clusters with $D \leq 3$ kpc).

gas-free.

Concerning triggered star formation, we see that only EC2, OC0, and OC1 clusters are able to produce it, in roughly 10% of the cases. EC1 clusters are not able because they are too embedded and have not yet started to sweep up the surrounding material; in turn, their formation might be triggered itself by another cluster or massive star, but in only a very small fraction (see Column 4). We warn, however, that the possible triggered star formation has been established just through morphological features, so that its real existence in these cases is definitely not conclusive.

Infrared dark clouds are significant mostly in the first morphological type, confirming the fact that they trace the earliest phases of star cluster formation. Interestingly, we found that the presence of IRDCs and PAH emission are almost mutually exclusive: within the representative sample, both tracers practically account for the totality of EC1 clusters, with almost null intersection. In other words, IRDCs and PAH emission trace, respectively, an earlier and later stage within the deeply embedded phase (type EC1). A simple interpretation from this behavior is that at some point IRDCs are "illuminated" by the feedback of the recently formed embedded clusters, before their actual disruption, so that they become undetectable as extinction features in the mid-infrared but still prominent in the submm dust continuum emission traced by ATLASGAL.

Although we have not identified the totality of complexes of physically related clusters in our sample, from the table is clear the tendency that embedded

clusters are often grouped in complexes, whereas open clusters are relatively much more isolated (the type OC2 dominates the open cluster population). Only those OCs that are still associated with some molecular gas (types OC0, OC1) present a similar degree of grouping with other clusters as ECs. This is consistent with the fact that star formation occurs in giant molecular complexes with a hierarchical structure, in which star-forming regions with a relatively higher stellar density would be identified observationally as "embedded clusters". Many of them will dissolve, while others, if close enough, will undergo a merging process as a result of dynamical evolution (Maschberger et al. 2010), all in a timescale shorter than $\sim$ 15 Myr (see § 4.2.4). The final outcome, after the molecular cloud is destroyed, might be therefore a very few or even an unique bound open cluster, which will appear relatively in isolation.

5

Follow-up ^{13}CO(2−1) and C^{18}O(2−1) mapping observations

In this thesis, we started a follow-up project consisting of mapping observations in CO isotopologues of a significant number of young star clusters from our sample, which show evidence of ongoing stellar feedback. The aim of this project is to study in detail the dynamical evolution of the associated molecular gas under the influence of the clusters, investigating in particular whether or not the observed kinematics is the result of gas dispersal through stellar feedback. Whereas the submillimeter dust continuum emission observed in ATLASGAL, in conjunction with IR images at different wavelengths, has shown to be very efficient in identifying statistically the presence of feedback in young stellar clusters (as demonstrated in the previous chapter), the kinematic information from line observations is strictly needed to really disentangle the cluster-gas interaction within an individual region. In Sections § 5.1 and § 5.2 we describe the observations and overall results for a sample of 14 regions observed so far, and in Section § 5.3 we present a detailed study of the IR bubble G10.31−0.14, powered by the young clusters [BDS2003] 112 & 113.

5.1 Observations

Following Ridge et al. (2003), who carried out an analogous (though only morphological) study of nearby (low-mass) young star clusters, we observed

the $J = 2 \rightarrow 1$ transition of ^{13}CO and C^{18}O (220.399 and 219.560 GHz, respectively) towards a sample of 14 regions containing young star clusters with signposts of stellar feedback. These CO isotopologues are ideal tracers of warm medium-density molecular gas, and are abundant enough to be easily detected in luminous star-forming regions, but much less abundant than the main isotope ^{12}CO. Therefore, they are less affected by confusion by diffuse, low-intensity gas projected on the same line of sight, and they have a smaller optical depth than ^{12}CO (specially C^{18}O), being better tracers of column density.

The observed sample corresponds to stellar clusters still associated with molecular gas as traced by ATLASGAL dust emission, and with mid-infrared morphology suggesting the presence of stellar feedback (`bub-cen`, `bub-cen-trig`, or `pah`, see § 4.1.3). The mapped regions are listed in Table 5.1, and they usually cover one cluster or few close clusters belonging to the same complex. Column 1 gives the designation of each region used throughout this chapter, which is based on its Galactic coordinates; Columns 2 and 3 list, respectively, the associated cluster(s) ID(s) and names(s) from our compiled catalog (see § 4.1.1). The remaining columns give, for each cluster, additional information taken from our catalog, namely, its distance, age, morphological type (as defined in § 4.2.1), morphological flag (`Morph` in our catalog, see § 4.1.2 and § 4.1.3), and associated H II region and IR bubble. We see that all the observed fields are associated with known H II regions, indicating that the selected clusters (or the total stellar population of the region when it comprises more than one identified cluster) have at least one massive star in order to produce a detectable region of ionized gas. According to our estimate presented in § 2.2.1, the clusters must have stellar masses in excess of $\sim 100 M_{\odot}$. The selected clusters were also required to be relatively well studied in the near-infrared (`ref_Conf` not empty in out catalog), but without detailed molecular line mapping observations in the literature.

The observations were carried out using the APEX telescope for sources located in the IV quadrant, and the IRAM 30-m telescope for regions in the I quadrant. The mapped regions correspond to rectangular areas centered in the positions listed in Table 5.2, and with sizes of a few arcminutes, also given in the table. We defined the areas to be observed based on the ATLASGAL emission, and some fields were rotated in order to map optimally the structures seen by ATLASGAL. The following two columns of Table 5.2 give the median rms per position achieved in the final ^{13}CO and C^{18}O maps, respectively. Note that, given the difference in angular resolution between both telescopes (factor 2.5 better for IRAM-30m), these rms values translate into much longer integration times for IRAM-30m than for APEX. The last two columns of Table 5.2 list the

velocity range covered by the main velocity component of each region, used in § 5.2 to compute integrated and moment maps. The details of the observations are described in the following subsections.

5.1.1 APEX

In July 2008, June 2009, and November 2009, we observed 9 regions in the IV Galactic quadrant with the APEX telescope (Güsten et al. 2006), a 12 m diameter antenna located on Llano de Chajnantor (5100 m altitude), Chile. We used the APEX-1 receiver of the Swedish Heterodyne Facility Instrument (SHeFI, Vassilev et al. 2008), connected simultaneously to two units of Fast Fourier Transform Spectrometers (FFTS Klein et al. 2006) of 1 GHz bandwidth each, centered in the two observed lines. We used 4096 channels for the FFTS, corresponding to a velocity resolution of 0.33 km s^{-1} at the observed frequency. The observations were carried out in on-the-fly (OTF) mapping mode scanning along two perpendicular directions, and using position switching with an emission-free reference position located up to one degree away from the target source. The dumps (positions at which one spectrum is written after continuous integration) within each region are spaced by $10''$, resulting in fully-sampled maps for a telescope beam width of $28.6''$ at 220 GHz.

The telescope pointing was checked and corrected every $\sim$ 1 h on IRAS 15194−5115, X-TrA, or RAFGL 1922, and found to be accurate within $\sim 5''$. Focus checks and adjustments were made on Saturn or Jupiter at the beginning of the observing sessions, which had durations of less than 5 h. The observations were done under average weather conditions, with a precipitable water vapor (PWV) in the range $\sim 1 - 3.5$ mm, resulting in system temperatures $T_{\rm sys} \simeq 150 - 250$ K. We mapped every region for a total on-source integration time (not including overheads) of $15 - 30$ minutes, depending on the map size. In the final data cubes (after gridding), we achieved median rms values of typically $0.15 - 0.30$ K (see Table 5.2).

The data were reduced using the CLASS software, which is part of the GILDAS package[1]. We first subtracted baselines defined by polynomials of order ≤ 3 fitted to emission-free velocity ranges of the spectra. Then, we combined the reduced spectra into a table and used the CLASS gridding routine `xy_map`, which constructs a data cube with a pixel size of half the original beam width. This procedure convolves the irregularly gridded OTF data with a Gaussian kernel with a FWHM of 1/3 the beam width, yielding a final angular resolution of $30.1''$.

[1] http://www.iram.fr/IRAMFR/GILDAS/

Table 5.1: The sample of regions mapped in $^{13}CO(2-1)$ and $C^{18}O(2-1)$.

Region	Cl. ID	Cl. Name	Distance (kpc)	Age (Myr)	Type	Morphology	H II Region	IR Bubble
(1)	(2)	(3)	(4)	(5)	(6)	(7)	(8)	(9)
G305.26+0.22	32	[DBS2003] 131	3.80 (0.60)	2.00 (1.00)	OC0	surr.bub-cen	[CH87] 305.254+0.204	S156
G305.27−0.01	33	[DBS2003] 130	3.80 (0.60)	2.00 (1.00)	EC2	p-emb.bub-cen	[DWS84] G305.27−0.01	S155
G305.32+0.07	35	[DBS2003] 132	3.80 (0.60)		EC1	emb.pah	[DWS84] G305.32+0.07	S154
	36	Danks 1	3.80 (0.60)	2.00 (1.00)	OC0	surr		
G320.17+0.80	157	RCW 87 IR Cluster	1.23 (0.30)		EC2	p-emb.bub-cen-trig	[CH87] 320.153+0.780	S96
G332.54−0.14	251	[DBS2003] 160	3.49 (0.41)	2.75 (0.96)	EC2	p-emb.bub-cen	[CH87] 332.541−0.111	Bub(ID:251)
	252	[DBS2003] 161	3.49 (0.41)	2.75 (0.96)	EC2	p-emb.bub-cen-trig	[CH87] 332.541−0.111	Bub(ID:252)
G348.25−0.97	377	[DBS2003] 118	1.94 (0.90)	4.20 (1.47)	EC2	p-emb.bub-cen	[CH87] 348.231−0.982	S6
G350.51+0.95	390	[DBS2003] 121	1.74 (0.31)	1.50 (0.52)	EC2	p-emb.bub-cen	GM 1−24	CS103
	391	[DBS2003] 122	1.74 (0.31)		EC1	emb.pah	GM 1−24	CS102
	392	[DBS2003] 123	1.74 (0.31)	2.50 (0.88)	OC0	surr		
G353.41−0.37	415	[DB2001] Cl 40	3.25 (0.99)		EC1	emb.pah	[CH87] 353.430−0.368	CS55
G354.67+0.47	418	[DB2001] Cl 41	4.21 (0.80)		EC2	p-emb.bub-cen-trig	[CH87] 354.664+0.470	CS44
G1.12−0.11	453	[DB2000] 26	5.90 (2.00)	1.00 (0.35)	EC1	emb.pah	Sgr D	CN24
G5.90−0.44	470	[BDS2003] 108	1.28 (0.09)		EC2	p-emb.pah	[L89b] 5.899−00.427	CN71
	471	[BDS2003] 107	1.28 (0.09)		EC2	p-emb.bub-cen	[L89b] 5.899−00.427	CN71
G10.31−0.14	498	[BDS2003] 112	2.77 (1.07)		EC2	p-emb.bub-cen-trig	G10.3−0.1	CN148
	499	[BDS2003] 113	2.77 (1.07)		EC2	p-emb.bub-cen-trig	G10.3−0.1	CN148
G18.15−0.30	539	[BDS2003] 8	4.30 (0.35)		EC2	p-emb.bub-cen	[L89b] 18.143−00.289	Bub(ID:539)
G25.39−0.16	569	W42 IR Cluster	4.05 (0.37)		EC1	emb.pah	[L89b] 25.382−00.177	N39

Notes. Column 1: name of the observed region, based on its Galactic coordinates; Column 2: ID(s) of the cluster(s) covered by the map (as defined in § 4.1.1); Column 3: name of the cluster; Column 4: cluster distance and uncertainty; Column 5: cluster age and uncertainty; Column 6: cluster morphological type as defined in § 4.2.1; Column 7: cluster morphological flag `Morph` (see § 4.1.2 and § 4.1.3); Column 8: associated H II region; Column 9: associated IR bubble. The horizontal line in the middle of the table divides the regions located in the IV quadrant (observed with APEX) from the ones in the I quadrant (observed with IRAM 30-m).

Table 5.2: Summary of the ^{13}CO(2−1) and C^{18}O(2−1) mapping observations.

Region	α (J2000)	δ (J2000)	Map size ($'$) × ($'$)	$\sigma_{^{13}\mathrm{CO}}$ (K)	$\sigma_{\mathrm{C}^{18}\mathrm{O}}$ (K)	v_1 (km s^{-1})	v_2 (km s^{-1})
G305.26+0.22	13:11:39.8	−62:33:36	5.2 × 5.5	0.34	0.32	−49.1	−29.6
G305.27−0.01	13:11:54.0	−62:47:02	3.5 × 3.5	0.22	0.21	−39.1	−25.1
G305.32+0.07	13:12:18.0	−62:42:16	3.5 × 3.5	0.26	0.26	−47.7	−34.2
G320.17+0.80	15:05:21.7	−57:30:55	4.7 × 5.2	0.23	0.22	−44.6	−31.6
G332.54−0.14	16:17:05.0	−50:47:39	4.0 × 3.8	0.19	0.22	−53.5	−45.5
G348.25−0.97	17:18:25.7	−39:18:20	4.3 × 4.8	0.23	0.22	−20.5	−4.5
G350.51+0.95	17:17:03.0	−36:21:10	3.5 × 5.5	0.32	0.30	−14.3	−5.3
G353.41−0.37	17:30:28.9	−34:41:55	5.0 × 3.8	0.27	0.25	−23.0	−9.5
G354.67+0.47	17:30:26.4	−33:11:10	3.2 × 3.7	0.13	0.15	−26.8	−15.8
G1.12−0.11	17:48:42.6	−28:02:07	3.9 × 3.0	0.16	0.17	−25.7	−10.7
G5.90−0.44	18:00:42.0	−24:04:38	2.9 × 2.9	0.14	0.16	3.2	13.7
G10.31−0.14	18:08:56.8	−20:05:12	6.6 × 4.2	0.13	0.16	6.9	17.9
G18.15−0.30	18:25:04.7	−13:15:37	3.4 × 3.9	0.13	0.16	40.4	58.4
G25.39−0.16	18:38:12.3	−06:46:55	3.6 × 3.2	0.16	0.19	54.7	70.7

Notes. Units of right ascension are hours, minutes, and seconds, and units of declination are degrees, arcminutes, and arcseconds. The horizontal line in the middle of the table divides the regions located in the IV quadrant (observed with APEX) from the ones in the I quadrant (observed with IRAM 30-m). $\sigma_{^{13}\mathrm{CO}}$ and $\sigma_{\mathrm{C}^{18}\mathrm{O}}$ refer to median rms per position achieved in the final ^{13}CO and C^{18}O maps, respectively, in units of forward-beam antenna temperature T_{A}^{*}. Depending on the telescope, these values are for an angular resolution of 30.1″ (APEX) or 11.8″ (IRAM 30-m), and a spectral resolution of 0.33 km s^{-1} (APEX) or 0.43 km s^{-1} (IRAM 30-m). The velocities v_1 and v_2 define the range $[v_1, v_2]$ of the main velocity component for each region, which was used to compute all the integrated maps presented in § 5.2.

5.1.2 IRAM 30-m

The 5 regions from our selected sample that are located in the I Galactic quadrant were observed with the IRAM-30m telescope on Pico Veleta, Spain, in December 2008 and January 2009, as part of pool observations. The sources were mapped in OTF mode, using the Heterodyne Receiver Array (HERA, Schuster et al. 2004), connected to the VESPA autocorrelator backend. HERA is a multipixel receiver that simultaneously observes 9 positions on the sky at two orthogonal linear polarizations. Given that the HERA pixels are separated by 24″, the standard strategy to fully sample the 11.2″ beam of the telescope (at 220 GHz) is to rotate the array by 9.5° with respect to the direction of the scanning, and repeat each scan line in reverse with an offset of 11.9″ in the perpendicular direction. All this results in a sampling of 4″ over the entire map. Several OTF scans along two perpendicular directions on the sky were done for each region. The two polarization arrays, HERA1 and HERA2, were tuned to the two observed lines frequencies, ^{13}CO and C^{18}O respectively, so that both lines could be observed simultaneously. The VESPA autocorrelator was set to a bandwidth of 160 MHz in each polarization, and a spectral resolution

of 320 kHz, which translates into a velocity resolution of 0.43 km s^{-1} at the observed frequency.

The telescope pointing was checked on Mercury, Mars, G34.3+0.2, J1733-131, J1800-241, or 1757-240 every $1-1.5$ h, and the corrections were in general within $3''$. The telescope focus was optimized on Mercury, Mars, Saturn, or G34.3+0.2 at the beginning of the observing sessions, which had durations of less than 4.5 h. The observing runs were carried out under good winter weather conditions[2], with PWV $\simeq 1-2$ mm, and $T_{\rm sys} \simeq 300-400$ K for HERA1 and $T_{\rm sys} \simeq 350-500$ K for HERA2. The higher system temperatures with respect to the ones obtained with APEX are mainly due to the lower average elevation of the sources in the northern hemisphere. The total on-source integration time for each map was typically $1-2$ h, which means that the effective integration time was $9-18$ h if we multiply by the number of pixels (9) that observed simultaneously. The achieved median rms in the final data cubes are in the range $0.13-0.19$ K (see Table 5.2), which were lower than expected because the observing scripts were prepared for average winter conditions.

Data reduction was done in a very similar fashion than for APEX observations. After gridding, the final angular resolution of the data cubes is $11.8''$.

5.2 General Results

In this Section, we present some general properties of the observed regions that can be derived from the ^{13}CO(2−1) and C^{18}O(2−1) emission. Here, we exclude two sources which have a low signal-to-noise ratio (S/N) in the C^{18}O map, namely G305.32+0.07 and G354.67+0.47. Almost all the remaining regions have an unique dominant velocity component which appears clearly in the averaged spectrum (they are not shown here, see Fig. 5.16 for an example) and whose velocity-integrated emission over the map correlates quite well with the ATLASGAL emission thought to be associated with each stellar cluster, as opposed to the other velocity components with lower intensity. This good agreement can be clearly seen in Figure 5.1, which shows the ^{13}CO(2−1) maps integrated over the range covered by the main velocity component of all the 12 regions studied here, overlaid with ATLASGAL contours. The velocity ranges were selected manually based on the averaged spectrum of each source, and the corresponding limits are listed in the last two columns of Table 5.2. The only exception is the source G25.39−0.16, which had originally two dominant velocity components separated by ~ 30 km s^{-1}, and we selected the one whose

[2]Note that the nomenclature for "average" or "good" weather conditions depends on the telescope site.

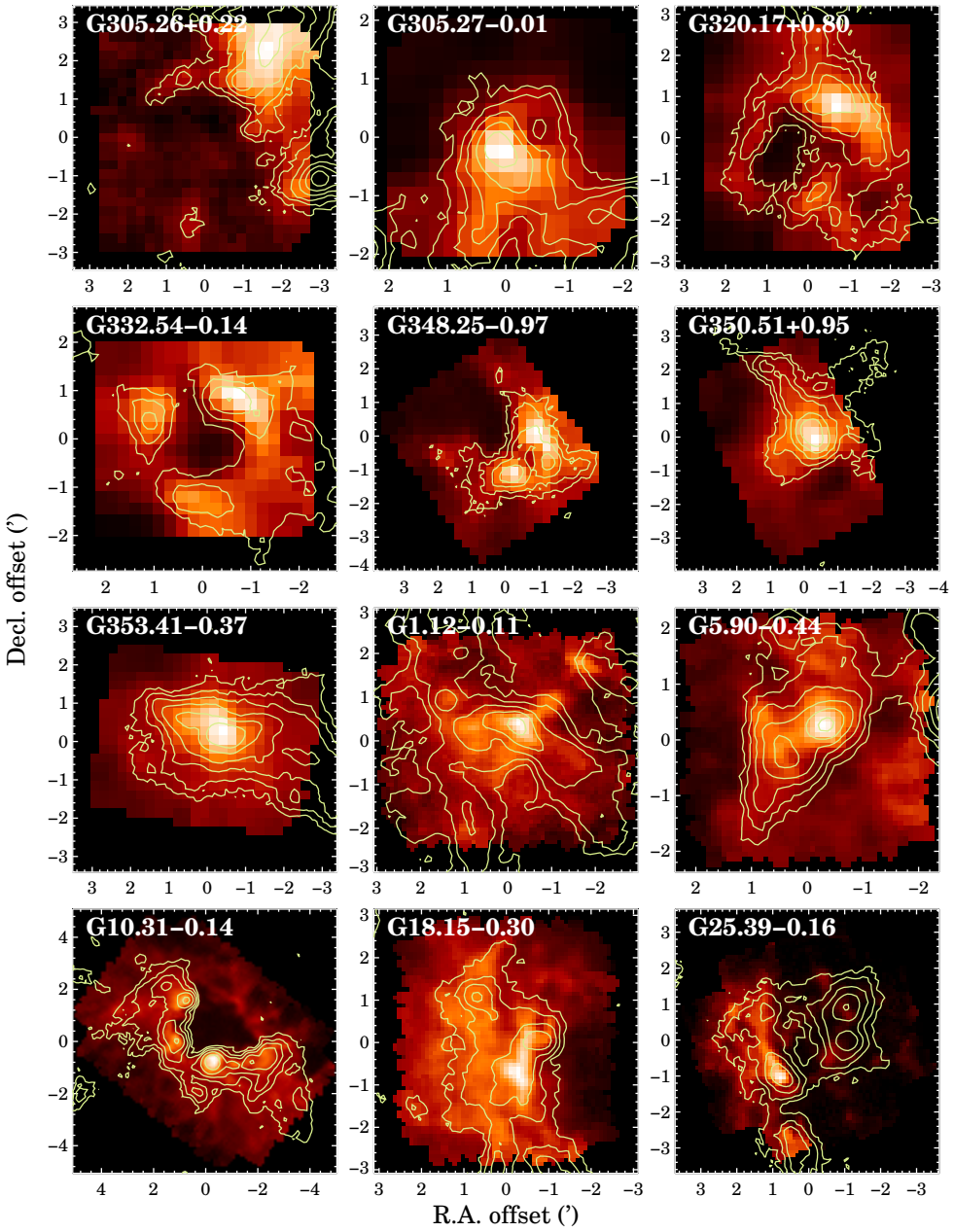

Figure 5.1: ^{13}CO(2−1) maps integrated over the velocity range indicated in the last two columns of Table 5.2, corresponding to the main velocity component of each region. The name of the source is indicated in the upper left corner of each panel. The maps are displayed in inverse hyperbolic sine scale, from 0 K km s^{-1} to the maximum value (114, 132, 88, 57, 98, 154, 140, 53, 99, 107, 103 and 101 K km s^{-1}, respectively, from left to right, top to bottom). The overlaid contours correspond to ATLASGAL emission (870 μm), with levels $\{0.3, 0.57, 1.0, 1.9, 4.0, 8.5\}$ mJy/beam. The images are in equatorial coordinates, with offsets relative to the positions listed in Table 5.2.

integrated emission correlates with the ATLASGAL clump spatially associated with the cluster. The western ATLASGAL clumps correspond to the other velocity component, and therefore do not present emission in our integrated map. Given its high velocity difference, this second component is more likely an unrelated source projected in the same line of sight.

We do not show the $C^{18}O(2-1)$ maps, because they exhibit very similar morphologies to that seen in $^{13}CO(2-1)$, but much fainter due to its lower abundance. Instead, the $C^{18}O$ observations are really useful to quantify the column density, as its emission is mostly optically thin. In addition, we can combine both ^{13}CO and $C^{18}O$ maps to solve for the opacity, and then, for the excitation in our regions. We computed column density $N(H_2)$ and excitation temperature T_{ex} maps for the 12 regions shown in Fig. 5.1, as explained in the following. For each isotopologue, assuming a filled telescope beam and constant excitation along the line of sight (or equivalently, constant source function), the equation of radiative transfer can be written as (e.g., Eq. (15.29) of Wilson et al. 2009)

$$T_{MB}(v) = [J_{\nu_0}(T_{ex}) - J_{\nu_0}(T_{bg})](1 - e^{-\tau(v)}) \ , \tag{5.1}$$

where

$$J_{\nu_0}(T) \equiv \frac{h\nu_0/k}{e^{-h\nu_0/(kT)} - 1} \ ,$$

ν_0 is the frequency of the transition, $T_{bg} = 2.73$ K is the cosmic background temperature, and $\tau(v)$ is the optical depth. Because both observed isotopologues have very similar rotational constants and Einstein coefficients, their frequencies and excitation temperatures can be considered equal in the above equation. For the same reason, their corresponding optical depths are approximately proportional to each other via the relative abundance $A \equiv [^{13}CO]/[C^{18}O]$. The ratio between the observed peak intensities of $^{13}CO(2-1)$ and $C^{18}O(2-1)$ then becomes

$$\frac{T_{MB}(^{13}CO)}{T_{MB}(C^{18}O)} = \frac{1 - e^{-A\tau_{18}}}{1 - e^{-\tau_{18}}} \ , \tag{5.2}$$

where τ_{18} is the optical depth of $C^{18}O(2-1)$ in the line center. In every map pixel, we solved Equation (5.2) for τ_{18} assuming $A = [^{13}C][^{16}O]/[^{12}C][^{18}O]$, and the isotopic ratios from Wilson & Rood (1994), which depend on the Galactocentric radius of the region, but in our sample resulted to be constrained within the range $\sim [7.0, 7.5]$. We blanked the pixels where the peak intensity was below 5σ in the $C^{18}O$ data. The excitation temperature T_{ex} can then be derived from the Equation (5.1) applied to the peak intensity of ^{13}CO (better S/N than $C^{18}O$), using $\tau_{13} = A\tau_{18}$ as the corresponding optical depth.

Since we have assumed constant excitation along the line of sight, we can

use the derived excitation temperature at each pixel to solve for the $C^{18}O$ opacity in the entire velocity range, $\tau_{18}(v)$, applying again Equation (5.1) but now to the whole $C^{18}O$ data cube. In this case, $C^{18}O$ was chosen instead of ^{13}CO because it is optically thinner and therefore less sensitive to line profile features caused by the combined effect of opacity and deviations from the constant excitation approximation. Once obtained $\tau_{18}(v)$, we can easily calculate the $C^{18}O$ column density, $N(C^{18}O)$. It can be shown that $N(C^{18}O)$ is proportional to the velocity-integrated opacity of the $J \rightarrow J-1$ transition via the equation

$$N(C^{18}O) = \frac{8\pi\nu_0^3}{c^3(2J+1)A_{J,J-1}} f_J(T_{ex}) \int_{v_1}^{v_2} \tau_{18}(v)\mathrm{d}v \ , \tag{5.3}$$

where

$$f_J(T) \equiv \sqrt{1+\left(\frac{2JT}{T_0}\right)^2} \cdot \frac{e^{(J+1)T_0/2T}}{e^{T_0/T}-1} \ , \tag{5.4}$$

$T_0 \equiv h\nu_0/k$, and $A_{J,J-1}$ is the Einstein coefficient for spontaneous decay. For $C^{18}O(2{-}1)$, $T_0 = 10.54$ K, and $A_{21} = 6.01 \times 10^{-7}$, which gives 3.28×10^{14} cm^{-2}/(km s^{-1}) for the constant of proportionality in Equation (5.3). This equation was obtained by using the expression for the column density of a single rotational level, N_J (e.g., Eq. (A5) of Ginsburg et al. 2011) and converting it to the total column density under the assumption that all levels are thermalized to the same temperature T_{ex}, which allows us to use a partition function (we used Eq. (19.17) of Draine 2011). Finally, we derived H_2 column densities adopting again the $[^{18}O]/[^{16}O]$ isotopic ratio from Wilson & Rood (1994) and the CO abundance as a function of Galactocentric radius provided by Fontani et al. (2012). The obtained conversion factors, $[H_2]/[C^{18}O]$, are in the range $\sim [0.9, 4.7] \times 10^6$.

The resulting $N(H_2)$ and T_{ex} maps of each region are presented, respectively, in panels (c) and (d) of Figures 5.2–5.13. Pixels with a $N(H_2)$ uncertainty larger than the solution[3] and pixels with errors $> 50\%$ in excitation temperature were blanked in the corresponding maps. For comparison, we also show *Spitzer*-IRAC three color images (panels (a)) and ATLASGAL maps (panels (b)) of the regions. Since the dust continuum emission from ATLASGAL is optically thin (see Schuller et al. 2009), it is roughly proportional to the H_2 column density, and therefore can be directly compared with the $N(H_2)$ maps computed above. The beam-averaged column density $N(H_2)_{dust}$ derived

[3]For column density, we keep pixels with errors within the order of the solution because they always correspond to the lowest column densities in the region, which thus still represent well constrained estimations relative to the rest of the map.

from ATLASGAL is related with the observed 870 μm flux at each pixel, F_ν, through

$$N(\mathrm{H_2})_{\mathrm{dust}} = \frac{F_\nu}{\Omega_{\mathrm{MB}}\sigma_\nu B_\nu(T_{\mathrm{d}})} = 2.5\,(e^{16.54\,\mathrm{K}/T_{\mathrm{d}}} - 1)\left(\frac{F_\nu}{\mathrm{Jy/beam}}\right) \times 10^{22}\,\mathrm{cm^{-2}}, \tag{5.5}$$

where Ω_{MB} is the main beam solid angle, $B_\nu(T_{\mathrm{d}})$ is the Planck function at the dust temperature, T_{d}, and $\sigma_\nu = 2R_{\mathrm{dH}}m_{\mathrm{H}}\kappa_\nu$ is the dust cross section per hydrogen molecule, with R_{dH} the dust-to-H mass ratio, m_{H} the hydrogen mass, and κ_ν the absorption opacity per mass of dust. The numeric evaluation in Equation (5.5) was done for a beam FWHM of 19.2″ (Siringo et al. 2009), $R_{\mathrm{dH}} \simeq 1/100$ (Draine et al. 2007), and $\kappa_\nu \simeq 2$ cm^2 g^{-1} (interpolation to 870 μm of the tabulated opacities by Ossenkopf & Henning 1994). We remark that for an average dust temperature of $T_{\mathrm{d}} = 30$ K over the observed areas, appropriate for dust heated by the radiation from the stellar clusters residing there, the conversion factor from ATLASGAL flux in Jy/beam to column density in units of 10^{22} cm^{-2} is simply ~ 1.8. In general, it can be noted that, dust continuum-derived column densities (obtained by multiplying the color scale in panels (b) by 1.8) are in very good agreement with the ones determined from the CO observations (panels (d)), within a factor of 2 (typical uncertainty of the dust opacities) or even better. Median values of $N(\mathrm{H_2})$ in our regions are from ~ 1 to few times 10^{22} cm^{-2}, and maximum values at the peaks of the submm clumps usually reach 10^{23} cm^{-2}. ATLASGAL-derived column densities are different (higher) by a factor > 2 from the CO-derived column densities in only two regions (G353.41−0.37 and G1.12−0.11). We think that this discrepancy is probably due to a dust temperature higher than 30 K in these particular sources, so the real conversion factor from Eq. (5.5) is lower than 1.8. Significant CO depletion due to the condensation of the molecule onto dust grains (e.g., Caselli et al. 1999) is unlikely for gas being illuminated by stellar sources.

Average excitation temperatures (see panels (c)) are in the range $[10, 30]$ K, with peaks of a few tens of Kelvin higher. If we assume that the regions have average kinetic temperatures around 30 K, based on the dust temperature adopted above which led to a consistent conversion of the dust continuum fluxes into column densities, this would mean that the observed CO emission is close to being thermalized. Although we cannot ensure that this is really the case, the fact that the critical densities of the observed CO species are not too high ($\sim 5\times10^3$ cm^{-3} for the $2-1$ transition) makes the excitation temperature roughly follow the kinetic temperature variations. Consequently, the relative values of the excitation temperature are useful to trace stellar feedback, as can

be noticed with the overall good correlation between infrared-bright regions (see panels (a)) and zones with higher $T_{\rm ex}$. A clear example is the IR bubble G10.31−0.14 studied later, where the part of the ring that is closer to the stellar clusters has a higher excitation temperature than the opposite side (see Fig. 5.11).

Finally, we quickly examined the kinematics of the observed regions by computing the ^{13}CO(2−1) moment maps of the main velocity component. In each of the Figures 5.2−5.13, panel (e) shows the first moment map, corresponding the the intensity-weighted velocity, whereas panel (f) displays the second moment map, corresponding to the intensity-weighted velocity dispersion. Although the number of observed sources is low, the first moment maps together with a quick inspection of the channel maps (not shown here) are suggestive of a possible trend: regions with more concentrated submm clumps with respect to the clusters exhibit coherent velocity structures, i.e., the main emission is at roughly the same velocity (G348.25−0.97, G353.41−0.37 and G1.12−0.11), whereas more dispersed submm emission with respect to the clusters is usually spread in velocity gradients, probably indicating the presence of expanding motions produced by stellar feedback. In particular, regions G320.17+0.80, G332.54−0.14 and G10.31−0.14 exhibit expanding ring-like kinematics, with G320.17+0.80 additionally showing a redshifted emission at the center, indicating that is more likely an incomplete shell instead of just a ring (see § 5.3.2). Similarly, though more chaotic, regions G5.90−0.44 and G18.15−0.30 present a center-to-outside velocity gradient which could also indicate expanding shell motions with one of the back or front faces missing, depending on the direction of the gradient. The second moment maps (panels (f)) show in many cases linewidth broadening in clumps directly associated or in the vicinity of the stellar clusters, probably produced by turbulent motions driven by stellar feedback. Interestingly, the fact that most of the regions with more condensed clumps relative to the clusters exhibit this feature suggests that this particular manifestation of the feedback starts earlier than the actual gas dispersal.

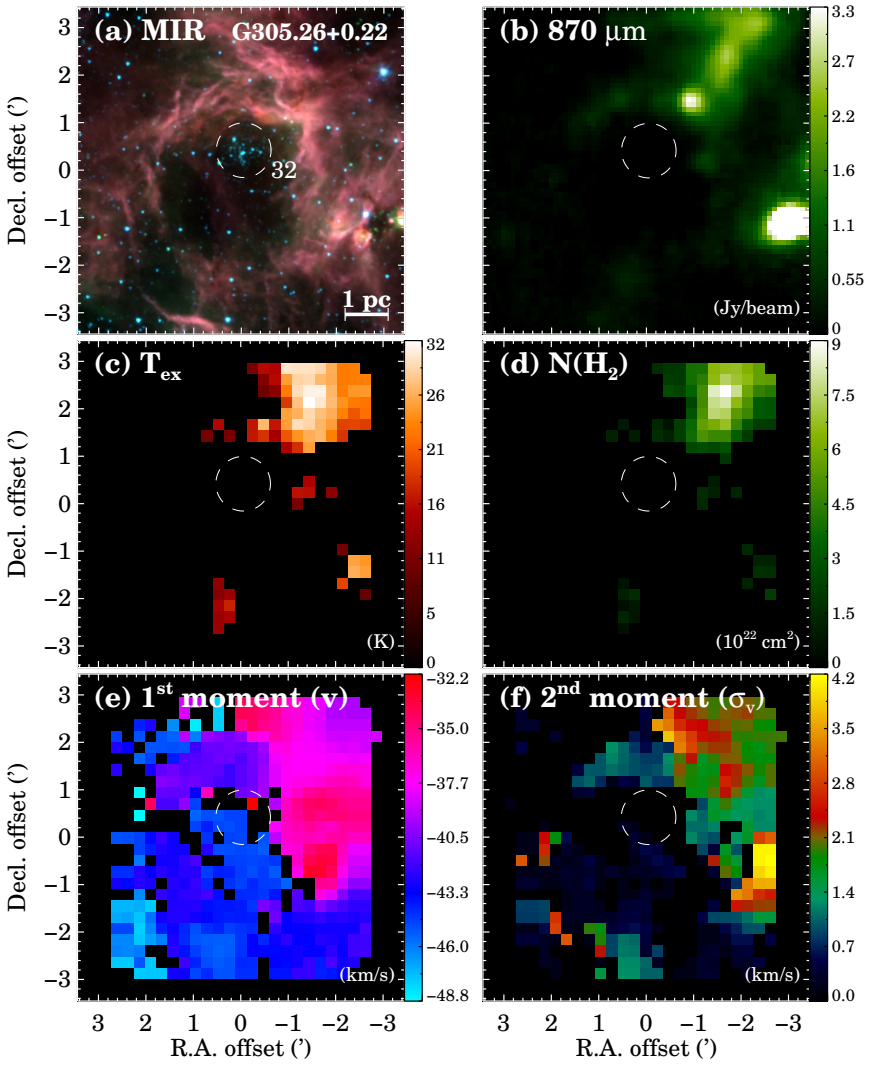

Figure 5.2: $^{13}CO(2-1)$ and $C^{18}O(2-1)$ analysis for G305.26+0.22. (a) *Spitzer*-IRAC three-color image made with the 3.6 (blue), 4.5 (green) and 8.0 μm (red) bands. (b) ATLASGAL (870 μm) image. (c) Excitation temperature T_{ex} map derived from the $^{13}CO(2-1)$ and $C^{18}O(2-1)$ peak emissions. (d) Column density $N(H_2)$ map derived from T_{ex} and the integrated $C^{18}O(2-1)$ emission. (e) $^{13}CO(2-1)$ first moment map (intensity-weighted velocity). (f) $^{13}CO(2-1)$ second moment map (intensity-weighted velocity dispersion). The scale of each image for panels (b)–(f) is shown in the vertical color bar to the right of the panel, and the units are indicated in the bottom-right corner. The images are in equatorial coordinates, with offsets relative to the position listed in Table 5.2. The dashed circle in each panel represents the location and angular size of the stellar cluster present in the region, and the numeric label in panel (a) is the corresponding ID (Column 2 of Table 5.1). The 1 pc scale-bar in panel (a) was estimated using the cluster distance adopted in our catalog (Column 4 of Table 5.1).

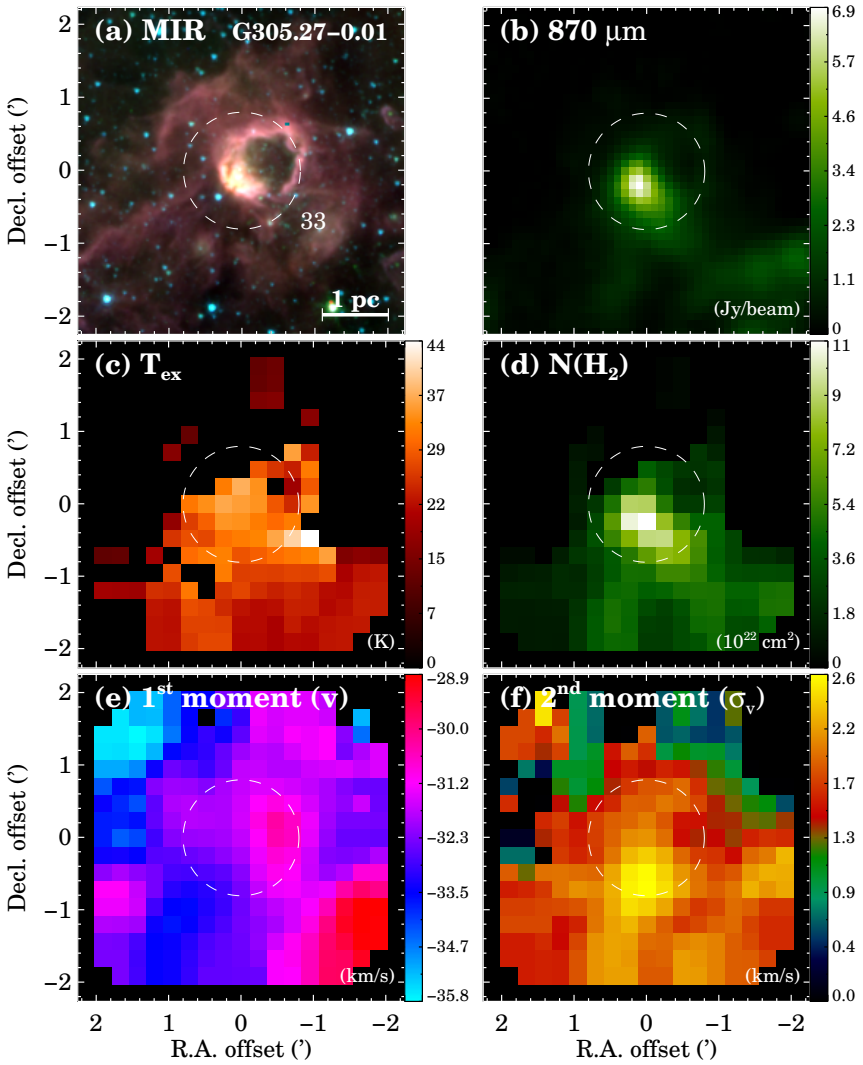

Figure 5.3: ^{13}CO(2−1) and C^{18}O(2−1) analysis for G305.27−0.01. See caption of Fig. 5.2 for more details.

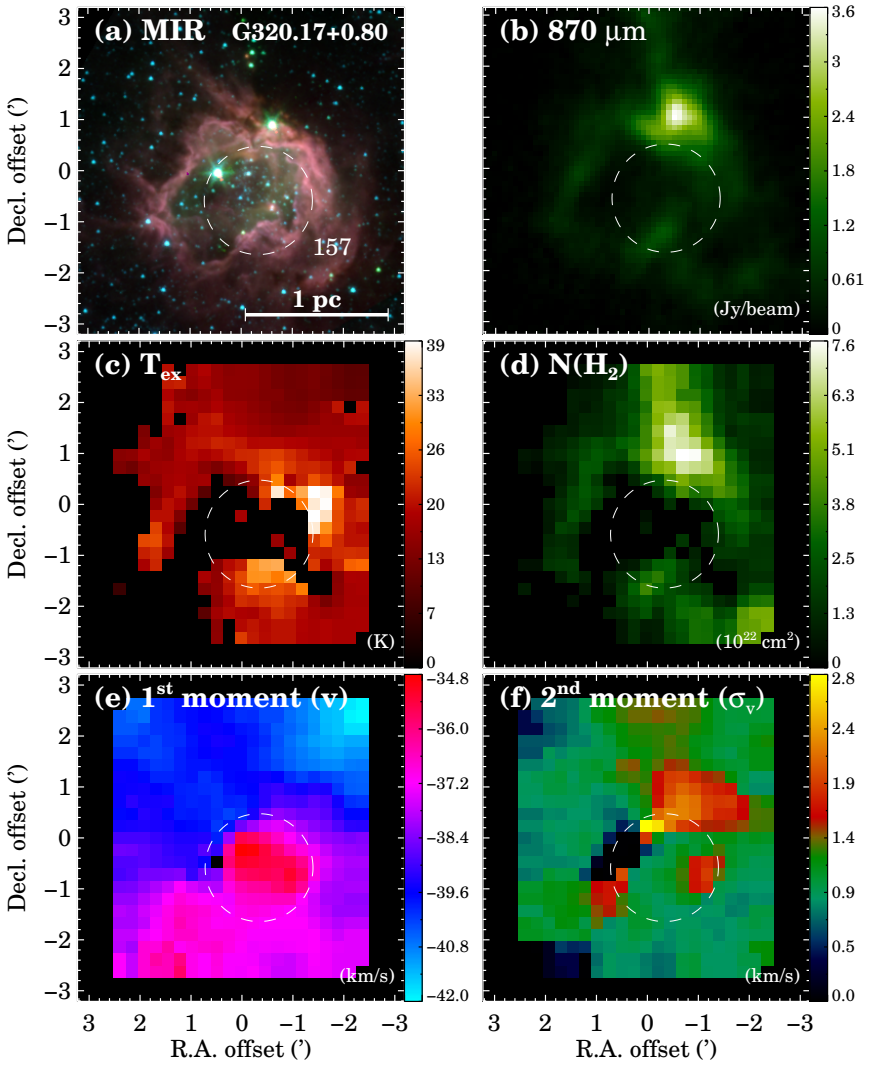

Figure 5.4: $^{13}CO(2-1)$ and $C^{18}O(2-1)$ analysis for G320.17+0.80. See caption of Fig. 5.2 for more details.

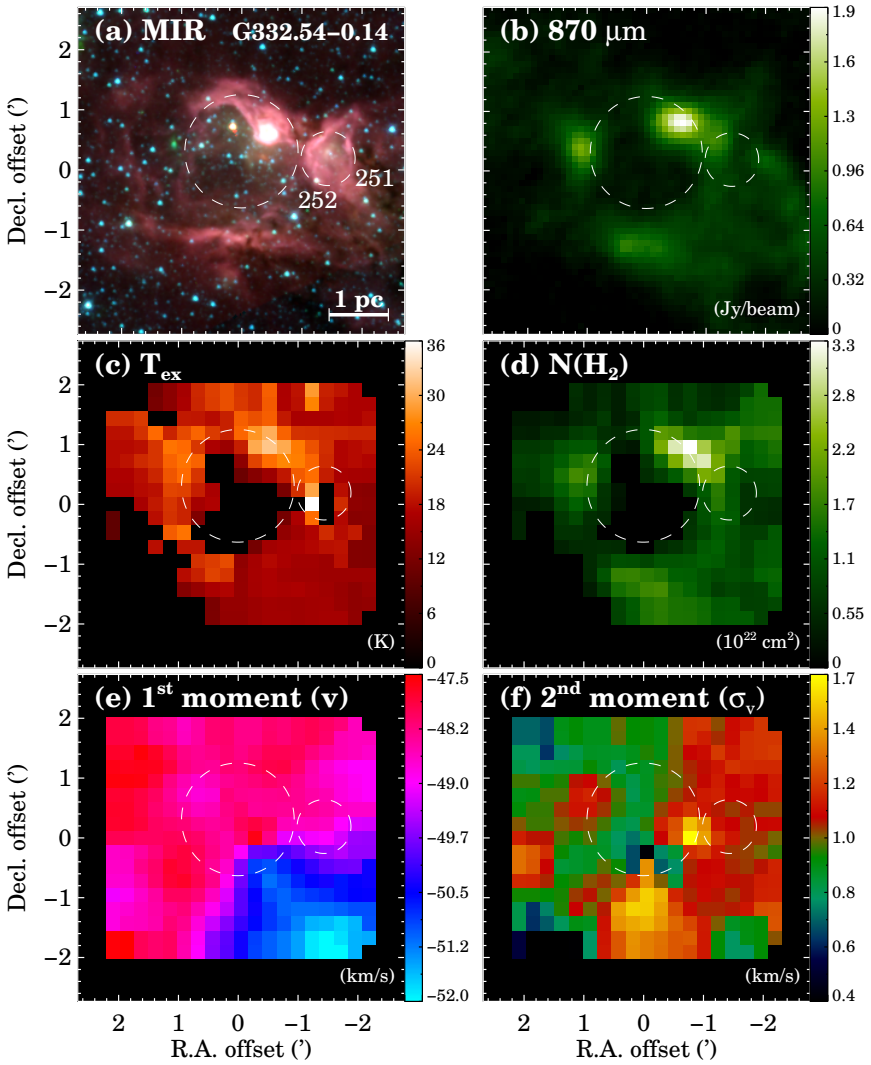

Figure 5.5: ^{13}CO(2−1) and C^{18}O(2−1) analysis for G332.54−0.14. See caption of Fig. 5.2 for more details.

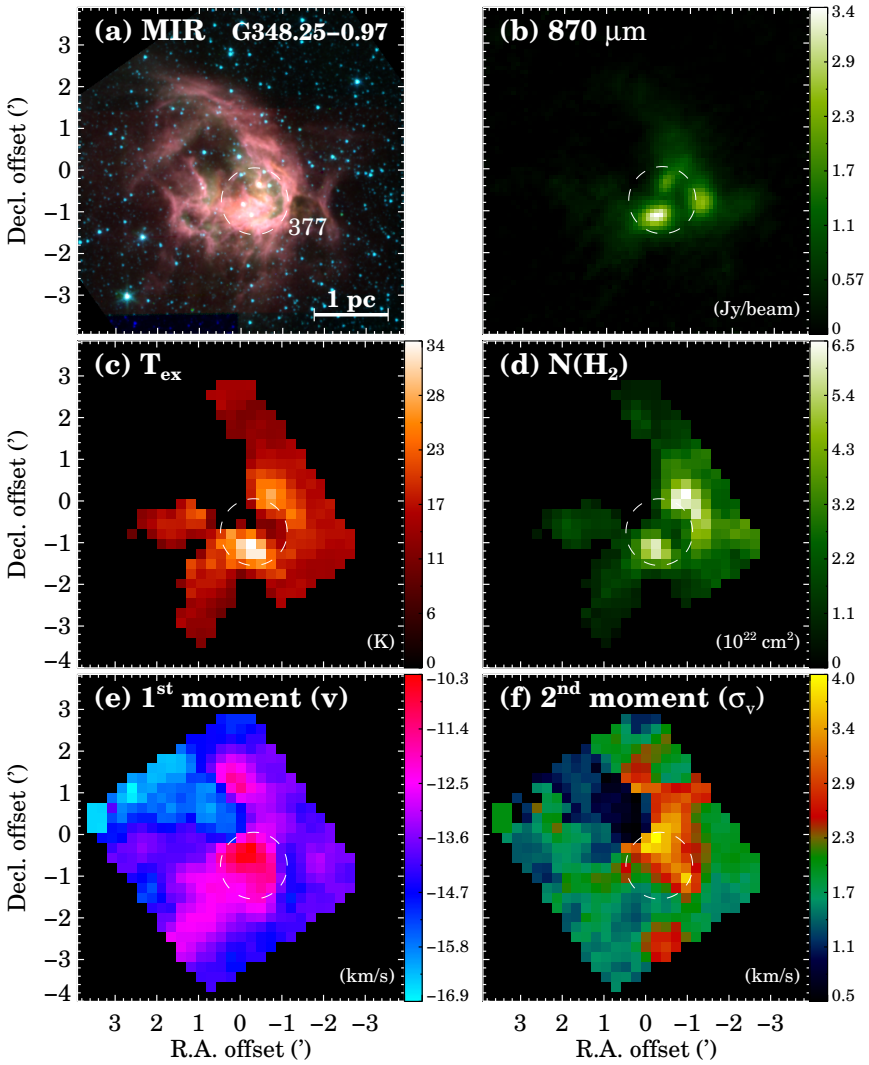

Figure 5.6: $^{13}CO(2-1)$ and $C^{18}O(2-1)$ analysis for G348.25−0.97. See caption of Fig. 5.2 for more details.

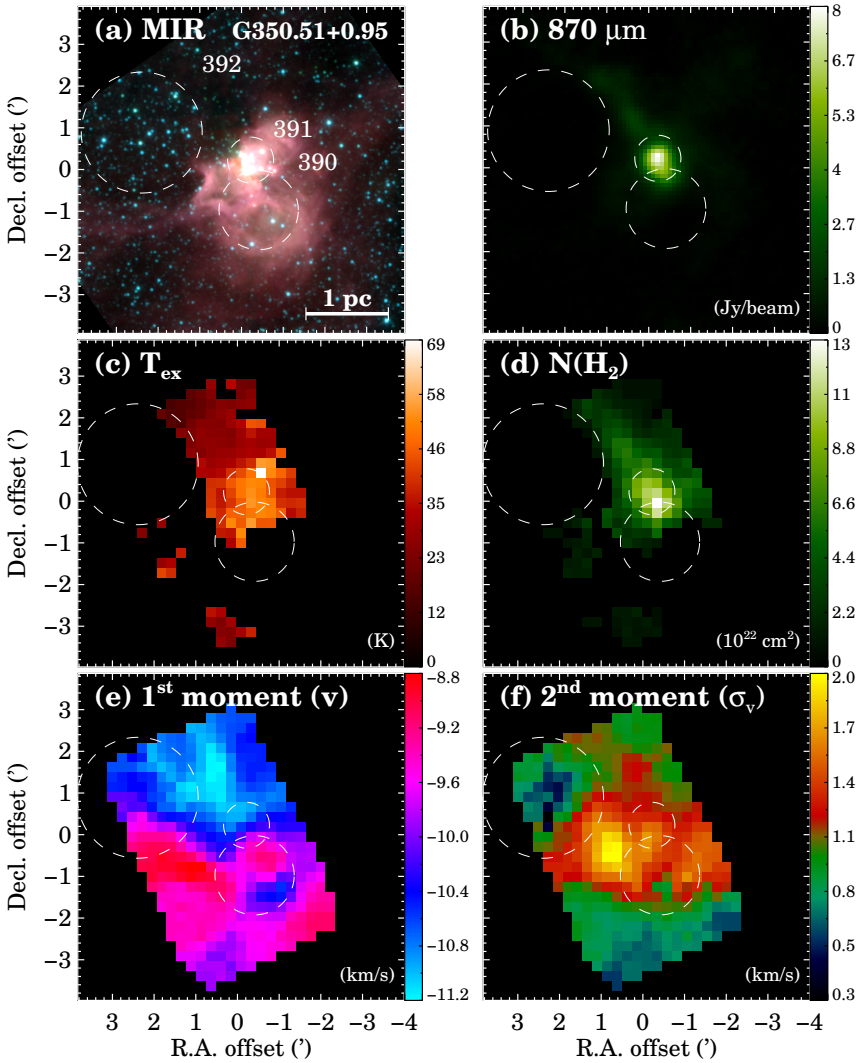

Figure 5.7: ^{13}CO(2−1) and C^{18}O(2−1) analysis for G350.51+0.95. See caption of Fig. 5.2 for more details.

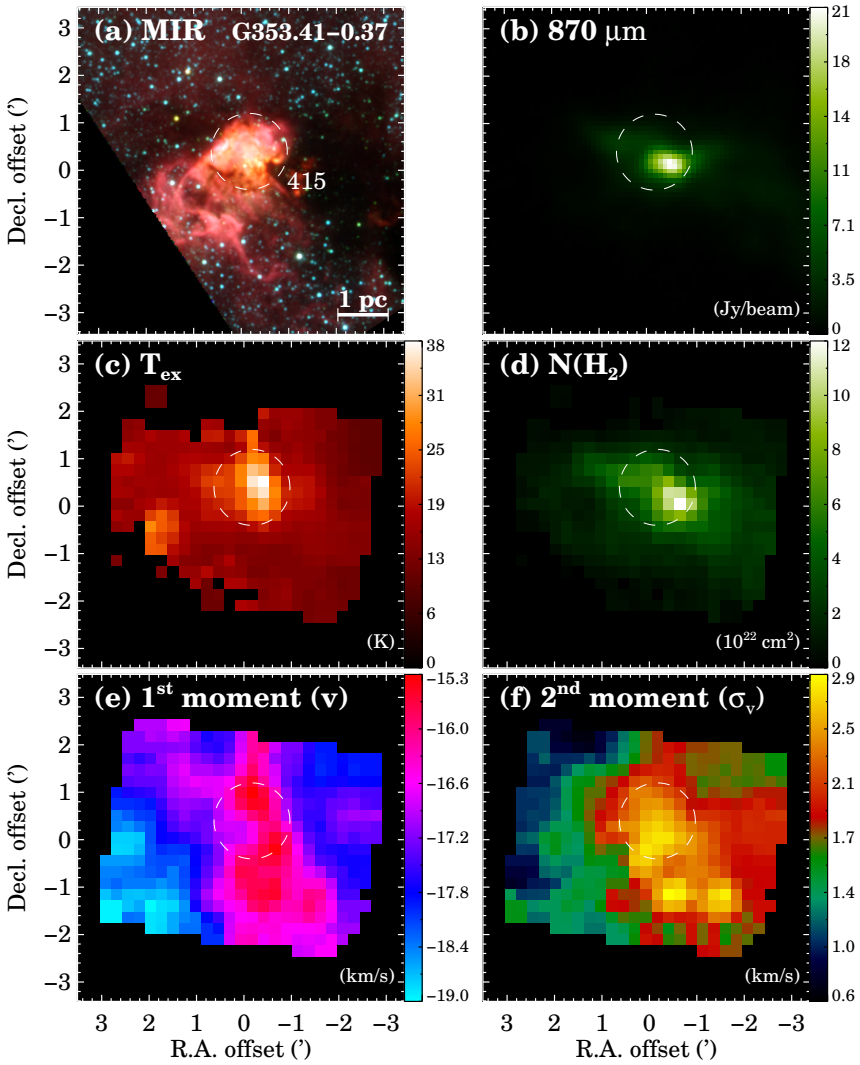

Figure 5.8: $^{13}CO(2-1)$ and $C^{18}O(2-1)$ analysis for G353.41−0.37. See caption of Fig. 5.2 for more details.

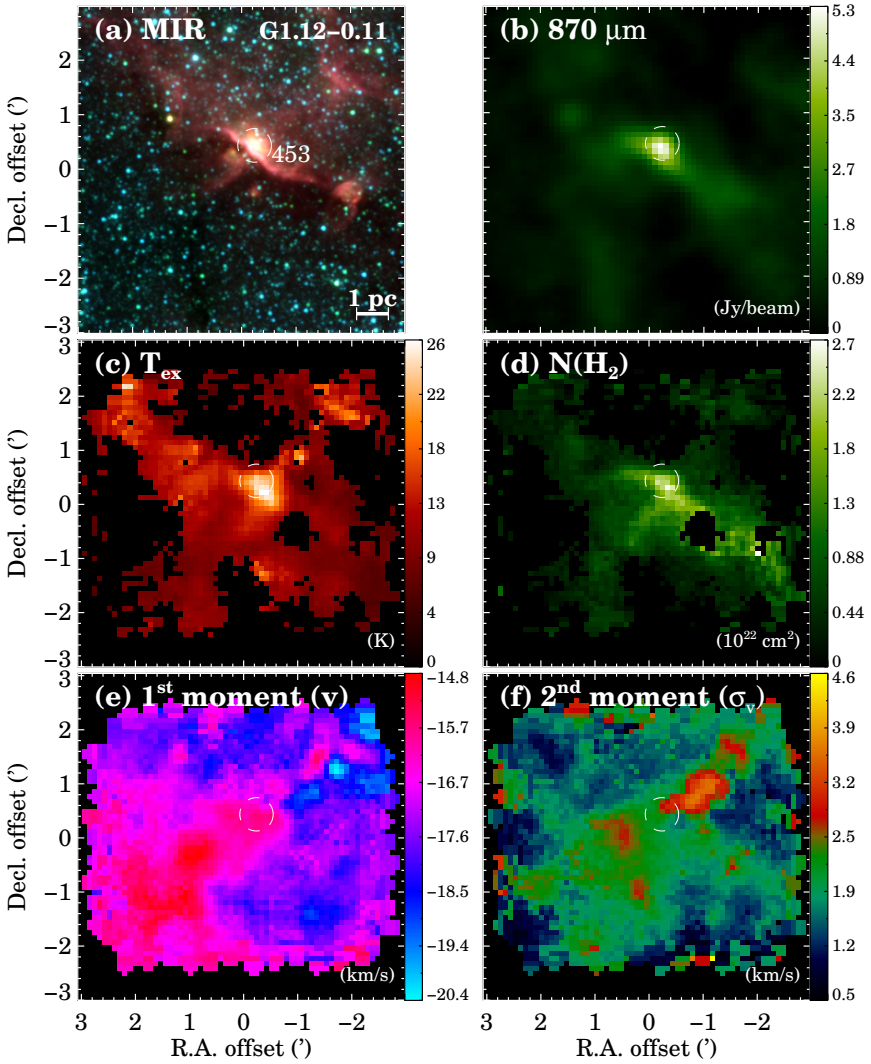

Figure 5.9: ^{13}CO(2−1) and C^{18}O(2−1) analysis for G1.12−0.11. See caption of Fig. 5.2 for more details.

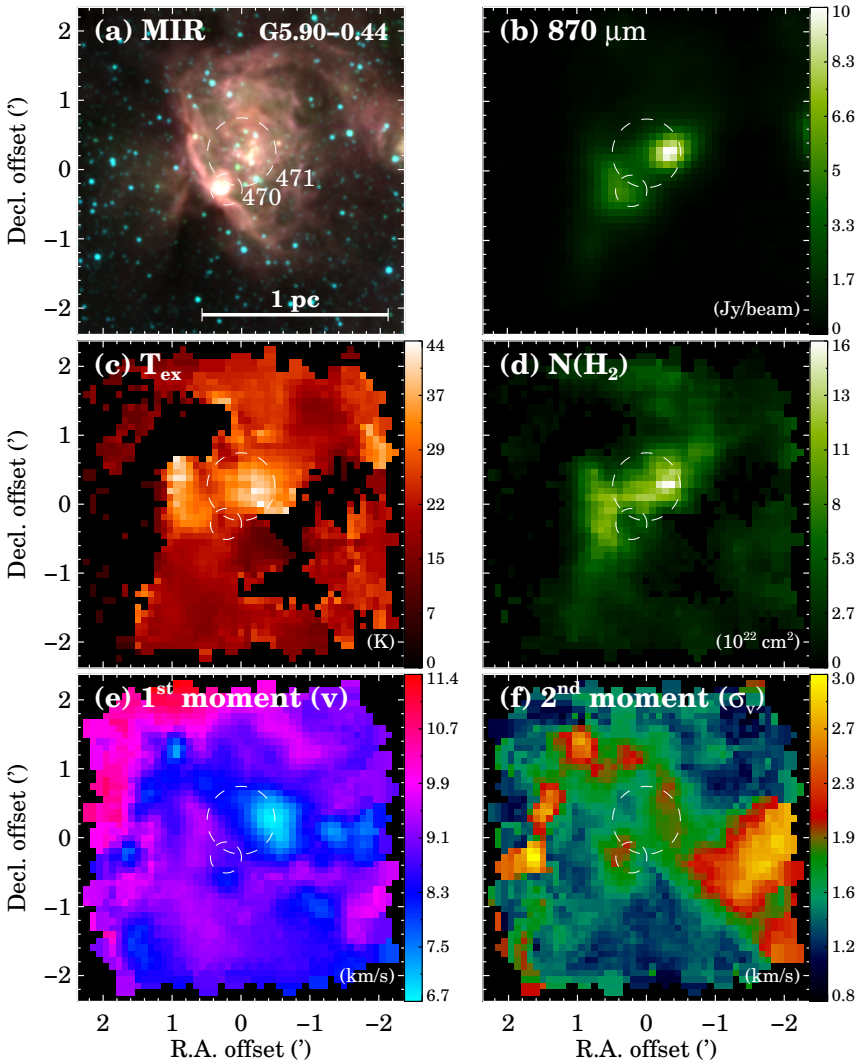

Figure 5.10: $^{13}CO(2-1)$ and $C^{18}O(2-1)$ analysis for G5.90−0.44. See caption of Fig. 5.2 for more details.

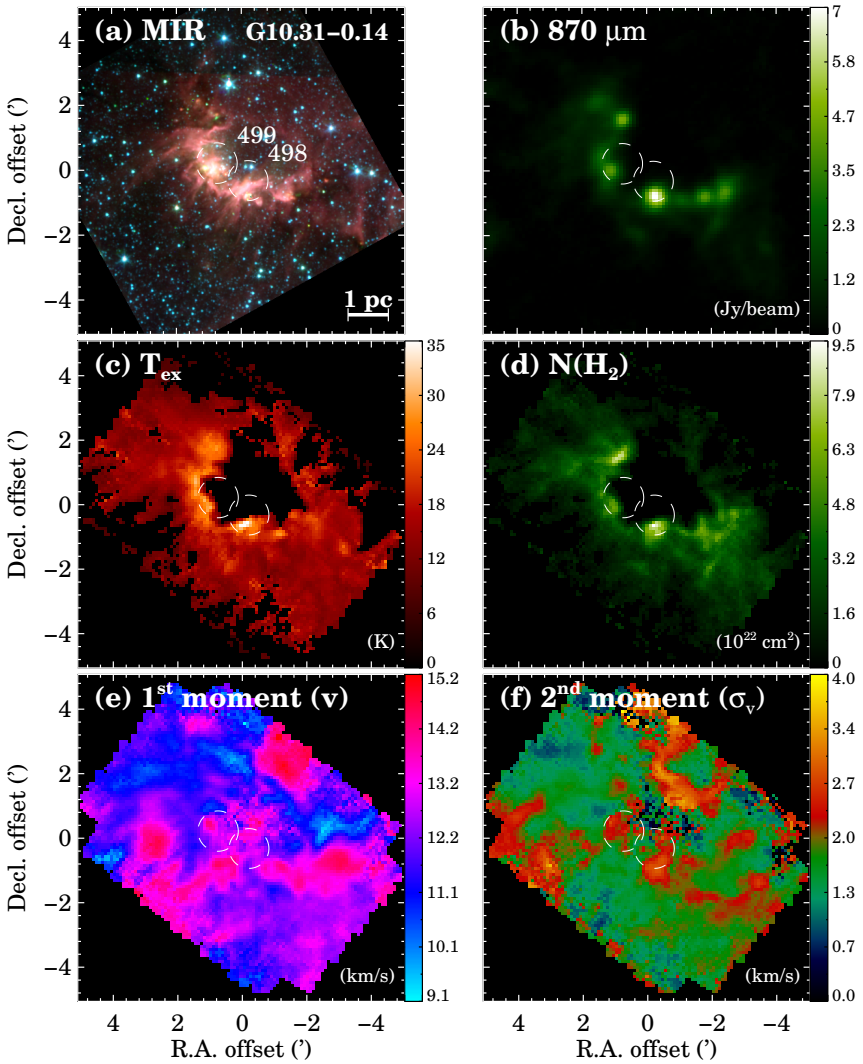

Figure 5.11: ^{13}CO(2−1) and C^{18}O(2−1) analysis for G10.31−0.14. See caption of Fig. 5.2 for more details.

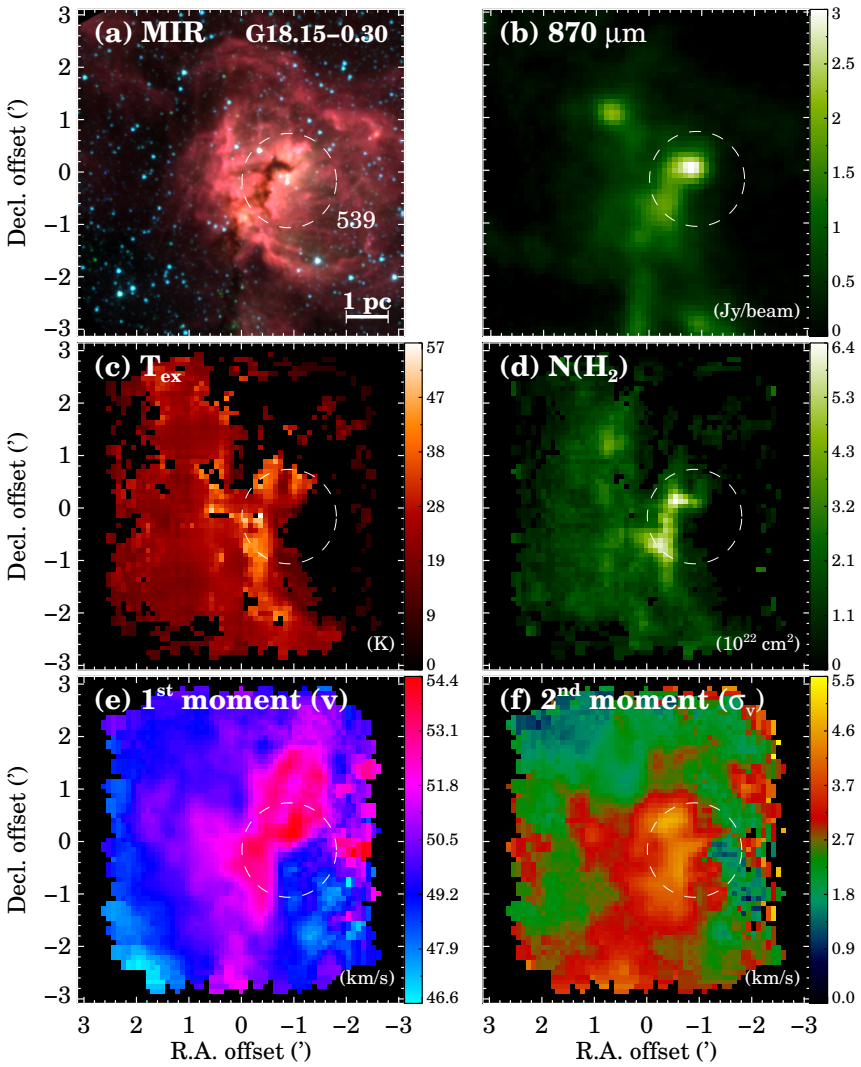

Figure 5.12: $^{13}CO(2-1)$ and $C^{18}O(2-1)$ analysis for G18.15−0.30. See caption of Fig. 5.2 for more details.

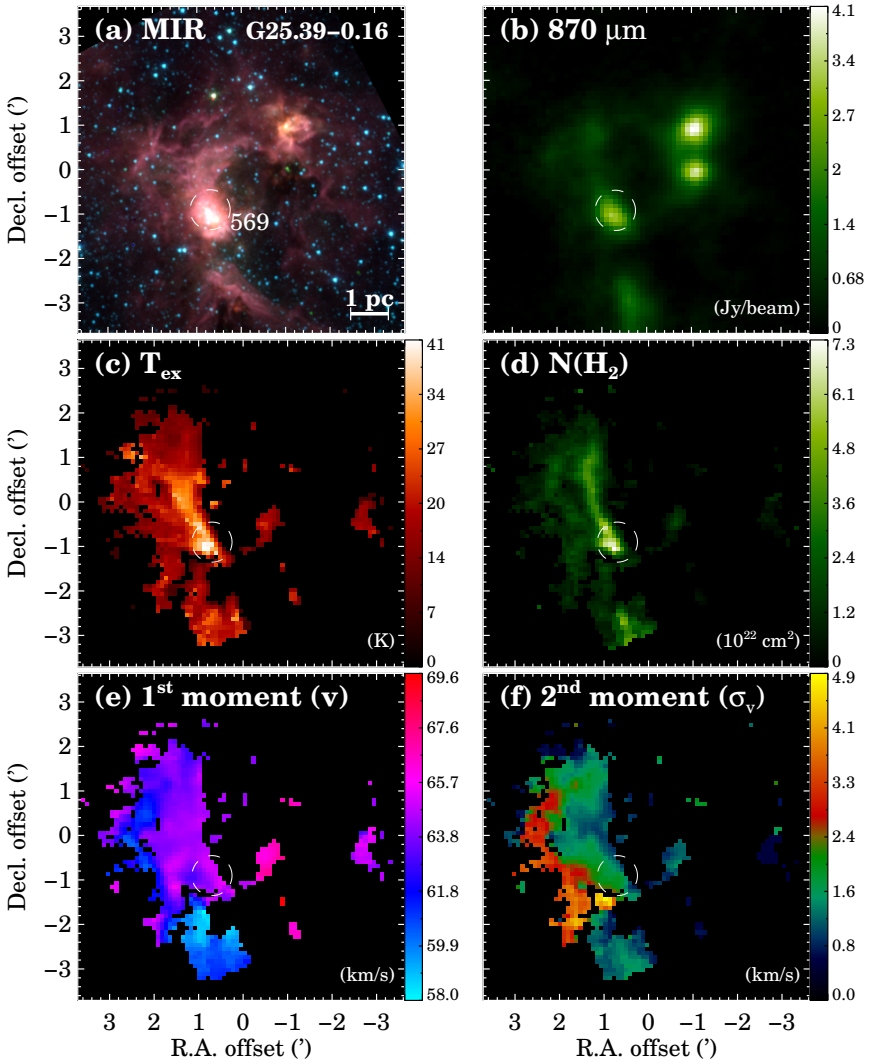

Figure 5.13: ^{13}CO(2−1) and C^{18}O(2−1) analysis for G25.39−0.16. See caption of Fig. 5.2 for more details.

5.3 The infrared bubble G10.31−0.14

At the time of our observations, the G10.31−0.14 bubble had been already mapped in molecular line emission but with relatively low angular resolution, of the order of 1′ (e.g., Kim & Koo 2002). The whole W31 complex has been recently observed in ^{13}CO(2−1) and C^{18}O(2−1) by Beuther et al. (2011) using the APEX telescope (resolution of $\sim 30''$). However, since our observations for G10.31−0.14 were carried out with the IRAM 30-m telescope, the molecular line maps presented here are so far the ones with the highest angular resolution ($\sim 12''$) for this particular region. Furthermore, our sensitivity is also considerably better (~ 0.15 K compared to 0.83 K in $T_{\rm A}^{*}$).

In the next subsection, we describe the region using data at different wavelengths. Then, we analyze the velocity field observed in our ^{13}CO(2−1) and C^{18}O(2−1) observations, including some simple expanding bubble models. Finally, some discussion is presented.

5.3.1 Description of the region

The infrared bubble G10.31−0.14 is a well known luminous H II region (usually referred to as G10.3−0.1) that has been recognized easily in Galactic radio continuum surveys, since several decades ago (e.g., Altenhoff et al. 1979). It belongs to the giant molecular cloud W31, one of the brightest H II region complexes in the inner Galaxy, which has been studied in detail by Kim & Koo (2002), and more recently by Beuther et al. (2011) using multiwavelength data. The distance of the W31 complex is quite debated in the literature, and the adopted value in these two studies is 6 kpc. However, in our cluster catalog (see § 4.1) we follow the arguments by Pandian et al. (2008) which support the location of the complex at ~ 3 kpc from the Sun, as derived by the spectrophotometric method in the near-infrared towards some individual stars of the associated young clusters. Recently, Moisés et al. (2011) has recomputed spectrophotometric distances of an important number of H II regions in the Galaxy, using compiled data from the literature and an homogeneous calibration which takes into account the uncertainties in spectral type determination and extinction law variations. Averaging the two H II regions in their sample that are part of W31, we obtain a distance of 2.8 ± 1.1 kpc for the whole complex. Pandian et al. (2008) proposed that the H II region [L89b] 10.617−00.384 is also part of the complex, and that a large peculiar motion would explain its radial velocity difference of about -15 km s^{-1} with respect to the rest of the complex. The W31 complex would therefore be composed of three main H II regions: G10.2−0.3, G10.3−0.1, and [L89b] 10.617−00.384, contain-

ing the stellar clusters [BDB2003] G010.16−00.36, [BDS2003] 112/113, and [BDB2003] G010.62-00.38, respectively. We remark that the computed kinematic distances of the associated ATLASGAL clumps in our cluster catalog (see 4.1.4) for G10.2−0.3 and G10.3−0.1 are consistent, within the uncertainties, with the adopted distance of 2.8 ± 1.1 kpc. Figure 5.14 presents the ATLASGAL image of the whole complex, and shows that all the three main H II regions contain a large amount of continuum dust radiation from the still existing parent molecular material which has not been (completely) dispersed yet.

We now focus in the G10.3−0.1 region, which we mapped in ^{13}CO(2−1) and C^{18}O(2−1). Figure 5.15 presents a multiwavelength view of the region. The panel (a) shows in the background a near-infrared three-color image obtained from the so far available data[4] of the UKIDSS Galactic Plane Survey (Lucas et al. 2008), which has a better angular resolution ($\sim 0.8''$) and sensitivity (magnitude limit of 18.3 in the K band) than 2MASS. It can be seen in the image that the infrared clusters [BDS2003] 112 & 113, originally identified by Bica et al. (2003b) on the 2MASS data, constitute actually an unique rich stellar cluster which covers an important fraction of the interior area of the bubble, close to its geometrical center but shifted towards the submm clumps 2 and 3 in the ring (labeled in panel (b)); the two 2MASS-identified clusters have indeed a "subcluster" flag in our cluster catalog (see § 4.1.6). The dust emission present in this kind of regions corresponds mainly to reprocessed stellar radiation which has been absorbed by the dust, either directly or after being processed in the nebula. Because this emission peaks in the far-infrared (FIR), an estimate of the true bolometric luminosity of the stellar population can be derived from observed FIR flux densities at a few different frequencies. Scaling the FIR luminosity determined by Ghosh et al. (1989) to our assumed distance, we obtain $L \simeq 1.3 \times 10^5\ L_\odot$, implying that the whole cluster is quite luminous and have enough ionizing feedback to produce the observed bubble. In fact, bright ionized gas emission in the radio continuum can be observed in the cluster vicinity (panel (d) of Figure 5.15), and a cluster member was identified spectroscopically by Bik et al. (2005) as an O star (panel (a)).

At mid-infrared wavelengths, the *Spitzer*-IRAC three-color image (Figure 5.15(b)) exhibits the typical ring structure at 8.0 μm, corresponding to UV-excited PAH emission on the inner surface of the swept-up molecular material, which is traced by ATLASGAL (contours) and the ^{13}CO(2−1) integrated emission (panel (c)). We will argue in the following Sections that the observed molecular structure is more consistent with being a ring inclined with respect

[4] We used the `colorImage` image extraction tool on the "Data Release 7", publicly available on `http://surveys.roe.ac.uk:8080/wsa/colourImage_form.jsp`.

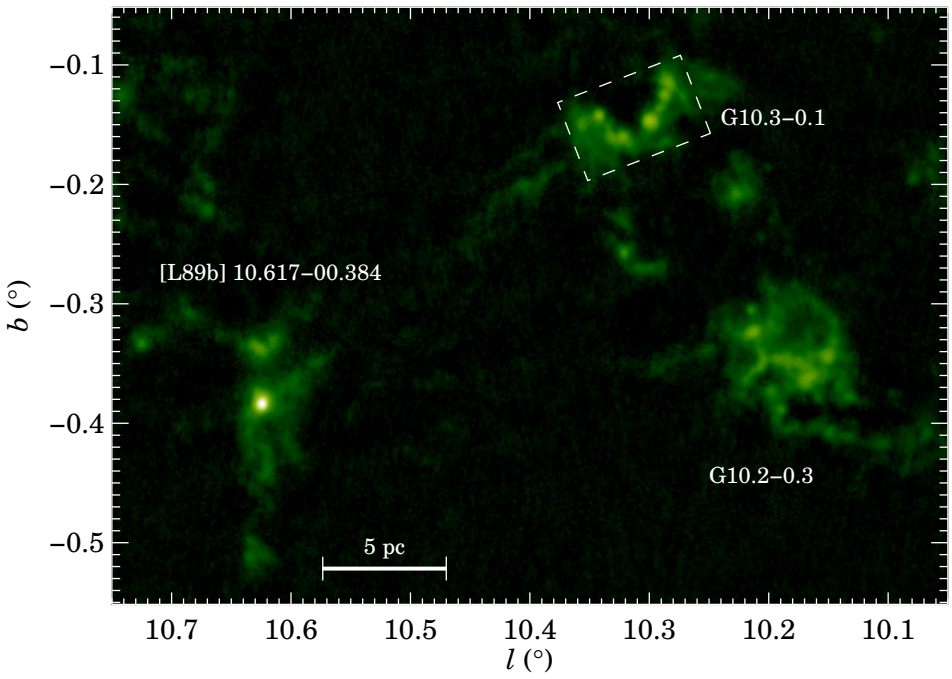

Figure 5.14: ATLASGAL image (870 μm) of the W31 complex in Galactic coordinates, displayed in inverse hyperbolic sine scale, from $-\sigma = -47$ mJy/beam to the maximum pixel value of 30.3 Jy/beam. Name labels indicate the locations of the three main H II regions that constitute the complex. The dashed-line box shows the region where we conducted ^{13}CO(2−1) and C^{18}O(2−1) mapping observations. The 5 pc scale-bar was estimated using the adopted distance of 2.8 kpc.

to the plane of the sky rather than a 3D shell seen in projection. Note that the molecular ring is asymmetrical, presenting a high intensity side to the south-east, which is bright at 8 μm and 870 μm, and an opposite fainter side that is barely seen at 8 μm and is not detected by ATLASGAL. The integrated ^{13}CO(2−1) map shows a good correspondence with the ATLASGAL emission, but it is able to trace the full molecular ring, including the fainter side. The molecular material is fragmented in at least 5 main clumps that can be easily recognized in the ATLASGAL emission and are labeled from 1 to 5 in panel (b). As already noted by Beuther et al. (2011), clumps $1-4$ are all associated with star formation signposts, such as 6.7-GHz methanol maser emission (Walsh et al. 1998), "extended green objects" at 4.5 μm (Cyganowski et al. 2008) towards clumps 1 and 4 indicating the possible presence of outflows (see Figure 5.15(b)), and an UC H II region in clump 3 (Wood & Churchwell 1989). Clump 5, on the other hand, is potentially still in a starless phase prior to any star formation activity, as it is completely quiescent at radio continuum and

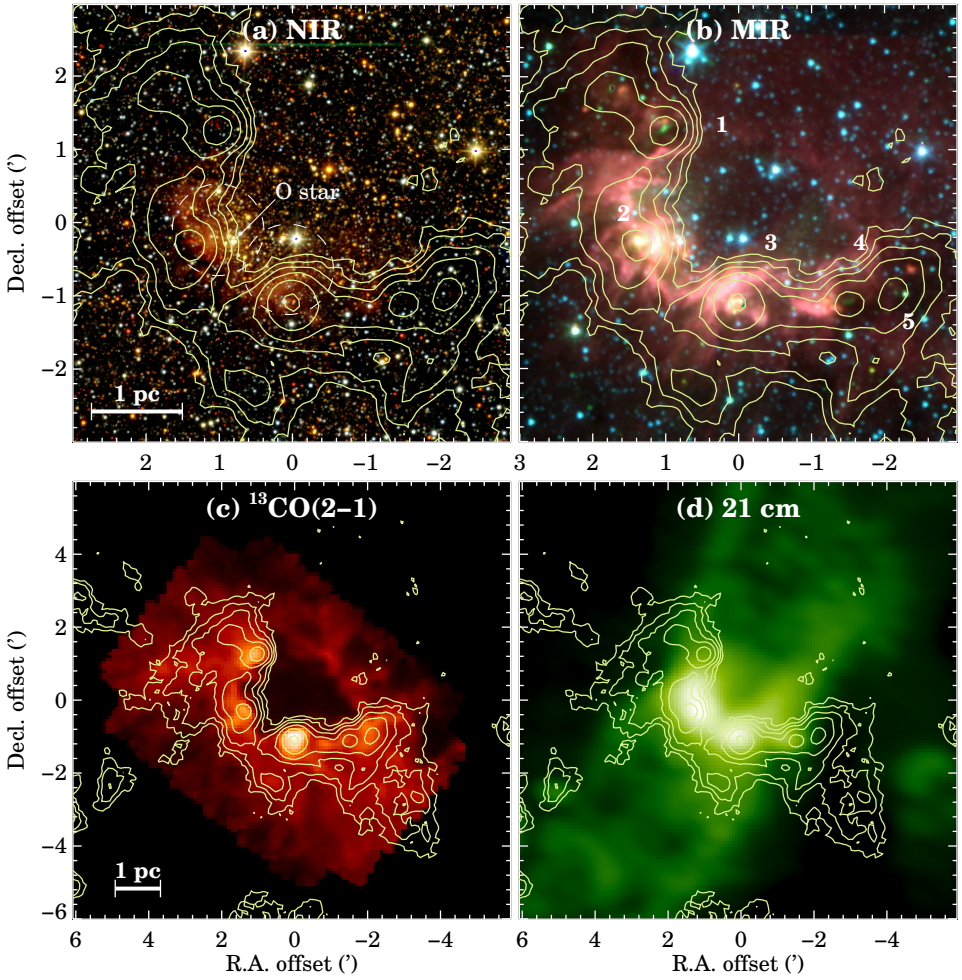

Figure 5.15: Multiwavelength view of the G10.31−0.14 bubble. In all panels, the overplotted contours correspond to ATLASGAL emission (870 μm), with contour levels $\{5, 9.4, 17, 32, 66, 140\} \times \sigma$, where $\sigma = 47$ mJy/beam is the local rms noise level. (a) UKIDSS three-color image constructed with the J (blue), H (green), and K (red) bands. The two dashed circles mark the infrared clusters [BDS2003] 112 & 113 (from west to east) identified by Bica et al. (2003b) using 2MASS images; the O star identified spectroscopically by Bik et al. (2005) is also indicated. (b) *Spitzer*-IRAC three-color image made with the 3.6 (blue), 4.5 (green) and 8.0 μm (red) bands. Numbers label the main submm clumps refereed to in the text. (c) ^{13}CO(2−1) integrated map in the velocity range $[7, 17]$ km s^{-1}, displayed in inverse hyperbolic sine scale, from 0 to 101 K km s^{-1}. (d) 21 cm radio continuum image from Kim & Koo (2002), shown in logarithmic scale from −1.2 mJy/beam to 1.4 Jy/beam. The 1 pc scale-bars are for the adopted distance of 2.8 kpc. The images are in equatorial coordinates, with offsets relative to the bubble center ($\alpha_{\rm J2000} = 18^{\rm h}08^{\rm m}55^{\rm s}.7$, $\delta_{\rm J2000} = -20°04'53''$).

24 μm emission (not shown here).

5.3.2 Kinematics

Similarly to the entire W31 complex (Beuther et al. 2011), our ^{13}CO(2−1) observations of the G10.3−0.1 region exhibit emission in various velocity ranges, as is shown in Figure 5.16, which presents the averaged ^{13}CO spectrum over the whole field of view of our map. In the ^{13}CO integrated map from 7 to 17 km s^{-1} (Figure 5.15(c)), we already noticed that the main velocity component clearly traces the ring structure of the bubble, which means that the systemic velocity of the source is about 12 km s^{-1}, if we adopt the peak of the integrated spectrum. This velocity is consistent with that assumed for the associated ATLASGAL clumps to compute the kinematic distances in our cluster catalog (12.8 km s^{-1} for [BDS2003] 112, and 12.0 km s^{-1} for [BDS2003] 113). The other velocity components in the G10.3−0.1 region could be either chance alignments of sources at different distances projected in the same field of view, or the result of large scale motions within the W31 complex (Beuther et al. 2011). Here we focus on the main component between $\sim$ 0 km s^{-1} and $\sim$ 29 km s^{-1}, decomposed in channel maps in Figure 5.17. It can be seen that the central $\sim$ 13 km s^{-1} around the peak trace the molecular ring, from $\sim$ 5 km s^{-1} to $\sim$ 18 km s^{-1}. The asymmetry of the profile of the main velocity component in this velocity range (Fig. 5.16) is probably caused by the higher excitation and/or density of the receding side of the molecular ring, which is closer to the stellar cluster (see below for more details about the geometry of the region). The asymmetry remains for even higher velocities, showing an excess of emission in the range $\sim [20, 30]$ km s^{-1}, but by examining the channel maps we found that this particular emission corresponds to fainter diffuse emission spread over a large area. This can be clearly understood by comparing the channel maps in the range $[0, 4]$ km s^{-1} with those in the range $[20, 24]$ km s^{-1}, symmetrically shifted from the velocity peak of $\sim$ 12 km s^{-1}; the first range has almost no extended emission, appearing darker. We found also that the submm clump 3 is prominent over a wide range in velocity, suggesting the presence of a molecular outflow, which indeed was detected previously by Kim & Koo (2002) using lower resolution molecular line data. Figure 5.18 shows the ^{13}CO(2−1) spectrum averaged over a circular area of 44″ (0.6 pc) radius, centered at the peak of clump 3; the observed profile exhibits the characteristic high-velocity wings of an outflow, with a full width of about 30 km s^{-1}.

To study more in detail the velocity field of the observed ring structure, we present in Figures 5.19 and 5.20, respectively, the ^{13}CO(2−1) and C^{18}O(2−1) channel maps in a more restricted velocity range, from 5 km s^{-1} to 20 km s^{-1}.

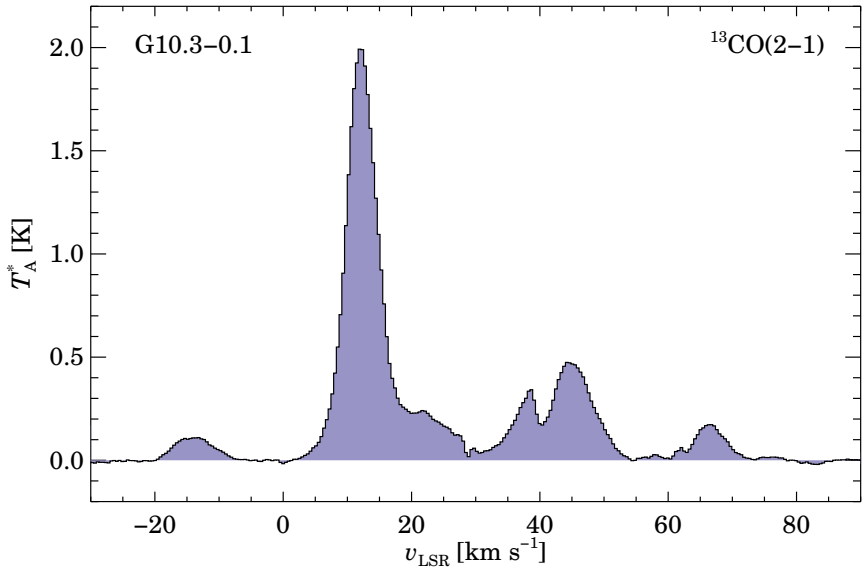

Figure 5.16: ^{13}CO(2−1) spectrum of the G10.31−0.14 bubble averaged over the whole field of view of our observations.

As can be seen in ^{13}CO, there is a clear velocity gradient along the minor axis of the observed ring, starting from the northwest, where low velocities trace the filamentary low intensity side of the ring, and moving towards the southeast, where higher velocities trace the clumpy high intensity side. Although less symmetrically with respect to the minor axis, the same kinematic behavior is observed in C^{18}O. The kinematics of the G10.31−0.14 bubble is therefore inconsistent with a completely spherical expansion, because in that case we would observe the ring structure (which would correspond to the 2D projection of a 3D shell) at roughly the same LSR velocity. The presence of a velocity gradient requires that the bubble is open on at least one side, which must also be inclined with respect to the plane of the sky in order to produce the gradient. In addition, the lack of emission towards the center suggests that the bubble is indeed open on two sides, one in the front and one in the back, since otherwise we would detect one of those faces at high velocities with respect to the ring (blueshifted for the front, and redshifted for the back), which is not observed. In other words, the most likely scenario for G10.31−0.14 is that the host molecular cloud is flat and inclined with respect to the plane of the sky, so that stellar feedback initially produced an expanding shell which eventually broke out of the cloud at the front and back sides, becoming a molecular ring. This situation was originally proposed by Beaumont & Williams (2010) for their sample of 43 IR bubbles, based on the lack of emission towards the

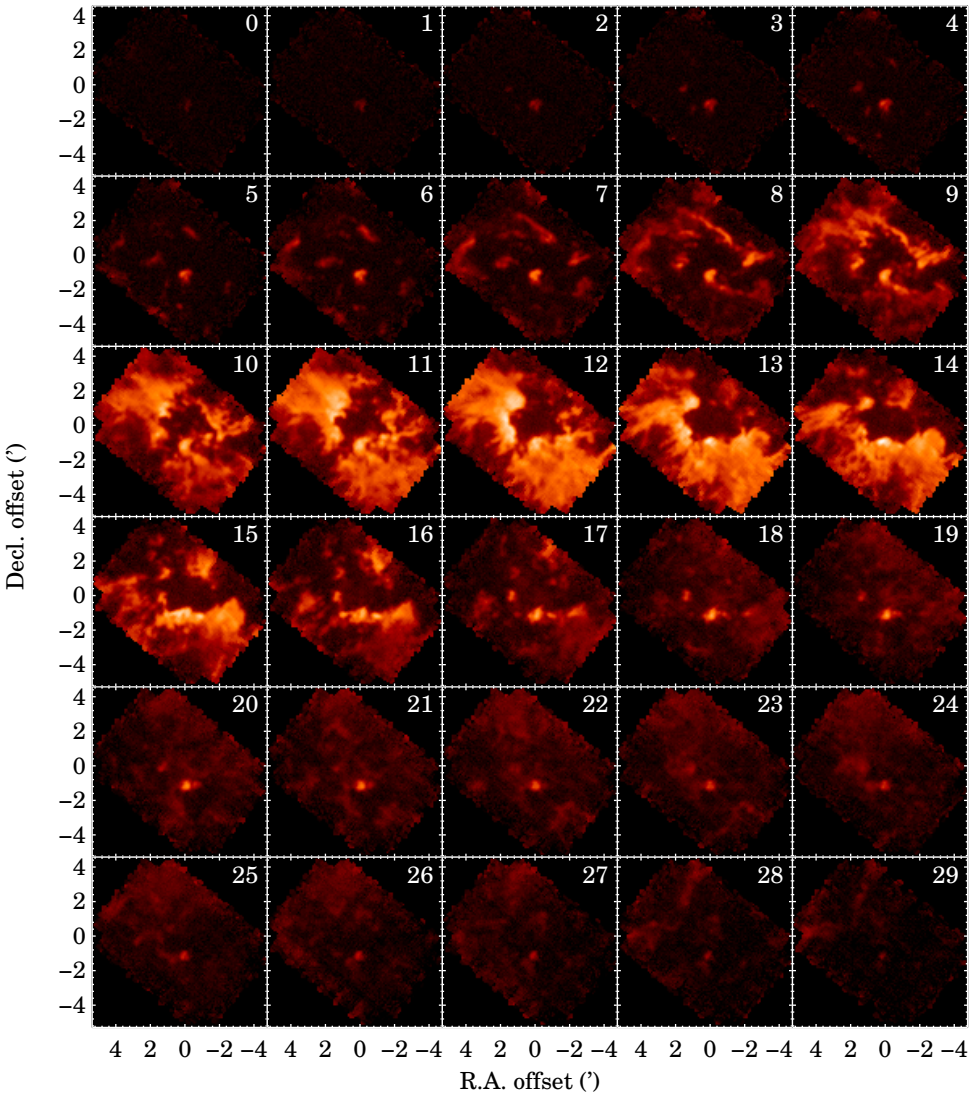

Figure 5.17: ^{13}CO(2−1) channel maps of G10.31−0.14, integrated over velocity intervals of 1 km s^{-1}. The central velocity of each bin is marked in the upper right corner of each panel, in km s^{-1}. The maps are displayed in inverse hyperbolic sine scale (in order to show more easily the faint diffuse emission), from −0.15 to 18.6 K in $T_{\rm A}^*$. The coordinate system is equatorial, with offsets relative to the bubble center ($\alpha_{\rm J2000} = 18^{\rm h}08^{\rm m}55^{\rm s}.7$, $\delta_{\rm J2000} = -20°04'53''$).

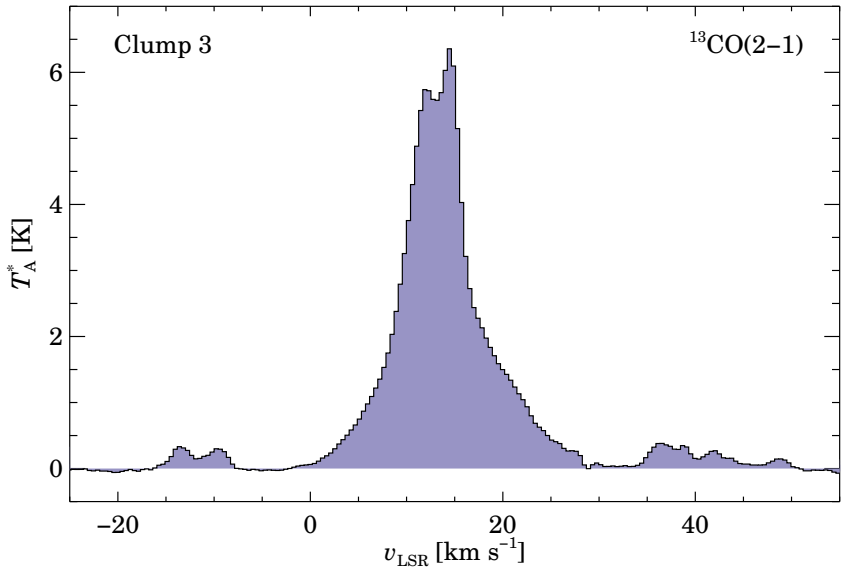

Figure 5.18: ^{13}CO(2−1) spectrum of the submm clump 3 in the G10.31−0.14 bubble, where a molecular outflow is found. The spectrum shown is the average over a circular area centered at the peak of the clump and with an angular radius of 44″.

center of the bubbles in their CO(3 − 2) maps.

In order to test this hypothesis, we constructed synthetic data cubes from simple geometrical models of expanding rings and bubbles, and compared with the observed velocity field of G10.31−0.14. We ignored opacity and excitation effects in this analysis, i.e., we simply superimposed all the velocity profiles along a given line of sight. While the assumption of constant excitation should be kept in mind when comparing relative intensities in the model, ignoring opacity effects is quite reasonable for sources with velocity gradients, where line emission from moving gas at a certain velocity is not affected by gas located in front on the line of sight, if its velocity is different enough. Further, as mentioned before, ^{13}CO and specially C^{18}O are much less optically thick than the main isotope ^{12}CO. The simple geometrical models described below are therefore appropriate to study the observed velocity field.

The configuration of the model is shown in Figure 5.21, in the plane perpendicular to the plane of the sky and to the planes defining the host molecular cloud's edges. The coordinate system is defined such that the bubble center is in the origin, the line of sight of the observer is in the z-direction, and thus the x-y plane corresponds to the plane of the sky. We have created a ring structure in 3D space by intersecting a full bubble, of inner and outer radii $r_{\rm in}$ and $r_{\rm out}$, with two parallel planes Π_1 and Π_2 which define the edges of the flat molecular

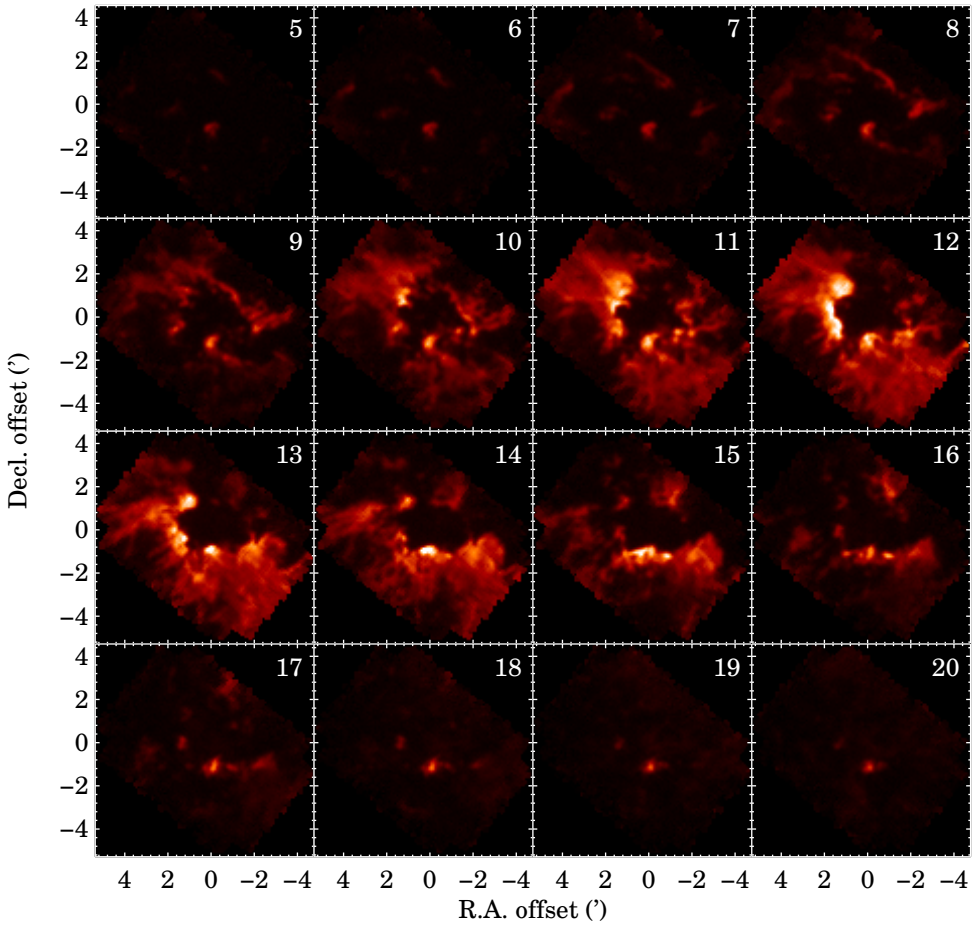

Figure 5.19: ^{13}CO(2−1) channel maps of G10.31−0.14, integrated over velocity intervals of 1 km s^{-1}. The central velocity of each bin is marked in the upper right corner of each panel, in km s^{-1}. The maps are displayed in linear scale from −0.3 to 13 K in $T_{\rm A}^*$. The coordinate system is the same as in Fig. 5.17.

cloud where the ring resides. The planes are separated from the origin by a distance of $s_1 \times r_{\rm in}$ and $s_2 \times r_{\rm in}$, respectively, and are inclined by an angle ψ with respect to the plane of the sky. Note that the inclination is needed to generate the velocity gradient, but also to reproduce the elliptical shape of the ring when projected on the plane of the sky. In our coordinate system, the x-axis is parallel to the minor axis, i.e., from southeast to northwest in G10.31−0.14. The parameters of the geometrical model allow us to also construct bubbles that are open only on one side (half-shells), by just setting s_1 or s_2 to a value larger than $r_{\rm out}/r_{\rm in}$.

The ring is assumed to be expanding at a constant velocity v_0, in a isotropic turbulent field characterized by a Gaussian with a FWHM of Δv (per spatial

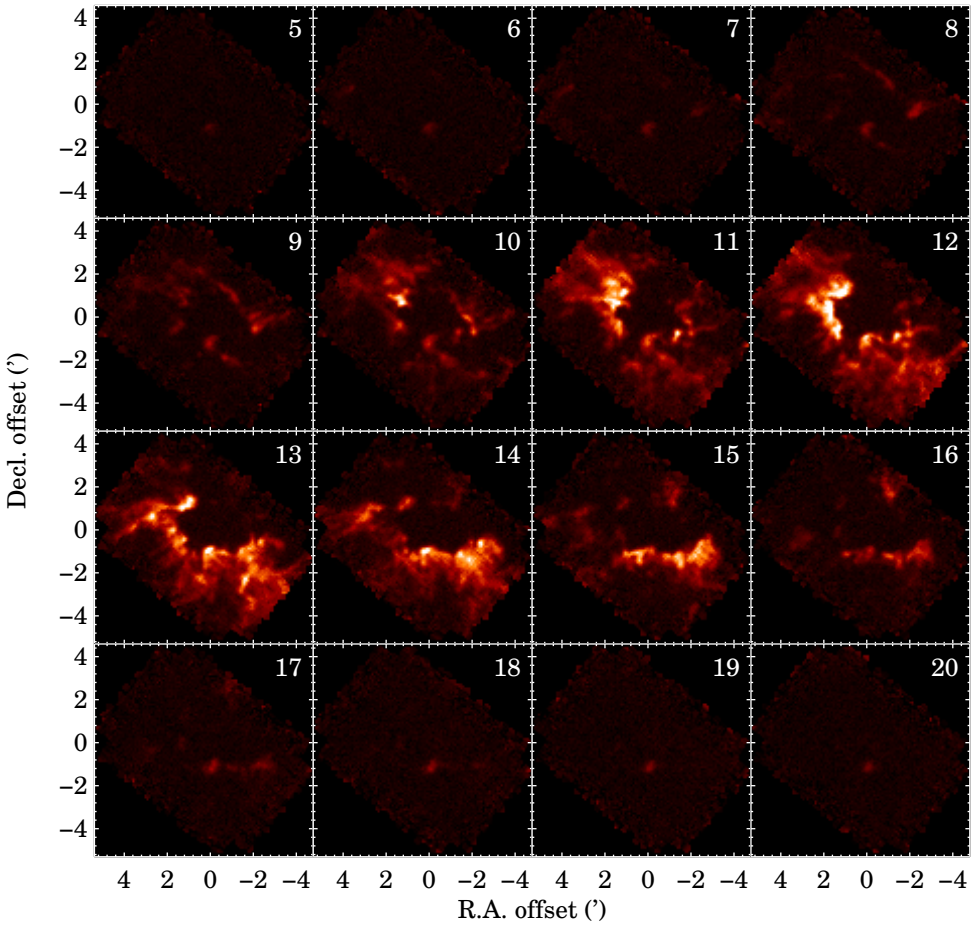

Figure 5.20: $C^{18}O(2-1)$ channel maps of G10.31−0.14, displayed in linear scale from −0.3 to 5 K in T_A^*. See caption of Fig. 5.19 for more details.

direction). Assuming also a constant density $n(x, y, z) = n_0 \neq 0$ within the ring, zero density everywhere else, constant excitation, and optically thin emission, it can be shown that the observed intensity $I(x, y, v)$, for a certain line of sight (x, y) and LSR velocity v, is (in arbitrary units)

$$I(x,y,v) = \int_{n(x,y,z)\neq 0} \exp\left(-\frac{4\ln 2}{\Delta v^2}\left[v_{\rm sys} + \frac{v_0\, z}{\sqrt{x^2+y^2+z^2}} - v \right]^2 \right) {\rm d}z \ , \quad (5.6)$$

where $v_{\rm sys}$ is the systemic velocity of the source. A specific model is defined by the set of parameters $\{s_1, s_2, \psi\}$ which indicate the integration domain in Equation (5.6), and the parameters $\{v_0, \Delta v\}$ that determine the velocity field. We then calculated the synthetic $I(x, y, v)$ cube by constructing a grid in the (x, y, v) space and integrating Eq. (5.6) numerically for every voxel. We

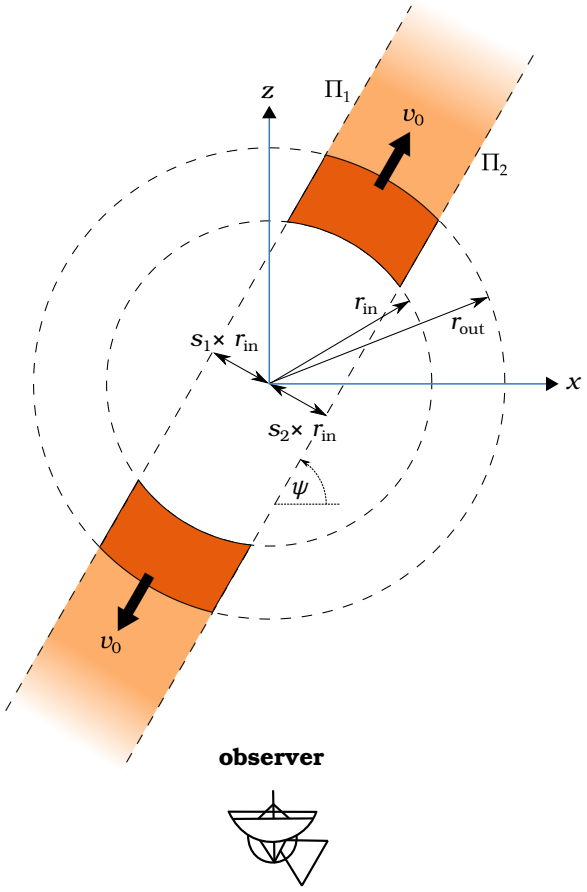

Figure 5.21: Schematic description of the expanding ring geometrical model (see the text for the definition of the parameters).

used $r_{\rm in} = 1.7'$ (1.4 pc) and $r_{\rm out} = 2.5'$ (2.0 pc), as measured approximately along the major axis of G10.31−0.14 on images at different wavelengths (see Fig. 5.15), and $v_{\rm sys} = 12$ km s^{-1}, corresponding to the peak of the observed averaged spectrum.

We first tested the possibility that the G10.31−0.14 bubble is open on one side only, so either the back or the front face of the shell remains. Figures 5.22 and 5.23 present the corresponding channel maps for the model without the back face (parameters $\{s_1, s_2, \psi\} = \{0.1, 2.0, 60°\}$), and the one without the front face ($\{s_1, s_2, \psi\} = \{2.0, 0.1, 60°\}$), respectively. The angle $\psi = 60°$ was chosen based on the approximate eccentricity of the observed ring, and we have used the best velocity combination from the ring-like model described below ($\{v_0, \Delta v\} = \{3.2, 4.2\}$ km s^{-1}). The overall velocity structure of the shell model without the back face (Fig. 5.22) matches quite well the channel

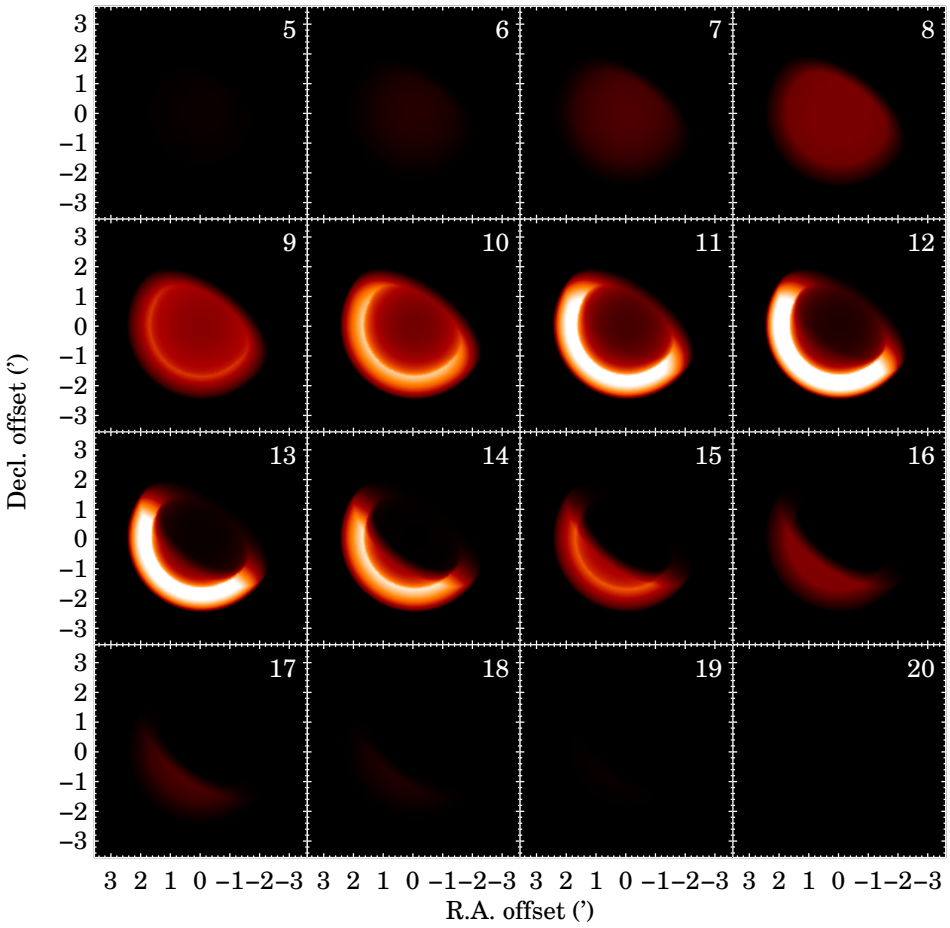

Figure 5.22: Channel maps of expanding shell model with the back face missing, corresponding to parameters $\{s_1, s_2, \psi\} = \{0.1, 2.0, 60°\}$, and $\{v_0, \Delta v\} = \{3.2, 4.2\}$ km s^{-1}. The shown velocity intervals are the same as for the real maps (Fig. 5.19 and 5.20). The images are shown in linear scale from 0.0 to 0.8 times the maximum intensity in the whole cube. The coordinate system is equatorial, with offsets relative to the bubble center. Note that we have rotated the x-y coordinate system of the model by an angle of 36° to resemble the orientation of the observed ring.

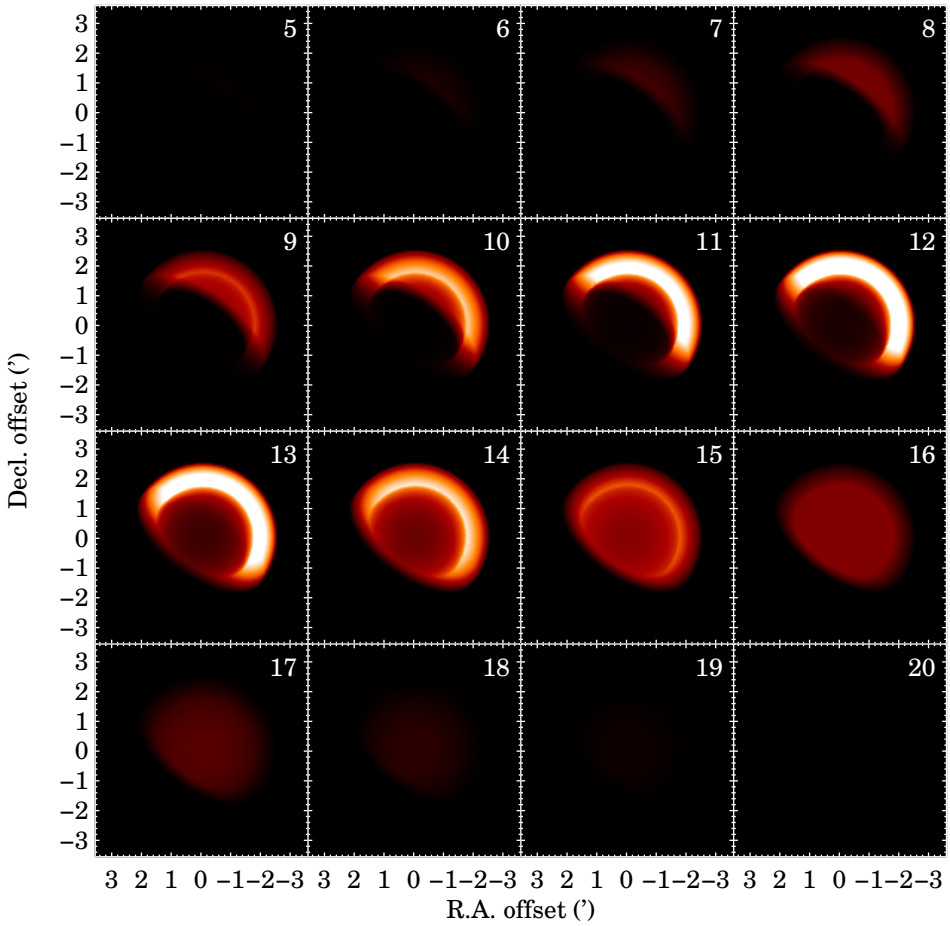

Figure 5.23: Channel maps of expanding shell model with the front face missing, corresponding to parameters $\{s_1, s_2, \psi\} = \{2.0, 0.1, 60^\circ\}$, and $\{v_0, \Delta v\} = \{3.2, 4.2\}$ km s^{-1}. See caption of Fig. 5.22 for more details.

maps of the real observations for velocities $\gtrsim 10$ km s^{-1}. Even the difference in intensity between the northwest side and the southeast side of the observed ring is well reproduced (qualitatively); this is the result of the geometry of this particular model, in which the receding side of the bubble has a higher column of material, and therefore, higher line intensity for constant excitation and optically thin emission. However, since the front face of the shell remains, there is a considerable excess of emission at the center of the bubble at blueshifted velocities ($v \lesssim 9$ km s^{-1}), which is not observed at all in the real map. An analogous situation occurs for the shell model without the front face (Fig. 5.23), with an excess of emission towards the center at redshifted velocities ($v \gtrsim 15$ km s^{-1}), which is hard to account for in the real observations by the very faint diffuse central emission at $\sim 18 - 19$ km s^{-1} (see

Fig. 5.19). We note that the central emission for the expanding shell models tested above has a brightness of more than 25% of the maximum value and is distributed quite uniformly throughout the whole bubble interior. The observed ring structure has a typical brightness of $T_{\rm A}^{*} \simeq 10$ K in ^{13}CO(2−1), which means that we would observe emission of the order of 2.5 K at the center of the bubble, far above the noise level. We indeed observe emission above the noise level at the bubble center, but considerable fainter (~ 1 K) and without the velocity structure required by the shell models. As remarked before, there is diffuse emission throughout the whole region at redshifted velocities, up to ~ 30 km s^{-1}, which likely correspond to lower density gas, probably also part of the W31 complex, projected on the same line of sight of the molecular cloud containing the G10.31−0.14 bubble.

In order to get rid of the excess of emission towards the center, we took the shell model without the back face (which matched better the observations than the opposite case) and removed a part of the front face also by setting $s_2 = 0.8$, creating then a ring-like structure in 3D space. To really remove a frontal section of the shell instead of a lateral one, we were forced to change also the inclination angle to $\psi = 45°$, which unavoidably translates into a lower projected eccentricity than the observed. The resulting velocity structure (Figure 5.24) is, however, very similar to that of the real observations, and although the approaching side of the ring appears wider in the model, the excess of central emission has gone. If we want to keep both the observed eccentricity and the lack of emission towards the center of the bubble, we necessarily have to place the edges of the host molecular cloud symmetrically with respect to the origin. Figure 5.25 shows the outcome of the ring model with parameters $\{s_1, s_2, \psi\} = \{0.4, 0.4, 60°\}$, where we recover again the observed velocity field, but the emission along the gradient is completely symmetrical for the receding and approaching sides, as expected from the geometry. Recall, however, that in the model we have assumed constant density and excitation within the ring. As discussed in § 5.3.3, the higher excitation and possibly higher density of the receding side can explain its higher line intensity.

For the ring-like model with parameters $\{s_1, s_2, \psi\} = \{0.4, 0.4, 60°\}$, we tested various combinations for the values of the expansion velocity, v_0, and the velocity width of the uniform local profile, Δv. These parameters were varied under the restriction $v_0 + \Delta v \simeq 7.5$ km s^{-1}, in order to reproduce the observed differences in the velocity gradient. We found that $v_0 \simeq 3$ km s^{-1}, and that Δv is of the same order but slightly higher, $\Delta v \simeq 4$ km s^{-1}. The uncertainties are estimated to be about 1 km s^{-1}. Higher expansion velocities (for which we were forced to reduce Δv) resulted in a velocity gradient too steep across the plane of the sky, and lower expansion velocities (for which we

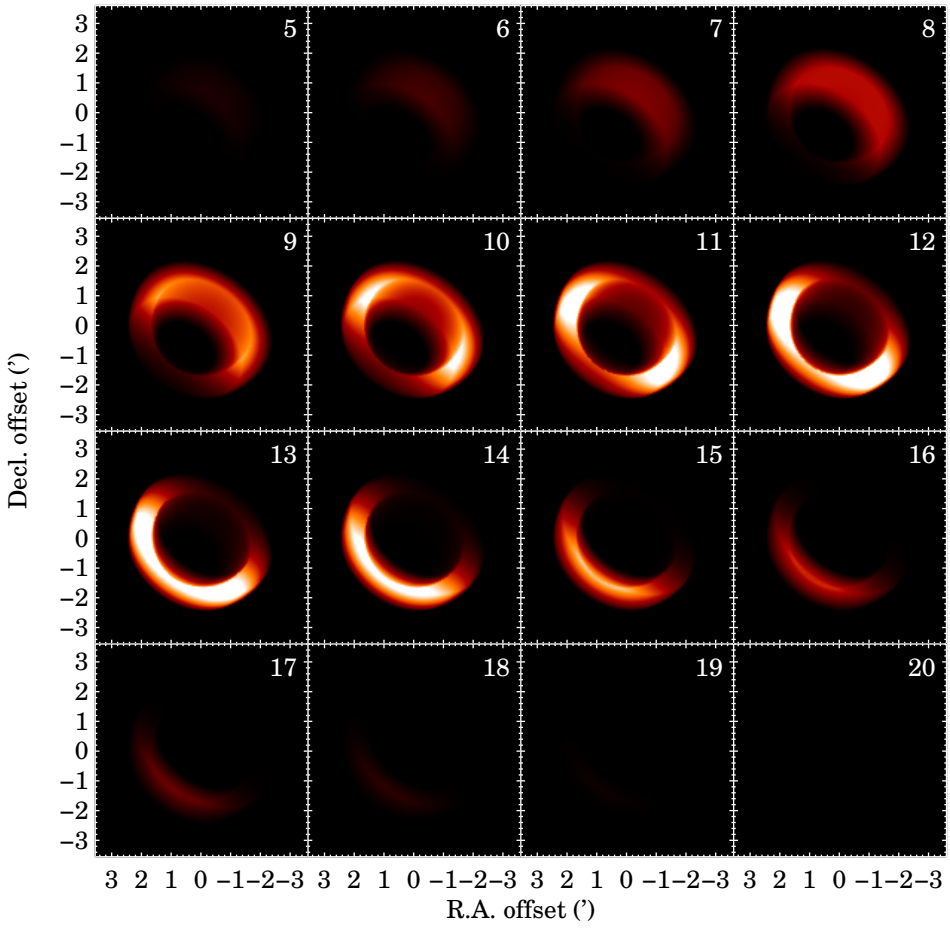

Figure 5.24: Channel maps of expanding ring model with parameters $\{s_1, s_2, \psi\} = \{0.1, 0.8, 45°\}$ (asymmetrical case), and $\{v_0, \Delta v\} = \{3.5, 4.5\}$ km s^{-1} (we have slightly increased the velocities to compensate for the lower inclination angle). See caption of Fig. 5.22 for more details.

had to increase Δv) produced more static rings, with a velocity gradient too smooth compared to that observed.

5.3.3 Discussion

The comparison of the observed velocity field with the simple geometrical models presented in the previous Section indicate that G10.31−0.14 is more likely a molecular ring inclined with respect to the plane of the sky, rather than a 3D shell seen in projection, and therefore, the host molecular cloud would be a flat structure with a width of the order of 1 pc. Additional empirical evidence for this scenario comes from the ionized gas radio continuum emission

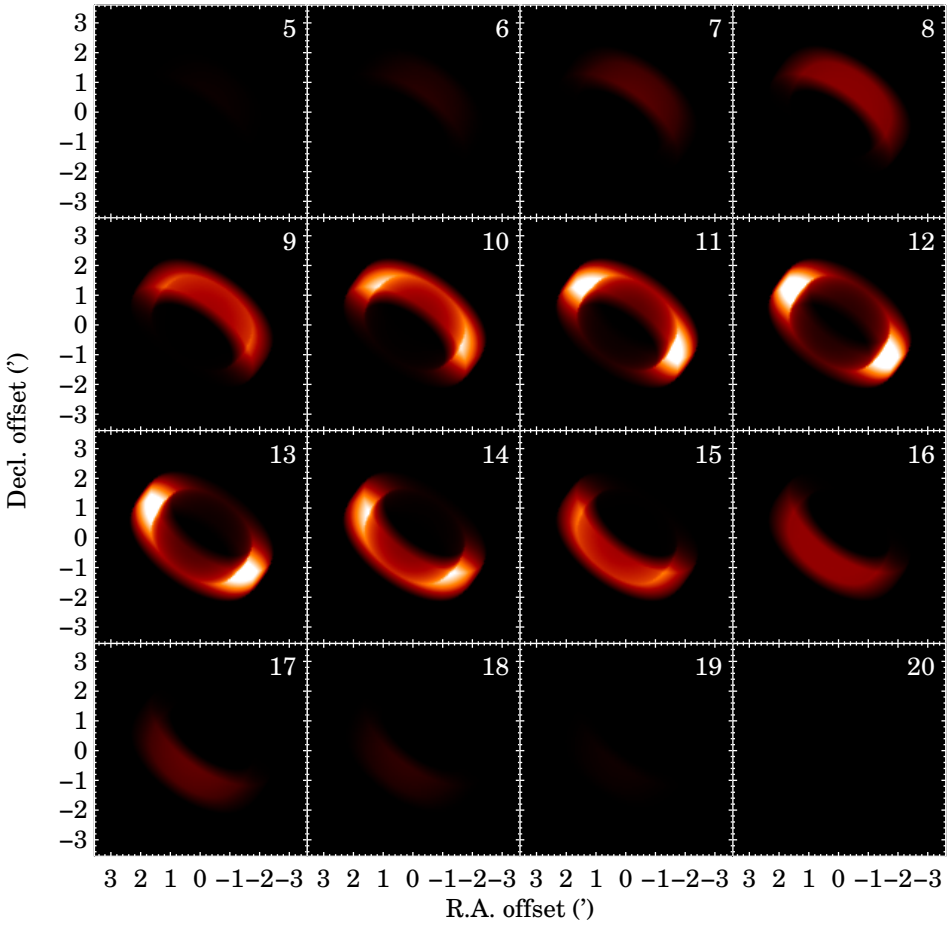

Figure 5.25: Channel maps of expanding ring model with parameters $\{s_1, s_2, \psi\} = \{0.4, 0.4, 60°\}$ (symmetrical case), and $\{v_0, \Delta v\} = \{3.2, 4.2\}$ km s^{-1}. See caption of Fig. 5.22 for more details.

observed by Kim & Koo (2002), shown in panel (d) of Figure 5.15[5]. As already noted in the original paper, the bipolar morphology of the extended radio continuum emission could be the result of an ionized champagne flow produced when an initially confined H II region broke out of the host molecular cloud at the two flat boundaries. The ionized flow would be perpendicular to the plane of the cloud, i.e., to the planes Π_1 and Π_2 in our schematic representation in Fig. 5.21. The large scale distribution of the molecular gas is indeed elongated in the direction orthogonal to the bipolar axis (see Fig. 9 of Kim & Koo 2002), supporting this picture. However, the few positions with available ionized gas velocities from radio recombination line (RRL) observations by Kim & Koo (2002) do not reveal the champagne flow. The explanation provided by these authors is that the bipolar flow has probably a low inclination angle, or equivalently, the molecular cloud hosting the ring would have a high inclination angle. While this is consistent with the geometry proposed by us (see previous Section), we think that the low resolution of the RRL observations (about 1 arcminute) could be also affecting the measured velocities. A high-resolution RRL map would be ideal to test this hypothesis.

As already warned before, our geometrical models constructed to study the observed kinematics of the molecular gas do not consider possible differences in excitation and density throughout the molecular cloud. We note that the side of the molecular ring that is closer to the exciting massive cluster has indeed a higher excitation temperature and column density than the opposite side (see Fig. 5.11(c) and (d)). In the symmetrical geometrical model (Fig. 5.22), since the line-of-sight path length through the shell is the same for the receding and approaching sides, a higher column density translates directly into a higher volume density. This could have been caused by a volume density gradient in the original cloud, which at the same time would explain why the stellar cluster is having more troubles in pushing away the receding side compared to the approaching side. In an uniform medium, there would not be a side of the ring that is relatively closer to the exciting cluster. In summary, the higher line intensity of the receding side is likely the result of its higher density, inherited from the original cloud, and higher excitation, produced by its proximity to the stellar cluster.

Concerning star formation, the fragmentation of the molecular material swept up by the massive stellar cluster and the presence of star formation activity within the formed clumps (see § 5.3.1) might be the result of a triggering process, particularly the "collect and collapse" model might be taking place here (Elmegreen & Lada 1977), in which fragmentation follows the accu-

[5]These observations were made public by Beuther et al. (2011).

mulation of cold gas around the H II region. Nevertheless, we cannot rule out the scenario in which the clumps are the result of the initial substructure of the molecular cloud and would have formed and collapsed anyway without the presence of feedback (see § 2.2.3). Beuther et al. (2011) claim that each one of the submm clumps will likely form a stellar cluster by its own. We note, however, that the involved spatial scales are comparable to, e.g., those in the simulations by Bonnell et al. (2011, see § 2.1.1), so that the formed clusters will likely merge resulting in a very few or an unique massive cluster.

6
Conclusions

Given that star formation takes place in dense clumps of giant molecular clouds, stars are born correlated in space and time, constituting young stellar agglomerates known as embedded clusters. The study of these objects is essential to understand the different processes which lead to the production of the field stars, and in some cases, of bound open clusters, as well as the mechanisms of interaction of these young stars with their parent molecular material. In this thesis, we studied systematically all embedded clusters and open clusters known so far in the inner Galactic plane, taking particular advantage of the improved cluster sample over the last decade and the ATLASGAL submm continuum survey, which traces dense molecular gas, together with dedicated CO map observations for a subsample of 14 clusters. The main results and conclusions presented in this thesis are summarized as follows.

1. We compiled a merged full-sky list of 3904 embedded and open clusters in the Galaxy, collected from several optical and infrared cluster catalogs in the literature, dealing properly with cross-identifications. We argued that $\sim 50\%$ of the open clusters not confirmed yet by follow-up studies are spurious detections originated by crowding of unrelated stars projected on the line of sight (due to, e.g., localized low extinction in the IR). On the other hand, we expect minimal contamination by spurious detections in the embedded cluster sample, under the definition of embedded cluster used in this work.

2. As part of the above compilation, we performed our own search for embedded clusters on the mid-infrared GLIMPSE survey, complementing the catalog of 92 exposed and less-embedded clusters detected by Mercer et al. (2005) on the same data. Our method consisted basically on visual inspection of three-color images around positions previously selected as potential YSO overdensities. The initial positions correspond to enhancements on a stellar density map constructed with all GLIMPSE catalog sources satisfying a red color criterion: $[4.5]-[8.0] \geq 1$, following Robitaille et al. (2008). With this technique, we found 71 new embedded clusters.

3. The sample of 695 embedded and open clusters within the ATLASGAL Galactic range ($|l| \leq 60°$ and $|b| \leq 1.5°$) was studied in more detail, particularly regarding the correlation with submm emission. We constructed a big catalog with all the relevant information of these objects, including: the characteristics of the submm and mid-infrared emission; correlation with IRDCs, IR bubbles, and H II regions; distances (kinematic and/or stellar) and ages; and membership in big molecular complexes.

4. Based on the morphology of the submm emission and, for exposed clusters, on the agreement of the clump kinematic distances and cluster stellar distances, we defined an evolutionary sequence with decreasing correlation with ATLASGAL emission: deeply embedded clusters (EC1), partially embedded clusters (EC2), emerging exposed clusters (OC0), totally exposed clusters still physically associated with molecular gas in their surrounding neighborhood (OC1), and all the remaining exposed clusters, with no correlation with ATLASGAL emission (OC2).

5. The morphological evolutionary sequence correlates well with other observational indicators of evolution. In particular, we found that IR bubbles/PAH emission and H II regions are both equivalently important in the first four stages of the evolutionary sequence, suggesting that ionization is one of the main feedback mechanisms in our cluster sample. IRDCs are significant mostly in the first type (EC1), tracing a very early phase prior to the stage in which the embedded cluster starts to "illuminate" the host molecular clump while still embedded (EC1 clusters with PAH emission). The presence of big complexes containing several clusters is, again, relevant in the first four morphological types, which is consistent with the fact that star formation occurs in giant molecular clouds, and that older open clusters (OC2) are just the bound survivors of a very complex process of merging and dissolution of young agglomerates.

6. We defined observationally and embedded cluster (EC) as any cluster with morphological types EC1 or EC2; open clusters (OC) were defined as all the remaining types, OC0, OC1, and OC2, but were required to be confirmed by follow-up studies, in order to minimize the contamination by spurious candidates. We found that our observational definition of open cluster agrees with the physical one (a bound exposed cluster, referred to in this work as a *physical open cluster*) for ages greater than $\sim$ 16 Myr. In our sample, some OCs younger than this limit can be actually unbound associations.

7. By fitting the observed heliocentric distance distribution for open and embedded clusters within the ATLASGAL range, we found that our OC and EC samples are roughly complete up to a distance of $\sim$ 1 kpc and $\sim$ 1.8 kpc, respectively. Beyond these limits, the completeness of the OC and EC samples decay exponentially with scale lengths of $\sim$ 0.7 kpc and $\sim$ 1.8 kpc, respectively. We argued that ECs probe deeper the inner Galactic plane than OCs because, at infrared wavelengths, ECs can be more easily distinguished from the field population than OCs. On the other hand, a very distant embedded cluster is hardly detected due to the combined effect of extinction, the faint apparent brightness of its low-mass population and confusion of its members.

8. From a subsample of 23 embedded clusters with available age estimates, we derived an upper limit of 3 Myr for the duration of the embedded phase. The much higher number of open clusters with available age estimates allowed us to study the OC age distribution within 3 kpc from the Sun, which we used to fit the theoretical parametrization of Lamers & Gieles (2006) of different disruption mechanisms for bound open clusters. We found an excess of observed young OCs with respect to the fit, thought to be a combined effect of age dependent incompleteness and presence of unbound associations for ages $\lesssim$ 16 Myr. We derived formation rates of 0.54, 1.18, and 6.50 Myr^{-1} kpc^{-2} for bound open clusters, all observed young exposed clusters, and embedded clusters, respectively, which translates into a EC dissolution fraction of $88 \pm 8\%$.

9. We carried out follow-up ^{13}CO(2−1) and C^{18}O(2−1) map observations towards a subsample of 14 clusters showing evidence of ongoing stellar feedback. A simple excitation analysis reveals good correlation between bright PAH emission and high excitation temperatures in the observed regions, and gives average H_2 column densities of few $10^{22}\,\mathrm{cm}^{-2}$ with peaks reaching $10^{23}\,\mathrm{cm}^{-2}$. The kinematics exhibits in many regions (turbulent)

linewidth broadening in clumps directly associated or in the vicinity of the stellar clusters; and velocity gradients in the regions with more dispersed gas morphologies, suggesting expanding motions.

10. We studied more in detail the kinematics of one of the observed regions, the IR bubble G10.31−0.14. By comparing its velocity field with simple geometrical models, we concluded that G10.31−0.14 is more likely an expanding molecular ring inclined with respect to the plane of the sky, rather than a 3D shell seen in projection; the ring would be located within a flat molecular cloud. Observations at other wavelengths support this scenario, in particular the radio continuum emission from the ionized gas suggests the presence of a champagne flow emerging out of the flat boundaries of the host cloud.

Overall, the results presented and discussed in this thesis, together with the ideas proposed in recent works and reviewed in Chapter 2, point to the following general picture. A giant molecular cloud fragments in clumps which begin to form stars correlated and space and time. Within the newly formed (or forming) stellar population, which as a whole has a higher stellar density than the Galactic field population, agglomerates relatively more crowded are identified observationally as "embedded clusters" (these can cover up to the totality of the formed stars, depending on the observer's criterion). Some embedded clusters could be unbound from birth even considering the gas potential, and quickly disperse into the field. Others might merge and form fewer and larger embedded clusters within the molecular complex. If a certain embedded cluster achieves to remain gravitationally bound in the gas potential, at some point the effect of stellar feedback starts to influence the parent molecular material in the vicinity, by first injecting small-scale internal turbulence. When UV radiation is important, the initially dark gas clump begins also to be illuminated, becoming bright at mid-infrared PAH emission. After a typical duration of ~ 3 Myr for the embedded phase, the energy and momentum introduced by stellar feedback eventually disrupts the clump and sweeps up the residual gas out of the cluster volume. The stars of this emerging cluster are now tied to each other uniquely by the stellar gravitational potential, which might be not enough to keep the stars together (typical in low density regions), and hence, the cluster dissolves (dissolution due to gas expulsion). If the gas-free cluster is still gravitationally bound, it can be destroyed anyway through tidal shocks from the surrounding gas (typical in dense regions) or collisional N-body dynamics (systems with a low number of members). An exposed cluster that does not survive to any of these processes is dissolved at an age not longer than ~ 15 Myr. Bound exposed clusters are the few clustered remnants

($\sim$ 10% of the total of embedded clusters formed) of the star formation and subsequent dynamical evolution in a giant molecular cloud. They are found relatively in isolation (compared to embedded clusters) and evolve in a longer timescale.

As already remarked in Chapter 3, the new generation of all-sky near-infrared surveys, such as UKIDSS and VVV, will constitute valuable tools to discover new open and embedded clusters in the Galactic plane and to start to fill in the highly incomplete parts of the plane beyond 1 or 2 kpc from the Sun (for OCs and ECs, respectively). In the future, we plan to update our cluster database in the inner Galaxy to include the new discoveries. Furthermore, the improved sensitivity and resolution of these surveys relative to 2MASS will allow to study the stellar population of embedded clusters which appear too crowded and/or extinguished in the 2MASS data. This is very important to increase the number of young clusters with available estimates of their physical properties, like ages and masses. In particular, stellar masses can be combined with estimates of gas masses (e.g., from ATLASGAL) to derive star formation efficiencies and investigate possible trends with the age and the presence of feedback, obtaining important constraints to star formation theories.

A

Cluster Classical Evolution

Here, some basic facts about the dynamical evolution of an exposed star cluster are summarized, mainly in the context of classical N-body dynamics. These notes are based on some parts of the book by Binney & Tremaine (2008), the reviews by Kroupa (2008) and Portegies Zwart et al. (2010), and on the lectures of the course "Dense stellar systems" by P. Kroupa which I personally attended in Bonn. A much more complete description is given in these references.

For the sake of clarity, we consider here an ideal and fictitious stellar cluster already formed with certain initial conditions (for example, the ones given by the parent molecular cloud), without residual gas, and neglecting gas expulsion dynamical effects. Cluster formation and early evolution is a highly complex and less understood process, and is described in § 2. Such an ideal cluster will have its stellar population mixed in a time-scale comparable to the *crossing time*, defined as the time required for an individual star with a velocity equal to the typical velocity dispersion, σ, to move across the whole system in a ballistic trajectory:

$$t_{\rm cross} \equiv \frac{2r_{\rm h}}{\sigma} \ , \tag{A.1}$$

where $r_{\rm h}$ is the radius containing half of the mass of the cluster and is usually taken as a characteristic radius. For a time $t < t_{\rm cross}$, the system cannot be mixed and is still close to its initial state.

Due to the r^{-2} dependence of the two-body gravitational force, in a stellar system the net force on a given member is dominated by the most distant stars,

rather than by its closest neighbors (§1.2 of Binney & Tremaine 2008), so that we can assume that the movement of each star is determined by a smooth force field generated by the system as whole, which prevails over occasional gravitational encounters with individual stars (the so-called "collisions" in stellar dynamics). This holds until the star has experienced so many two-body collisions that it loses completely the memory of its initial orbit. The time needed for this to happen is called *relaxation time*, and is often estimated by computing the amount of time required to change the velocity v of a star by a quantity $\Delta v \simeq v$ (Binney & Tremaine 2008, their equation 1.38):

$$t_{\text{relax}} \simeq 0.1 \frac{N}{\ln \Lambda} t_{\text{cross}} \ , \tag{A.2}$$

where N is the total number of stars in the system, and $\ln \Lambda$ is the *Coulomb logarithm* (in analogy to the theory of plasmas), whose parameter Λ is of the order of N, as discussed below. For a time $t \geq t_{\text{relax}}$, the exchange of energy between the stars within the cluster due to two-body collisions is significant, whereas for $t < t_{\text{relax}}$, stellar encounters are unimportant and the cluster can be described as a *collision-less* system, in which their members move under the influence of a smooth potential $\Phi(\boldsymbol{x}, t)$ produced by all other stars as a continuous density distribution $\rho(\boldsymbol{x}, t)$. Under this description, the phase-space distribution function of the system, $f(\boldsymbol{x}, \boldsymbol{v}, t)$, satisfies the *collision-less Boltzmann equation*:

$$\frac{\partial f}{\partial t} + \frac{\partial f}{\partial \boldsymbol{x}} \cdot \boldsymbol{v} - \nabla \Phi \cdot \frac{\partial f}{\partial \boldsymbol{v}} = 0 \ .$$

A very important corollary of the this formula is the *virial equation*, which in its scalar form becomes

$$\frac{\ddot{I}}{2} = 2K + W \ ,$$

where K and W are the total kinetic and potential energies, respectively, and I is the generalized moment of inertia, defined as

$$I = \int \rho(\boldsymbol{x}, t) \boldsymbol{x}^2 \, \mathrm{d}^3 \boldsymbol{x} \ .$$

It follows from above that a *stationary system*, i.e., a system with a phase-space distribution function (and therefore its density) independent of time, satisfies the *scalar virial theorem*, which states that[1]

$$2K + W = 0 \ . \tag{A.3}$$

[1] $W < 0$ for any gravitational system.

In summary, any collision-less stationary system fulfills equation (A.3), and we say that the system is in dynamical or virial equilibrium, or simply *virialized*.

It is useful to define the *virial ratio* by

$$Q \equiv \frac{K}{-W} \ , \tag{A.4}$$

so that for a virialized system, $Q = 1/2$. It results that a system out of equilibrium, i.e., at the beginning of an expansion ($Q > 1/2$) or contraction ($Q < 1/2$), reaches approximate virialization in a time scale of a few $t_{\rm cross}$, but it will tend to oscillate around exact virial equilibrium for some time (e.g., Smith et al. 2011). If $Q \geq 1$, the total energy is positive ($K + W \geq 0$) and the system is *unbound*: it has the capacity to expand indefinitely to infinity (however, a fraction of the stars can remain bound, see § 2.2.2).

Besides relaxation, another consequence of the exchange of energy between the cluster members through two-body collisions is *mass segregation*, a process in which the more massive stars slow down and sink towards the center of the cluster, while the average stars speed up, moving to an outer halo. This process occurs simply because two-body encounters favor equipartition of kinetic energy, i.e., there is a statistical tendency for the velocity dispersions of stars with different masses to have $mv^2 \simeq$ constant. The timescale of mass segregation, $t_{\rm ms}$, can be estimated for an effective two-component system composed of a dominant population of stars with mass $\langle m \rangle$, the mean mass of the real cluster, and a population of massive stars with mass $m_{\rm b}$ (Spitzer 1969):

$$t_{\rm ms} \simeq \frac{\langle m \rangle}{m_{\rm b}} t_{\rm relax} \ . \tag{A.5}$$

Mass segregation is achieved, therefore, quite before relaxation. In fact, by performing numerical experiments, Portegies Zwart & McMillan (2002) and Gürkan et al. (2004) found that, for clusters with realistic distributions of stellar masses, and in the limit where stellar mass loss is negligible, the timescale for the most massive stars to reach the center and form a well-defined highly-concentrated core is

$$t_{\rm ms} \simeq 0.15\, t_{\rm relax} \ . \tag{A.6}$$

While the most massive stars in the cluster fall to the center, they increase their kinetic energy, which, however, is transfered again through energy equipartition to the lower mass stars they found on their road. Hence, the massive stars slow down again and sink even deeper towards the cluster center, leading finally to the collapse of the central core. This phenomenon can be also understood by considering the concept of "heat capacity" (§7.3.1 of Binney & Tremaine

2008), which results to be negative for any virialized self-gravitating system, and therefore a loss of energy is equivalent to an increase of the temperature. Provided that the system can transfer energy (in our case, the system is the central core which transfers energy to the rest of the cluster), it is then able to experience endless cycles of heating up and energy loss, which translates in contraction until collapse. Nevertheless, in real clusters the *core collapse* is temporarily balanced by three-body collisions between single stars and binaries (§3.4.1 of Portegies Zwart et al. 2010), which can be thought as internal sources or "creators" of kinetic energy, since such encounters, if the interacting binary is bound enough, tend to produce a resultant binary even more bound, so that the excess of energy is carried by the final single star in kinetic form. The internal kinetic energy generation by these encounters naturally produces expansion which compensates against core collapse.

Another process that helps the central core not to collapse is mass loss via *stellar evolution* (§4.3 of Portegies Zwart et al. 2010). The most massive stars ($\gtrsim 50\ M_\odot$) leave the main sequence at about 3–4 Myr and have lost $\sim 90\%$ of their mass when they collapse to a black hole following a supernova. A $5\,M_\odot$ star loses more than 80% of its mass by the time it becomes a white dwarf at about 100 Myr. Consequently, from the moment the most massive stars start to lose mass, the whole cluster mass decreases, which, as can be shown by simple dynamical arguments, causes expansion. If the cluster had time enough to already be moderately mass-segregated, the massive population of the core tends to lose more mass than the lower mass halo stars, resulting in a more severe expansion of the core compared to the outer regions. Hence, stellar evolution reverses core collapse at some point, and can even induce the total disruption of the cluster. The bulk of stellar mass loss takes between 100 Myr and 1 Gyr, depending on the initial mass, size, density profile of the cluster, and distribution of stellar masses. During this period, this process completely dominates the overall evolution of the cluster, and make it lose about 30% of its initial mass (Baumgardt & Makino 2003).

The long-term evolution of clusters that survive stellar mass loss is dominated by purely stellar dynamical processes. It is a well known fact from statistical mechanics that a collisional system in which their particles interact through a central force tends to establish a Maxwell-Boltzmann velocity distribution (e.g., Huang 1987, chapters 3 & 4). Although for a self-gravitating system the process of relaxation is more complex due to its core-halo structure (§7.5 of Binney & Tremaine 2008), we can consider at first order the Maxwell-Boltzmann distribution as the equilibrium state of a relaxed star cluster. Therefore, after a timescale of about the relaxation time, there will be a fraction ξ_e of stars in the tail of the distribution with speeds exceeding

the escape velocity which then *evaporate* from the cluster. Assuming that this high-velocity tail is refilled every $t_{\rm relax}$, the total dissolution timescale is $t_{\rm diss} \simeq t_{\rm relax}/\xi_{\rm e}$ (Equation (7.5) of Binney & Tremaine 2008). For a Maxwell-Boltzmann distribution, $\xi_{\rm e} \simeq 0.0074$, and hence $t_{\rm diss} \simeq 140\, t_{\rm relax}$. We then conclude that the phenomenon of *evaporation* sets an upper limit to the lifetime of an isolated stellar cluster of about a hundred relaxation times.

However, a real cluster is not isolated but exposed to the *tidal field* of the Galaxy. At a distance from the cluster center longer than a certain value $r_{\rm tid}$, called the *tidal radius*, this external force removes cluster's stars which would be bound if the cluster were isolated, increasing the evaporation rate up to $\xi_{\rm e} \simeq 0.1$ (see, e.g., Fig. 1 of Gieles & Baumgardt 2008), and thus reducing the cluster lifetime to a few tens of relaxation times. The tidal radius can be estimated as (Equation (24) of King 1962, assuming a flat rotation curve)

$$r_{\rm tid} = \left(\frac{GM}{2V_{\rm G}^2}\right)^{1/3} R_{\rm G}^{2/3} \,, \tag{A.7}$$

where M is the total mass of the cluster, $V_{\rm G}$ is the circular velocity of the Galaxy, and $R_{\rm G}$ is the distance of the cluster from the Galactic Center. By doing a more detailed analysis of the lifetime of clusters within a tidal field, Gieles & Baumgardt (2008) found that the dissolution timescale is only dependent, roughly, on the cluster's number of stars and Galactocentric distance:

$$t_{\rm diss} = A \left(\frac{N}{\ln \Lambda}\right)^{3/4} \frac{R_{\rm G}}{V_{\rm G}} \,, \tag{A.8}$$

where A is a constant of the order of $\simeq 0.3$.

Another important external disruptive agent is encounters between clusters and giant molecular clouds (§4.4 of Portegies Zwart et al. 2010). The cluster dissolution timescale due to heating by passing clouds is inversely proportional to the mean volume density of molecular gas, $\rho_{\rm gas} = n_{\rm clouds} M_{\rm cloud}$ (where $n_{\rm clouds}$ is the number density of clouds and $M_{\rm cloud}$ is the typical mass of an individual cloud), and proportional to the density of the cluster:

$$t_{\rm diss}^{\rm GMC} \simeq \left(\frac{0.03\, M_\odot\, {\rm pc}^{-3}}{\rho_{\rm gas}}\right) \left(\frac{\rho_{\rm hm}}{10\, M_\odot\, {\rm pc}^{-3}}\right) {\rm Gyr}. \tag{A.9}$$

Here, $\rho_{\rm hm}$ represents the cluster mean density at the half-mass radius, and the value 0.03 $M_\odot$ pc^{-3} is the mean molecular gas density in the solar neighborhood (Gieles et al. 2006). For low-density clusters, the lifetime can therefore be determined mainly by encounters with giant molecular clouds rather than by the Galactic tidal field.

Estimations for the Crossing and Relaxation Times

The virial theorem allows us to estimate the velocity dispersion of a cluster in equilibrium, and thus its crossing time, as follows. The kinetic energy can be expressed as $K = M\langle v^2\rangle/2$, where $\langle v^2\rangle$ is the square speed of the cluster's stars averaged over the whole phase-space, and M is the total mass of the system. If we define the *gravitational radius* as $r_\mathrm{g} = GM^2/|W|$, we have from equation (A.3) that

$$\langle v^2\rangle = \frac{GM}{r_\mathrm{g}} \ .$$

Since r_g is not straightforward to calculate, we can apply an useful approximation given by Spitzer (1969), who noted that for many simple spherical systems, $r_\mathrm{h} \simeq 0.4 r_\mathrm{g}$, where r_h is the half-mass radius defined before. Assuming also that the mean velocity vanishes at every position[2], $\langle \boldsymbol{v}(\boldsymbol{x})\rangle_v = 0$, which holds, e.g., for any stationary system with a phase-space distribution function depending uniquely on the Hamiltonian (in particular, this condition is satisfied by the Plummer and King models, widely used in the literature to describe star clusters), then the averaged square velocity dispersion equals the mean square speed, $\langle v^2\rangle = \sigma^2$, and we obtain the convenient approximation

$$\sigma^2 \simeq 0.4\frac{GM}{r_\mathrm{h}} \ . \tag{A.10}$$

Replacing σ from above into equation (A.1), and expressing it in useful physical units, yields

$$t_\mathrm{cross} = 4.72 \left(\frac{100\,M_\odot}{M}\right)^{1/2} \left(\frac{r_\mathrm{h}}{\mathrm{pc}}\right)^{3/2} \mathrm{Myr}. \tag{A.11}$$

For the relaxation time, a more precise estimation than equation (A.2) can be obtained using the diffusion coefficients of the *Fokker-Planck approximation*, which deals with collisional systems. Under this description, Spitzer & Hart (1971) derived

$$t_\mathrm{relax} = \sqrt{\frac{2}{3}}\frac{(0.4)^{3/2}}{9g_0}\frac{M^{1/2}r_\mathrm{h}^{3/2}}{G^{1/2}\langle m\rangle \ln\Lambda} \ , \tag{A.12}$$

where $\langle m\rangle$ is the mean stellar mass, and $g_0 \simeq 0.166$ is a dimensionless constant arising from the diffusion coefficients [3]. Note that the term $(0.4)^{3/2}$ appears from using equation (A.10). In convenient physical units, equation (A.12)

[2] The averaging $\langle\cdot\rangle_v$ is now over the velocity domain only.

[3] $g_0 = G(X)/X$ with $X = \sqrt{3/2}$, and $G(X)$ is the function defined in equation (7.93) of Binney & Tremaine (2008).

becomes

$$t_{\rm relax} = \frac{20.7}{\ln\Lambda}\left(\frac{M_\odot}{\langle m\rangle}\right)\left(\frac{M}{100\,M_\odot}\right)^{1/2}\left(\frac{r_{\rm h}}{\rm pc}\right)^{3/2}\ {\rm Myr}. \tag{A.13}$$

Hénon (1975) showed that the argument of the Coulomb logarithm can be approximated at first order by $\Lambda = 0.4N$, but that a more accurate derivation gives $\Lambda = 0.15N$ for systems where all stars have the same mass, and considerably lower values for systems with a wide range of stellar masses. This is consistent with the value found by Giersz & Heggie (1996) from numerical experiments of multi-mass clusters, $\Lambda \simeq 0.02N$.

Using the fact that $\langle m\rangle = M/N$, we can rewrite the formula (A.12) in two useful forms. First, as a function of the crossing time,

$$t_{\rm relax} = 0.0438\,\frac{N}{\ln\Lambda}\,t_{\rm cross}\ , \tag{A.14}$$

and equivalently, as a function of N only:

$$t_{\rm relax} = 3.35\left(\frac{0.38\,M_\odot}{\langle m\rangle}\right)^{1/2}\left(\frac{r_{\rm h}}{\rm pc}\right)^{3/2}\frac{\sqrt{N}}{\ln\Lambda}\quad {\rm Myr}, \tag{A.15}$$

where the normalization $\langle m\rangle = 0.38M_\odot$ corresponds to the average stellar mass for the canonical IMF (Kroupa 2007).

B

Catalog of stellar clusters in the inner Galaxy

In this appendix, we list all embedded and open clusters within the ATLASGAL Galactic range ($|l| \leq 60°$ and $|b| \leq 1.5°$) with the most relevant columns (24 out of 40) from our catalog described in § 4.1. This information is organized in two tables, B.1 and B.2, which provide, respectively, the main data and some additional information for all these clusters. The column names are the same as defined in § 4.1, and we refer to that Section for a more comprehensive explanation of the catalog construction.

In table B.1, `ID` and `Name` are, respectively, the cluster identification number and name; `Cat` lists the original catalogs from which each cluster was extracted (labeled in Table 3.2); `RAJ2000` and `DECJ2000` are the equatorial coordinates; `Diam` is the angular size; `Dist` and `e_Dist` is the adopted distance and its error; `ref_Dist` is the distance reference (codes are explained in § 4.1.6); `Age` and `e_Age` is the age and its error; `ref_Age` is the literature reference for the age; `ref_Conf` is the literature reference for cluster confirmation (as real cluster) or further studies; and `Morph_type` is the morphological type as defined in § 4.2.1. In Table B.2, `Clump_sep` is the projected distance to the nearest ATLASGAL emission pixel (normalized to the cluster radius); `Clump_flag` (denoted by `Cf`) is a flag which gives information about the correlation with ATLASGAL and line velocity available (described in Sections § 4.1.2 and § 4.1.4); `Vlsr`, `ref_Vlsr` and `KDA` are, respectively, the gas line radial velocity, its literature

reference, and the solution of the kinematic distance ambiguity (see § 4.1.4); `Morph` is the morphological flag described in § 4.1.2 and § 4.1.3; `HII_reg`, `Bub` and `IRDC` are, respectively, the associated H II region, infrared bubble, and infrared dark cloud; and in the column `Complex`, spatially associated clusters are grouped.

A companion list of all the references with the corresponding identification numbers used throughout the catalog is given in Table B.3. The full catalog will be available electronically to the community at the VizieR service[1].

[1] `http://vizier.u-strasbg.fr/viz-bin/VizieR`

Table B.1: Catalog of embedded and open clusters within the Galactic range $|l| \leq 60°$ and $|b| \leq 1.5°$ (main information).

ID	Name	Cat	RAJ2000 (h: m: s)	DECJ2000 (°: ′: ″)	Diam (″)	Dist (kpc)	e_Dist (kpc)	ref_Dist	Age (Myr)	e_Age (Myr)	ref_Age	ref_Conf	Morph_type
1	BH 131	(01),13	12:26:13.7	−63:24:50	300	6.25	0.94	S	1259	290	96	96	OC2
2	[MCM2005b] 32	09	12:26:52.0	−62:49:27	36	···	···	···	···	···	···	···	OC2
3	BH 132	01	12:27:00.0	−64:04:00	240	···	···	···	150	50	176	···	OC2
4	VVV CL013	14	12:28:37.0	−62:58:25	54	4.16	0.54	K	···	···	···	···	EC2
5	[FSR2007] 1616	11	12:29:26.0	−63:25:58	101	···	···	···	···	···	···	···	OC2
6	[MCM2005b] 33	09	12:30:05.0	−62:56:50	96	9.41	0.60	K	···	···	···	···	EC1
7	Ruprecht 105	01	12:34:14.0	−61:33:60	720	0.95	0.14	S	1023	471	115	115	OC2
8	G3CC 5	17	12:34:16.2	−61:55:04	76	4.24	0.50	KC	···	···	···	···	EC1
9	[DBS2003] 77	05	12:34:52.0	−61:39:15	138	4.24	0.50	KC	···	···	···	···	EC2
10	VVV CL015	14	12:34:52.0	−61:40:16	40	4.24	0.50	KC	···	···	···	···	EC2
11	VVV CL016	14	12:35:00.0	−61:41:40	80	4.24	0.50	KC	···	···	···	···	OC0
12	[DBS2003] 78	05	12:36:03.0	−61:50:60	72	4.24	0.50	KC	···	···	···	···	EC2
13	VVV CL017	14,17	12:35:35.2	−63:02:34	57	4.26	0.68	K	···	···	···	102	EC1
14	[FSR2007] 1622	11	12:37:57.0	−63:16:16	281	···	···	···	···	···	···	···	OC2
15	G3CC 6	17	12:40:02.6	−63:05:01	67	···	···	···	···	···	···	···	EC1
16	NGC 4609	01	12:42:18.0	−62:59:42	780	1.32	0.20	S	50.1	15.0	120	120	OC2
17	G3CC 7	17	12:42:53.7	−62:32:32	65	···	···	···	···	···	···	···	OC2
18	Hogg 15	01	12:43:37.0	−63:05:60	420	3.20	0.48	S	20.0	10.0	177	120	OC1
19	VVV CL018	14	12:44:40.0	−62:47:46	60	···	···	···	···	···	···	···	EC2
20	[MCM2005b] 34	09	12:47:03.0	−62:58:21	156	···	···	···	···	···	···	···	EC2
21	[FSR2007] 1630	11	12:48:42.0	−62:09:14	346	···	···	···	···	···	···	···	OC2
22	[DBS2003] 79	05	12:48:48.0	−63:44:35	66	···	···	···	···	···	···	···	OC2
23	[DBS2003] 80	05	12:50:23.0	−61:34:55	78	4.46	2.40	K	···	···	···	···	OC0
24	Teutsch 109	02	12:57:50.4	−63:15:56	132	···	···	···	···	···	···	···	OC2
25	G3CC 8	17	13:00:22.2	−63:32:30	107	12.10	0.66	K	···	···	···	···	EC1
26	G3CC 9	17	13:00:40.3	−62:23:17	82	···	···	···	···	···	···	···	OC2
27	VVV CL019	14	13:07:06.0	−61:25:03	100	2.11	0.72	K	···	···	···	···	EC2
28	[MCM2005b] 35	09	13:08:09.0	−62:43:46	36	···	···	···	···	···	···	···	OC2
29	VVV CL020	14	13:07:36.0	−61:19:28	48	···	···	···	···	···	···	···	OC2
30	G3CC 10	17	13:08:12.3	−62:10:23	41	3.80	0.60	C(ID:36)	···	···	···	···	EC1
31	[DBS2003] 82	05	13:08:36.0	−62:14:58	102	3.80	0.60	C(ID:36)	···	···	···	···	EC2
32	[DBS2003] 131	05,17	13:11:39.3	−62:33:12	69	3.80	0.60	C(ID:36)	2.00	1.00	11	130,126,11	OC0
33	[DBS2003] 130	05	13:11:54.0	−62:47:02	96	3.80	0.60	C(ID:36)	2.00	1.00	11	11	EC2
34	VVV CL021	14	13:11:51.0	−62:36:52	58	3.80	0.60	C(ID:36)	···	···	···	···	EC2
35	[DBS2003] 132	05	13:12:18.0	−62:42:16	39	3.80	0.60	C(ID:36)	···	···	···	···	EC1
36	Danks 1	01,17	13:12:26.9	−62:41:59	66	3.80	0.60	S	2.00	1.00	68	68	OC0
37	VVV CL022	14	13:12:36.0	−62:37:16	106	3.80	0.60	C(ID:36)	···	···	···	···	EC1
38	[MCM2005b] 36	09	13:13:04.0	−63:00:21	96	···	···	···	···	···	···	···	EC1
39	Danks 2	01,17	13:12:54.1	−62:40:40	93	3.80	0.60	S	4.00	2.00	68	68	OC1

Table B.1: continued.

ID	Name	Cat	RAJ2000	DECJ2000	Diam	Dist	e_Dist	ref_Dist	Age	e_Age	ref_Age	ref_Conf	Morph_type
40	VVV CL023	14	13:13:13.0	−62:33:26	54	3.80	0.60	C(ID:36)	···	···	···	···	OC1
41	NGC 5045	01	13:14:10.0	−63:23:24	2712	1.50	0.23	S	12.9	5.9	115	115	OC2
42	[DBS2003] 133	05	13:13:58.0	−62:24:22	129	3.80	0.60	C(ID:36)	···	···	···	···	EC2
43	[DBS2003] 134	05	13:14:22.0	−62:44:40	96	3.80	0.60	C(ID:36)	···	···	···	···	EC2
44	[MCM2005b] 37	09	13:16:52.0	−62:47:22	144	3.80	0.60	C(ID:36)	···	···	···	···	EC2
45	[DBS2003] 85	05	13:18:31.0	−62:39:47	102	1.98	0.52	S	···	···	···	···	OC0
46	VVV CL024	14	13:18:45.0	−62:44:39	54	···	···	···	···	···	···	···	EC2
47	[DBS2003] 86	05	13:19:05.0	−62:34:16	122	2.71	0.80	K	···	···	···	···	EC2
48	Stock 16	01	13:19:29.0	−62:37:60	180	1.81	0.27	S	7.94	2.78	164	164	OC2
49	[FSR2007] 1645	(01),11	13:21:10.0	−61:56:46	641	···	···	···	···	···	···	···	OC2
50	Teutsch 79	01,(02)	13:23:39.0	−63:40:24	264	1.25	0.30	S	600	120	37	37	OC2
51	Loden 807	01	13:24:40.0	−62:28:60	1200	0.93	0.14	S	200	92	115	115	OC2
52	Teutsch 110	02	13:26:35.7	−64:06:12	108	···	···	···	···	···	···	···	OC2
53	G3CC 11	17	13:26:58.8	−62:03:25	71	···	···	···	···	···	···	···	EC1
54	Basel 18	01	13:27:44.0	−62:18:46	360	2.23	0.33	S	38.9	11.7	128	128	OC2
55	VVV CL025	14	13:31:22.0	−63:28:27	34	···	···	···	···	···	···	···	EC2
56	VVV CL026	14	13:31:26.0	−63:27:52	36	···	···	···	···	···	···	···	EC2
57	Hogg 16	01	13:29:18.0	−61:12:00	360	1.59	0.24	S	11.1	3.9	128	128	OC2
58	Trumpler 21	01	13:32:14.0	−62:48:00	300	1.26	0.19	S	49.7	14.9	128	128	OC2
59	Collinder 272	01	13:30:26.0	−61:18:60	600	2.05	0.31	S	16.9	5.9	128	128	OC2
60	VVV CL027	14	13:32:24.0	−62:43:39	26	···	···	···	···	···	···	···	OC2
61	[FSR2007] 1653	11	13:33:50.0	−63:01:51	43	···	···	···	···	···	···	···	OC2
62	C1331−622	01	13:34:12.0	−62:25:02	420	1.09	0.16	S	63.1	18.9	46	46	OC2
63	ESO 132−14	01	13:36:30.0	−62:12:49	180	1.10	0.17	S	800	200	166	166	OC2
64	Pismis 18	01	13:36:55.0	−62:05:36	240	2.24	0.34	S	891	178	46	46	OC2
65	BH 151	01,17	13:40:12.0	−61:43:48	76	6.10	0.93	KC	2.30	0.80	138	138	OC1
66	VVV CL028	14	13:40:23.0	−61:43:60	24	6.10	0.93	KC	···	···	···	···	OC1
67	SAI 118	(01),13	13:43:03.8	−63:09:53	480	1.14	0.37	S	5623	3237	96	96	OC2
68	Dias 4	01	13:43:25.0	−63:00:48	384	2.15	0.32	S	1260	252	230	230	OC2
69	VVV CL029	14	13:41:54.0	−62:07:38	54	6.10	0.93	KC	···	···	···	···	EC1
70	NGC 5269	01	13:44:44.0	−62:54:54	180	1.41	0.21	S	160	110	231	231	OC2
71	[MCM2005b] 38	09,(11),13,17	13:44:15.9	−62:04:05	100	6.10	0.93	KC	···	···	···	···	OC1
72	NGC 5281	01	13:46:35.0	−62:55:00	420	1.11	0.17	S	14.0	4.9	128	128	OC2
73	VVV CL030	14	13:45:28.0	−62:14:33	40	9.32	0.55	K	···	···	···	···	EC2
74	Loden 991	01	13:45:24.0	−62:00:60	300	···	···	···	···	···	···	···	OC2
75	[MCM2005b] 39	09	13:47:19.0	−62:47:27	108	···	···	···	···	···	···	···	OC2
76	ASCC 75	01	13:47:10.0	−62:25:12	1224	3.00	0.45	S	4.47	2.06	116	116	OC0
77	VVV CL031	14	13:47:20.0	−62:18:44	90	3.00	0.45	C(ID:76)	···	···	···	···	EC2
78	G3CC 12	17	13:48:38.1	−62:46:11	48	3.00	0.45	C(ID:76)	···	···	···	···	EC1
79	G3CC 13	17	13:49:51.6	−62:51:42	38	3.00	0.45	C(ID:76)	···	···	···	···	EC1

Table B.1: continued.

ID	Name	Cat	RAJ2000	DECJ2000	Diam	Dist	e_Dist	ref_Dist	Age	e_Age	ref_Age	ref_Conf	Morph_type
80	Platais 12	01	13:51:44.0	−63:27:12	7200	0.44	0.07	S	170	78	115	115	OC2
81	[FSR2007] 1666	11	13:48:35.0	−61:25:60	216	···	···	···	···	···	···	···	OC2
82	[MCM2005b] 40	09	13:50:36.0	−61:40:12	108	5.28	0.71	KC	···	···	···	···	EC1
83	VVV CL032	14	13:50:41.0	−61:35:13	108	5.28	0.71	KC	···	···	···	2	EC1
84	G3CC 14	17	13:51:25.6	−61:44:51	40	5.28	0.71	KC	···	···	···	···	EC1
85	G3CC 15	17	13:51:15.8	−61:32:30	88	3.15	0.73	K	···	···	···	···	EC2
86	NGC 5316	01	13:53:57.0	−61:52:06	840	1.05	0.23	S	166	33	165	165	OC2
87	[FSR2007] 1668	11	13:54:49.0	−61:34:12	101	···	···	···	···	···	···	···	OC2
88	[FSR2007] 1669	11	13:56:25.0	−61:45:50	86	···	···	···	···	···	···	···	OC2
89	Loden 1101	01	13:58:18.0	−61:47:00	600	···	···	···	···	···	···	···	OC2
90	SAI 120	13	13:58:42.0	−61:40:08	120	2.55	0.38	S	562	129	96	96	OC2
91	Lynga 1	01	14:00:02.0	−62:08:60	180	1.90	0.28	S	113	23	241	241	OC2
92	[MCM2005b] 41	09	13:59:28.0	−61:22:00	36	5.40	2.35	K	···	···	···	···	OC1
93	[MCM2005b] 42	09	14:00:37.0	−61:06:59	168	···	···	···	···	···	···	···	OC2
94	[MCM2005b] 43	09	14:00:28.0	−60:59:15	108	5.42	1.33	K	···	···	···	···	OC0
95	VVV CL033	14	14:03:27.0	−61:16:13	54	5.45	1.18	KC	···	···	···	···	OC0
96	[MCM2005b] 44	09	14:03:36.0	−61:18:29	96	5.45	1.18	KC	···	···	···	···	EC2
97	[MCM2005b] 45	09	14:05:34.0	−62:05:24	96	3.91	0.99	K	···	···	···	···	OC0
98	VVV CL034	14	14:04:08.0	−61:19:55	68	7.11	0.95	KC	···	···	···	···	EC2
99	VVV CL035	14	14:06:27.0	−61:29:35	56	···	···	···	···	···	···	···	EC2
100	[MCM2005b] 46	09	14:07:36.0	−61:27:12	108	7.11	0.95	KC	···	···	···	···	EC2
101	[MCM2005b] 47	09	14:07:35.0	−61:19:42	108	7.11	0.95	KC	···	···	···	···	EC2
102	[MCM2005b] 48	09	14:07:53.0	−61:17:51	36	···	···	···	···	···	···	···	OC2
103	ASCC 77	01	14:10:48.0	−62:19:48	2304	2.20	0.33	S	9.77	4.50	116	116	OC0
104	VVV CL037	14	14:09:07.0	−61:24:43	86	7.11	0.95	KC	···	···	···	···	EC2
105	[DBS2003] 135	05	14:08:42.0	−61:10:38	46	7.11	0.95	KC	···	···	···	···	EC1
106	VVV CL036	14,17	14:09:03.0	−61:16:00	81	···	···	···	···	···	···	···	OC2
107	VVV CL038	14	14:12:44.0	−61:47:06	40	9.40	0.52	K	···	···	···	···	EC1
108	VVV CL039	14	14:15:32.0	−61:41:47	120	2.00	0.70	S	75.0	40.0	41	41	OC2
109	[MCM2005b] 49	09	14:17:31.0	−61:36:57	24	3.61/7.61	0.78/0.78	K	···	···	···	···	OC2
110	Loden 1256	01	14:18:12.0	−61:25:60	600	1.40	0.21	S	257	118	115	115	OC1
111	[MCM2005b] 50	09,05	14:19:39.5	−61:25:19	84	1.82	0.52	K	1.20	0.50	219	219	EC2
112	VVV CL014	14	14:19:09.0	−60:30:46	60	···	···	···	···	···	···	···	OC2
113	G3CC 16	17	14:24:58.6	−61:44:56	80	3.95	0.88	K	···	···	···	···	EC1
114	[MCM2005b] 51	09	14:20:42.0	−60:16:04	72	5.70	2.36	K	···	···	···	···	EC2
115	Lynga 2	01	14:24:35.0	−61:19:50	780	0.90	0.14	S	90.0	27.0	18	18	OC2
116	G3CC 17	17	14:25:15.4	−60:35:22	86	5.74	1.30	KC	···	···	···	···	EC2
117	[MCM2005b] 52	09	14:25:03.0	−60:27:35	72	5.74	1.30	KC	···	···	···	···	OC0
118	[DBS2003] 136	05	14:24:60.0	−60:22:30	72	5.74	1.30	KC	···	···	···	···	EC2
119	G3CC 18	17	14:26:06.6	−60:40:43	87	3.80	0.80	K	···	···	···	···	EC1

Table B.1: continued.

ID	Name	Cat	RAJ2000	DECJ2000	Diam	Dist	e_Dist	ref_Dist	Age	e_Age	ref_Age	ref_Conf	Morph_type
120	Loden 1339	01	14:33:29.0	−62:00:60	240	...	...	...	...	...	...	...	OC2
121	Trumpler 22	01	14:31:02.0	−61:09:60	600	1.52	0.23	S	89.1	26.7	128	128	OC2
122	NGC 5617	01	14:29:44.0	−60:42:42	600	2.00	0.30	S	80.0	24.0	50	50	OC2
123	Pismis 19	01,17	14:30:39.4	−60:53:00	194	2.40	0.36	S	1122	258	135	135	OC2
124	[FSR2007] 1680	11	14:28:33.0	−60:01:09	43	...	...	...	...	...	...	...	OC2
125	NGC 5606	01	14:27:47.0	−59:37:54	180	1.80	0.27	S	11.9	4.2	128	128	OC2
126	Hogg 17	01	14:33:58.0	−61:22:00	240	1.31	0.20	S	107	21	128	128	OC2
127	[FSR2007] 1681	11	14:28:40.0	−59:45:33	36	...	...	...	...	...	...	...	OC2
128	Ruprecht 111	01	14:35:54.0	−59:58:00	420	1.12	0.17	S	1413	283	46	46	OC2
129	[MCM2005b] 53	(09),11,13	14:40:11.9	−60:22:46	254	4.02	0.60	S	891	178	96	96,22	OC2
130	[DBS2003] 137	05	14:42:02.0	−60:30:22	34	4.92	1.02	K	...	...	...	...	EC2
131	[DBS2003] 89	05	14:45:03.0	−59:49:32	119	9.38	0.51	KC	...	...	...	245	EC2
132	[MCM2005b] 54	09	14:45:10.0	−59:50:24	84	9.38	0.51	KC	...	...	...	...	OC0
133	[DBS2003] 90	05	14:45:19.0	−59:49:45	67	9.38	0.51	KC	...	...	...	245	EC2
134	[DBS2003] 91	05	14:45:26.0	−59:49:15	53	9.38	0.51	KC	...	...	...	...	EC1
135	[MCM2005b] 55	09	14:45:34.0	−59:46:50	12	...	...	...	...	...	...	...	OC2
136	VVV CL040	14	14:44:22.0	−59:11:47	64	...	...	...	...	...	...	...	OC2
137	ESO 134−12	01	14:44:46.0	−59:09:54	240	...	...	...	...	...	...	...	OC2
138	VVV CL041	14	14:46:26.0	−59:23:17	108	0.90	0.50	S	27.5	8.2	41	41	OC2
139	[FSR2007] 1689	11	14:46:50.0	−59:29:15	252	...	...	...	...	...	...	...	OC2
140	Teutsch 80	(01),02	14:53:25.6	−60:28:57	204	2.50	0.60	S	126	43	122	122	OC2
141	[MCM2005b] 56	09	14:49:19.0	−59:25:54	60	...	...	...	...	...	...	...	OC2
142	G3CC 19	17	14:51:19.3	−59:50:46	45	2.93	0.54	K	...	...	...	...	EC1
143	G3CC 20	17	14:53:45.6	−59:31:34	74	2.35	0.48	K	...	...	...	...	EC1
144	G3CC 21	17	14:53:42.2	−59:08:49	88	3.40	0.59	K	...	...	...	...	EC1
145	G3CC 22	17	14:59:33.5	−59:00:59	105	2.48	0.48	K	...	...	...	...	EC1
146	SAI 122	13	15:00:03.9	−58:48:13	480	1.67	0.25	S	178	61	96	96	OC2
147	[MCM2005b] 57	09	15:03:00.0	−59:01:23	96	11.44	0.49	K	...	...	...	...	OC1
148	G3CC 23	17	14:59:31.0	−57:49:18	65	2.84	0.51	K	...	...	...	...	EC2
149	VVV CL043	14	15:02:56.0	−58:35:55	108	11.50	0.49	KC	...	...	...	...	EC2
150	[MCM2005b] 58	09	15:03:19.0	−58:36:09	132	11.50	0.49	KC	...	...	...	...	EC1
151	VVV CL045	14	15:03:47.0	−58:40:11	108	...	...	...	...	...	...	...	OC2
152	VVV CL044	14	15:03:40.0	−58:35:07	80	11.50	0.49	KC	...	...	...	...	EC2
153	[FSR2007] 1696	11	15:01:07.0	−57:39:43	720	...	...	...	...	...	...	...	OC2
154	[DBS2003] 92	05	15:03:33.0	−57:40:04	36	1.23	0.30	C(ID:157)	...	...	...	...	EC2
155	VVV CL047	14	15:11:52.0	−59:30:30	42	7.90	1.30	S	60.0	30.0	41	41	OC2
156	Loden 2045	01	15:10:24.0	−58:46:60	1200	...	...	...	...	...	...	...	OC2
157	RCW 87 IR Cluster	04,17	15:05:19.1	−57:31:28	127	1.23	0.30	S	...	...	...	181,39	EC2
158	[DBS2003] 138	05	15:05:23.0	−57:26:37	51	1.23	0.30	C(ID:157)	...	...	...	...	EC2
159	[MCM2005b] 59	09	15:07:13.0	−57:47:52	120	2.03	0.46	K	...	...	...	...	EC2

Table B.1: continued.

ID	Name	Cat	RAJ2000	DECJ2000	Diam	Dist	e_Dist	ref_Dist	Age	e_Age	ref_Age	ref_Conf	Morph_type
160	[DBS2003] 139	05	15:10:06.0	−58:25:58	86	7.70	0.88	K	···	···	···	···	EC2
161	VVV CL048	14	15:14:01.0	−59:15:13	54	3.48	0.55	K	···	···	···	···	EC2
162	[DBS2003] 140	05	15:09:58.0	−58:17:35	95	12.14	0.51	K	···	···	···	···	EC2
163	VVV CL046	14	15:10:08.0	−58:17:06	40	12.14	0.51	K	···	···	···	···	EC2
164	Pismis 20	01	15:15:23.0	−59:03:60	240	2.02	0.30	S	7.31	2.56	128	128	OC2
165	VVV CL067	14	15:10:36.0	−57:54:42	60	···	···	···	···	···	···	···	OC2
166	VVV CL049	14	15:14:30.0	−58:11:49	60	2.98/9.79	0.51/0.51	K	···	···	···	···	EC2
167	[MCM2005b] 60	09	15:16:36.0	−58:10:07	72	8.98	0.55	K	···	···	···	···	OC0
168	VVV CL050	14	15:21:06.0	−57:57:32	30	···	···	···	···	···	···	···	EC2
169	G3CC 24	17	15:19:43.2	−57:18:04	33	2.07	0.45	K	···	···	···	···	EC1
170	G3CC 25	17	15:19:44.6	−57:16:35	37	2.07	0.45	K	···	···	···	···	EC2
171	[DBS2003] 93	05	15:18:37.0	−56:38:44	72	3.75	0.52	K	···	···	···	···	EC2
172	VVV CL051	14	15:20:39.0	−56:51:37	100	···	···	···	···	···	···	···	OC2
173	VVV CL052	14	15:21:44.0	−56:52:40	72	1.87/11.17	0.45/0.45	K	···	···	···	···	EC2
174	[FSR2007] 1701	11	15:28:28.0	−57:01:12	50	···	···	···	···	···	···	···	OC2
175	[DBS2003] 141	05	15:28:32.0	−56:22:29	96	8.78	0.56	K	···	···	···	···	EC2
176	VVV CL053	14	15:27:45.0	−55:48:38	156	3.10/10.17	0.48/0.48	K	···	···	···	···	OC0
177	VVV CL054	14	15:31:36.0	−56:10:20	108	9.56	0.49	K	···	···	···	···	EC2
178	[DBS2003] 142	05	15:32:13.0	−55:52:06	72	6.67	0.50	KC	···	···	···	···	EC1
179	[DBS2003] 143	05	15:32:53.0	−55:56:21	46	6.67	0.50	KC	1.00	0.35	53	53	EC1
180	Lynga 4	01	15:33:19.0	−55:14:11	360	1.10	0.17	S	1300	260	35	35	OC2
181	Lynga 5	01	15:41:54.0	−56:39:00	600	1.95	0.35	S	50.0	15.0	134	134	OC2
182	[FSR2007] 1703	11	15:41:55.0	−54:59:48	151	···	···	···	···	···	···	···	OC2
183	[MCM2005b] 61	09	15:45:59.0	−55:10:28	84	4.32/9.35	0.47/0.47	K	···	···	···	···	EC2
184	[DBS2003] 94	05	15:42:18.0	−53:58:28	66	2.67	0.47	KC	···	···	···	···	EC1
185	G3CC 26	17	15:43:18.0	−54:07:23	81	2.67	0.47	KC	···	···	···	···	EC1
186	Teutsch 81	02	15:52:27.6	−55:36:58	108	···	···	···	···	···	···	···	OC2
187	VVV CL055	14,17	15:43:36.1	−53:57:48	47	2.67	0.47	KC	···	···	···	···	EC1
188	[DBS2003] 96	05	15:44:45.0	−54:06:41	178	2.67	0.47	KC	1.75	0.61	197	201	EC2
189	[DBS2003] 97	05	15:45:09.0	−54:10:30	66	2.67	0.47	KC	···	···	···	···	EC2
190	[MCM2005b] 62	09	15:45:05.0	−54:08:14	216	2.67	0.47	KC	···	···	···	···	EC2
191	IRAS 15411−5352 Cluster	15	15:44:59.7	−54:02:05	27	2.67	0.47	KC	1.75	0.61	197	202	EC1
192	G3CC 27	17	15:46:20.3	−54:10:35	54	1.40	0.48	K	···	···	···	···	EC1
193	[MCM2005b] 63	09	15:49:50.0	−54:38:42	96	3.05	0.46	K	···	···	···	···	EC2
194	VVV CL056	14	15:52:38.0	−54:34:38	54	3.23	0.45	KC	···	···	···	···	OC0
195	[DBS2003] 146	05	15:53:04.0	−54:35:03	122	3.23	0.45	KC	···	···	···	···	EC1
196	[MCM2005b] 64	09	15:55:37.0	−54:38:38	24	2.61	0.46	S	···	···	···	···	OC1
197	[DBS2003] 147	05	15:54:37.0	−54:08:47	48	4.92	0.49	K	···	···	···	···	EC2
198	[FSR2007] 1709	11	15:57:34.0	−54:21:47	662	···	···	···	···	···	···	···	OC2
199	[DBS2003] 148	05	15:54:42.0	−53:47:46	70	10.93	0.45	K	···	···	···	···	EC2

Table B.1: continued.

ID	Name	Cat	RAJ2000	DECJ2000	Diam	Dist	e_Dist	ref_Dist	Age	e_Age	ref_Age	ref_Conf	Morph_type
200	ASCC 83	01	15:50:13.0	−52:48:00	1512	0.60	0.09	S	251	116	116	116	OC2
201	G3CC 28	17	15:52:42.6	−53:09:48	31	6.33	0.66	KC	···	···	···	···	EC1
202	[MCM2005b] 65	09	15:57:50.0	−54:02:09	144	2.97	0.45	KC	···	···	···	···	EC2
203	[MCM2005b] 66	09	15:57:27.0	−53:57:44	120	2.97	0.45	KC	···	···	···	···	EC2
204	G3CC 29	17	15:57:58.9	−53:58:02	58	2.97	0.45	KC	···	···	···	···	EC1
205	[DBS2003] 149	05	15:54:07.0	−53:11:32	80	6.33	0.66	KC	1.00	0.35	53	53	EC1
206	[MCM2005b] 67	09	15:58:33.0	−53:58:21	120	2.97	0.45	KC	···	···	···	···	OC0
207	Moffat 1	01	16:01:30.0	−54:06:60	420	2.10	0.31	S	10.0	3.5	147	147	OC2
208	[DBS2003] 98	05	15:59:38.0	−53:45:25	99	2.97	0.45	KC	···	···	···	···	EC1
209	[DBS2003] 150	05	15:58:46.0	−53:16:27	93	3.17/10.91	0.44/0.44	K	···	···	···	···	OC0
210	[MCM2005b] 68	09,11	15:54:46.1	−52:31:47	53	1.80	0.30	S	1000	600	85	85	OC2
211	G3CC 30	17	15:55:48.4	−52:43:00	82	2.80	0.46	K	···	···	···	···	EC1
212	Trumpler 23	01	16:00:49.0	−53:32:10	300	1.90	0.28	S	900	180	35	35	OC2
213	VVV CL057	14	16:02:11.0	−53:22:37	28	5.07/9.05	0.46/0.46	K	···	···	···	···	EC1
214	G3CC 31	17	16:01:47.0	−53:11:40	73	3.31	0.43	K	···	···	···	···	EC1
215	NGC 6031	01	16:07:35.0	−54:00:54	180	1.82	0.27	S	117	23	128	128	OC2
216	[CMG2010] G329.337+0.147	15	16:00:33.1	−52:44:46	84	7.08	0.50	KC	1.00	0.35	53	53	EC1
217	VVV CL058	14	16:02:19.0	−52:55:28	56	9.21	0.45	K	···	···	···	···	EC1
218	[DBS2003] 151	05	16:00:56.0	−52:36:17	36	7.08	0.50	KC	···	···	···	···	EC1
219	[MCM2005b] 69	09	16:04:53.0	−53:00:30	108	2.33	0.46	K	···	···	···	···	OC0
220	[MCM2005b] 70	09	16:00:27.0	−52:10:49	48	···	···	···	···	···	···	···	OC2
221	G3CC 32	17	16:00:09.4	−51:36:52	56	3.32	0.43	K	···	···	···	···	EC1
222	[DBS2003] 152	05	16:00:55.0	−51:36:16	48	···	···	···	···	···	···	···	OC2
223	[DBS2003] 153	05	16:07:38.0	−52:31:11	36	9.07	0.45	K	···	···	···	···	EC1
224	Lynga 6	01	16:04:52.0	−51:55:60	300	1.79	0.27	S	35.0	10.5	165	165	OC2
225	[DBS2003] 154	05	16:09:30.0	−52:15:44	53	4.30	0.39	KC	···	···	···	···	EC2
226	[DBS2003] 155	05	16:10:15.0	−52:08:31	48	4.30	0.39	KC	···	···	···	···	OC0
227	Ruprecht 115	01	16:12:52.0	−52:24:00	300	2.00	0.33	S	398	92	156	156	OC2
228	VVV CL061	14	16:11:28.0	−52:01:33	44	4.30	0.39	KC	···	···	···	···	EC2
229	[DBS2003] 156	05	16:12:15.0	−52:02:47	161	4.30	0.39	KC	···	···	···	···	EC1
230	VVV CL062	14	16:12:08.0	−51:58:08	78	4.30	0.39	KC	···	···	···	···	EC2
231	VVV CL059	14	16:05:52.0	−50:47:49	90	5.05	0.41	K	25.0	7.5	41	41	EC2
232	VVV CL060	14	16:11:23.0	−51:42:49	96	5.55	0.46	KC	···	···	···	···	EC2
233	[MCM2005b] 71	09	16:12:25.0	−51:51:43	72	4.30	0.39	KC	···	···	···	···	OC0
234	[DBS2003] 157	05	16:12:20.0	−51:46:14	106	4.30	0.39	KC	···	···	···	···	EC2
235	[MCM2005b] 72	09	16:12:30.0	−51:46:59	72	4.30	0.39	KC	···	···	···	···	EC2
236	[DBS2003] 159	05	16:06:25.0	−50:43:14	78	5.05	0.41	K	···	···	···	···	EC1
237	[DBS2003] 158	05	16:11:05.0	−51:31:03	126	5.55	0.46	KC	···	···	···	···	EC2
238	VVV CL063	14	16:12:42.0	−51:45:03	42	4.30	0.39	KC	···	···	···	···	EC1
239	Pismis 22	01,17	16:14:08.8	−51:52:07	195	1.00	0.40	S	40.0	15.0	174	174	OC2

Table B.1: continued.

ID	Name	Cat	RAJ2000	DECJ2000	Diam	Dist	e_Dist	ref_Dist	Age	e_Age	ref_Age	ref_Conf	Morph_type
240	[DBS2003] 144	05	16:12:09.0	−51:27:38	66	5.55	0.46	KC	···	···	···	···	EC2
241	[DBS2003] 145	05	16:12:09.0	−51:26:24	74	5.55	0.46	KC	···	···	···	···	EC2
242	[MCM2005b] 73	09	16:12:01.0	−51:22:06	36	···	···	···	···	···	···	···	OC2
243	SAI 123	13	16:08:17.4	−50:32:06	420	1.86	0.28	S	1585	317	96	96	OC2
244	Ruprecht 176	01	16:14:48.0	−51:19:60	180	···	···	···	···	···	···	···	OC2
245	[MCM2005b] 74	09	16:16:45.0	−51:17:04	60	3.49	0.41	CV(Ref:9)	···	···	···	···	EC2
246	VVV CL064	14	16:15:18.0	−50:56:48	56	3.49	0.41	CV(Ref:9)	···	···	···	···	EC2
247	VVV CL066	14	16:17:59.0	−51:15:10	98	3.49	0.41	CV(Ref:9)	···	···	···	···	EC2
248	[DBS2003] 99	05	16:13:04.0	−50:23:33	83	3.01	0.44	K	···	···	···	···	EC2
249	[MCM2005b] 75	09	16:14:22.0	−50:36:13	48	···	···	···	···	···	···	···	OC2
250	VVV CL070	14	16:21:48.0	−51:44:11	52	2.00	0.90	S	600	120	41	41	OC2
251	[DBS2003] 160	05	16:16:56.0	−50:47:26	54	3.49	0.41	CV(Ref:9)	2.75	0.96	197	200	EC2
252	[DBS2003] 161	05	16:17:05.0	−50:47:19	113	3.49	0.41	CV(Ref:9)	2.75	0.96	197	200	EC2
253	[MCM2005b] 76	09	16:19:43.0	−51:03:37	120	3.49	0.41	CV(Ref:9)	···	···	···	···	EC2
254	VVV CL065	14	16:17:31.0	−50:32:30	64	6.08	0.52	K	···	···	···	···	EC1
255	[MCM2005b] 77	09	16:17:27.0	−50:30:39	60	6.08	0.52	K	···	···	···	···	OC0
256	[DBS2003] 100	05	16:20:26.0	−50:54:27	65	3.49	0.41	CV(Ref:9)	···	···	···	···	OC0
257	[DBS2003] 102	05	16:15:01.0	−49:50:41	78	3.15	0.43	K	···	···	···	···	EC2
258	[DBS2003] 162	05	16:20:35.0	−50:41:23	90	3.49	0.41	CV(Ref:9)	···	···	···	···	EC2
259	[DBS2003] 163	05	16:18:37.0	−50:18:58	48	3.49	0.41	CV(Ref:9)	···	···	···	···	EC2
260	[MCM2005b] 78	09	16:21:08.0	−50:39:57	84	3.49	0.41	CV(Ref:9)	···	···	···	···	EC2
261	ESO 226−06	01	16:24:14.0	−51:09:06	240	···	···	···	···	···	···	···	OC2
262	[FBD2005] G333.1−0.4	15	16:21:01.5	−50:35:26	127	3.49	0.41	CV(Ref:9)	···	···	···	82	EC1
263	[DBS2003] 164	05	16:19:23.0	−50:09:27	66	3.49	0.41	CV(Ref:9)	···	···	···	···	EC2
264	Lynga 8	01	16:20:04.0	−50:13:59	180	1.05	0.16	S	2000	1000	166	166	OC2
265	VVV CL069	14	16:21:34.0	−50:27:29	120	3.49	0.41	CV(Ref:9)	···	···	···	···	EC2
266	VVV CL068	14	16:21:28.0	−50:26:24	20	3.49	0.41	CV(Ref:9)	···	···	···	···	EC2
267	[DBS2003] 165	05	16:21:31.0	−50:25:04	82	3.49	0.41	CV(Ref:9)	2.75	0.96	197	196	EC1
268	[DBS2003] 166	05	16:21:27.0	−50:00:43	104	3.49	0.41	CV(Ref:9)	···	···	···	···	OC1
269	[BDB2003] G333.60−00.21	04	16:22:10.0	−50:05:49	90	3.49	0.41	CV(Ref:9)	···	···	···	88	EC1
270	VVV CL071	14	16:22:16.0	−50:04:30	50	3.49	0.41	CV(Ref:9)	···	···	···	···	EC2
271	VVV CL072	14	16:23:49.0	−50:14:20	116	3.49	0.41	CV(Ref:9)	···	···	···	···	OC0
272	[DBS2003] 167	05	16:23:24.0	−49:32:28	147	10.21	0.36	K	···	···	···	···	OC0
273	[FSR2007] 1725	11	16:30:27.0	−50:07:46	79	···	···	···	···	···	···	···	OC2
274	[MCM2005b] 79	09	16:21:42.0	−48:43:40	84	9.89	0.35	K	···	···	···	···	OC1
275	Lynga 9	01	16:20:41.0	−48:31:44	360	1.70	0.26	S	700	140	35	35	OC2
276	Pismis 23	01	16:23:58.0	−48:53:33	60	2.60	0.60	S	300	100	180	180	OC2
277	[FSR2007] 1727	11	16:29:52.0	−49:45:08	130	···	···	···	···	···	···	···	OC2
278	NGC 6134	01	16:27:46.0	−49:09:06	360	0.91	0.14	S	929	186	128	128	OC2
279	G3CC 33	17	16:29:23.5	−49:12:25	63	2.86	0.45	K	···	···	···	···	EC1

Table B.1: continued.

ID	Name	Cat	RAJ2000	DECJ2000	Diam	Dist	e_Dist	ref_Dist	Age	e_Age	ref_Age	ref_Conf	Morph_type
280	Hogg 19	01	16:28:57.0	−49:06:00	240	2.60	0.39	S	2500	1250	215	215	OC2
281	NGC 6167	01	16:34:34.0	−49:46:18	420	1.11	0.17	S	77.1	23.1	128	128	OC2
282	Teutsch 82	02	16:30:58.1	−48:23:57	132	···	···	···	···	···	···	···	EC2
283	VVV CL073	14	16:30:24.0	−48:13:06	40	···	···	···	···	···	···	···	OC2
284	VVV CL078	14	16:35:09.0	−48:46:24	82	11.57	0.41	K	···	···	···	···	EC2
285	VVV CL075	14	16:33:30.0	−48:03:35	54	9.98	0.33	K	···	···	···	···	EC1
286	VVV CL074	14	16:32:06.0	−47:49:32	66	···	···	···	···	···	···	···	OC2
287	Ruprecht 120	01	16:35:10.0	−48:16:60	180	1.98	0.33	S	100	23	156	156	OC2
288	Patchick 94	(01),02	16:29:35.7	−47:18:38	78	···	···	···	···	···	···	···	OC2
289	RCW 108 IR Cluster	04	16:40:01.0	−48:52:03	54	1.30	0.20	Ref:252	1.00	0.35	252	252,59,60	EC2
290	[DBS2003] 103	05	16:39:60.0	−48:46:58	38	1.19	0.31	S	···	···	···	···	OC2
291	VVV CL076	14	16:33:48.0	−47:38:49	40	···	···	···	···	···	···	···	EC2
292	[MCM2005b] 80	09	16:34:12.0	−47:36:16	48	···	···	···	···	···	···	···	OC0
293	VVV CL077	14	16:34:48.0	−47:32:49	30	7.57	0.52	K	···	···	···	···	EC2
294	VVV CL079	14	16:35:22.0	−47:28:33	30	···	···	···	···	···	···	···	OC2
295	VVV CL082	14	16:40:39.0	−48:16:07	68	3.02	0.45	K	···	···	···	···	EC2
296	[DBS2003] 168	05	16:36:45.0	−47:31:26	46	10.23	0.32	K	···	···	···	···	EC2
297	G3CC 34	17	16:37:48.5	−47:38:53	49	3.15	0.44	KC	···	···	···	···	EC1
298	VVV CL080	14	16:38:56.0	−47:27:01	50	3.15	0.44	KC	···	···	···	···	EC2
299	[DBS2003] 169	05	16:38:50.0	−47:17:34	66	6.16	0.35	K	···	···	···	···	OC0
300	[DBS2003] 171	05	16:38:11.0	−47:04:08	35	11.53	0.39	K	···	···	···	···	EC2
301	Patchick 93	02	16:36:05.0	−46:42:18	90	···	···	···	···	···	···	···	OC0
302	VVV CL081	14	16:39:43.0	−47:06:57	20	···	···	···	···	···	···	···	OC2
303	Hogg 20	01	16:44:30.0	−47:38:00	240	···	···	···	···	···	···	···	OC2
304	Hogg 21	01	16:45:37.0	−47:44:00	240	···	···	···	···	···	···	···	OC2
305	IRAS 16353−4636 Cluster	15	16:39:03.2	−46:42:29	12	7.63	0.68	K	···	···	···	12	EC1
306	NGC 6200	01	16:44:07.0	−47:27:48	840	2.05	0.31	S	8.47	2.97	128	128	OC2
307	Lynga 11	01	16:38:09.0	−46:19:00	240	2.30	0.50	S	630	126	179	179	OC2
308	VVV CL085	14	16:45:26.0	−47:13:02	80	···	···	···	···	···	···	···	OC2
309	[MCM2005b] 81	09	16:40:24.0	−46:23:38	72	12.80	0.52	K	3.70	1.29	70	70	OC1
310	G3CC 35	17	16:42:43.2	−46:43:36	65	3.03	0.46	K	···	···	···	···	EC1
311	NGC 6178	01	16:35:47.0	−45:38:36	300	1.01	0.15	S	17.7	6.2	128	128	OC2
312	NGC 6204	01	16:46:09.0	−47:00:60	300	1.20	0.20	S	80.0	24.0	50	50	OC2
313	Hogg 22	01	16:46:37.0	−47:05:00	180	1.22	0.18	S	6.03	2.11	128	128	OC2
314	Ruprecht 121	01	16:41:42.0	−46:09:00	480	···	···	···	···	···	···	···	OC2
315	[DBS2003] 173	05,17	16:40:17.3	−45:39:48	97	4.40	0.34	K	···	···	···	···	OC0
316	G3CC 36	17	16:41:15.7	−45:48:23	97	2.08	0.55	K	···	···	···	···	EC1
317	G3CC 37	17	16:45:08.6	−46:22:50	80	3.01	0.46	K	···	···	···	···	EC1
318	[DBS2003] 105	05	16:43:16.0	−46:05:59	62	3.45	0.42	K	···	···	···	···	EC2
319	Teutsch 83	02	16:40:35.3	−45:27:52	138	···	···	···	···	···	···	···	OC0

Table B.1: continued.

ID	Name	Cat	RAJ2000	DECJ2000	Diam	Dist	e_Dist	ref_Dist	Age	e_Age	ref_Age	ref_Conf	Morph_type
320	BH 197	01	16:46:30.0	−45:51:36	240	···	···	···	···	···	···	···	OC2
321	Westerlund 1	01,17	16:47:04.4	−45:50:46	180	4.00	0.60	S	4.00	1.40	91	91	OC0
322	G3CC 38	17	16:45:59.1	−45:38:44	53	2.83	0.49	K	···	···	···	···	EC1
323	ASCC 85	01	16:47:31.0	−45:27:36	1584	1.20	0.18	S	26.3	12.1	116	116	OC2
324	VVV CL086	14	16:48:15.0	−45:26:06	70	···	···	···	···	···	···	···	OC2
325	[DBS2003] 174	(05),17	16:48:12.4	−45:21:39	81	4.05	0.36	K	···	···	···	···	EC2
326	VVV CL087	14	16:48:50.0	−45:09:32	120	3.67	0.40	K	···	···	···	···	EC2
327	NGC 6216	01	16:49:24.0	−44:43:42	240	4.30	0.80	S	35.0	15.0	174	174	OC2
328	VVV CL090	14,17	16:54:03.1	−45:18:50	51	2.49	0.55	KC	···	···	···	···	EC1
329	[DBS2003] 106	05	16:54:17.0	−45:17:31	60	2.49	0.55	KC	···	···	···	38	EC2
330	VVV CL091	14	16:54:39.0	−45:14:09	160	2.49	0.55	KC	···	···	···	···	OC0
331	Lynga 14	01	16:55:04.0	−45:13:60	180	0.88	0.13	S	5.15	1.80	128	128	OC2
332	VVV CL088	14	16:52:34.0	−44:36:07	24	3.59	0.42	KC	···	···	···	···	EC2
333	BH 200	01	16:49:56.0	−44:10:60	300	1.48	0.22	S	22.4	6.7	46	46	OC2
334	[MCM2005b] 82	09	16:52:56.0	−44:26:03	36	3.59	0.42	KC	···	···	···	···	OC0
335	NGC 6249	01	16:57:41.0	−44:48:42	300	0.98	0.15	S	24.3	7.3	128	128	OC2
336	Lynga 13	01	16:48:53.0	−43:25:60	540	···	···	···	···	···	···	···	OC2
337	[DBS2003] 175	05	16:52:36.0	−43:23:28	89	5.01	0.29	K	···	···	···	···	EC2
338	[MCM2005b] 83	09	16:53:28.0	−43:23:42	48	···	···	···	···	···	···	···	OC2
339	VVV CL089	14	16:53:47.0	−43:16:03	68	7.04	0.35	K	···	···	···	···	OC1
340	VVV CL092	14	16:54:56.0	−43:21:46	54	5.88/9.80	0.25/0.25	K	···	···	···	···	EC1
341	VVV CL093	14,17	16:56:02.6	−43:04:48	66	12.12	0.43	K	···	···	···	···	EC1
342	[FSR2007] 1744	(11),13	16:51:35.8	−42:25:47	180	3.13	0.47	S	708	326	96	96	OC2
343	NGC 6231	01	16:54:10.0	−41:49:30	840	1.65	0.19	S	3.00	1.05	211	210	OC2
344	[DBS2003] 176	05,17	16:59:23.7	−42:34:38	87	2.73	0.57	K	···	···	···	···	OC0
345	[DBS2003] 177	05	17:04:13.0	−42:20:02	48	2.39	0.64	KC	···	···	···	38	EC1
346	G3CC 39	17	17:04:06.6	−42:18:57	51	2.39	0.64	KC	···	···	···	···	EC2
347	[MCM2005b] 84	09	17:04:38.0	−42:18:13	24	···	···	···	···	···	···	···	OC2
348	[MCM2005b] 85	09	17:04:22.0	−42:15:07	24	···	···	···	···	···	···	···	OC2
349	[DBS2003] 178	05	17:02:10.0	−41:46:48	121	5.04	0.29	K	···	···	···	···	EC1
350	Teutsch 84	(01),02	17:04:20.1	−42:04:24	240	2.20	0.33	S	1000	230	122	122	OC2
351	Trumpler 24	01	16:57:00.0	−40:40:00	3600	1.14	0.17	S	8.30	2.90	128	128	OC0
352	[MCM2005b] 86	09	17:04:40.0	−41:42:21	72	···	···	···	···	···	···	···	OC2
353	BH 211	01	17:02:11.0	−41:05:60	240	1.38	0.21	S	1585	317	46	46	OC2
354	G3CC 40	17	17:05:09.7	−41:29:26	75	2.87	0.58	K	···	···	···	···	EC1
355	[DBS2003] 113	05	17:00:35.0	−40:33:44	119	1.61	0.78	CV(Ref:131)	2.75	0.96	197	197	EC2
356	[DBS2003] 114	05	16:59:10.0	−40:12:05	115	1.61	0.78	CV(Ref:131)	2.50	0.88	219	219	EC2
357	[MCM2005b] 87	09	17:05:55.0	−41:08:47	96	···	···	···	···	···	···	···	OC2
358	[DBS2003] 117	05	16:59:39.0	−40:11:22	114	1.61	0.78	CV(Ref:131)	···	···	···	···	EC2
359	[DBS2003] 116	05	17:09:34.0	−41:35:58	116	2.23	0.70	K	···	···	···	220	EC1

Table B.1: continued.

ID	Name	Cat	RAJ2000	DECJ2000	Diam	Dist	e_Dist	ref_Dist	Age	e_Age	ref_Age	ref_Conf	Morph_type
360	[MCM2005b] 88	09	17:04:31.0	−40:46:31	108	1.61	0.78	CV(Ref:131)	···	···	···	···	EC2
361	[MCM2005b] 89	09	17:04:20.0	−40:44:47	120	1.61	0.78	CV(Ref:131)	···	···	···	···	EC2
362	[MCM2005b] 90	09	17:05:53.0	−40:41:09	84	10.33	0.24	K	···	···	···	···	OC2
363	ESO 332−22	01	17:07:29.0	−40:48:48	420	···	···	···	···	···	···	···	OC2
364	VVV CL096	14	17:11:41.0	−41:19:03	34	2.34	0.70	K	···	···	···	···	EC2
365	VVV CL097	14	17:11:46.0	−41:18:13	40	2.34	0.70	K	···	···	···	···	EC2
366	NGC 6268	01	17:02:10.0	−39:43:42	360	1.05	0.16	S	224	45	55	55	OC2
367	VVV CL094	14	17:07:54.0	−40:31:39	40	10.15	0.22	K	···	···	···	···	EC1
368	VVV CL095	14	17:10:55.0	−39:41:49	60	3.00	1.40	S	200	40	41	41	OC2
369	Teutsch 85	01,(02)	17:13:14.0	−39:42:23	240	1.26	0.30	S	600	120	37	37	OC2
370	Moffat 2	01	17:14:28.0	−39:46:00	120	2.20	0.90	S	···	···	···	···	OC2
371	[DBS2003] 179	05,17	17:11:31.7	−39:10:36	128	6.30	0.19	KC	3.50	1.50	40	40	OC0
372	G3CC 41	17	17:14:27.3	−39:12:35	62	6.30	0.19	KC	···	···	···	···	EC1
373	VVV CL098	14	17:13:06.0	−38:59:45	40	12.50	0.53	K	···	···	···	···	EC2
374	NGC 6318	01	17:16:11.0	−39:25:30	240	2.10	0.50	S	158	36	178	178	OC2
375	G3CC 42	17	17:12:08.1	−38:30:54	38	1.33	0.36	C(Ref:257)	···	···	···	···	EC1
376	[MCM2005b] 91	09	17:12:26.0	−38:31:27	132	1.33	0.36	C(Ref:257)	···	···	···	···	EC2
377	[DBS2003] 118	05	17:18:24.0	−39:19:05	96	1.94	0.90	KC	4.20	1.47	197	203	EC2
378	[FSR2007] 1755	(01),11	17:12:20.0	−38:27:44	382	1.33	0.36	C(Ref:257)	···	···	···	···	OC0
379	Teutsch 86	02	17:15:45.0	−38:43:32	78	···	···	···	···	···	···	···	OC2
380	VVV CL100	14	17:19:15.0	−39:04:34	40	1.94	0.90	KC	7.50	2.62	41	41	EC1
381	G3CC 43	17	17:19:11.6	−39:00:08	52	1.94	0.90	KC	···	···	···	···	EC1
382	Havlen−Moffat 1	01	17:18:54.0	−38:48:60	300	3.35	0.50	S	3.00	1.05	243	243	OC2
383	[DBS2003] 119	05	17:20:06.0	−38:57:25	188	1.94	0.90	KC	···	···	···	220	EC1
384	VVV CL099	14	17:14:26.0	−38:09:51	60	0.70	0.60	S	35.0	15.0	41	41	OC2
385	BH 222	01,17	17:18:46.7	−38:17:06	127	6.00	2.70	S	60.0	30.0	180	180	OC2
386	[MCM2005b] 92	09	17:21:22.0	−37:47:19	132	3.46	0.64	K	···	···	···	···	OC0
387	[DBS2003] 120	05	17:21:13.0	−37:45:29	90	3.46	0.64	K	···	···	···	···	EC2
388	Ruprecht 123	01	17:23:26.0	−37:53:60	720	0.71	0.11	S	···	···	···	114	OC2
389	G3CC 44	17	17:19:26.7	−37:10:48	167	5.91	0.22	K	···	···	···	···	EC1
390	[DBS2003] 121	05	17:17:01.0	−36:22:10	114	1.74	0.31	C(Ref:153)	1.50	0.52	219	219	EC2
391	[DBS2003] 122	05	17:17:02.0	−36:20:58	66	1.74	0.31	C(Ref:153)	···	···	···	232,234	EC1
392	[DBS2003] 123	05	17:17:15.0	−36:20:18	174	1.74	0.31	C(Ref:153)	2.50	0.88	219	219	OC0
393	G3CC 45	17	17:19:04.7	−36:07:16	90	1.74	0.31	C(Ref:153)	···	···	···	···	EC2
394	NGC 6334 V	04	17:19:57.0	−35:57:31	177	1.74	0.31	C(Ref:153)	···	···	···	226	EC2
395	[BDS2003] 97	06	17:20:03.0	−35:58:18	72	1.74	0.31	C(Ref:153)	···	···	···	226	OC0
396	[BDS2003] 98	06	17:20:03.0	−35:55:58	48	1.74	0.31	C(Ref:153)	···	···	···	226	EC2
397	Bochum 13	01	17:17:24.0	−35:32:60	840	1.08	0.16	S	6.65	2.33	128	128	OC2
398	NGC 6334 IV	04	17:20:17.0	−35:54:55	120	1.74	0.31	C(Ref:153)	···	···	···	168	EC2
399	[BDS2003] 99	06	17:18:59.0	−35:41:48	89	1.74	0.31	C(Ref:153)	···	···	···	···	OC0

Table B.1: continued.

ID	Name	Cat	RAJ2000	DECJ2000	Diam	Dist	e_Dist	ref_Dist	Age	e_Age	ref_Age	ref_Conf	Morph_type
400	BH 223	01	17:20:41.0	−35:52:60	360	1.74	0.31	C(Ref:153)	···	···	···	···	EC2
401	NGC 6334 III	04	17:20:32.0	−35:51:29	80	1.74	0.31	C(Ref:153)	···	···	···	226	EC2
402	NGC 6334 II	04	17:20:45.0	−35:49:23	108	1.74	0.31	C(Ref:153)	···	···	···	226	EC2
403	NGC 6334 I	04,07	17:20:53.0	−35:46:57	107	1.74	0.31	C(Ref:153)	···	···	···	233,169,170	EC1
404	NGC 6334E IR Cluster	04	17:20:51.0	−35:46:08	24	1.74	0.31	C(Ref:153)	···	···	···	233,169,170	EC2
405	[BDS2003] 164	06	17:25:32.0	−36:21:58	48	3.51	0.72	K	···	···	···	39	EC2
406	[DB2001] Cl 38	04	17:23:23.0	−35:53:44	21	4.95/11.34	0.39/0.39	K	···	···	···	···	EC1
407	[BDS2003] 165	06	17:29:17.0	−36:40:03	100	2.21	1.11	KC	···	···	···	220	EC1
408	[BDS2003] 166	06	17:29:02.0	−36:33:53	99	2.21	1.11	KC	···	···	···	···	EC2
409	G3CC 46	17	17:26:43.1	−36:09:18	93	<1.96	-	K	···	···	···	256	EC1
410	G3CC 47	17	17:23:15.6	−34:48:53	84	1.74	0.31	C(Ref:153)	···	···	···	···	EC1
411	[DB2001] Cl 39	04	17:28:19.0	−35:04:15	18	5.93	0.24	K	···	···	···	···	EC1
412	ESO 392−13	01	17:26:52.0	−34:41:12	600	···	···	···	···	···	···	···	OC2
413	AH03 J1725−34.4	01,06	17:25:32.5	−34:24:12	124	1.74	0.31	C(Ref:153)	···	···	···	64	EC2
414	Pismis 24	01	17:24:43.0	−34:12:23	120	1.74	0.31	C(Ref:153)	1.74	0.61	139	139,248	OC0
415	[DB2001] Cl 40	04	17:30:28.0	−34:41:30	96	3.25	0.99	K	···	···	···	73,126,38	EC1
416	Collinder 333	01	17:31:31.0	−34:00:60	420	0.86	0.13	S	794	366	115	115	OC2
417	Ruprecht 126	01	17:35:01.0	−34:16:00	300	···	···	···	···	···	···	···	OC2
418	[DB2001] Cl 41	04	17:30:24.0	−33:11:10	50	4.21	0.80	K	···	···	···	73	EC2
419	Trumpler 27	01	17:36:20.0	−33:30:60	360	1.21	0.18	S	11.6	4.0	128	128	OC2
420	Antalova 4	01	17:32:39.0	−32:57:24	210	···	···	···	···	···	···	···	OC2
421	Antalova 2	01	17:29:42.0	−32:28:60	180	3.50	0.53	S	1259	252	46	46	OC2
422	[BDS2003] 102	06	17:32:52.0	−32:34:33	92	···	···	···	···	···	···	···	OC2
423	Antalova 3	01	17:30:34.0	−32:12:30	1260	···	···	···	···	···	···	···	OC2
424	NGC 6404	01	17:39:37.0	−33:14:48	300	2.42	0.36	S	500	100	49	49	OC2
425	NGC 6383	01	17:34:48.0	−32:34:00	1200	1.30	0.10	S	2.50	0.88	190	191	OC2
426	BH 231	01	17:31:56.0	−31:54:36	120	···	···	···	···	···	···	···	OC2
427	[DB2000] 50	(01),03	17:36:09.9	−32:24:05	130	···	···	···	···	···	···	···	OC2
428	Trumpler 28	01	17:36:60.0	−32:29:00	300	1.34	0.20	S	19.5	6.8	128	128	OC2
429	[BDS2003] 167	06	17:37:18.0	−32:10:48	39	<3.39/17.19	-/4.16	K	···	···	···	···	EC2
430	NGC 6405	01	17:40:20.0	−32:15:12	1200	0.47	0.02	S	71.0	21.3	165	165	OC2
431	G3CC 48	17	17:43:37.5	−30:33:51	57	<5.35	-	K	···	···	···	···	EC1
432	[DB2000] 52	03	17:42:28.1	−29:56:23	48	8.23	0.20	C(ID:438)	···	···	···	73,38	OC0
433	Ruprecht 130	01	17:47:32.0	−30:06:00	180	2.10	0.40	S	50.0	15.0	174	174	OC2
434	[DB2001] Cl 42	04	17:44:53.0	−29:40:48	111	<6.58/>9.88	-/-	K	···	···	···	···	EC2
435	BH 245	01	17:46:16.0	−29:42:00	60	1.10	0.30	S	15.0	10.0	175	175	OC2
436	[DB2000] 55	03	17:44:24.4	−29:12:13	31	···	···	···	···	···	···	73	OC2
437	Collinder 347	01	17:46:18.0	−29:19:60	600	1.51	0.23	S	12.0	4.2	132	132	OC2
438	Nuclear Star Cluster	04	17:45:40.0	−29:00:28	42	8.23	0.20	Ref:95	···	···	···	214	EC1
439	[DB2000] 1	03	17:46:51.2	−29:03:47	39	···	···	···	···	···	···	···	OC2

Table B.1: continued.

ID	Name	Cat	RAJ2000	DECJ2000	Diam	Dist	e_Dist	ref_Dist	Age	e_Age	ref_Age	ref_Conf	Morph_type
440	Arches Cluster	04	17:45:50.0	−28:49:22	23	8.23	0.20	C(ID:438)	2.50	0.88	74	74,221	EC2
441	Ruprecht 131	01	17:49:16.0	−29:14:60	420	0.60	0.09	S	1479	681	115	115	OC2
442	Quintuplet Cluster	04	17:46:15.0	−28:49:35	30	8.23	0.20	C(ID:438)	4.00	1.40	78	78	OC0
443	[DB2000] 5	(01),03,(17)	17:47:07.0	−28:46:04	24	···	···	···	···	···	···	73	EC2
444	[DB2000] 6	(01),03	17:47:09.6	−28:46:26	40	···	···	···	···	···	···	73	EC2
445	[DB2000] 18	(01),03	17:42:48.4	−28:06:28	74	···	···	···	···	···	···	···	OC2
446	Collinder 351	01	17:49:00.0	−28:44:09	504	1.31	0.20	S	160	32	228	228	OC2
447	[DB2000] 10	(01),03	17:50:17.6	−28:53:40	36	···	···	···	···	···	···	73	EC2
448	[DB2000] 11	(01),03	17:50:24.1	−28:53:06	60	···	···	···	···	···	···	73	EC2
449	[DB2000] 12	(01),03	17:50:16.4	−28:51:42	50	···	···	···	···	···	···	···	OC0
450	G3CC 49	17	17:47:23.7	−28:22:59	140	8.10	0.20	Ref:95,Ref:192	···	···	···	···	EC2
451	[DB2000] 17	03	17:45:57.7	−27:53:16	35	···	···	···	···	···	···	···	OC2
452	Ruprecht 133	01	17:52:29.0	−28:40:00	300	···	···	···	···	···	···	···	OC2
453	[DB2000] 26	03	17:48:41.5	−28:01:42	37	5.90	2.00	Ref:31	1.00	0.35	38	38	EC1
454	[DB2000] 27	03	17:54:11.6	−28:41:53	76	···	···	···	···	···	···	···	OC2
455	Ruprecht 168	01	17:52:46.0	−28:26:00	240	0.82	0.12	S	2000	1000	228	228	OC2
456	[DB2000] 28	(01),03	17:53:28.7	−28:20:52	82	···	···	···	···	···	···	···	OC2
457	[DB2000] 31	(01),03	17:50:49.5	−27:47:07	47	···	···	···	···	···	···	···	OC2
458	Czernik 37	01	17:53:17.0	−27:22:10	300	1.70	0.26	S	600	120	35	35	OC2
459	[DB2000] 35	03	17:45:48.6	−26:15:03	42	···	···	···	···	···	···	···	OC2
460	[DB2000] 42	03	17:50:43.1	−26:17:29	49	···	···	···	···	···	···	···	OC2
461	[BDS2003] 104	06	17:54:25.0	−25:51:36	60	<3.97/15.41	-/2.95	K	···	···	···	···	OC0
462	[DB2000] 49	(01),03	17:58:34.0	−26:06:55	48	2.50	0.40	Ref:111	···	···	···	···	EC1
463	G3CC 50	17	17:53:34.5	−25:19:57	56	3.54	1.36	K	···	···	···	···	EC2
464	Ruprecht 137	01	18:00:16.0	−25:13:39	336	1.45	0.22	S	800	160	228	228	OC2
465	Ruprecht 169	01	17:59:22.0	−24:46:01	312	1.39	0.21	S	1000	200	228	228	OC2
466	Ruprecht 136	01	17:59:18.0	−24:41:60	180	···	···	···	···	···	···	···	OC2
467	Ruprecht 138	01	17:59:56.0	−24:40:57	360	0.93	0.14	S	2000	1000	228	228	OC2
468	[BDS2003] 106	06	18:01:35.0	−24:50:06	90	···	···	···	···	···	···	···	OC2
469	G3CC 51	17	17:57:33.9	−23:58:05	65	1.91	1.68	K	···	···	···	···	EC1
470	[BDS2003] 108	06	18:00:43.0	−24:04:55	27	1.28	0.09	Ref:150	···	···	···	38,101	EC2
471	[BDS2003] 107	06	18:00:42.0	−24:04:23	59	1.28	0.09	Ref:150	···	···	···	38,101	EC2
472	Hourglass Nebula Cluster	06	18:03:41.0	−24:22:40	105	1.30	0.10	C(ID:473)	1.50	0.52	6	6	EC1
473	NGC 6530	01	18:04:31.0	−24:21:30	840	1.30	0.10	S	1.50	0.52	236	236	OC0
474	[BDS2003] 109	06	18:02:01.0	−23:57:40	96	12.14	0.71	K	···	···	···	···	OC0
475	[FSR2007] 22	(01),11	17:56:28.0	−23:11:34	281	···	···	···	···	···	···	···	OC2
476	Bochum 14	01	18:01:60.0	−23:40:60	120	0.97	0.20	S	9.91	3.47	128	128	OC2
477	Ruprecht 139	01	18:01:03.0	−23:32:00	720	0.55	0.08	S	1122	517	115	115	OC2
478	G3CC 52	17	18:01:57.6	−23:12:26	50	2.70	0.50	C(Ref:48)	···	···	···	···	EC1
479	NGC 6514	01,(07)	18:02:42.0	−22:58:18	1680	2.70	0.50	C(Ref:48)	···	···	···	193	OC0

Table B.1: continued.

ID	Name	Cat	RAJ2000	DECJ2000	Diam	Dist	e_Dist	ref_Dist	Age	e_Age	ref_Age	ref_Conf	Morph_type
480	Teutsch 72	02	18:02:50.2	−22:49:00	180	2.70	0.50	C(Ref:48)	···	···	···	···	OC1
481	NGC 6546	01	18:07:22.0	−23:17:48	840	0.94	0.14	S	70.6	21.2	128	128	OC2
482	NGC 6531	01	18:04:13.0	−22:29:24	840	1.21	0.18	S	11.7	4.1	128	128	OC2
483	Teutsch 14b	02	18:03:32.1	−22:08:17	30	1.72	0.41	C(ID:484)	···	···	···	···	OC2
484	Teutsch 14a	(01),02	18:03:31.3	−22:07:32	132	1.72	0.41	S	100	20	37	37	OC2
485	ESO 589−26	01	18:02:14.0	−21:54:54	150	···	···	···	···	···	···	···	OC2
486	[BDS2003] 110	06	18:02:05.0	−21:48:12	62	···	···	···	···	···	···	···	OC2
487	[BDS2003] 111	06	18:02:06.0	−21:46:21	88	···	···	···	···	···	···	···	OC2
488	ASCC 93	01	18:08:13.0	−22:15:36	1944	2.50	0.38	S	16.6	7.6	116	116	OC0
489	G3CC 53	17	18:06:59.3	−21:54:55	126	1.51	0.75	Ref:136	···	···	···	···	EC2
490	[BDS2003] 3	06	18:06:15.0	−21:37:27	63	4.45	0.48	K	···	···	···	···	EC2
491	[FSR2007] 31	(01),11,13	18:06:28.4	−21:22:60	244	1.60	0.24	S	1100	220	36	36	OC2
492	vdBergh 113	01	18:08:36.0	−21:25:00	840	3.47	0.52	S	31.6	14.6	115	115	OC2
493	G3CC 54	17	18:05:31.3	−20:53:21	42	···	···	···	···	···	···	···	EC1
494	[FSR2007] 35	(01),11	18:04:16.0	−20:11:27	115	···	···	···	···	···	···	···	OC2
495	SGR 1806−20 Cluster	04	18:08:39.0	−20:24:39	42	8.86	1.61	S	4.00	1.40	80	15,80	OC2
496	[BDB2003] G010.16−00.36	04	18:09:27.0	−20:19:30	69	2.77	1.07	SC	0.60	0.21	89	30,89	EC2
497	[FSR2007] 39	(01),11	18:07:05.3	−19:55:01	59	3.50	0.53	S	1000	200	86	86	OC2
498	[BDS2003] 112	06	18:08:56.0	−20:05:30	74	2.77	1.07	SC	···	···	···	25	EC2
499	[BDS2003] 113	06	18:08:60.0	−20:04:57	75	2.77	1.07	SC	···	···	···	25	EC2
500	[BDB2003] G010.62−00.38	04,17	18:10:28.6	−19:55:50	53	2.77	1.07	SC	···	···	···	···	EC1
501	NGC 6554	01	18:08:59.0	−18:26:06	1200	···	···	···	···	···	···	···	OC2
502	Markarian 38	01	18:15:17.0	−19:00:00	120	1.47	0.22	S	7.62	2.67	128	128	OC2
503	Turner 2	01	18:17:11.0	−18:49:27	456	1.19	0.18	S	100	20	228	228	OC2
504	Turner 3	01	18:17:34.0	−18:51:50	120	1.79	0.27	S	29.0	8.7	237	237	OC2
505	[BDS2003] 6	06	18:16:51.0	−18:41:52	48	4.15	0.43	K	···	···	···	···	EC2
506	Turner 4	01	18:17:08.0	−18:41:60	210	2.33	0.35	S	10.0	3.5	237	237	OC2
507	[BDS2003] 7	06	18:10:55.0	−17:41:25	108	···	···	···	···	···	···	···	OC2
508	[MDF2011] cl2	15	18:14:08.0	−18:00:15	60	3.79	0.48	KC	···	···	···	···	EC2
509	Collinder 469	01	18:16:34.0	−18:18:42	180	1.48	0.22	S	63.0	18.9	128	128	OC2
510	[MCM2005b] 1	09	18:13:55.0	−17:56:55	96	3.79	0.48	KC	···	···	···	···	OC1
511	[MFD2008] Cluster	(13)	18:13:24.0	−17:53:31	210	3.79	0.48	KC	4.25	1.49	144	141,144	OC2
512	[BDB2003] G012.80−00.19	04	18:14:13.0	−17:55:55	48	3.79	0.48	KC	···	···	···	···	EC1
513	[MDF2011] cl1	15	18:14:22.0	−17:56:10	108	3.79	0.48	KC	···	···	···	···	EC2
514	NGC 6603	01	18:18:26.0	−18:24:24	360	3.60	0.54	S	200	100	16	16	OC2
515	[BDS2003] 114	06	18:14:40.0	−17:52:07	59	3.79	0.48	KC	···	···	···	···	EC1
516	[BDS2003] 115	06	18:14:05.0	−17:28:40	108	4.53	0.36	K	···	···	···	···	EC2
517	[FSR2007] 46	(01),11	18:14:20.0	−17:19:19	380	···	···	···	···	···	···	···	OC2
518	NGC 6561	01	18:10:30.0	−16:43:30	900	3.40	0.51	S	8.32	3.83	115	115	OC2
519	Mol 45 Cluster	12	18:17:24.1	−17:22:12	48	11.61	0.37	K	···	···	···	76	EC1

Table B.1: continued.

ID	Name	Cat	RAJ2000	DECJ2000	Diam	Dist	e_Dist	ref_Dist	Age	e_Age	ref_Age	ref_Conf	Morph_type
520	[BDS2003] 116	06	18:14:36.0	−16:45:17	59	4.44	0.36	K	...	...	...	...	EC2
521	[MCM2005b] 2	09	18:16:20.0	−16:50:51	84	3.67	0.47	K	...	...	...	...	EC2
522	G3CC 55	17	18:18:12.4	−16:57:18	57	1.12	0.13	C(ID:525)	...	...	...	...	EC1
523	NGC 6613	01	18:19:58.0	−17:06:06	300	1.30	0.19	S	16.7	5.8	128	128	OC2
524	NGC 6596	01	18:17:33.0	−16:38:60	600	1.10	0.17	S	398	183	115	115	OC2
525	G3CC 56	17	18:18:55.2	−16:47:15	124	1.12	0.13	Ref:212	...	...	...	...	EC2
526	Mol 50 Cluster	12	18:19:07.6	−16:11:21	48	4.91	0.30	K	...	...	...	76	EC1
527	NGC 6618	(01),04,(07)	18:20:30.0	−16:10:55	98	1.99	0.13	Ref:255	1.00	0.35	184	104	EC2
528	[MCM2005b] 4	09	18:20:32.0	−16:02:59	84	1.99	0.13	C(ID:527)	...	...	...	...	EC2
529	ASCC 94	01	18:15:36.0	−14:59:24	1800	0.85	0.13	S	603	277	116	116	OC2
530	Kronberger 25	01,(02)	18:22:40.0	−14:43:41	48	1.22	0.18	S	50.0	15.0	229	229	OC2
531	Kharchenko 2	01	18:22:17.0	−14:35:24	168	1.99	0.30	S	100	20	117	117	OC2
532	Kharchenko 3	01	18:22:47.0	−14:38:00	480	2.13	0.32	S	100	20	117	117	OC2
533	Kronberger 2	01,(02)	18:21:19.0	−14:17:24	150	3.07	0.46	S	100	20	229	229	OC2
534	NGC 6611	01,(07),17	18:18:44.0	−13:47:50	303	1.80	0.10	S	2.50	0.88	161	161	OC0
535	Dolidze 28	01	18:25:29.0	−14:39:21	696	...	...	...	...	...	...	...	OC2
536	G3CC 57	17	18:19:08.4	−13:36:29	61	1.80	0.10	C(ID:534)	...	...	...	107	EC1
537	Trumpler 32	01	18:17:30.0	−13:21:00	300	1.72	0.26	S	300	60	117	117	OC1
538	[FSR2007] 55	11	18:24:42.0	−13:23:40	122	...	...	...	...	...	...	...	OC2
539	[BDS2003] 8	06	18:25:01.0	−13:15:47	108	4.30	0.35	K	...	...	...	2	EC2
540	Bica 3	01	18:26:04.0	−13:03:32	210	1.64	0.25	S	26.0	7.8	17	17	OC2
541	[MCM2005b] 6	09	18:25:38.0	−12:28:38	36	...	...	...	...	...	...	...	OC2
542	[MCM2005b] 7	09	18:25:44.0	−12:26:18	72	4.09	0.36	K	...	...	...	...	OC0
543	NGC 6625	01	18:22:50.0	−11:57:42	924	1.34	0.20	S	500	100	228	228	OC2
544	NGC 6631	01	18:27:11.0	−12:01:48	360	2.60	0.50	S	400	100	208	208	OC2
545	Dias 6	01	18:30:30.0	−12:18:59	360	2.19	0.33	S	515	115	17	17	OC2
546	Ruprecht 141	01	18:31:18.0	−12:19:00	960	1.80	0.27	S	30.0	20.0	47	47	OC2
547	[FSR2007] 59	(01),11	18:29:04.0	−11:58:31	324	...	...	...	...	...	...	...	OC2
548	Ruprecht 142	01	18:32:11.0	−12:13:47	396	1.74	0.26	S	400	80	228	228	OC2
549	Ruprecht 143	01	18:32:36.0	−12:08:00	300	...	...	...	...	...	...	...	OC2
550	[FSR2007] 60	11	18:30:05.0	−11:29:07	79	...	...	...	...	...	...	...	OC2
551	[MCM2005b] 8	09	18:28:49.0	−10:55:55	60	...	...	...	...	...	...	...	OC2
552	Ruprecht 144	01	18:33:34.0	−11:25:00	720	1.60	0.24	S	450	100	47	47	OC2
553	Ruprecht 170	01	18:25:12.0	−10:00:00	480	...	...	...	...	...	...	...	OC2
554	NGC 6649	01	18:33:27.0	−10:24:12	300	1.37	0.21	S	36.8	11.0	128	128	OC2
555	[MCM2005b] 9	09,17	18:34:08.7	−09:14:05	50	4.20	1.26	S	21.0	6.3	143	143	OC1
556	[BDS2003] 117	06	18:34:27.0	−09:15:44	66	4.62	0.36	Ref:45	...	...	...	...	EC2
557	[MCM2005b] 10	09	18:34:47.0	−08:47:17	96	...	...	...	...	...	...	...	OC2
558	[BDS2003] 118	06	18:34:20.0	−08:21:27	72	5.69	0.34	K	...	...	...	...	EC2
559	[BDS2003] 119	06	18:33:54.0	−08:07:32	50	7.03	0.50	K	...	...	...	...	EC2

Table B.1: continued.

ID	Name	Cat	RAJ2000	DECJ2000	Diam	Dist	e_Dist	ref_Dist	Age	e_Age	ref_Age	ref_Conf	Morph_type
560	[BDS2003] 120	06	18:34:25.0	−07:54:50	33	3.25	0.41	Ref:10	···	···	···	106	EC1
561	Trumpler 34	01	18:39:48.0	−08:24:60	300	1.20	0.18	S	200	100	215	215	OC2
562	NGC 6664	01	18:36:37.0	−07:48:48	720	1.16	0.17	S	14.5	5.1	128	128	OC2
563	[BDS2003] 121	06	18:34:10.0	−07:18:01	66	6.43	0.49	K	···	···	···	···	EC1
564	Alicante 8	15	18:34:51.0	−07:14:00	420	7.44	0.50	S	18.0	6.3	50	154	OC0
565	[FSR2007] 72	11	18:35:12.0	−07:10:53	497	···	···	···	···	···	···	···	OC2
566	Quartet Cluster	16	18:36:17.0	−07:05:02	90	6.30	2.00	S	6.00	2.10	142	142	OC2
567	RSGC 1	06,17	18:37:57.5	−06:52:54	160	7.44	0.50	S	12.0	4.2	66	66,81	OC2
568	G3CC 58	17	18:36:20.5	−06:38:57	39	2.92	0.45	K	···	···	···	···	OC1
569	W42 IR Cluster	04	18:38:15.0	−06:47:50	54	4.05	0.37	K	···	···	···	29	EC1
570	RSGC 2	(01),04,17	18:39:19.9	−06:01:43	261	7.39	0.50	S	15.5	5.4	65	65	OC0
571	NGC 6683	01	18:42:13.0	−06:12:42	180	1.20	0.18	S	10.0	3.5	132	132	OC2
572	G3CC 59	17	18:38:40.0	−05:35:06	49	4.75	0.75	Ref:136	···	···	···	···	EC1
573	Teutsch 145	(01),02	18:42:28.9	−05:15:12	114	2.70	0.41	S	225	75	34	34	OC2
574	Andrews−Lindsay 5	01	18:44:19.0	−04:55:48	138	···	···	···	···	···	···	···	OC2
575	Dolidze 33	01	18:41:18.0	−04:21:37	540	···	···	···	···	···	···	···	OC2
576	Dolidze 34	01	18:41:54.0	−04:16:37	240	···	···	···	···	···	···	···	OC2
577	Dolidze 32	01	18:41:05.0	−04:04:51	588	···	···	···	···	···	···	···	OC2
578	Trumpler 35	01	18:42:54.0	−04:08:00	300	1.21	0.18	S	72.8	21.8	128	128	OC2
579	[BDS2003] 123	06	18:44:15.0	−04:17:55	33	3.18	0.43	K	···	···	···	···	EC1
580	[BDS2003] 124	06	18:43:16.0	−03:35:42	72	7.21	0.83	K	···	···	···	···	EC2
581	[BDS2003] 10	06	18:46:21.0	−03:47:42	94	10.83	0.41	K	···	···	···	···	OC0
582	Alicante 7	15	18:44:29.5	−03:30:02	660	7.18	1.52	S	20.0	6.0	155,57,1	155	OC2
583	[FSR2007] 87	(01),11	18:45:60.0	−03:37:15	281	···	···	···	···	···	···	···	OC2
584	RSGC 3	16,17	18:45:20.9	−03:23:54	233	7.18	1.52	S	20.0	6.0	57,1	57,1	OC2
585	[FSR2007] 89	(01),11	18:48:39.0	−03:30:34	73	2.20	0.33	S	1000	200	36	36	OC2
586	[FSR2007] 90	(01),11	18:50:20.0	−03:34:42	158	···	···	···	···	···	···	···	OC2
587	[MCM2005b] 11	09	18:46:41.0	−02:44:07	60	···	···	···	···	···	···	···	OC2
588	[BDS2003] 125	06	18:46:04.0	−02:39:19	29	6.47	0.62	CV(Ref:157)	···	···	···	185	EC1
589	W43 IR Cluster	04	18:47:36.0	−01:56:33	72	6.47	0.62	CV(Ref:157)	···	···	···	28	EC1
590	[MCM2005b] 12	09	18:47:48.0	−01:56:30	96	6.47	0.62	CV(Ref:157)	···	···	···	···	OC0
591	Berkeley 79	01	18:45:12.0	−01:12:60	360	2.30	0.34	S	65.0	30.0	209	209	OC2
592	G3CC 60	17	18:48:02.1	−01:33:26	50	11.42	0.46	K	···	···	···	···	EC1
593	GLIMPSE C01	16	18:48:50.1	−01:29:47	29	6.30	0.73	S	450	150	69	69	OC2
594	Berkeley 80	01	18:54:22.0	−01:12:60	240	1.43	0.21	S	398	80	235	235	OC2
595	[FSR2007] 98	(01),11	18:47:31.0	00:36:51	108	···	···	···	···	···	···	···	OC2
596	Teutsch 146	(01),02	18:51:33.5	00:11:10	96	3.80	0.57	S	400	100	34	34	OC2
597	[MCM2005b] 13	09	18:53:53.0	00:37:39	60	3.00	1.00	S	65.0	35.0	142	142	OC2
598	[BDS2003] 126	06	18:52:51.0	00:55:28	66	6.83	0.50	K	···	···	···	···	EC1
599	[BDS2003] 128	06	18:53:22.0	01:13:58	42	1.56	0.12	C(ID:601)	···	···	···	···	EC2

Table B.1: continued.

ID	Name	Cat	RAJ2000	DECJ2000	Diam	Dist	e_Dist	ref_Dist	Age	e_Age	ref_Age	ref_Conf	Morph_type
600	[BDS2003] 127	06	18:53:20.0	01:14:39	74	1.56	0.12	C(ID:601)	···	···	···	25	EC2
601	G3CC 61	17	18:53:18.4	01:24:47	91	1.56	0.12	Ref:124	···	···	···	217,218	EC1
602	Mol 75 Cluster	12	18:53:38.1	01:50:27	72	1.56	0.12	C(ID:601)	···	···	···	246,76	EC1
603	[MCM2005b] 14	09,17	18:58:06.3	01:36:45	74	2.21	0.22	C(ID:604)	···	···	···	87	EC2
604	[BDS2003] 129	06,17	18:58:12.8	01:40:36	85	2.21	0.22	Ref:258	···	···	···	···	EC1
605	[BDS2003] 130	06	18:56:32.0	02:24:03	111	10.08	0.47	K	···	···	···	···	OC0
606	Mol 82 Cluster	12	18:59:03.2	03:53:17	18	6.55	0.50	K	···	···	···	76	EC2
607	[MVM2011] G37.51−0.46	15	19:01:27.0	03:51:60	60	6.10	1.83	S	···	···	···	140	OC2
608	[MCM2005b] 15	09,17	19:03:40.7	05:10:20	95	10.25	0.48	K	···	···	···	···	EC2
609	[MCM2005b] 16	09	19:04:20.0	05:06:33	36	···	···	···	···	···	···	···	OC2
610	G3CC 62	17	19:06:60.0	05:23:05	53	3.63	0.55	K	···	···	···	···	EC1
611	[BDS2003] 11	06	19:08:43.0	05:36:02	84	3.01	0.52	K	···	···	···	···	EC2
612	Mol 84 Cluster	12	18:59:14.3	07:04:52	54	1.93	0.46	K	···	···	···	76	EC1
613	Juchert 3	(01),02	19:07:33.0	06:17:10	180	0.83	0.12	S	891	178	46	46	OC2
614	[BDS2003] 131	06	19:10:31.0	07:52:57	89	4.30	0.50	Ref:222	2.30	1.10	223	223	EC2
615	[MCM2005b] 17	09	19:09:19.0	08:11:45	36	···	···	···	···	···	···	···	OC2
616	[MCM2005b] 18	09	19:09:50.0	08:19:30	132	5.10	0.70	Ref:222	···	···	···	···	EC2
617	SGR 1900+14 Cluster	04	19:07:14.0	09:19:21	12	13.53	0.63	S	14.0	4.9	67	67,247	OC2
618	G3CC 63	17	19:11:38.7	08:46:40	52	7.68	0.84	K	···	···	···	···	EC1
619	[AH2003] 3,4	(04)	19:10:11.4	09:05:21	48	11.40	1.20	C(ID:621)	···	···	···	3	EC1
620	[AH2003] 2	15	19:10:21.9	09:05:04	42	11.40	1.20	C(ID:621)	···	···	···	3	EC1
621	W49A Welch Ring	(04)	19:10:14.0	09:06:19	36	11.40	1.20	Ref:99	···	···	···	61,3	EC1
622	[AH2003] 1	(04)	19:10:17.5	09:06:21	84	11.40	1.20	C(ID:621)	···	···	···	3,105	EC2
623	[BDS2003] 132	06	19:10:11.0	09:07:03	57	11.40	1.20	C(ID:621)	···	···	···	···	EC2
624	Alessi 56	(01),02,09	19:06:52.5	09:34:58	90	3.90	0.59	S	···	···	···	122	OC2
625	[BDS2003] 133	06	19:10:33.0	09:07:37	66	11.40	1.20	C(ID:621)	···	···	···	···	EC2
626	G3CC 64	17	19:14:26.8	09:22:44	63	4.40	0.60	Ref:222	···	···	···	···	EC1
627	Mol 99 Cluster	12	19:11:51.4	09:49:35	60	5.92	1.46	K	···	···	···	76	EC1
628	[MCM2005b] 20	09,17	19:12:24.2	09:57:27	84	4.50	1.30	S	7.00	2.45	142	142	OC2
629	Teutsch 148	02	19:10:26.6	10:18:34	72	···	···	···	···	···	···	···	OC2
630	IRAS 19110+1045 Cluster	15	19:13:20.6	10:50:47	90	4.40	0.60	C(Ref:222)	···	···	···	244	EC1
631	[BDS2003] 135	06	19:13:28.0	10:53:35	42	4.40	0.60	C(Ref:222)	···	···	···	244	EC1
632	[BDS2003] 134	06	19:13:27.0	10:54:27	72	4.40	0.60	C(Ref:222)	···	···	···	244	EC2
633	[BDB2003] G045.45+00.06	04	19:14:21.0	11:09:11	12	6.66	0.90	KC	···	···	···	77,32	EC1
634	[BDS2003] 136	06	19:14:09.0	11:12:32	68	6.66	0.90	KC	···	···	···	···	EC2
635	Berkeley 43	01	19:15:36.0	11:13:00	300	1.03	0.15	S	299	60	227	227	OC2
636	[BDS2003] 137	06	19:16:19.0	11:19:08	90	6.66	0.90	KC	···	···	···	···	EC2
637	[FSR2007] 123	(01),11	19:11:42.2	12:03:02	73	4.50	0.68	S	501	100	86	86	OC2
638	Juchert 1	(01),02	19:22:32.0	12:40:00	192	2.62	0.39	S	1259	252	46	46	OC2
639	G3CC 65	17	19:18:04.1	13:24:41	68	5.52	0.50	K	···	···	···	···	EC2

Table B.1: continued.

ID	Name	Cat	RAJ2000	DECJ2000	Diam	Dist	e_Dist	ref_Dist	Age	e_Age	ref_Age	ref_Conf	Morph_type
640	[FSR2007] 126	(01),11	19:21:09.0	13:46:30	374	···	···	···	···	···	···	···	OC2
641	[MCM2005b] 21	09	19:20:30.0	13:55:24	216	5.03	0.19	Ref:152	···	···	···	···	EC2
642	[BDS2003] 138	06	19:22:15.0	14:03:32	105	5.43	0.30	C(ID:657)	···	···	···	123	EC2
643	[BDS2003] 139	06	19:22:26.0	14:06:54	126	5.43	0.30	C(ID:657)	3.30	2.10	223	123,223	EC1
644	[BDS2003] 140	06	19:22:30.0	14:11:03	126	5.43	0.30	C(ID:657)	···	···	···	···	EC2
645	[BDS2003] 141	06	19:22:53.0	14:09:22	84	5.43	0.30	C(ID:657)	···	···	···	···	EC2
646	Teutsch 26	02	19:26:06.1	13:45:48	162	···	···	···	···	···	···	···	OC2
647	Kronberger 13	(01),02	19:25:14.9	13:56:44	90	1.38	0.21	S	400	80	229	229	OC2
648	[NKD2004] G49.2−0.3	15	19:23:02.0	14:16:37	90	5.43	0.30	C(ID:657)	···	···	···	123	EC2
649	[BDS2003] 142	06	19:23:04.0	14:28:05	60	5.43	0.30	C(ID:657)	···	···	···	123	EC2
650	[BDS2003] 143	06	19:23:14.0	14:27:33	81	5.43	0.30	C(ID:657)	···	···	···	···	EC2
651	[FSR2007] 129	(01),11	19:26:56.0	13:58:56	374	···	···	···	···	···	···	···	OC2
652	[BDS2003] 144	06	19:23:19.0	14:29:23	68	5.43	0.30	C(ID:657)	···	···	···	···	EC2
653	[BDS2003] 147	06	19:23:33.0	14:29:47	36	5.43	0.30	C(ID:657)	···	···	···	···	EC2
654	[BDS2003] 148	06	19:23:41.0	14:29:15	36	5.43	0.30	C(ID:657)	···	···	···	···	EC2
655	[BDS2003] 145	06	19:23:29.0	14:31:43	78	5.43	0.30	C(ID:657)	···	···	···	···	EC2
656	[BDS2003] 149	06	19:23:43.0	14:29:55	61	5.43	0.30	C(ID:657)	···	···	···	···	EC2
657	[BDS2003] 151	06	19:23:43.0	14:30:34	42	5.43	0.30	Ref:213	···	···	···	123	EC2
658	[BDS2003] 152	06	19:23:40.0	14:31:13	42	5.43	0.30	C(ID:657)	···	···	···	123,83	EC1
659	[BDS2003] 146	06	19:23:35.0	14:32:02	54	5.43	0.30	C(ID:657)	···	···	···	···	EC2
660	[BDS2003] 153	06	19:23:48.0	14:33:15	60	5.43	0.30	C(ID:657)	···	···	···	···	EC2
661	[BDS2003] 154	06	19:23:51.0	14:32:57	60	5.43	0.30	C(ID:657)	···	···	···	···	EC2
662	[BDS2003] 155	06	19:23:55.0	14:35:40	66	5.43	0.30	C(ID:657)	···	···	···	···	OC1
663	G3CC 66	17	19:21:47.7	15:14:20	55	10.17	0.54	K	···	···	···	···	EC2
664	Berkeley 45	01	19:19:12.0	15:43:00	120	2.35	0.35	S	355	71	227	227	OC2
665	G3CC 67	17	19:23:11.3	15:13:10	107	5.28	1.31	K	···	···	···	···	EC1
666	Alessi 57	(01),02	19:20:53.8	15:40:36	150	3.90	0.59	S	···	···	···	122	OC2
667	King 26	01	19:29:01.0	14:52:02	264	2.60	0.39	S	440	88	230	230	OC2
668	[FSR2007] 131	(01),11	19:30:42.2	15:25:59	83	5.50	0.83	S	631	126	86	86	OC2
669	[FSR2007] 133	(01),11,13	19:29:47.7	15:33:44	278	1.90	0.28	S	600	120	19	19	OC2
670	[BDS2003] 157	06	19:26:02.0	16:20:10	119	5.14	0.97	K	···	···	···	···	EC2
671	[FSR2007] 134	(01),11	19:24:30.4	16:53:32	64	3.20	0.48	S	794	159	86	86	OC2
672	Mol 103 Cluster	12	19:23:36.2	17:28:58	72	3.98	0.57	Ref:159	···	···	···	76	EC1
673	[MCM2005b] 22	09	19:25:00.0	17:27:38	120	10.01	0.56	K	···	···	···	···	EC2
674	Berkeley 47	01	19:28:36.0	17:22:06	180	1.07	0.16	S	473	95	227	227	OC2
675	G3CC 68	17	19:31:54.7	16:56:44	44	5.00	0.50	K	···	···	···	···	EC1
676	G3CC 69	17	19:29:18.0	17:56:41	119	1.71	0.62	KC	···	···	···	···	EC1
677	G3CC 70	17	19:29:32.3	18:00:57	76	1.71	0.62	KC	···	···	···	···	EC2
678	[BDS2003] 12	06,17	19:30:22.7	18:20:44	66	1.71	0.62	KC	···	···	···	···	EC2
679	Teutsch 42	(01),02,09	19:30:13.1	18:32:12	60	6.66	1.21	S	3.00	1.05	100	100	OC1

Table B.1: continued.

ID	Name	Cat	RAJ2000	DECJ2000	Diam	Dist	e_Dist	ref_Dist	Age	e_Age	ref_Age	ref_Conf	Morph_type
680	[BDS2003] 156	06	19:31:43.0	18:41:57	108	7.00	1.00	Ref:222	···	···	···	···	EC2
681	Kronberger 79	(01),02	19:33:55.0	18:31:12	126	2.70	0.41	S	224	52	122	122	OC2
682	Teutsch 27	01,(02)	19:37:23.0	18:41:55	216	2.48	0.47	S	600	120	37	37	OC2
683	NGC 6802	01	19:30:35.0	20:15:42	300	1.79	0.21	S	955	330	109	109	OC2
684	[FSR2007] 142	(01),11	19:35:39.0	20:07:44	274	···	···	···	···	···	···	···	OC2
685	[MCM2005b] 24	09,17	19:36:29.8	20:32:60	82	4.57	2.22	K	2.00	1.00	160	160	EC2
686	G3CC 71	17	19:38:16.7	21:08:02	58	4.49	2.50	K	···	···	···	···	EC1
687	[FSR2007] 148	11	19:37:28.0	21:18:52	65	···	···	···	···	···	···	···	OC2
688	Czernik 40	01	19:42:36.0	21:09:14	864	3.05	0.93	S	794	183	133	133	OC2
689	G3CC 72	17	19:38:58.4	22:46:32	73	4.30	1.54	K	···	···	···	···	EC1
690	Collinder 404	01	19:42:28.0	23:05:16	48	2.16	0.10	C(ID:693)	···	···	···	···	EC2
691	NGC 6823	01,17	19:43:09.5	23:18:00	215	2.16	0.10	C(ID:693)	4.00	2.00	20	20	OC1
692	Mol 109 Cluster	(12),17	19:39:35.0	24:00:05	94	2.16	0.10	C(ID:693)	···	···	···	76	EC2
693	G3CC 73	17	19:43:09.9	23:44:14	120	2.16	0.10	Ref:254	···	···	···	13,137	EC1
694	Mol 110 Cluster	12	19:40:58.5	24:04:36	48	2.16	0.10	C(ID:693)	···	···	···	76	EC1
695	[FSR2007] 154	(01),(11),13	19:48:00.8	23:20:53	180	2.79	0.42	S	1122	224	96	96	OC2

Table B.2: Catalog of embedded and open clusters within the Galactic range $|l| \leq 60°$ and $|b| \leq 1.5°$ (additional information).

ID	Clump_sep (Diam/2)	Cf[a]	Vlsr (km s^{-1})	ref_Vlsr	KDA	Morph	HII_reg	Bub	IRDC	Complex
1	>3.77	00	···	···	···	exp	···	···	···	···
2	4.47	01	−39.40	249	T	exp	···	···	···	···
3	>7.46	00	···	···	···	exp	···	···	···	···
4	0.00	11	−38.50	187	T	p-emb.pah	···	···	···	···
5	>17.81	00	···	···	···	exp	···	···	···	···
6	0.00	11	9.40	249	F	emb.pah	[CH87] 300.479−0.192	···	···	···
7	0.91	01	−42.50	249	T	exp*	···	···	···	···
8	0.00	11	−40.90	249	T	emb	···	···	···	KC-01
9	0.00	11	−42.50	249	T	p-emb.pah	[CH87] 300.956+1.161	···	···	KC-01
10	0.00	11	−42.50	249	T	p-emb.pah	···	···	···	KC-01
11	0.46	11	−42.00	249	T	surr.bub-cen	···	Bub(ID:11)	···	KC-01
12	0.00	11	−40.10	249	T	p-emb.bub-cen-trig	[CH87] 301.109+0.969	Bub(ID:12)	···	KC-01
13	0.00	11	−39.60	249	T	emb.bub-edge	[WBH98] 12326−6245 (UC)	S169	SDC G301.147−0.228	···
14	5.55	00	···	···	···	exp	···	···	···	···
15	0.00	10	···	···	···	emb.bub-edge	···	S167	IRDC(ID:15)	···
16	1.29	01	−34.43	253	T	exp	···	···	···	···
17	8.72	01	−37.10	249	T	exp	···	···	···	···
18	2.75	01	−34.43	253	T	exp	···	···	···	···
19	0.00	10	···	···	···	p-emb.pah	···	···	···	···
20	0.13	10	···	···	···	p-emb.pah	[MCG2002] G302.4−0.1	···	···	···
21	>5.18	00	···	···	···	exp	···	···	···	···
22	8.85	01	26.40	187	F	exp	···	···	···	···
23	0.60	24	−32.00	51	T	surr	[CH87] 302.804+1.306	···	···	···
24	9.04	00	···	···	···	exp	···	···	···	···
25	0.00	11	30.88	253	F	emb.pah	···	S163	···	···
26	5.74	00	···	···	···	exp	···	S162	···	···
27	0.00	11	−26.21	84	N	p-emb	···	···	MSXDC G304.74+01.32	···
28	22.64	00	···	···	···	exp	···	···	···	···
29	6.76	00	···	···	···	exp	···	···	···	···
30	0.00	11	−36.10	249	NT	emb	···	···	IRDC(ID:30)	G305
31	0.00	11	−34.51	253	NT	p-emb.bub-cen-trig	PMN J1308−6215	Bub(ID:31)	···	G305
32	1.14	11	−38.30	249	NT	surr.bub-cen	[CH87] 305.254+0.204	S156	···	G305
33	0.00	11	−31.50	249	N	p-emb.bub-cen	[DWS84] G305.27−0.01	S155	···	G305
34	0.22	10	···	···	···	p-emb.pah	[DWS84] G305.27+0.17	···	···	G305
35	0.00	10	···	···	···	emb.pah	[DWS84] G305.32+0.07	S154	···	G305
36	1.20	20	···	···	···	surr	···	···	···	G305
37	0.00	11	−38.50	249	NT	emb.pah	[CH87] 305.363+0.179	···	···	G305
38	0.00	10	···	···	···	emb.bub-cen	···	S152	···	···
39	4.13	20	···	···	···	exp	···	···	···	G305

Table B.2: continued.

ID	Clump_sep	Cf[a]	Vlsr	ref_Vlsr	KDA	Morph	HII_reg	Bub	IRDC	Complex
40	1.89	21	−38.49	253	NT	exp.pah	···	···	···	G305
41	0.35	01	−20.80	43	F	few	···	···	···	···
42	0.00	11	−34.80	249	N	p-emb.bub-cen-trig	[CH87] 305.537+0.338	S150	···	G305
43	0.00	11	−38.80	249	NT	p-emb.bub-cen-trig	[CH87] 305.551−0.005	S149	···	G305
44	0.07	14	−30.00	51	N	p-emb.pah	[CH87] 305.807−0.063	···	···	G305
45	0.68	10	···	···	···	surr.bub-cen	···	···	···	···
46	0.00	10	···	···	···	p-emb.pah	···	···	···	···
47	0.24	11	−32.46	253	N	p-emb.pah	···	···	···	···
48	2.51	01	−32.46	253	N	exp	···	···	···	···
49	>2.80	00	···	···	···	exp	···	···	···	···
50	>6.80	00	···	···	···	exp	···	···	···	···
51	0.52	00	···	···	···	few	···	···	···	···
52	>7.09	00	···	···	···	exp	···	···	···	···
53	0.00	10	···	···	···	emb	···	···	IRDC(ID:53)	···
54	0.27	00	···	···	···	few	···	···	···	···
55	0.00	10	···	···	···	p-emb.pah	···	···	···	···
56	0.00	10	···	···	···	p-emb.pah	···	···	···	···
57	>3.62	00	···	···	···	exp	···	···	···	···
58	0.72	01	−36.50	249	F	exp*	···	···	···	···
59	>2.20	00	···	···	···	exp	···	···	···	···
60	5.08	01	−36.50	249	F	exp	···	···	···	···
61	6.82	01	36.70	187	F	exp	···	···	···	···
62	1.56	00	···	···	···	exp	···	···	···	···
63	10.70	00	···	···	···	exp	···	···	···	···
64	4.74	00	···	···	···	exp	···	···	···	···
65	3.35	13	−47.39	253	FT	exp.bub-cen-trig	[CH87] 308.647+0.579	S145	···	KC-02
66	13.72	23	−47.39	253	FT	exp.bub-cen	[CH87] 308.647+0.579	S145	···	KC-02
67	3.38	00	···	···	···	exp	···	···	···	···
68	1.75	00	···	···	···	exp	···	···	···	···
69	0.00	11	−50.44	84	FT	emb.pah	···	···	···	KC-02
70	3.14	00	···	···	···	exp	···	···	···	···
71	3.06	24	−47.00	51	FT	exp.bub-cen-trig	[CH87] 309.057+0.186	S143	···	KC-02
72	1.97	01	−48.30	187	T	exp	···	···	···	···
73	0.00	11	−16.40	187	F?	p-emb.pah	RMS G309.1760−00.0277 (UC)	···	···	···
74	1.00	00	···	···	···	exp	···	···	···	···
75	2.98	00	···	···	···	exp	···	···	···	···
76	0.35	00	···	···	···	few*	[KMO2009] G309.24−0.18	···	···	Gum 48d
77	0.15	11	−49.89	249	NT	p-emb.pah	···	···	···	Gum 48d
78	0.00	11	−42.00	253	N	emb	···	···	MSXDC G309.42−00.64	Gum 48d
79	0.00	11	−52.00	249	NT	emb.bub-edge	[CH87] 309.548−0.737 (bub)	S141	SDC G309.530−0.742	Gum 48d

Table B.2: continued.

ID	Clump_sep	Cf[a]	Vlsr	ref_Vlsr	KDA	Morph	HII_reg	Bub	IRDC	Complex
80	0.35	02	−42.00	253	···	exp*	···	···	···	···
81	9.20	01	−56.70	249	T	exp	···	···	···	···
82	0.00	11	−56.70	253	T	emb.pah	[CH87] 309.905+0.373	···	···	KC-03
83	0.00	11	−56.70	249	T	emb	[WBH98] 13471−6120 (UC)	···	···	KC-03
84	0.00	11	−59.04	253	T	emb	···	···	SDC G309.975+0.301	KC-03
85	0.00	13	−40.30	253	N	p-emb.pah	···	···	MSXDC G309.97+00.52	···
86	1.67	00	···	···	···	exp	···	···	···	···
87	4.79	00	···	···	···	exp	···	···	···	···
88	15.28	00	···	···	···	exp	···	···	···	···
89	0.70	00	···	···	···	few	···	···	···	···
90	9.83	01	−57.00	249	T	exp	···	···	···	···
91	2.14	01	28.92	253	F	exp	···	···	···	···
92	4.54	11	−48.00	182	T	exp.bub-cen	[CH87] 310.994+0.389	S137	···	···
93	3.29	00	···	···	···	exp	···	···	···	···
94	0.83	24	−57.00	51	T	few	[CH87] 311.197+0.752	S136	···	···
95	1.18	21	−57.96	253	T	surr.bub-cen	[CH87] 311.489+0.368	S135	···	KC-04
96	0.00	11	−58.92	84	T	p-emb.bub-cen	[CH87] 311.489+0.368	S134	···	KC-04
97	1.08	24	−47.00	51	N	surr	[CH87] 311.497−0.483	···	···	···
98	0.00	13	−49.13	253	FT	p-emb.pah	···	···	···	KC-05
99	0.00	10	···	···	···	p-emb.pah	···	···	···	···
100	0.00	11	−50.25	253	FT	p-emb.pah	[CH87] 311.894+0.100	···	···	KC-05
101	0.00	11	−48.35	253	F	p-emb.pah	[CH87] 311.922+0.229	···	···	KC-05
102	4.26	00	···	···	···	exp	···	···	···	···
103	0.25	01	−41.04	253	N	few*	···	···	···	···
104	0.00	11	−42.69	253	F	p-emb.bub-cen	···	Bub(ID:104)	···	KC-05
105	0.00	11	−47.10	249	F	emb.pah	[CH87] 312.112+0.314	···	···	KC-05
106	3.66	00	···	···	···	exp	···	···	···	···
107	0.00	11	−25.00	43	F	emb.pah	RMS G312.3834−00.4154 (UC)	···	···	···
108	8.73	00	···	···	···	exp	···	···	···	···
109	69.93	04	−47.00	51	···	exp.bub-cen	[CH87] 312.953−0.449	S123	···	···
110	1.74	01	−26.90	43	N	exp	···	···	···	···
111	0.42	11	−26.90	43	N	p-emb.bub-cen	[TUW2004] SFO 74	Bub(ID:111)	···	···
112	25.93	00	···	···	···	exp	···	···	···	···
113	0.00	11	−50.50	249	N	emb.pah	···	···	SDC G313.774−0.863	···
114	0.30	14	−53.40	146	T	p-emb.bub-cen	[MCG2002] G313.8+0.7	S121	···	···
115	0.98	00	···	···	···	exp	···	···	···	···
116	0.00	13	−60.30	249	T	p-emb	···	···	···	KC-06
117	1.04	13	−60.30	249	T	surr.bub-cen	···	S117	···	KC-06
118	0.00	11	−65.80	43	T	p-emb.pah	[CH87] 314.228+0.437	S116	···	KC-06
119	0.00	11	−50.00	249	N	emb	···	···	MSXDC G314.25+00.07	···

Table B.2: continued.

ID	Clump_sep	Cf[a]	Vlsr	ref_Vlsr	KDA	Morph	HII_reg	Bub	IRDC	Complex
120	>3.64	00	···	···	···	exp	···	···	···	···
121	>2.99	00	···	···	···	exp	···	···	···	···
122	0.15	00	···	···	···	few	···	···	···	···
123	6.87	00	···	···	···	exp	···	···	···	···
124	>41.44	00	···	···	···	exp	···	···	···	···
125	>9.97	00	···	···	···	exp	···	···	···	···
126	>7.46	00	···	···	···	exp	···	···	···	···
127	>49.72	00	···	···	···	exp	···	···	···	···
128	2.40	00	···	···	···	exp	···	···	···	···
129	2.77	01	−7.90	43	···	exp	···	···	···	···
130	0.00	11	−60.70	249	NT	p-emb.pah	[CH87] 316.156−0.492	···	···	···
131	0.00	11	−39.30	249	F	p-emb.pah	[VGO2007] 14416−5937 B	S111	···	IRAS 14416−5937
132	0.42	11	−39.60	187	F	surr.bub-cen	···	S111	···	IRAS 14416−5937
133	0.00	11	−38.10	249	F	p-emb.pah	[VGO2007] 14416−5937 A	S111	SDC G316.786−0.044	IRAS 14416−5937
134	0.00	11	−38.10	249	F	emb.pah	[VGO2007] 14416−5937 A	S110	···	IRAS 14416−5937
135	10.38	01	−38.10	249	···	exp	···	···	···	···
136	23.75	01	−49.46	253	···	exp	···	···	···	···
137	6.18	01	−49.46	253	···	exp	···	···	···	···
138	2.49	01	−44.20	205	···	exp	···	···	···	···
139	2.12	00	···	···	···	exp	···	···	···	···
140	7.21	00	···	···	···	exp	···	···	···	···
141	1.33	01	−40.20	249	N	exp	···	···	···	···
142	0.00	11	−43.04	253	N	emb	···	···	SDC G317.464−0.403	···
143	0.00	11	−35.50	249	N	emb	···	···	MSXDC G317.89−00.24	···
144	0.00	11	−49.30	249	N	emb	RMS G318.0498+00.0856 (UC)	···	IRDC(ID:144)	···
145	0.00	11	−37.36	253	N	emb.pah	···	···	···	···
146	2.43	00	···	···	···	exp	···	···	···	···
147	2.12	23	−16.00	249	F	exp.bub-cen	[CH87] 319.157−0.423	S100	···	···
148	0.00	11	−42.50	43	N	p-emb	···	···	···	···
149	0.00	11	−19.20	187	F	p-emb.pah	RMS G319.3618+00.0133 (UC)	···	···	KC-07
150	0.00	11	−11.60	43	F	emb.pah	[CH87] 319.380−0.025	···	···	KC-07
151	4.86	00	···	···	···	exp	···	···	···	···
152	0.00	11	−16.70	187	F	p-emb.pah	RMS G319.4519−00.0217 (UC)	···	···	KC-07
153	0.94	00	···	···	···	exp	···	···	···	···
154	0.00	11	−41.16	253	N	p-emb.pah	[CH87] 319.874+0.770	S97	···	KC-08
155	28.19	00	···	···	···	exp	···	···	···	···
156	0.55	02	−8.47	253	N	few	···	···	···	···
157	0.00	11	−36.30	43	N	p-emb.bub-cen-trig	[CH87] 320.153+0.780	S96	···	KC-08
158	0.00	11	−40.48	253	N	p-emb.pah	···	···	···	KC-08
159	0.00	14	−31.00	51	N	p-emb.pah	[CH87] 320.236+0.417	···	···	···

Table B.2: continued.

ID	Clump_sep	Cf[a]	Vlsr	ref_Vlsr	KDA	Morph	HII_reg	Bub	IRDC	Complex
160	0.00	13	−65.90	249	F	p-emb.pah	[CH87] 320.252−0.332	···	···	···
161	0.00	11	−51.27	84	N	p-emb	···	···	···	···
162	0.00	11	−9.30	249	F	p-emb.pah	PMN J1510−5817	···	···	MC-01
163	0.00	23	−9.30	249	F	p-emb.pah	PMN J1510−5817	···	···	MC-01
164	5.49	00	···	···	···	exp	···	···	···	···
165	2.43	00	···	···	···	exp	···	S92	···	···
166	0.24	21	−44.81	253	···	p-emb	···	S91	···	···
167	1.20	14	−56.00	51	F	surr.bub-cen-trig	[CH87] 321.105−0.549	Bub(ID:167)	···	···
168	0.00	10	···	···	···	p-emb.pah	···	···	···	···
169	0.00	11	−31.60	249	N	emb	···	···	SDC G321.936−0.003	MC-02
170	0.00	13	−31.60	249	N	p-emb	···	···	···	MC-02
171	0.00	11	−55.50	249	N	p-emb.pah	[CH87] 322.153+0.613	···	···	···
172	9.34	00	···	···	···	exp	···	···	···	···
173	0.00	11	−28.47	84	···	p-emb.pah	[CH87] 322.407+0.221	···	···	···
174	21.69	00	···	···	···	exp	···	···	···	···
175	0.00	11	−65.12	253	F?	p-emb.pah	···	···	···	···
176	0.55	11	−46.79	84	···	few.pah	···	···	···	···
177	0.00	11	−56.00	43	F?	p-emb.bub-cen	RMS G323.9158+00.0336	S84	···	···
178	0.00	14	−91.00	51	T	emb.pah	[CH87] 324.147+0.231	···	···	KC-09
179	0.00	11	−87.50	249	T	emb.pah	[CH87] 324.192+0.109	···	···	KC-09
180	>4.97	00	···	···	···	exp	···	···	···	···
181	>2.99	00	···	···	···	exp	···	···	···	···
182	4.27	00	···	···	···	exp	···	···	···	···
183	0.00	14	−65.00	51	···	p-emb.pah	[CH87] 326.141−0.328	···	···	···
184	0.00	11	−42.56	253	N	emb.bub-cen	[CH87] 326.441+0.914	Bub(ID:184)	···	KC-10
185	0.00	11	−40.20	253	N	emb	···	···	SDC G326.476+0.706	KC-10
186	17.52	00	···	···	···	exp	···	···	···	···
187	0.00	11	−36.70	253	N	emb	···	···	SDC G326.611+0.811	KC-10
188	0.00	11	−39.70	249	N	p-emb.pah	[CH87] 326.645+0.589	···	···	KC-10
189	0.00	13	−39.60	249	N	p-emb	···	S79	···	KC-10
190	0.12	11	−39.60	249	N	p-emb.bub-cen	···	S79	···	KC-10
191	0.00	11	−41.50	249	N	emb.pah	Wray 16−185	···	···	KC-10
192	0.00	11	−20.67	253	N	emb	···	···	SDC G326.796+0.386	···
193	0.00	11	−45.76	253	N	p-emb	···	···	···	···
194	1.32	23	−49.88	253	N	surr.pah	···	···	···	KC-11
195	0.00	11	−46.80	249	N	emb.pah	[CH87] 327.313−0.536	···	···	KC-11
196	5.99	21	−36.20	249	N	exp	RCW 98	S73	···	···
197	0.00	11	−74.50	249	N	p-emb.pah	[CH87] 327.759−0.351	···	···	···
198	0.77	01	−40.90	108	N	few	···	···	···	···
199	0.00	14	−45.00	51	F	p-emb.pah	[CH87] 327.985−0.086	S71	···	···

Table B.2: continued.

ID	Clump_sep	Cf[a]	Vlsr	ref_Vlsr	KDA	Morph	HII_reg	Bub	IRDC	Complex
200	0.39	00	···	···	···	few	···	···	···	···
201	0.00	11	−92.98	253	NT	emb	RMS G328.1642+00.5867 (UC)	···	···	KC-12
202	0.00	11	−42.50	43	N	p-emb.pah	···	···	···	KC-13
203	0.00	10	···	···	···	p-emb.bub-cen	···	Bub(ID:203)	···	KC-13
204	0.00	11	−44.10	249	N	emb	···	···	MSXDC G328.25−00.51	KC-13
205	0.00	11	−91.40	249	NT	emb.pah	[CH87] 328.310+0.448	···	···	KC-12
206	0.65	14	−43.00	51	N	surr.bub-cen	[CH87] 328.283−0.586	Bub(ID:206)	···	KC-13
207	3.03	00	···	···	···	exp	···	···	···	···
208	0.00	11	−46.60	249	N	emb.pah	[CH87] 328.593−0.518	···	···	KC-13
209	1.97	24	−47.00	51	···	surr	[CH87] 328.806−0.083	···	···	···
210	18.03	00	···	···	···	exp	···	···	···	···
211	0.00	11	−41.30	249	N	emb	[CH87] 328.812+0.637	···	MSXDC G328.80+00.64	···
212	3.01	00	···	···	···	exp	···	···	···	···
213	0.00	11	−77.58	84	···	emb.pah	···	···	···	···
214	0.00	11	−49.10	249	N	emb	···	···	MSXDC G329.18−00.32	···
215	>4.06	00	···	···	···	exp	···	···	···	···
216	0.00	11	−107.49	253	T	emb	[CH87] 329.353+0.144	···	···	KC-14
217	0.00	11	−76.10	43	F	emb.pah	RMS G329.4213−00.1619	···	···	···
218	0.00	11	−99.88	253	T	emb.pah	[CH87] 329.489+0.207	···	···	KC-14
219	1.04	13	−33.50	108	N	surr.bub-cen	···	S69	···	···
220	11.34	00	···	···	···	exp	···	···	···	···
221	0.00	11	−48.90	249	N	emb	···	···	MSXDC G330.03+01.05	···
222	11.51	00	···	···	···	exp	···	···	···	···
223	0.00	11	−80.65	253	F	emb.pah	[CH87] 330.305−0.385	···	···	···
224	0.23	00	···	···	···	few	···	···	···	···
225	0.00	11	−63.42	253	N	p-emb.bub-cen-trig	[CH87] 330.677−0.396	S67	···	KC-15
226	1.42	21	−63.17	253	N	surr	···	···	···	KC-15
227	2.99	01	−5.07	42	···	exp	···	···	···	···
228	0.00	11	−63.50	43	N	p-emb.bub-cen	···	Bub(ID:228)	···	KC-15
229	0.00	11	−67.82	253	N	emb.pah	[CH87] 331.110−0.506	···	···	KC-15
230	0.00	11	−69.27	253	N	p-emb.bub-cen	···	Bub(ID:230)	···	KC-15
231	0.18	13	−78.30	43	N	p-emb.pah	···	···	···	MC-03
232	0.00	11	−87.25	253	N	p-emb.bub-cen	[CH87] 331.259−0.186	Bub(ID:232)	···	KC-16
233	1.89	23	−64.90	249	N	surr	···	···	···	KC-15
234	0.00	11	−64.80	43	N	p-emb.bub-cen	[CH87] 331.314−0.336	S62	···	KC-15
235	0.00	13	−65.43	253	N	p-emb.bub-cen	···	S62	···	KC-15
236	0.00	11	−78.30	43	N	emb.bub-cen	[CH87] 331.354+1.072	S59	···	MC-03
237	0.00	14	−81.00	51	N	p-emb.pah	[CH87] 331.353−0.013	···	···	KC-16
238	0.00	11	−65.60	187	N	emb.pah	···	···	···	KC-15
239	1.39	00	···	···	···	exp	···	···	···	···

Table B.2: continued.

ID	Clump_sep	Cf[a]	Vlsr	ref_Vlsr	KDA	Morph	HII_reg	Bub	IRDC	Complex
240	0.00	11	−89.30	249	N	p-emb.bub-cen	[CH87] 331.517−0.069	Bub(ID:240)	···	KC-16
241	0.00	11	−88.10	249	N	p-emb.bub-cen-trig	[CH87] 331.517−0.069	Bub(ID:241)	···	KC-16
242	6.78	00	···	···	···	exp	···	···	···	···
243	5.13	00	···	···	···	exp	···	···	···	···
244	1.50	00	···	···	···	exp	···	···	···	···
245	0.00	11	−55.60	249	N	p-emb.pah	[CH87] 332.148−0.446	···	···	G333
246	0.00	21	−46.92	253	N	p-emb.pah	···	···	···	G333
247	0.00	11	−51.90	43	N	p-emb.bub-cen	···	S54	···	G333
248	0.00	11	−42.60	249	N	p-emb.pah	···	···	···	···
249	5.20	00	···	···	···	exp	···	···	···	···
250	>34.68	00	···	···	···	exp	···	···	···	···
251	0.00	11	−46.53	253	N	p-emb.bub-cen	[CH87] 332.541−0.111	Bub(ID:251)	···	G333
252	0.00	11	−46.53	253	N	p-emb.bub-cen-trig	[CH87] 332.541−0.111	Bub(ID:252)	···	G333
253	0.00	11	−49.20	249	N	p-emb.bub-cen	[CH87] 332.662−0.607	S51	···	G333
254	0.00	11	−95.00	43	N	emb.pah	RMS G332.7656−00.0080 (UC)	···	···	···
255	0.85	21	−95.00	43	N	surr	···	···	···	···
256	0.87	23	−57.30	249	N	surr	···	···	···	G333
257	0.00	11	−44.50	43	N	p-emb.bub-cen-trig	···	Bub(ID:257)	···	···
258	0.00	11	−54.17	253	N	p-emb.bub-cen-trig	[KC97c] G333.0−00.4	S48	···	G333
259	0.00	11	−45.30	187	N	p-emb.pah	[GS70] 333.0+00.0	···	···	G333
260	0.00	11	−55.99	253	N	p-emb	···	···	···	G333
261	>7.45	00	···	···	···	exp	···	···	···	···
262	0.00	11	−51.90	249	N	emb.pah	[CH87] 333.114−0.441	···	···	G333
263	0.00	11	−46.90	43	N	p-emb.pah	IRAS 16156−5002	···	···	G333
264	0.81	00	···	···	···	few	···	···	···	···
265	0.00	11	−51.60	249	N	p-emb.pah	[CH87] 333.292−0.371	···	···	G333
266	0.00	11	−51.60	249	N	p-emb.pah	[CH87] 333.292−0.371	···	···	G333
267	0.00	11	−50.20	249	N	emb.pah	[CH87] 333.292−0.371	···	···	G333
268	1.78	24	−53.70	250	N	exp	[WMG70] 333.6−00.1	···	···	G333
269	0.00	11	−47.07	253	N	emb.pah	[CH87] 333.610−0.208	···	···	G333
270	0.00	11	−47.07	253	N	p-emb.pah	···	···	···	G333
271	1.10	24	−49.90	250	N	surr	[WMG70] 333.7−00.5	···	···	G333
272	0.48	24	−70.00	51	F	surr	[CH87] 334.173+0.068	···	···	···
273	15.85	00	···	···	···	exp	···	···	···	···
274	2.37	24	−77.00	51	F	exp.bub-cen	[CH87] 334.529+0.825	S44	···	···
275	1.97	00	···	···	···	exp	···	···	···	···
276	0.45	20	···	···	···	exp*	···	···	···	···
277	9.23	00	···	···	···	exp	···	···	···	···
278	0.83	00	···	···	···	few	···	···	···	···
279	0.00	11	−38.40	249	N	emb	···	···	SDC G335.077−0.421	···

Table B.2: continued.

ID	Clump_sep	Cf[a]	Vlsr	ref_Vlsr	KDA	Morph	HII_reg	Bub	IRDC	Complex
280	1.35	00	···	···	···	exp	···	···	···	···
281	>2.95	00	···	···	···	exp	···	···	···	···
282	0.00	20	···	···	···	p-emb	···	···	···	···
283	9.96	00	···	···	···	exp	···	···	···	···
284	0.00	11	−47.40	249	F	p-emb.pah	[WBH98] 16313−4840 (UC)	···	···	···
285	0.00	11	−79.02	253	F	emb.pah	[CH87] 336.375−0.131	···	···	···
286	1.38	00	···	···	···	exp	···	···	···	···
287	7.51	01	−87.40	249	F	exp	···	···	···	···
288	24.97	00	···	···	···	exp	···	···	···	···
289	0.00	11	−23.40	187	N	p-emb	RCW 108	···	···	···
290	3.93	00	···	···	···	exp	···	···	···	···
291	0.22	20	···	···	···	p-emb	···	···	···	···
292	0.68	20	···	···	···	surr	···	···	···	···
293	0.00	11	−121.20	43	T	p-emb.pah	···	···	···	···
294	5.12	01	−120.90	253	T	exp	···	···	···	···
295	0.00	11	−39.09	84	N	p-emb	···	···	···	···
296	0.00	11	−74.97	253	F	p-emb.pah	[CH87] 337.147−0.181	···	···	···
297	0.00	11	−40.10	249	N	emb	···	···	MSXDC G337.16−00.38	KC-17
298	0.00	13	−41.35	253	N	p-emb.pah	[MCG2002] G337.4−0.4	···	···	KC-17
299	0.87	24	−101.00	51	N	surr	[CH87] 337.548−0.304	···	···	···
300	0.00	21	−49.50	249	F	p-emb	[KC97c] G337.6−00.1	···	···	···
301	0.59	20	···	···	···	surr	···	···	···	···
302	12.71	00	···	···	···	exp	···	···	···	···
303	>7.48	00	···	···	···	exp	···	···	···	···
304	>4.89	00	···	···	···	exp	···	···	···	···
305	0.00	11	−122.33	253	T	emb.pah	IRAS 16353−4636	···	···	···
306	2.05	00	···	···	···	exp	···	···	···	···
307	2.90	01	−62.20	187	N?	exp	···	···	···	···
308	15.22	00	···	···	···	exp	···	···	···	···
309	2.29	23	−30.30	249	F	exp	···	···	···	···
310	0.00	11	−37.80	43	N	emb	···	···	MSXDC G338.40−00.41	···
311	>5.98	00	···	···	···	exp	···	···	···	···
312	0.54	00	···	···	···	few	···	···	···	···
313	1.10	00	···	···	···	exp	···	···	···	···
314	0.61	00	···	···	···	few	···	···	···	···
315	0.44	11	−61.60	249	N	surr.bub-cen-trig	[CH87] 338.943+0.604	S29	···	···
316	0.00	11	−23.94	253	N	emb.pah	[WBH98] 16376−4542 (UC)	···	···	···
317	0.00	11	−36.90	187	N	emb	···	···	SDC G338.927−0.490	···
318	0.00	11	−43.90	187	N	p-emb.pah	[KC97c] G338.9−00.1	···	···	···
319	1.82	20	···	···	···	surr	···	···	···	···

Table B.2: continued.

ID	Clump_sep	Cf[a]	Vlsr	ref_Vlsr	KDA	Morph	HII_reg	Bub	IRDC	Complex
320	2.85	01	−38.30	187	···	exp	···	···	···	···
321	0.00	20	···	···	···	few	···	···	···	···
322	0.00	11	−33.50	249	N	emb	[CH87] 339.578−0.124	···	MSXDC G339.60−00.12	···
323	0.27	02	−51.20	43	N	exp*	···	···	···	···
324	5.05	00	···	···	···	exp	···	···	···	···
325	0.00	11	−53.00	249	N	p-emb.pah	[CH87] 340.047−0.253	···	···	···
326	0.13	13	−45.80	249	N	p-emb.pah	[KC97c] G340.3−00.2	S26	···	···
327	0.83	00	···	···	···	few	···	···	···	···
328	0.00	11	−28.33	253	N	emb	···	···	MSXDC G340.69−00.94	KC-18
329	0.00	11	−26.54	253	N	p-emb.pah	[CH87] 340.777−1.008	···	···	KC-18
330	0.82	13	−28.30	187	N	surr.bub-cen	···	Bub(ID:330)	···	KC-18
331	1.28	00	···	···	···	exp	···	···	···	···
332	0.00	11	−40.45	253	N	p-emb.pah	···	···	···	KC-19
333	2.09	00	···	···	···	exp	···	···	···	···
334	0.89	11	−45.50	43	N	surr.bub-cen-trig	[CH87] 341.264−0.317	S22	···	KC-19
335	1.37	00	···	···	···	exp	···	···	···	···
336	1.34	00	···	···	···	exp	···	···	···	···
337	0.00	11	−70.13	253	N	p-emb.bub-cen	[CH87] 342.085+0.423	S18	···	···
338	8.56	01	−118.96	84	···	exp	···	···	···	···
339	2.41	24	−122.00	51	N	exp	[CH87] 342.300+0.314	···	···	···
340	0.00	11	−92.70	43	···	emb.pah	···	···	···	···
341	0.00	11	−40.80	249	F	emb.pah	[GMB2007b] J165602.7−430448 (UC)	···	SDC G342.684+0.122	···
342	>9.94	00	···	···	···	exp	···	···	···	···
343	>2.13	00	···	···	···	exp	···	···	···	···
344	0.61	13	−27.50	249	N	surr.bub-cen-trig	[CH87] 343.490−0.033	S17	···	···
345	0.00	11	−23.20	249	N	emb.pah	[CH87] 344.226−0.588	···	···	KC-20
346	0.00	11	−22.00	249	N	p-emb	···	···	···	KC-20
347	11.95	01	−23.20	249	···	exp	···	···	···	···
348	11.42	01	−23.20	249	···	exp	···	···	···	···
349	0.00	11	−65.90	249	N	emb.pah	[CH87] 344.439+0.048	···	···	···
350	3.21	00	···	···	···	exp	···	···	···	···
351	0.36	01	−13.40	187	N	few*	[CH87] 345.031+1.540	···	···	···
352	3.96	00	···	···	···	exp	···	···	···	···
353	2.06	00	···	···	···	exp	···	···	···	···
354	0.00	11	−27.10	249	N	emb	[GBM2006] 17016−4124 (UC)	···	SDC G345.000−0.232	···
355	0.00	11	−15.00	249	N	p-emb.pah	RCW 116B	···	···	G345.5+1.0
356	0.15	14	−15.00	51	N	p-emb.pah	[CH87] 345.308+1.471	···	···	G345.5+1.0
357	2.02	00	···	···	···	exp	···	···	···	···
358	0.17	11	−11.90	43	N	p-emb.pah	[CH87] 345.404+1.406	···	···	G345.5+1.0
359	0.00	11	−19.60	249	N	emb.pah	[CH87] 345.425−0.940	···	···	···

Table B.2: continued.

ID	Clump_sep	Cf[a]	Vlsr	ref_Vlsr	KDA	Morph	HII_reg	Bub	IRDC	Complex
360	0.00	11	−17.30	249	N	p-emb.pah	[GBM2006] 17009−4042 (UC)	···	···	G345.5+1.0
361	0.00	11	−17.10	249	N	p-emb.pah	[GBM2006] 17008−4040 (UC)	S11	···	G345.5+1.0
362	3.76	04	−77.90	4	F	exp.pah	HRDS G345.722+0.153	···	···	···
363	0.87	00	···	···	···	few	···	···	···	···
364	0.00	11	−20.18	84	N	p-emb.bub-cen	···	Bub(ID:364)	···	MC-04
365	0.00	11	−20.18	84	N	p-emb.bub-cen	···	Bub(ID:365)	···	MC-04
366	1.61	00	···	···	···	exp	···	···	···	···
367	0.00	11	−83.34	253	F	emb.pah	HRDS G346.077−0.056	···	···	···
368	2.59	00	···	···	···	exp	···	···	···	···
369	>7.46	00	···	···	···	exp	···	···	···	···
370	15.77	00	···	···	···	exp	···	···	···	···
371	0.84	11	−95.10	249	N	surr.bub-cen-trig	[CH87] 347.600+0.211	Bub(ID:371)	···	KC-21
372	0.00	13	−93.00	43	N	emb.pah	···	···	···	KC-21
373	0.00	14	−31.00	51	F	p-emb.pah	[CH87] 347.893+0.044	···	···	···
374	2.06	01	6.10	4	N	exp	···	···	···	···
375	0.00	11	−6.30	249	N	emb.bub-edge	[CH87] 348.225+0.459 (bub)	S7	···	RCW 120
376	0.00	13	−6.01	253	N	p-emb.pah	[CH87] 348.225+0.459 (bub)	S7	···	RCW 120
377	0.00	11	−12.89	253	N	p-emb.bub-cen	[CH87] 348.231−0.982	S6	···	KC-22
378	0.88	21	−6.30	249	N	surr.bub-cen-trig	[CH87] 348.225+0.459	S7	···	RCW 120
379	13.87	00	···	···	···	exp	···	···	···	···
380	0.00	11	−15.40	249	N	emb.pah	HRDS G348.533−0.972	···	···	KC-22
381	0.00	11	−13.63	253	N	emb	···	···	···	KC-22
382	2.58	00	···	···	···	exp	···	···	···	···
383	0.00	11	−12.70	187	N	emb.pah	[CH87] 348.715−1.031	···	···	KC-22
384	12.67	00	···	···	···	exp	···	···	···	···
385	8.12	00	···	···	···	exp	···	···	···	···
386	0.49	23	−25.36	253	N	few.bub-cen	[KC97c] G349.8−00.6	CS116	···	MC-05
387	0.00	11	−25.36	253	N	p-emb.pah	[KC97c] G349.8−00.6	CS116	···	MC-05
388	1.05	00	···	···	···	exp	···	···	···	···
389	0.00	11	−70.50	249	N	emb.pah	IRAS 17160−3707	CS112	···	···
390	0.00	11	−10.60	249	N	p-emb.bub-cen	GM 1−24	CS103	···	NGC 6334/6357
391	0.00	11	−10.60	249	N	emb.pah	GM 1−24	CS102	···	NGC 6334/6357
392	0.89	11	−10.60	249	N	surr	···	···	···	NGC 6334/6357
393	0.00	11	−3.31	253	N	p-emb	···	···	MSXDC G350.92+00.74	NGC 6334/6357
394	0.00	11	−6.50	249	N	p-emb.pah	[WBH98] 17165−3554 (UC)	···	IRDC(ID:394)	NGC 6334/6357
395	0.49	11	−6.50	249	N	surr.pah	···	···	···	NGC 6334/6357
396	0.00	13	−6.50	249	N	p-emb.pah	···	···	···	NGC 6334/6357
397	>2.05	00	···	···	···	exp	···	···	···	···
398	0.00	11	−2.90	249	N	p-emb.pah	NGC 6334A (UC)	CS88	···	NGC 6334/6357
399	0.67	14	−3.60	4	N	surr.bub-cen	HRDS G351.265+1.019	CS87	···	NGC 6334/6357

Table B.2: continued.

ID	Clump_sep	Cf[a]	Vlsr	ref_Vlsr	KDA	Morph	HII_reg	Bub	IRDC	Complex
400	0.13	10	···	···	···	p-emb	···	···	···	NGC 6334/6357
401	0.00	10	···	···	···	p-emb.pah	NGC 6334C	···	···	NGC 6334/6357
402	0.00	10	···	···	···	p-emb.bub-cen-trig	NGC 6334D	CS85	···	NGC 6334/6357
403	0.00	11	−5.70	249	N	emb.pah	NGC 6334F (UC)	···	···	NGC 6334/6357
404	0.00	11	−5.70	249	N	p-emb.pah	NGC 6334E	···	···	NGC 6334/6357
405	0.00	11	−22.30	43	N	p-emb.bub-cen	[CH87] 351.467−0.462	CS84	···	···
406	0.00	11	−40.30	249	···	emb.pah	[CH87] 351.617+0.171	···	···	···
407	0.00	11	−11.90	43	N	emb	[CH87] 351.641−1.256	···	···	KC-23
408	0.00	11	−12.45	84	N	p-emb	[CH87] 351.694−1.165	···	···	KC-23
409	0.00	11	−2.70	249	N	emb	[WBH98] 17233−3606 (UC)	···	MSXDC G351.77−00.51	···
410	0.00	11	−2.70	43	N	emb.pah	···	···	···	NGC 6334/6357
411	0.00	11	−55.86	253	N	emb.pah	[CH87] 352.866−0.199	···	···	···
412	1.01	00	···	···	···	exp	···	···	···	···
413	0.31	13	−7.00	249	N	p-emb.bub-cen	[CH87] 353.136+0.660	CS63	···	NGC 6334/6357
414	0.59	11	−5.06	253	N	surr.bub-cen	[CH87] 353.206+0.905	CS61	···	NGC 6334/6357
415	0.00	11	−16.20	249	N	emb.pah	[CH87] 353.430−0.368	CS55	···	···
416	1.37	00	···	···	···	exp	···	···	···	···
417	>5.97	00	···	···	···	exp	···	···	···	···
418	0.00	11	−20.01	253	N	p-emb.bub-cen-trig	[CH87] 354.664+0.470	CS44	···	···
419	1.41	00	···	···	···	exp	···	···	···	···
420	0.61	00	···	···	···	few	···	···	···	···
421	7.23	00	···	···	···	exp	···	···	···	···
422	4.63	01	−37.50	43	-	exp	···	···	···	···
423	1.26	00	···	···	···	exp	···	···	···	···
424	5.92	00	···	···	···	exp	···	···	···	···
425	0.23	01	4.20	108	N	few	···	···	···	···
426	2.83	00	···	···	···	exp	···	···	···	···
427	1.40	00	···	···	···	exp	···	···	···	···
428	1.84	00	···	···	···	exp	···	···	···	···
429	0.00	14	−2.00	51	···	p-emb	[CH87] 356.307−0.210	CS32	···	···
430	1.57	00	···	···	···	exp	···	···	···	···
431	0.00	11	−2.50	253	N	emb	[WBH98] 17403−3032 (UC)	···	IRDC(ID:431)	···
432	0.77	24	−200.00	62	-	surr.pah	[GWC93] 30	···	···	Galactic Center
433	5.25	00	···	···	···	exp	···	···	···	···
434	0.29	14	−2.40	251	···	p-emb.bub-cen	[WAM82] 359.277−0.264	CS4	···	···
435	2.36	00	···	···	···	exp	···	···	···	···
436	8.66	00	···	···	···	exp	···	···	···	···
437	0.37	00	···	···	···	exp*	···	···	···	···
438	0.00	10	···	···	···	emb	Sgr A West	···	···	Galactic Center
439	1.73	00	···	···	···	exp	···	···	···	···

Table B.2: continued.

ID	Clump_sep	Cf[a]	Vlsr	ref_Vlsr	KDA	Morph	HII_reg	Bub	IRDC	Complex
440	0.00	20	···	···	···	p-emb	···	···	···	Galactic Center
441	2.00	00	···	···	···	exp	···	···	···	···
442	0.69	10	···	···	···	surr	···	···	···	Galactic Center
443	0.00	11	18.70	43	-	p-emb.bub-cen	LBN 000.33−00.20	CN8	···	MC-06
444	0.00	11	18.70	43	-	p-emb.bub-cen	LBN 000.33−00.20	CN9	···	MC-06
445	17.03	00	···	···	···	exp	···	···	···	···
446	0.62	00	···	···	···	few	···	···	···	···
447	0.00	13	16.70	27	-	p-emb.pah	[KC97c] G000.6−00.9	CN15	···	MC-07
448	0.00	13	16.70	27	-	p-emb.bub-cen	[KC97c] G000.6−00.9	CN16	···	MC-07
449	0.40	13	16.70	27	-	surr	[KC97c] G000.6−00.9	CN17	···	MC-07
450	0.00	11	50.80	43	-	p-emb	Sgr B2 (UC)	···	···	···
451	5.39	00	···	···	···	exp	···	···	···	···
452	>5.97	00	···	···	···	exp	···	···	···	···
453	0.00	11	−15.60	43	-	emb.pah	Sgr D	CN24	···	···
454	>10.41	00	···	···	···	exp	···	···	···	···
455	>7.46	00	···	···	···	exp	···	···	···	···
456	>22.02	00	···	···	···	exp	···	···	···	···
457	3.95	00	···	···	···	exp	···	···	···	···
458	1.10	00	···	···	···	exp	···	···	···	···
459	>41.09	00	···	···	···	exp	···	···	···	···
460	2.76	00	···	···	···	exp	···	···	···	···
461	0.95	24	4.60	127	···	surr	[L89b] 3.655−00.111	CN43	···	···
462	0.00	11	10.40	194	N	emb	···	···	IRDC(ID:462)	···
463	0.00	11	12.40	43	N	p-emb.pah	···	···	···	···
464	2.19	00	···	···	···	exp	···	···	···	···
465	2.36	00	···	···	···	exp	···	···	···	···
466	2.87	00	···	···	···	exp	···	···	···	···
467	0.90	00	···	···	···	few	···	···	···	···
468	>19.98	00	···	···	···	exp	···	···	···	···
469	0.00	11	7.94	249	N	emb.pah	[SCK2004] G005.63+0.23 (UC)	···	MSXDC G005.64+00.25	···
470	0.00	11	9.10	249	N	p-emb.pah	[L89b] 5.899−00.427	CN71	···	MC-08
471	0.00	11	6.64	249	N	p-emb.bub-cen	[L89b] 5.899−00.427	CN71	···	MC-08
472	0.00	10	···	···	···	emb.pah	[WC89] 005.97−1.17A (UC)	···	···	Lagoon Nebula
473	0.27	01	14.78	249	N	few*	M8	···	···	Lagoon Nebula
474	0.53	14	22.70	127	F	surr.bub-cen-trig	[L89b] 6.148−00.635	CN77	···	···
475	7.19	00	···	···	···	exp	···	···	···	···
476	1.34	00	···	···	···	exp	···	···	···	···
477	0.28	00	···	···	···	few	···	···	···	···
478	0.00	11	21.33	249	N	emb	···	···	MSXDC G006.81−00.25	Trifid Nebula
479	0.13	02	21.58	249	N	few*	M20	CN88	···	Trifid Nebula

Table B.2: continued.

ID	Clump_sep	Cf[a]	Vlsr	ref_Vlsr	KDA	Morph	HII_reg	Bub	IRDC	Complex
480	1.70	20	···	···	···	exp.bub-cen	···	CN95	···	Trifid Nebula
481	>1.87	00	···	···	···	exp	···	···	···	···
482	1.23	00	···	···	···	exp	···	···	···	···
483	6.75	00	···	···	···	exp	···	···	···	MC-09
484	1.40	00	···	···	···	exp	···	···	···	MC-09
485	6.74	00	···	···	···	exp	···	···	···	···
486	13.01	00	···	···	···	exp	···	···	···	···
487	9.14	00	···	···	···	exp	···	···	···	···
488	0.53	02	16.00	249	N	few*	···	···	···	···
489	0.00	10	···	···	···	p-emb	···	···	MSXDC G008.47−00.61	···
490	0.00	11	33.50	43	N	p-emb.bub-cen	[L89b] 8.666−00.351	CN120	···	···
491	1.07	01	40.20	43	···	exp*	···	···	···	···
492	0.34	00	···	···	···	few	···	···	···	···
493	0.00	10	···	···	···	emb	···	CN127	SDC G009.220+0.169	···
494	5.99	00	···	···	···	exp	···	···	···	···
495	7.70	00	···	···	···	exp	···	···	···	···
496	0.00	11	15.80	187	N	p-emb.bub-cen	G10.2−0.3	CN143	···	W31
497	24.34	00	···	···	···	exp	···	···	···	···
498	0.00	11	12.83	249	N	p-emb.bub-cen-trig	G10.3−0.1	CN148	···	W31
499	0.00	11	12.02	249	N	p-emb.bub-cen-trig	G10.3−0.1	CN148	···	W31
500	0.00	11	−2.20	187	N	emb.pah	[L89b] 10.617−00.384	N2	···	W31
501	0.62	02	24.80	187	···	few	···	···	···	···
502	11.26	00	···	···	···	exp	···	···	···	···
503	1.96	01	39.75	249	N	exp	···	···	···	···
504	13.01	01	39.75	249	N	exp	···	···	···	···
505	0.00	11	39.75	249	N	p-emb.pah	RMS G012.4317−01.1112 (UC)	N5	···	···
506	1.93	01	39.75	249	N	exp	···	···	···	···
507	5.04	00	···	···	···	exp	···	···	···	···
508	0.00	11	34.09	249	N	p-emb.pah	W33 f	···	···	W33
509	6.39	00	···	···	···	exp	···	···	···	···
510	1.95	24	35.20	23	N	exp.bub-cen	W33 c	Bub(ID:510)	···	W33
511	0.64	00	···	···	···	few	···	···	···	W33
512	0.00	11	34.40	187	N	emb.pah	W33 g	···	···	W33
513	0.22	11	34.40	187	N	p-emb.bub-cen	W33 h	Bub(ID:513)	···	W33
514	>4.99	00	···	···	···	exp	···	···	···	···
515	0.00	11	36.73	249	N	emb	W33A (UC)	···	···	W33
516	0.00	11	48.55	249	N	p-emb.bub-cen-trig	[L89b] 13.186+00.045	N10	···	···
517	0.41	00	···	···	···	few	···	···	···	···
518	>1.99	00	···	···	···	exp	···	···	···	···
519	0.00	11	47.01	249	F	emb	···	···	MSXDC G013.68−00.60	···

Table B.2: continued.

ID	Clump_sep	Cf[a]	Vlsr	ref_Vlsr	KDA	Morph	HII_reg	Bub	IRDC	Complex
520	0.00	11	48.52	249	N	p-emb.pah	[L89b] 13.875+00.282	···	···	···
521	0.00	14	36.00	127	N	p-emb.bub-cen-trig	[L89b] 13.998−00.128	N14	···	···
522	0.00	11	20.11	249	N	emb	···	···	MSXDC G014.15−00.55	KC-24
523	7.35	00	···	···	···	exp	···	···	···	···
524	1.09	01	38.82	249	N	exp*	···	···	···	···
525	0.00	11	21.97	249	N	p-emb.pah	G14.33−00.64	···	SDC G014.333−0.646	KC-24
526	0.00	11	61.23	249	N	emb.pah	Mol 50 (UC)	···	···	···
527	0.00	13	19.00	249	N	p-emb.bub-cen	M17	Bub(ID:527)	···	M17
528	0.00	21	20.54	249	N	p-emb	[L89b] 15.181−00.625	···	···	M17
529	1.63	00	···	···	···	exp	···	···	···	···
530	0.49	20	···	···	···	exp*	···	···	···	···
531	0.38	01	44.90	127	F?	exp*	···	···	···	···
532	0.68	00	···	···	···	few	···	···	···	···
533	1.66	00	···	···	···	exp	···	···	···	···
534	0.63	01	24.87	249	N	few*	M16	···	···	M16
535	0.93	01	40.37	249	···	few	···	···	···	···
536	0.00	11	24.49	249	N	emb	···	···	SDC G017.171+0.808	M16
537	4.44	01	19.42	249	N	exp	···	···	···	···
538	2.96	01	46.93	249	···	exp	···	···	···	···
539	0.00	11	54.90	43	N	p-emb.bub-cen	[L89b] 18.143−00.289	Bub(ID:539)	···	···
540	2.10	00	···	···	···	exp	···	···	···	···
541	3.10	01	46.34	249	···	exp	···	···	···	···
542	1.15	24	52.30	127	N	surr.bub-cen	[L89b] 18.954−00.019	Bub(ID:542)	···	···
543	1.38	00	···	···	···	exp	···	···	···	···
544	0.07	01	37.80	4	F	exp*	···	···	···	···
545	2.24	01	34.00	43	F	exp	···	···	···	···
546	>1.99	00	···	···	···	exp	···	···	···	···
547	1.08	00	···	···	···	exp	···	···	···	···
548	>4.50	00	···	···	···	exp	···	···	···	···
549	>4.83	00	···	···	···	exp	···	···	···	···
550	11.48	00	···	···	···	exp	···	···	···	···
551	8.28	00	···	···	···	exp	···	···	···	···
552	>2.48	00	···	···	···	exp	···	···	···	···
553	>3.73	00	···	···	···	exp	···	···	···	···
554	3.77	00	···	···	···	exp	···	···	···	···
555	8.10	01	76.00	43	N	exp	···	···	···	···
556	0.14	11	76.00	43	N	p-emb.pah	[L89b] 22.760−00.485	···	···	···
557	1.61	01	77.53	249	F?	exp	···	···	···	···
558	0.64	14	91.30	127	N?	p-emb	[L89b] 23.538−00.041	···	···	···
559	0.00	11	113.90	43	NT	p-emb.bub-cen	[WC89] 023.71+0.17	Bub(ID:559)	···	···

Table B.2: continued.

ID	Clump_sep	Cf[a]	Vlsr	ref_Vlsr	KDA	Morph	HII_reg	Bub	IRDC	Complex
560	0.00	11	80.66	249	N	emb.pah	[WC89] 023.96+0.15	···	···	···
561	>6.00	00	···	···	···	exp	···	···	···	···
562	0.85	00	···	···	···	few	···	···	···	···
563	0.00	11	103.20	43	N	emb.bub-cen	[L89b] 24.467+00.489	Bub(ID:563)	···	···
564	0.53	01	106.20	171	NT	few*	···	···	···	···
565	0.96	00	···	···	···	exp	···	···	···	···
566	1.76	01	43.76	249	···	exp	···	···	···	···
567	2.16	01	61.50	249	···	exp	···	···	···	···
568	3.89	24	39.60	127	N	exp.bub-cen	[L89b] 25.294+00.307	N37	···	···
569	0.00	14	59.10	127	N	emb.pah	[L89b] 25.382−00.177	N39	···	···
570	0.59	21	104.51	5	NT	surr	···	···	···	···
571	7.53	00	···	···	···	exp	···	···	···	···
572	0.00	11	101.60	43	NT	emb	IRAS 18360−0537	···	MSXDC G026.51+00.29	···
573	6.39	00	···	···	···	exp	···	···	···	···
574	11.55	00	···	···	···	exp	···	···	···	···
575	0.53	01	41.70	249	···	few	···	···	···	···
576	1.10	00	···	···	···	exp	···	···	···	···
577	1.24	01	35.15	249	···	exp	···	···	···	···
578	0.04	01	44.40	4	···	exp*	···	···	···	···
579	0.00	11	45.80	187	N	emb.pah	[WBH98] 18416−0420 (UC)	···	···	···
580	0.00	11	104.11	249	T	p-emb.bub-cen	[L89b] 28.801+00.174	Bub(ID:580)	···	···
581	0.44	14	52.60	127	F	surr.bub-cen	[L89b] 28.983−00.603	Bub(ID:581)	···	···
582	0.70	00	···	···	···	few	···	···	···	···
583	2.33	00	···	···	···	exp	···	···	···	···
584	1.95	00	···	···	···	exp	···	···	···	···
585	22.95	00	···	···	···	exp	···	···	···	···
586	>9.73	00	···	···	···	exp	···	···	···	···
587	3.22	00	···	···	···	exp	···	···	···	···
588	0.00	11	97.15	249	NT	emb.pah	[WC89] 029.96−0.02 (UC)	···	···	W43
589	0.00	14	91.60	127	NT	emb.bub-cen	[L89b] 30.776−00.029	N52	···	W43
590	0.76	20	···	···	···	surr	···	···	···	W43
591	1.59	01	50.52	195	N	exp	···	···	···	···
592	0.00	11	39.18	249	F	emb	HRDS G031.159+0.048	···	···	···
593	1.97	00	···	···	···	exp	···	···	···	···
594	>7.48	00	···	···	···	exp	···	···	···	···
595	>16.58	00	···	···	···	exp	···	···	···	···
596	0.00	01	84.27	249	T	exp*	···	···	···	···
597	7.04	01	46.30	43	F	exp	···	···	···	···
598	0.00	11	107.80	43	T	emb.pah	[L89b] 33.914+00.111	···	···	···
599	0.00	11	57.16	249	N	p-emb.bub-cen	G34.3+0.2	Bub(ID:599)	···	KC-25

Table B.2: continued.

ID	Clump_sep	Cf[a]	Vlsr	ref_Vlsr	KDA	Morph	HII_reg	Bub	IRDC	Complex
600	0.00	11	57.20	43	N	p-emb.bub-cen	G34.3+0.2	Bub(ID:599)	···	KC-25
601	0.00	11	57.30	43	N	emb	G34.4+0.23 (UC)	···	MSXDC G034.43+00.24	KC-25
602	0.00	11	58.60	187	N	emb	···	···	···	KC-25
603	0.00	11	34.99	249	N	p-emb.bub-cen	···	Bub(ID:603)	···	KC-26
604	0.00	11	33.87	249	N	emb	···	···	MSXDC G035.19−00.72	KC-26
605	1.17	21	49.60	43	F	surr.bub-cen	IRAS 18540+0220	N68	···	···
606	0.00	11	91.60	149	T	p-emb	···	···	···	···
607	14.90	00	···	···	···	exp	···	···	···	···
608	0.00	11	38.70	163	F	p-emb.pah	···	···	···	···
609	9.41	01	41.60	187	···	exp.bub-cen	···	Bub(ID:609)	···	···
610	0.00	11	53.30	43	N	emb	···	···	···	···
611	0.14	11	45.00	204	N	p-emb	···	···	···	···
612	0.00	11	29.40	149	N	emb	Mol 84 (UC)	···	···	···
613	6.10	00	···	···	···	exp	···	···	···	···
614	0.38	11	67.50	187	NT	p-emb.bub-cen	[L89b] 42.108−00.623	N82	···	···
615	14.04	00	···	···	···	exp	···	···	···	···
616	0.00	11	65.60	43	NT	p-emb.bub-cen	[L89b] 42.431−00.264	Bub(ID:616)	···	···
617	>149.38	00	···	···	···	exp	···	···	···	···
618	0.00	11	57.30	163	F	emb.pah	···	···	···	···
619	0.00	11	10.90	163	F	emb.pah	[DJW84] W49 S,Q	···	···	W49A
620	0.00	11	11.80	187	F	emb.pah	W49A South	···	···	W49A
621	0.00	11	11.80	187	F	emb	W49A Welch Ring (UC)	···	···	W49A
622	0.00	11	1.70	163	F	p-emb.bub-cen	W49A extended	Bub(ID:622)	···	W49A
623	0.00	11	11.80	187	F	p-emb.pah	[DJW84] W49 CC	···	···	W49A
624	>19.98	00	···	···	···	exp	···	···	···	···
625	0.00	21	8.25	249	F	p-emb	[WWB83] G043.23−0.05	···	···	W49A
626	0.00	11	54.20	43	N	emb.pah	[L89b] 43.890−00.790	···	···	···
627	0.00	11	65.40	43	T	emb	···	···	···	···
628	5.01	00	···	···	···	exp	···	···	···	···
629	10.67	00	···	···	···	exp	···	···	···	···
630	0.00	11	59.00	187	NT	emb.pah	IRAS 19110+1045	···	···	GRSMC G045.14+00.14
631	0.00	11	59.00	43	NT	emb.pah	IRAS 19111+1048	···	···	GRSMC G045.14+00.14
632	0.00	11	59.00	43	NT	p-emb.pah	IRAS 19111+1048	···	···	GRSMC G045.14+00.14
633	0.00	11	58.00	43	FT	emb.pah	[L89b] 45.451+00.060	···	···	KC-27
634	0.00	11	60.83	249	FT	p-emb.pah	[L89b] 45.475+00.130	···	···	KC-27
635	1.49	00	···	···	···	exp	···	···	···	···
636	0.00	11	60.40	43	FT	p-emb.bub-cen	[L89b] 45.824−00.290	Bub(ID:636)	···	KC-27
637	>24.46	00	···	···	···	exp	···	···	···	···
638	>9.35	00	···	···	···	exp	···	···	···	···
639	0.00	11	63.50	8	T	p-emb.pah	···	···	···	···

Table B.2: continued.

ID	Clump_sep	Cf[a]	Vlsr	ref_Vlsr	KDA	Morph	HII_reg	Bub	IRDC	Complex
640	2.66	00	···	···	···	exp	···	···	···	···
641	0.00	11	17.55	249	F	p-emb.pah	[L89b] 48.596+00.042	···	···	···
642	0.00	11	68.58	249	T	p-emb.bub-cen	[L89b] 48.930−00.286	Bub(ID:642)	···	W51
643	0.00	11	67.37	249	T	emb.bub-cen	[L89b] 48.997−00.295	Bub(ID:643)	···	W51
644	0.41	14	64.10	127	T	p-emb	[L89b] 49.060−00.260	···	···	W51
645	0.18	14	67.90	127	T	p-emb.pah	[L89b] 49.076−00.377	···	···	W51
646	6.87	01	39.19	249	···	exp	···	···	···	···
647	11.79	01	39.19	249	N	exp	···	···	···	···
648	0.00	11	65.40	43	T	p-emb.bub-cen	[L89b] 49.204−00.345	N101	···	W51
649	0.00	11	49.79	249	T	p-emb.bub-cen	[M94] 49.4−0.3 a	Bub(ID:649)	···	W51
650	0.00	11	52.19	249	T	p-emb.pah	[L89b] 49.384−00.298	···	···	W51
651	>4.78	00	···	···	···	exp	···	···	···	···
652	0.00	10	···	···	···	p-emb.pah	[M94] 49.4−0.3 c	···	···	W51
653	0.00	11	56.90	187	T	p-emb.pah	[M94] 49.5−0.4 b	···	···	W51
654	0.00	11	56.90	187	T	p-emb.pah	[M94] 49.5−0.4 c1	···	···	W51
655	0.00	11	62.00	187	T	p-emb.pah	[M94] 49.5−0.4 a	···	···	W51
656	0.00	11	56.60	163	T	p-emb.pah	[M94] 49.5−0.4 e	···	···	W51
657	0.00	11	56.60	163	T	p-emb.pah	[M94] 49.5−0.4 e	···	···	W51
658	0.00	11	60.60	163	T	emb	[M94] 49.5−0.4 d (UC)	···	···	W51
659	0.00	11	56.90	187	T	p-emb.bub-cen	[M94] 49.5−0.4 b1	Bub(ID:659)	···	W51
660	0.00	13	56.90	187	T	p-emb.pah	[M94] 49.5 −0.4 f	···	···	W51
661	0.00	11	56.90	187	T	p-emb.pah	[M94] 49.5−0.4 g	···	···	W51
662	2.03	24	62.10	127	T	exp.pah	[M94] 49.5−0.4 h	···	···	W51
663	0.00	11	8.10	110	F	p-emb	···	···	···	···
664	>14.92	00	···	···	···	exp	···	···	···	···
665	0.00	11	54.80	188	T	emb	···	···	SDC G050.066+0.057	···
666	6.71	01	25.80	43	F	exp	···	···	···	···
667	>6.79	00	···	···	···	exp	···	···	···	···
668	>12.69	00	···	···	···	exp	···	···	···	···
669	>6.45	00	···	···	···	exp	···	···	···	···
670	0.00	11	53.86	249	T	p-emb.pah	[L89b] 51.362−00.001	···	···	···
671	13.79	01	3.76	195	F	exp	···	···	···	···
672	0.00	11	42.10	43	NT	emb.bub-cen	HRDS G052.098+1.042	Bub(ID:672)	···	···
673	0.00	11	3.45	249	F	p-emb.bub-cen	[L89b] 52.233+00.736	N113	···	···
674	4.54	00	···	···	···	exp	···	···	···	···
675	0.00	11	63.77	249	T	emb	···	···	···	···
676	0.00	11	22.00	187	N	emb	···	···	SDC G053.158+0.068	KC-28
677	0.00	11	23.90	189	N	p-emb	···	···	MSXDC G053.25+00.04	KC-28
678	0.00	11	23.70	187	N	p-emb	···	···	···	KC-28
679	16.43	01	37.74	249	T	exp	···	···	···	···

Table B.2: continued.

ID	Clump_sep	Cf[a]	Vlsr	ref_Vlsr	KDA	Morph	HII_reg	Bub	IRDC	Complex
680	0.10	11	39.90	43	FT	p-emb.pah	[L89b] 54.092−00.066	N117	···	···
681	10.49	01	31.33	249	F	exp	···	···	···	···
682	>8.33	00	···	···	···	exp	···	···	···	···
683	>5.96	00	···	···	···	exp	···	···	···	···
684	3.27	00	···	···	···	exp	···	···	···	···
685	0.00	14	35.30	4	T	p-emb.bub-cen	HRDS G056.252−0.160	Bub(ID:685)	···	···
686	0.00	11	31.54	249	T	emb.pah	···	···	···	···
687	20.45	00	···	···	···	exp	···	···	···	···
688	>2.07	00	···	···	···	exp	···	···	···	···
689	0.00	11	36.37	249	T	emb.pah	···	···	···	···
690	0.00	11	25.89	249	N	p-emb.pah	···	···	···	Vul OB1
691	1.96	01	29.00	43	NT	exp	Sh 2−86	···	···	Vul OB1
692	0.00	11	36.90	43	NT	p-emb.pah	Mol 109 (UC)	···	···	Vul OB1
693	0.00	11	22.40	43	N	emb.pah	IRAS 19410+2336 (UC)	···	···	Vul OB1
694	0.00	11	34.40	43	NT	emb.pah	Mol 110 (UC)	···	···	Vul OB1
695	>1.53	00	···	···	···	exp	···	···	···	···

Notes. [(a)] We denote by Cf the parameter Clump_flag.

Table B.3: References for Tables B.1 and B.2.

Number	Reference
1	Alexander et al. (2009)
2	Alvarez et al. (2004)
3	Alves & Homeier (2003)
4	Anderson et al. (2011)
5	Anderson & Bania (2009)
6	Arias et al. (2006)
7	Arnal et al. (2008)
8	Arvidsson et al. (2010)
9	Bains et al. (2006)
10	Bartkiewicz et al. (2008)
11	Baume et al. (2009)
12	Benaglia et al. (2010)
13	Beuther et al. (2002)
14	Beuther et al. (2011)
15	Bibby et al. (2008)
16	Bica et al. (1993)
17	Bica et al. (2004)
18	Bica et al. (2006)
19	Bica et al. (2008a)
20	Bica et al. (2008b)
21	Bica & Bonatto (2008)
22	Bica & Bonatto (2011)
23	Bieging et al. (1978)
24	Bieging et al. (2010)
25	Bik (2004)
26	Billot et al. (2010)
27	Blitz et al. (1982)
28	Blum et al. (1999)
29	Blum et al. (2000)
30	Blum et al. (2001)
31	Blum & Damineli (1999)
32	Blum & McGregor (2008)
33	Bonatto et al. (2006b)
34	Bonatto et al. (2010)
35	Bonatto & Bica (2007b)
36	Bonatto & Bica (2007a)
37	Bonatto & Bica (2010)
38	Borissova et al. (2005)
39	Borissova et al. (2006)
40	Borissova et al. (2008)
41	Borissova et al. (2011)
42	Bourke et al. (1995)
43	Bronfman et al. (1996)
44	Bronfman et al. (2008)
45	Brunthaler et al. (2009)
46	Bukowiecki et al. (2011)
47	Camargo et al. (2009)
48	Cambrésy et al. (2011)
49	Carraro et al. (2005)
50	Carraro & Munari (2004)
51	Caswell & Haynes (1987)
52	Chapin et al. (2008)
53	Chavarría et al. (2010)
54	Churchwell et al. (1990)
55	Clariá et al. (2006)
56	Clark et al. (2005)
57	Clark et al. (2009)
58	Clark & Porter (2004)
59	Comerón et al. (2005)
60	Comerón & Schneider (2007)
61	Conti & Blum (2002)
62	Cram et al. (1996)
63	Crowther & Furness (2008)
64	Damke et al. (2006)
65	Davies et al. (2007)
66	Davies et al. (2008)
67	Davies et al. (2009)
68	Davies et al. (2012a)
69	Davies et al. (2011)
70	Davies et al. (2012b)
71	Deharveng et al. (2010)
72	Downes et al. (1980)
73	Dutra et al. (2003b)
74	Espinoza et al. (2009)
75	Faúndez et al. (2004)
76	Faustini et al. (2009)
77	Feldt et al. (1998)
78	Figer et al. (1999)
79	Figer et al. (2002)
80	Figer et al. (2005)
81	Figer et al. (2006)
82	Figuerêdo et al. (2005)
83	Figuerêdo et al. (2008)
84	Fontani et al. (2005)
85	Froebrich et al. (2008)
86	Froebrich et al. (2010)
87	Froebrich & Ioannidis (2011)
88	Fujiyoshi et al. (2005)
89	Furness et al. (2010)
90	Garay et al. (2007)
91	Gennaro et al. (2011)
92	Georgelin et al. (1987)
93	Georgelin et al. (1994)
94	Georgelin et al. (1996)
95	Genzel et al. (2010)
96	Glushkova et al. (2010)
97	Gomez et al. (1990)
98	Green & McClure-Griffiths (2011)
99	Gwinn et al. (1992)
100	Hanson et al. (2010)
101	Hanson & Bubnick (2008)
102	Henning et al. (2000)
103	Herbst (1975)
104	Hoffmeister et al. (2008)
105	Homeier & Alves (2005)
106	Hunter et al. (2004)
107	Indebetouw et al. (2007)
108	Jackson et al. (2008)
109	Janes & Hoq (2011)
110	Johnston et al. (2009)
111	Kainulainen et al. (2011)
112	Kang et al. (2010)
113	Karr et al. (2009)
114	Kharchenko et al. (2003)
115	Kharchenko et al. (2005b)
116	Kharchenko et al. (2005a)
117	Kharchenko & Schilbach (1995)
118	Kim & Koo (2002)
119	Kolpak et al. (2003)
120	Kook et al. (2010)
121	Kothes & Dougherty (2007)
122	Kronberger et al. (2006)
123	Kumar et al. (2004)
124	Kurayama et al. (2011)
125	Lefloch et al. (2008)
126	Leistra et al. (2005)
127	Lockman (1989)
128	Loktin et al. (2001)
129	Loktin & Beshenov (2001)
130	Longmore et al. (2007)
131	López et al. (2011)

132 Lyngå (1987)
133 Maciejewski & Niedzielski (2007)
134 Majaess et al. (2007)
135 Majaess et al. (2012)
136 Marshall et al. (2009)
137 Martín-Hernández et al. (2008)
138 Martins et al. (2010)
139 Massey et al. (2001)
140 Mauerhan et al. (2011)
141 Messineo et al. (2008)
142 Messineo et al. (2009)
143 Messineo et al. (2010)
144 Messineo et al. (2011)
145 Miettinen & Harju (2010)
146 Misanovic et al. (2002)
147 Moffat (1976)
148 Moisés et al. (2011)
149 Molinari et al. (1996)
150 Motogi et al. (2011)
151 Nagayama et al. (2009)
152 Nagayama et al. (2011)
153 Neckel (1978)
154 Negueruela et al. (2010)
155 Negueruela et al. (2011)
156 Netopil et al. (2007)
157 Nguyen Luong et al. (2011)
158 Ogura & Ishida (1976)
159 Oh et al. (2010)
160 Ojha et al. (2010)
161 Oliveira (2008)
162 Pandian et al. (2008)
163 Pandian et al. (2009)
164 Paunzen et al. (2005)
165 Paunzen & Netopil (2006)
166 Pavani & Bica (2007)
167 Peña et al. (2003)
168 Persi et al. (2000)
169 Persi et al. (2005)
170 Persi & Tapia (2010)
171 Pestalozzi et al. (2005)
172 Piatti et al. (1998)
173 Piatti et al. (1999)
174 Piatti et al. (2000b)
175 Piatti et al. (2000a)
176 Piatti et al. (2002a)
177 Piatti et al. (2002b)
178 Piatti et al. (2005)
179 Piatti et al. (2006)
180 Piatti & Clariá (2002)
181 Pinheiro et al. (2010)
182 Pomarès et al. (2009)
183 Povich et al. (2007)
184 Povich et al. (2009)
185 Pratap et al. (1999)
186 Purcell et al. (2006)
187 RMS Survey (Urquhart et al. 2008)
188 Ragan et al. (2006)
189 Rathborne et al. (2006)
190 Rauw et al. (2010)
191 Rauw & De Becker (2008)
192 Reid et al. (2009)
193 Rho et al. (2006)
194 Rodríguez et al. (2002)
195 Roman-Duval et al. (2009)
196 Roman-Lopes et al. (2003)
197 Roman-Lopes (2007)
198 Roman-Lopes et al. (2009)
199 Roman-Lopes (2011)
200 Roman-Lopes & Abraham (2004b)
201 Roman-Lopes & Abraham (2004a)
202 Roman-Lopes & Abraham (2006a)
203 Roman-Lopes & Abraham (2006b)
204 Russeil (2003)
205 Russeil & Castets (2004)
206 Russeil et al. (2005)
207 Russeil et al. (2010)
208 Sagar et al. (2001)
209 Sagar & Cannon (1994)
210 Sana et al. (2006)
211 Sana et al. (2008)
212 Sato et al. (2010a)
213 Sato et al. (2010b)
214 Schödel et al. (2009)
215 Seleznev et al. (2010)
216 Sewilo et al. (2004)
217 Shepherd et al. (2004)
218 Shepherd et al. (2007)
219 Soares et al. (2008)
220 Sollins & Megeath (2004)
221 Stolte et al. (2008)
222 Stead & Hoare (2010)
223 Stead & Hoare (2011)
224 Stier et al. (1982)
225 Stier et al. (1984)
226 Straw et al. (1989)
227 Subramaniam et al. (2010)
228 Tadross (2008)
229 Tadross (2009b)
230 Tadross (2009a)
231 Tadross (2011)
232 Tapia et al. (1991)
233 Tapia et al. (1996)
234 Tapia et al. (2009)
235 Tapia et al. (2010)
236 Tothill et al. (2008)
237 Turner et al. (1993)
238 Turner & Forbes (2005)
239 Urquhart et al. (2012)
240 van den Bergh & Hagen (1975)
241 Vázquez et al. (2003)
242 Vasquez et al. (2005)
243 Vázquez & Baume (2001)
244 Vig et al. (2006)
245 Vig et al. (2007a)
246 Vig et al. (2007b)
247 Vrba et al. (2000)
248 Wang et al. (2007)
249 Wienen et al. (2012), Wienen et al. (in prep.)
250 Wilson et al. (1970)
251 Wink et al. (1982)
252 Wolk et al. (2008)
253 Wyrowski et al. (in prep.)
254 Xu et al. (2009)
255 Xu et al. (2011)
256 Zapata et al. (2008)
257 Zavagno et al. (2007)
258 Zhang et al. (2009)

Bibliography

Alexander, M. J., Kobulnicky, H. A., Clemens, D. P., et al. 2009, AJ, 137, 4824

Allen, L., Megeath, S. T., Gutermuth, R., et al. 2007, Protostars and Planets V, 361

Altenhoff, W. J., Downes, D., Pauls, T., & Schraml, J. 1979, A&AS, 35, 23

Alvarez, C., Feldt, M., Henning, T., et al. 2004, ApJS, 155, 123

Alves, J. & Homeier, N. 2003, ApJ, 589, L45

Anderson, L. D. & Bania, T. M. 2009, ApJ, 690, 706

Anderson, L. D., Bania, T. M., Balser, D. S., & Rood, R. T. 2011, ApJS, 194, 32

Arias, J. I., Barbá, R. H., Maíz Apellániz, J., Morrell, N. I., & Rubio, M. 2006, MNRAS, 366, 739

Arnal, E. M., Duronea, N. U., & Testori, J. C. 2008, A&A, 486, 807

Arthur, S. J. 2007, Wind-Blown Bubbles around Evolved Stars, ed. Hartquist, T. W., Pittard, J. M., & Falle, S. A. E. G., 183

Arvidsson, K., Kerton, C. R., Alexander, M. J., Kobulnicky, H. A., & Uzpen, B. 2010, AJ, 140, 462

Baba, J., Asaki, Y., Makino, J., et al. 2009, ApJ, 706, 471

Bains, I., Wong, T., Cunningham, M., et al. 2006, MNRAS, 367, 1609

Bartkiewicz, A., Brunthaler, A., Szymczak, M., van Langevelde, H. J., & Reid, M. J. 2008, A&A, 490, 787

Bastian, N. 2011, in Stellar Clusters & Associations: A RIA Workshop on Gaia, 85–97

Bastian, N., Covey, K. R., & Meyer, M. R. 2010, ARA&A, 48, 339

Baume, G., Carraro, G., & Momany, Y. 2009, MNRAS, 398, 221

Baumgardt, H. & Kroupa, P. 2007, MNRAS, 380, 1589

Baumgardt, H. & Makino, J. 2003, MNRAS, 340, 227

Beaumont, C. N. & Williams, J. P. 2010, ApJ, 709, 791

Benaglia, P., Ribó, M., Combi, J. A., et al. 2010, A&A, 523, A62

Benjamin, R. A., Churchwell, E., Babler, B. L., et al. 2003, PASP, 115, 953

Bertoldi, F. 1989, ApJ, 346, 735

Beuther, H., Churchwell, E. B., McKee, C. F., & Tan, J. C. 2007, Protostars and Planets V, 165
Beuther, H., Kerp, J., Preibisch, T., Stanke, T., & Schilke, P. 2002, A&A, 395, 169
Beuther, H., Linz, H., Henning, T., et al. 2011, A&A, 531, A26
Beuther, H., Tackenberg, J., Linz, H., et al. 2012, ApJ, 747, 43
Bibby, J. L., Crowther, P. A., Furness, J. P., & Clark, J. S. 2008, MNRAS, 386, L23
Bica, E. & Bonatto, C. 2008, MNRAS, 384, 1733
Bica, E. & Bonatto, C. 2011, A&A, 530, A32
Bica, E., Bonatto, C., & Blumberg, R. 2006, A&A, 460, 83
Bica, E., Bonatto, C., & Camargo, D. 2008a, MNRAS, 385, 349
Bica, E., Bonatto, C., & Dutra, C. M. 2004, A&A, 422, 555
Bica, E., Bonatto, C., & Dutra, C. M. 2008b, A&A, 489, 1129
Bica, E., Dutra, C. M., & Barbuy, B. 2003a, A&A, 397, 177
Bica, E., Dutra, C. M., Soares, J., & Barbuy, B. 2003b, A&A, 404, 223
Bica, E., Ortolani, S., & Barbuy, B. 1993, A&A, 270, 117
Bieging, J. H., Pankonin, V., & Smith, L. F. 1978, A&A, 64, 341
Bieging, J. H., Peters, W. L., & Kang, M. 2010, ApJS, 191, 232
Bik, A. 2004, Ph.D. Thesis, Amsterdam Univ.
Bik, A., Kaper, L., Hanson, M. M., & Smits, M. 2005, A&A, 440, 121
Billot, N., Noriega-Crespo, A., Carey, S., et al. 2010, ApJ, 712, 797
Binney, J. & Tremaine, S. 2008, Galactic Dynamics: Second Edition (Princeton University Press)
Blitz, L. 1991, in IAU Symposium, Vol. 144, The Interstellar Disk-Halo Connection in Galaxies, ed. H. Bloemen, 41–52
Blitz, L., Fich, M., & Stark, A. A. 1982, ApJS, 49, 183
Blum, R. D., Conti, P. S., & Damineli, A. 2000, AJ, 119, 1860
Blum, R. D. & Damineli, A. 1999, ApJ, 512, 237
Blum, R. D., Damineli, A., & Conti, P. S. 1999, AJ, 117, 1392
Blum, R. D., Damineli, A., & Conti, P. S. 2001, AJ, 121, 3149
Blum, R. D. & McGregor, P. J. 2008, AJ, 135, 1708
Bonatto, C. & Bica, E. 2007a, A&A, 473, 445
Bonatto, C. & Bica, E. 2007b, MNRAS, 377, 1301
Bonatto, C. & Bica, E. 2008, A&A, 485, 81
Bonatto, C. & Bica, E. 2010, A&A, 521, A74
Bonatto, C. & Bica, E. 2011, MNRAS, 415, 2827
Bonatto, C., Kerber, L. O., Bica, E., & Santiago, B. X. 2006a, A&A, 446, 121
Bonatto, C., Ortolani, S., Barbuy, B., & Bica, E. 2010, MNRAS, 402, 1685
Bonatto, C., Santos, Jr., J. F. C., & Bica, E. 2006b, A&A, 445, 567

Bonnell, I. A. & Bate, M. R. 2002, MNRAS, 336, 659
Bonnell, I. A. & Bate, M. R. 2006, MNRAS, 370, 488
Bonnell, I. A., Bate, M. R., Clarke, C. J., & Pringle, J. E. 2001, MNRAS, 323, 785
Bonnell, I. A., Bate, M. R., & Zinnecker, H. 1998, MNRAS, 298, 93
Bonnell, I. A., Smith, R. J., Clark, P. C., & Bate, M. R. 2011, MNRAS, 410, 2339
Borissova, J., Bonatto, C., Kurtev, R., et al. 2011, A&A, 532, A131
Borissova, J., Ivanov, V. D., Hanson, M. M., et al. 2008, A&A, 488, 151
Borissova, J., Ivanov, V. D., Minniti, D., & Geisler, D. 2006, A&A, 455, 923
Borissova, J., Ivanov, V. D., Minniti, D., Geisler, D., & Stephens, A. W. 2005, A&A, 435, 95
Borissova, J., Pessev, P., Ivanov, V. D., et al. 2003, A&A, 411, 83
Bourke, T. L., Hyland, A. R., Robinson, G., James, S. D., & Wright, C. M. 1995, MNRAS, 276, 1067
Brand, J. & Blitz, L. 1993, A&A, 275, 67
Bressert, E., Bastian, N., Gutermuth, R., et al. 2010, MNRAS, 409, L54
Bronfman, L., Garay, G., Merello, M., et al. 2008, ApJ, 672, 391
Bronfman, L., Nyman, L.-A., & May, J. 1996, A&AS, 115, 81
Brunthaler, A., Reid, M. J., Menten, K. M., et al. 2009, ApJ, 693, 424
Bukowiecki, Ł., Maciejewski, G., Konorski, P., & Strobel, A. 2011, Acta Astron., 61, 231
Camargo, D., Bonatto, C., & Bica, E. 2009, A&A, 508, 211
Cambrésy, L., Rho, J., Marshall, D. J., & Reach, W. T. 2011, A&A, 527, A141
Carpenter, J. M. 2000, AJ, 120, 3139
Carraro, G., Janes, K. A., Costa, E., & Méndez, R. A. 2006, MNRAS, 368, 1078
Carraro, G., Méndez, R. A., & Costa, E. 2005, MNRAS, 356, 647
Carraro, G. & Munari, U. 2004, MNRAS, 347, 625
Caselli, P., Walmsley, C. M., Tafalla, M., Dore, L., & Myers, P. C. 1999, ApJ, 523, L165
Caswell, J. L. & Haynes, R. F. 1987, A&A, 171, 261
Celnik, W., Rohlfs, K., & Braunsfurth, E. 1979, A&A, 76, 24
Chabrier, G. 2001, ApJ, 554, 1274
Chabrier, G. & Hennebelle, P. 2010, ApJ, 725, L79
Chapin, E. L., Ade, P. A. R., Bock, J. J., et al. 2008, ApJ, 681, 428
Chavarría, L., Mardones, D., Garay, G., et al. 2010, ApJ, 710, 583
Churchwell, E., Babler, B. L., Meade, M. R., et al. 2009, PASP, 121, 213
Churchwell, E., Povich, M. S., Allen, D., et al. 2006, ApJ, 649, 759
Churchwell, E., Walmsley, C. M., & Cesaroni, R. 1990, A&AS, 83, 119

Churchwell, E., Watson, D. F., Povich, M. S., et al. 2007, ApJ, 670, 428
Clariá, J. J., Mermilliod, J.-C., Piatti, A. E., & Parisi, M. C. 2006, A&A, 453, 91
Clark, J. S., Negueruela, I., Crowther, P. A., & Goodwin, S. P. 2005, A&A, 434, 949
Clark, J. S., Negueruela, I., Davies, B., et al. 2009, A&A, 498, 109
Clark, J. S. & Porter, J. M. 2004, A&A, 427, 839
Clarke, C. 2010, Royal Society of London Philosophical Transactions Series A, 368, 733
Comerón, F. & Schneider, N. 2007, A&A, 473, 149
Comerón, F., Schneider, N., & Russeil, D. 2005, A&A, 433, 955
Conti, P. S. & Blum, R. D. 2002, ApJ, 564, 827
Cram, L. E., Claussen, M. J., Beasley, A. J., Gray, A. D., & Goss, W. M. 1996, MNRAS, 280, 1110
Crowther, P. A. & Furness, J. P. 2008, A&A, 492, 111
Cyganowski, C. J., Whitney, B. A., Holden, E., et al. 2008, AJ, 136, 2391
Dale, J. E. & Bonnell, I. 2011, MNRAS, 414, 321
Dale, J. E., Bonnell, I. A., Clarke, C. J., & Bate, M. R. 2005, MNRAS, 358, 291
Dale, J. E., Ercolano, B., & Bonnell, I. A. 2012, MNRAS, 424, 377
Damke, G., Barbá, R., & Morrell, N. I. 2006, in Revista Mexicana de Astronomia y Astrofisica Conference Series, Vol. 26, 180
Davies, B., Bastian, N., Gieles, M., et al. 2011, MNRAS, 411, 1386
Davies, B., Clark, J. S., Trombley, C., et al. 2012a, MNRAS, 419, 1871
Davies, B., de La Fuente, D., Najarro, F., et al. 2012b, MNRAS, 419, 1860
Davies, B., Figer, D. F., Kudritzki, R.-P., et al. 2007, ApJ, 671, 781
Davies, B., Figer, D. F., Kudritzki, R.-P., et al. 2009, ApJ, 707, 844
Davies, B., Figer, D. F., Law, C. J., et al. 2008, ApJ, 676, 1016
Deharveng, L., Schuller, F., Anderson, L. D., et al. 2010, A&A, 523, A6
Dias, W. S., Alessi, B. S., Moitinho, A., & Lépine, J. R. D. 2002, A&A, 389, 871
Dobbs, C. L., Bonnell, I. A., & Clark, P. C. 2005, MNRAS, 360, 2
Downes, D., Wilson, T. L., Bieging, J., & Wink, J. 1980, A&AS, 40, 379
Draine, B. T. 2011, Physics of the Interstellar and Intergalactic Medium
Draine, B. T., Dale, D. A., Bendo, G., et al. 2007, ApJ, 663, 866
Dutra, C. M. & Bica, E. 2000, A&A, 359, L9
Dutra, C. M. & Bica, E. 2001, A&A, 376, 434
Dutra, C. M., Bica, E., Soares, J., & Barbuy, B. 2003a, A&A, 400, 533
Dutra, C. M., Ortolani, S., Bica, E., et al. 2003b, A&A, 408, 127
Elmegreen, B. G. 2007, ApJ, 668, 1064

Elmegreen, B. G. 2011, in EAS Publications Series, ed. C. Charbonnel & T. Montmerle, Vol. 51, 45–58
Elmegreen, B. G. & Lada, C. J. 1977, ApJ, 214, 725
Espinoza, P., Selman, F. J., & Melnick, J. 2009, A&A, 501, 563
Evans, II, N. J., Dunham, M. M., Jørgensen, J. K., et al. 2009, ApJS, 181, 321
Fall, S. M., Krumholz, M. R., & Matzner, C. D. 2010, ApJ, 710, L142
Faúndez, S., Bronfman, L., Garay, G., et al. 2004, A&A, 426, 97
Faustini, F., Molinari, S., Testi, L., & Brand, J. 2009, A&A, 503, 801
Fazio, G. G., Hora, J. L., Allen, L. E., et al. 2004, ApJS, 154, 10
Feldt, M., Stecklum, B., Henning, T., et al. 1998, A&A, 339, 759
Figer, D. F., MacKenty, J. W., Robberto, M., et al. 2006, ApJ, 643, 1166
Figer, D. F., McLean, I. S., & Morris, M. 1999, ApJ, 514, 202
Figer, D. F., Najarro, F., Geballe, T. R., Blum, R. D., & Kudritzki, R. P. 2005, ApJ, 622, L49
Figer, D. F., Najarro, F., Gilmore, D., et al. 2002, ApJ, 581, 258
Figuerêdo, E., Blum, R. D., Damineli, A., & Conti, P. S. 2005, AJ, 129, 1523
Figuerêdo, E., Blum, R. D., Damineli, A., Conti, P. S., & Barbosa, C. L. 2008, AJ, 136, 221
Fontani, F., Beltrán, M. T., Brand, J., et al. 2005, A&A, 432, 921
Fontani, F., Giannetti, A., Beltrán, M. T., et al. 2012, MNRAS, 423, 2342
Fritz, T. K., Gillessen, S., Dodds-Eden, K., et al. 2011, ApJ, 737, 73
Froebrich, D. & Ioannidis, G. 2011, MNRAS, 418, 1375
Froebrich, D., Meusinger, H., & Scholz, A. 2007a, MNRAS, 377, L54
Froebrich, D., Meusinger, H., & Scholz, A. 2008, MNRAS, 390, 1598
Froebrich, D., Schmeja, S., Samuel, D., & Lucas, P. W. 2010, MNRAS, 409, 1281
Froebrich, D., Scholz, A., & Raftery, C. L. 2007b, MNRAS, 374, 399
Fujiyoshi, T., Smith, C. H., Moore, T. J. T., et al. 2005, MNRAS, 356, 801
Furness, J. P., Crowther, P. A., Morris, P. W., et al. 2010, MNRAS, 403, 1433
Garay, G. & Lizano, S. 1999, PASP, 111, 1049
Garay, G., Mardones, D., Brooks, K. J., Videla, L., & Contreras, Y. 2007, ApJ, 666, 309
Gennaro, M., Brandner, W., Stolte, A., & Henning, T. 2011, MNRAS, 412, 2469
Genzel, R., Eisenhauer, F., & Gillessen, S. 2010, Reviews of Modern Physics, 82, 3121
Georgelin, Y. M., Amram, P., Georgelin, Y. P., Le Coarer, E., & Marcelin, M. 1994, A&AS, 108, 513
Georgelin, Y. M., Boulesteix, J., Georgelin, Y. P., Laval, A., & Marcelin, M. 1987, A&A, 174, 257

Georgelin, Y. M., Russeil, D., Marcelin, M., et al. 1996, A&AS, 120, 41
Ghosh, S. K., Iyengar, K. V. K., Rengarajan, T. N., et al. 1989, ApJ, 347, 338
Gieles, M. & Baumgardt, H. 2008, MNRAS, 389, L28
Gieles, M. & Portegies Zwart, S. F. 2011, MNRAS, 410, L6
Gieles, M., Portegies Zwart, S. F., Baumgardt, H., et al. 2006, MNRAS, 371, 793
Giersz, M. & Heggie, D. C. 1996, MNRAS, 279, 1037
Ginsburg, A., Bally, J., & Williams, J. P. 2011, MNRAS, 418, 2121
Glushkova, E. V., Koposov, S. E., Zolotukhin, I. Y., et al. 2010, Astronomy Letters, 36, 75
Gomez, J. F., Torrelles, J. M., Tapia, M., et al. 1990, A&A, 234, 447
Goodwin, S. P. 2009, Ap&SS, 324, 259
Green, J. A. & McClure-Griffiths, N. M. 2011, MNRAS, 417, 2500
Grocholski, A. J. & Sarajedini, A. 2003, MNRAS, 345, 1015
Gürkan, M. A., Freitag, M., & Rasio, F. A. 2004, ApJ, 604, 632
Güsten, R., Nyman, L. Å., Schilke, P., et al. 2006, A&A, 454, L13
Gutermuth, R. A., Megeath, S. T., Myers, P. C., et al. 2009, ApJS, 184, 18
Gwinn, C. R., Moran, J. M., & Reid, M. J. 1992, ApJ, 393, 149
Haisch, Jr., K. E., Lada, E. A., & Lada, C. J. 2001, ApJ, 553, L153
Hanson, M. M. & Bubnick, B. F. 2008, PASP, 120, 150
Hanson, M. M., Kurtev, R., Borissova, J., et al. 2010, A&A, 516, A35
Hennebelle, P. & Chabrier, G. 2008, ApJ, 684, 395
Hennebelle, P. & Chabrier, G. 2009, ApJ, 702, 1428
Henning, T., Lapinov, A., Schreyer, K., Stecklum, B., & Zinchenko, I. 2000, A&A, 364, 613
Hénon, M. 1975, in IAU Symposium, Vol. 69, Dynamics of the Solar Systems, ed. A. Hayli, 133
Herbst, W. 1975, AJ, 80, 212
Higuchi, A. E., Kurono, Y., Saito, M., & Kawabe, R. 2010, ApJ, 719, 1813
Hills, J. G. 1980, ApJ, 235, 986
Hoffmeister, V. H., Chini, R., Scheyda, C. M., et al. 2008, ApJ, 686, 310
Homeier, N. L. & Alves, J. 2005, A&A, 430, 481
Huang, K. 1987, Statistical Mechanics, 2nd Edition
Hunter, T. R., Zhang, Q., & Sridharan, T. K. 2004, ApJ, 606, 929
Indebetouw, R., Robitaille, T. P., Whitney, B. A., et al. 2007, ApJ, 666, 321
Ivanov, V. D., Borissova, J., Pessev, P., Ivanov, G. R., & Kurtev, R. 2002, A&A, 394, L1
Jackson, J. M., Finn, S. C., Rathborne, J. M., Chambers, E. T., & Simon, R. 2008, ApJ, 680, 349
Janes, K. A. & Hoq, S. 2011, AJ, 141, 92

Johnston, K. G., Shepherd, D. S., Aguirre, J. E., et al. 2009, ApJ, 707, 283
Jørgensen, J. K., Johnstone, D., Kirk, H., et al. 2008, ApJ, 683, 822
Kainulainen, J., Alves, J., Beuther, H., Henning, T., & Schuller, F. 2011, A&A, 536, A48
Kang, M., Bieging, J. H., Kulesa, C. A., et al. 2010, ApJS, 190, 58
Karr, J. L., Manoj, P., & Ohashi, N. 2009, ApJ, 697, 133
Kauffmann, J., Bertoldi, F., Bourke, T. L., Evans, II, N. J., & Lee, C. W. 2008, A&A, 487, 993
Kendrew, S., Simpson, R., Bressert, E., et al. 2012, ApJ, 755, 71
Kharchenko, N. & Schilbach, E. 1995, Astronomische Nachrichten, 316, 91
Kharchenko, N. V., Pakulyak, L. K., & Piskunov, A. E. 2003, Astronomy Reports, 47, 263
Kharchenko, N. V., Piskunov, A. E., Röser, S., Schilbach, E., & Scholz, R.-D. 2005a, A&A, 440, 403
Kharchenko, N. V., Piskunov, A. E., Röser, S., Schilbach, E., & Scholz, R.-D. 2005b, A&A, 438, 1163
Kim, K.-T. & Koo, B.-C. 2002, ApJ, 575, 327
King, I. 1962, AJ, 67, 471
Klein, B., Philipp, S. D., Krämer, I., et al. 2006, A&A, 454, L29
Klessen, R. S. 2011, in EAS Publications Series, ed. C. Charbonnel & T. Montmerle, Vol. 51, 133–167
Kolpak, M. A., Jackson, J. M., Bania, T. M., Clemens, D. P., & Dickey, J. M. 2003, ApJ, 582, 756
Kook, S.-H., Sung, H., & Bessell, M. S. 2010, Journal of Korean Astronomical Society, 43, 141
Kothes, R. & Dougherty, S. M. 2007, A&A, 468, 993
Kronberger, M., Teutsch, P., Alessi, B., et al. 2006, A&A, 447, 921
Kroupa, P. 2002, Science, 295, 82
Kroupa, P. 2005, in ESA Special Publication, Vol. 576, The Three-Dimensional Universe with Gaia, ed. C. Turon, K. S. O'Flaherty, & M. A. C. Perryman, 629
Kroupa, P. 2007, ArXiv Astrophysics e-prints (arXiv:astro-ph/0703124)
Kroupa, P. 2008, in Lecture Notes in Physics, Berlin Springer Verlag, Vol. 760, The Cambridge N-Body Lectures, ed. S. J. Aarseth, C. A. Tout, & R. A. Mardling, 181
Kroupa, P. 2011, in Stellar Clusters & Associations: A RIA Workshop on Gaia, 17–27
Kruijssen, J. M. D., Maschberger, T., Moeckel, N., et al. 2012, MNRAS, 419, 841
Krumholz, M. R., Klein, R. I., & McKee, C. F. 2007, ApJ, 656, 959

Krumholz, M. R., Klein, R. I., & McKee, C. F. 2011, ApJ, 740, 74
Krumholz, M. R., Klein, R. I., & McKee, C. F. 2012, ApJ, 754, 71
Krumholz, M. R. & Matzner, C. D. 2009, ApJ, 703, 1352
Krumholz, M. R. & McKee, C. F. 2005, ApJ, 630, 250
Krumholz, M. R. & Tan, J. C. 2007, ApJ, 654, 304
Kumar, M. S. N., Kamath, U. S., & Davis, C. J. 2004, MNRAS, 353, 1025
Kumar, M. S. N., Keto, E., & Clerkin, E. 2006, A&A, 449, 1033
Kurayama, T., Nakagawa, A., Sawada-Satoh, S., et al. 2011, PASJ, 63, 513
Kurtev, R., Ivanov, V. D., Borissova, J., & Ortolani, S. 2008, A&A, 489, 583
Lada, C. J. & Lada, E. A. 2003, ARA&A, 41, 57
Lamers, H. J. G. L. M. & Gieles, M. 2006, A&A, 455, L17
Lefloch, B., Cernicharo, J., & Pardo, J. R. 2008, A&A, 489, 157
Leisawitz, D., Bash, F. N., & Thaddeus, P. 1989, ApJS, 70, 731
Leistra, A., Cotera, A. S., Liebert, J., & Burton, M. 2005, AJ, 130, 1719
Levine, E. S., Heiles, C., & Blitz, L. 2008, ApJ, 679, 1288
Lockman, F. J. 1989, ApJS, 71, 469
Loktin, A. V. & Beshenov, G. V. 2001, Astronomy Letters, 27, 386
Loktin, A. V., Gerasimenko, T. P., & Malysheva, L. K. 2001, Astronomical and Astrophysical Transactions, 20, 607
Longmore, A. J., Kurtev, R., Lucas, P. W., et al. 2011, MNRAS, 416, 465
Longmore, S. N., Maercker, M., Ramstedt, S., & Burton, M. G. 2007, MNRAS, 380, 1497
López, C., Bronfman, L., Nyman, L.-Å., May, J., & Garay, G. 2011, A&A, 534, A131
Lucas, P. W., Hoare, M. G., Longmore, A., et al. 2008, MNRAS, 391, 136
Lyngå, G. 1987, Catalogue of open clusters data, Fifth edition (VizieR: VII/92A)
Maciejewski, G. & Niedzielski, A. 2007, A&A, 467, 1065
Majaess, D., Turner, D., Moni Bidin, C., et al. 2012, A&A, 537, L4
Majaess, D. J., Turner, D. G., & Lane, D. J. 2007, PASP, 119, 1349
Marasco, A. & Fraternali, F. 2012, in European Physical Journal Web of Conferences, Vol. 19, 8007
Markwardt, C. B. 2009, in Astronomical Society of the Pacific Conference Series, Vol. 411, Astronomical Data Analysis Software and Systems XVIII, ed. D. A. Bohlender, D. Durand, & P. Dowler, 251
Marshall, D. J., Joncas, G., & Jones, A. P. 2009, ApJ, 706, 727
Martín-Hernández, N. L., Bik, A., Puga, E., Nürnberger, D. E. A., & Bronfman, L. 2008, A&A, 489, 229
Martins, F., Pomarès, M., Deharveng, L., Zavagno, A., & Bouret, J. C. 2010, A&A, 510, A32

Martins, F., Schaerer, D., & Hillier, D. J. 2005, A&A, 436, 1049
Maschberger, T., Clarke, C. J., Bonnell, I. A., & Kroupa, P. 2010, MNRAS, 404, 1061
Massey, P., DeGioia-Eastwood, K., & Waterhouse, E. 2001, AJ, 121, 1050
Matzner, C. D. & McKee, C. F. 2000, ApJ, 545, 364
Mauerhan, J. C., Van Dyk, S. D., & Morris, P. W. 2011, AJ, 142, 40
McClure-Griffiths, N. M. & Dickey, J. M. 2007, ApJ, 671, 427
McKee, C. F. & Ostriker, E. C. 2007, ARA&A, 45, 565
McMillan, P. J. & Binney, J. J. 2010, MNRAS, 402, 934
Megeath, S. T., Flaherty, K. M., Hora, J., et al. 2005, in IAU Symposium, Vol. 227, Massive Star Birth: A Crossroads of Astrophysics, ed. R. Cesaroni, M. Felli, E. Churchwell, & M. Walmsley, 383–388
Mercer, E. P., Clemens, D. P., Meade, M. R., et al. 2005, ApJ, 635, 560
Messineo, M., Davies, B., Figer, D. F., et al. 2011, ApJ, 733, 41
Messineo, M., Davies, B., Ivanov, V. D., et al. 2009, ApJ, 697, 701
Messineo, M., Figer, D. F., Davies, B., et al. 2010, ApJ, 708, 1241
Messineo, M., Figer, D. F., Davies, B., et al. 2008, ApJ, 683, L155
Miettinen, O. & Harju, J. 2010, A&A, 520, A102
Misanovic, Z., Cram, L., & Green, A. 2002, MNRAS, 335, 114
Moeckel, N., Holland, C., Clarke, C. J., & Bonnell, I. A. 2012, MNRAS, 425, 450
Moffat, A. F. J. 1976, A&A, 50, 429
Moisés, A. P., Damineli, A., Figuerêdo, E., et al. 2011, MNRAS, 411, 705
Molinari, S., Brand, J., Cesaroni, R., & Palla, F. 1996, A&A, 308, 573
Motogi, K., Sorai, K., Habe, A., et al. 2011, PASJ, 63, 31
Mottram, J. C., Hoare, M. G., Davies, B., et al. 2011, ApJ, 730, L33
Nagayama, T., Omodaka, T., Handa, T., et al. 2011, PASJ, 63, 719
Nagayama, T., Sato, S., Nishiyama, S., et al. 2009, PASJ, 61, 283
Neckel, T. 1978, A&A, 69, 51
Negueruela, I., González-Fernández, C., Marco, A., & Clark, J. S. 2011, A&A, 528, A59
Negueruela, I., González-Fernández, C., Marco, A., Clark, J. S., & Martínez-Núñez, S. 2010, A&A, 513, A74
Netopil, M., Paunzen, E., Maitzen, H. M., et al. 2007, A&A, 462, 591
Nguyen Luong, Q., Motte, F., Schuller, F., et al. 2011, A&A, 529, A41
Offner, S. S. R., Hansen, C. E., & Krumholz, M. R. 2009, ApJ, 704, L124
Ogura, K. & Ishida, K. 1976, PASJ, 28, 35
Oh, C. S., Kobayashi, H., Honma, M., et al. 2010, PASJ, 62, 101
Ojha, D. K., Kumar, M. S. N., Davis, C. J., & Grave, J. M. C. 2010, MNRAS, 407, 1807

Oliveira, J. M. 2008, Star Formation in the Eagle Nebula, ed. B. Reipurth, 599
Ossenkopf, V. & Henning, T. 1994, A&A, 291, 943
Padoan, P. & Nordlund, Å. 2002, ApJ, 576, 870
Panagia, N. 1973, AJ, 78, 929
Pandian, J. D., Menten, K. M., & Goldsmith, P. F. 2009, ApJ, 706, 1609
Pandian, J. D., Momjian, E., & Goldsmith, P. F. 2008, A&A, 486, 191
Paunzen, E. & Netopil, M. 2006, MNRAS, 371, 1641
Paunzen, E., Netopil, M., Iliev, I. K., et al. 2005, A&A, 443, 157
Pavani, D. B. & Bica, E. 2007, A&A, 468, 139
Peña, J. H., García-Cole, A., Hobart, M. A., et al. 2003, Rev. Mexicana Astron. Astrofis., 39, 171
Peretto, N. & Fuller, G. A. 2009, A&A, 505, 405
Persi, P. & Tapia, M. 2010, Mem. Soc. Astron. Italiana, 81, 171
Persi, P., Tapia, M., & Roth, M. 2000, A&A, 357, 1020
Persi, P., Tapia, M., Roth, M., Gómez, M., & Marenzi, A. R. 2005, in IAU Symposium, Vol. 227, Massive Star Birth: A Crossroads of Astrophysics, ed. R. Cesaroni, M. Felli, E. Churchwell, & M. Walmsley, 291–296
Pestalozzi, M. R., Minier, V., & Booth, R. S. 2005, A&A, 432, 737
Pflamm-Altenburg, J., Weidner, C., & Kroupa, P. 2007, ApJ, 671, 1550
Phelps, R. L. & Janes, K. A. 1994, ApJS, 90, 31
Piatti, A. E., Bica, E., & Clariá, J. J. 2000a, A&A, 362, 959
Piatti, A. E., Bica, E., Clariá, J. J., Santos, J. F. C., & Ahumada, A. V. 2002a, MNRAS, 335, 233
Piatti, A. E., Bica, E., Santos, Jr., J. F. C., & Clariá, J. J. 2002b, A&A, 387, 108
Piatti, A. E. & Clariá, J. J. 2001, A&A, 379, 453
Piatti, A. E. & Clariá, J. J. 2002, A&A, 388, 179
Piatti, A. E., Clariá, J. J., & Ahumada, A. V. 2005, PASP, 117, 22
Piatti, A. E., Clariá, J. J., & Ahumada, A. V. 2006, New A, 11, 262
Piatti, A. E., Claria, J. J., & Bica, E. 1999, MNRAS, 303, 65
Piatti, A. E., Clariá, J. J., & Bica, E. 2000b, A&A, 360, 529
Piatti, A. E., Clariá, J. J., Bica, E., Geisler, D., & Minniti, D. 1998, AJ, 116, 801
Pinheiro, M. C., Copetti, M. V. F., & Oliveira, V. A. 2010, A&A, 521, A26
Piskunov, A. E., Kharchenko, N. V., Röser, S., Schilbach, E., & Scholz, R.-D. 2006, A&A, 445, 545
Piskunov, A. E., Schilbach, E., Kharchenko, N. V., Röser, S., & Scholz, R.-D. 2007, A&A, 468, 151
Pomarès, M., Zavagno, A., Deharveng, L., et al. 2009, A&A, 494, 987
Porras, A., Christopher, M., Allen, L., et al. 2003, AJ, 126, 1916

Portegies Zwart, S. F. & McMillan, S. L. W. 2002, ApJ, 576, 899
Portegies Zwart, S. F., McMillan, S. L. W., & Gieles, M. 2010, ARA&A, 48, 431
Povich, M. S. 2012, ArXiv e-prints (arXiv:1202.0791), to appear in the proceedings of the Frank N. Bash Symposium 2011: New Horizons in Astronomy
Povich, M. S., Churchwell, E., Bieging, J. H., et al. 2009, ApJ, 696, 1278
Povich, M. S., Stone, J. M., Churchwell, E., et al. 2007, ApJ, 660, 346
Pratap, P., Megeath, S. T., & Bergin, E. A. 1999, ApJ, 517, 799
Proszkow, E.-M., Adams, F. C., Hartmann, L. W., & Tobin, J. J. 2009, ApJ, 697, 1020
Purcell, C. R., Balasubramanyam, R., Burton, M. G., et al. 2006, MNRAS, 367, 553
Quillen, A. C., Thorndike, S. L., Cunningham, A., et al. 2005, ApJ, 632, 941
Ragan, S. E., Bergin, E. A., Plume, R., et al. 2006, ApJS, 166, 567
Rathborne, J. M., Jackson, J. M., & Simon, R. 2006, ApJ, 641, 389
Rauw, G. & De Becker, M. 2008, The Multiwavelength Picture of Star Formation in the Very Young Open Cluster NGC 6383, ed. B. Reipurth, 497
Rauw, G., Manfroid, J., & De Becker, M. 2010, A&A, 511, A25
Reid, M. J., Menten, K. M., Zheng, X. W., et al. 2009, ApJ, 700, 137
Rho, J., Reach, W. T., Lefloch, B., & Fazio, G. G. 2006, ApJ, 643, 965
Ridge, N. A., Wilson, T. L., Megeath, S. T., Allen, L. E., & Myers, P. C. 2003, AJ, 126, 286
Robitaille, T. P., Meade, M. R., Babler, B. L., et al. 2008, AJ, 136, 2413
Robitaille, T. P. & Whitney, B. A. 2010, ApJ, 710, L11
Rodríguez, M., Rodríguez, L. F., Gyulbudaghian, A. L., & May, J. 2002, Rev. Mexicana Astron. Astrofis., 38, 161
Roman-Duval, J., Jackson, J. M., Heyer, M., et al. 2009, ApJ, 699, 1153
Roman-Lopes, A. 2007, A&A, 471, 813
Roman-Lopes, A. 2011, MNRAS, 410, 161
Roman-Lopes, A. & Abraham, Z. 2004a, AJ, 128, 2364
Roman-Lopes, A. & Abraham, Z. 2004b, AJ, 127, 2817
Roman-Lopes, A. & Abraham, Z. 2006a, AJ, 131, 2223
Roman-Lopes, A. & Abraham, Z. 2006b, AJ, 131, 951
Roman-Lopes, A., Abraham, Z., & Lépine, J. R. D. 2003, AJ, 126, 1896
Roman-Lopes, A., Abraham, Z., Ortiz, R., & Rodriguez-Ardila, A. 2009, MNRAS, 394, 467
Russeil, D. 2003, A&A, 397, 133
Russeil, D., Adami, C., Amram, P., et al. 2005, A&A, 429, 497
Russeil, D. & Castets, A. 2004, A&A, 417, 107
Russeil, D., Zavagno, A., Motte, F., et al. 2010, A&A, 515, A55

Sagar, R. & Cannon, R. D. 1994, Bulletin of the Astronomical Society of India, 22, 381
Sagar, R., Naidu, B. N., & Mohan, V. 2001, Bulletin of the Astronomical Society of India, 29, 519
Sana, H., Gosset, E., Nazé, Y., Rauw, G., & Linder, N. 2008, MNRAS, 386, 447
Sana, H., Gosset, E., Rauw, G., Sung, H., & Vreux, J.-M. 2006, A&A, 454, 1047
Sato, M., Hirota, T., Reid, M. J., et al. 2010a, PASJ, 62, 287
Sato, M., Reid, M. J., Brunthaler, A., & Menten, K. M. 2010b, ApJ, 720, 1055
Schmeja, S. 2011, Astronomische Nachrichten, 332, 172
Schödel, R., Merritt, D., & Eckart, A. 2009, A&A, 502, 91
Schönrich, R., Binney, J., & Dehnen, W. 2010, MNRAS, 403, 1829
Schuller, F., Menten, K. M., Contreras, Y., et al. 2009, A&A, 504, 415
Schuster, K.-F., Boucher, C., Brunswig, W., et al. 2004, A&A, 423, 1171
Seleznev, A. F., Carraro, G., Costa, E., & Loktin, A. V. 2010, New A, 15, 61
Sewilo, M., Watson, C., Araya, E., et al. 2004, ApJS, 154, 553
Shepherd, D. S., Nürnberger, D. E. A., & Bronfman, L. 2004, ApJ, 602, 850
Shepherd, D. S., Povich, M. S., Whitney, B. A., et al. 2007, ApJ, 669, 464
Simon, R., Jackson, J. M., Rathborne, J. M., & Chambers, E. T. 2006, ApJ, 639, 227
Siringo, G., Kreysa, E., Kovács, A., et al. 2009, A&A, 497, 945
Skrutskie, M. F., Cutri, R. M., Stiening, R., et al. 2006, AJ, 131, 1163
Smith, R., Fellhauer, M., Goodwin, S., & Assmann, P. 2011, MNRAS, 414, 3036
Smith, R. J., Clark, P. C., & Bonnell, I. A. 2009, MNRAS, 396, 830
Soares, J. B., Bica, E., Ahumada, A. V., & Clariá, J. J. 2008, A&A, 478, 419
Solin, O., Ukkonen, E., & Haikala, L. 2012, A&A, 542, A3
Sollins, P. K. & Megeath, S. T. 2004, AJ, 128, 2374
Spitzer, L. 1978, Physical processes in the interstellar medium, ed. Spitzer, L.
Spitzer, Jr., L. 1969, ApJ, 158, L139+
Spitzer, Jr., L. & Hart, M. H. 1971, ApJ, 164, 399
Stead, J. J. & Hoare, M. G. 2010, MNRAS, 407, 923
Stead, J. J. & Hoare, M. G. 2011, MNRAS, 418, 2219
Stier, M. T., Fazio, G. G., Roberge, W. G., et al. 1982, ApJS, 48, 127
Stier, M. T., Jaffe, D. T., Rengarajan, T. N., et al. 1984, ApJ, 283, 573
Stolte, A., Ghez, A. M., Morris, M., et al. 2008, ApJ, 675, 1278
Strader, J. & Kobulnicky, H. A. 2008, AJ, 136, 2102
Straw, S. M., Hyland, A. R., & McGregor, P. J. 1989, ApJS, 69, 99
Subramaniam, A., Carraro, G., & Janes, K. A. 2010, MNRAS, 404, 1385

Tadross, A. L. 2008, New A, 13, 370
Tadross, A. L. 2009a, New A, 14, 200
Tadross, A. L. 2009b, Ap&SS, 323, 383
Tadross, A. L. 2011, Journal of Korean Astronomical Society, 44, 1
Tapia, M., Persi, P., & Roth, M. 1996, A&A, 316, 102
Tapia, M., Rodríguez, L. F., Persi, P., Roth, M., & Gómez, M. 2009, AJ, 137, 4127
Tapia, M., Roth, M., Lopez, J. A., et al. 1991, A&A, 242, 388
Tapia, M. T., Schuster, W. J., Michel, R., et al. 2010, MNRAS, 401, 621
Thompson, M. A., Urquhart, J. S., Moore, T. J. T., & Morgan, L. K. 2012, MNRAS, 421, 408
Tothill, N. F. H., Gagné, M., Stecklum, B., & Kenworthy, M. A. 2008, The Lagoon Nebula and its Vicinity, ed. B. Reipurth, 533
Turner, D. G. & Forbes, D. 2005, PASP, 117, 967
Turner, D. G., van den Bergh, S., Younger, P. F., Danks, T. A., & Forbes, D. 1993, ApJS, 85, 119
Urquhart, J. S., Hoare, M. G., Lumsden, S. L., Oudmaijer, R. D., & Moore, T. J. T. 2008, in Astronomical Society of the Pacific Conference Series, Vol. 387, Massive Star Formation: Observations Confront Theory, ed. H. Beuther, H. Linz, & T. Henning, 381
Urquhart, J. S., Hoare, M. G., Lumsden, S. L., et al. 2012, MNRAS, 420, 1656
Urquhart, J. S., Moore, T. J. T., Hoare, M. G., et al. 2011, MNRAS, 410, 1237
Urquhart, J. S., Morgan, L. K., & Thompson, M. A. 2009, A&A, 497, 789
van den Bergh, S. & Hagen, G. L. 1975, AJ, 80, 11
Vasquez, J., Cappa, C., & McClure-Griffiths, N. M. 2005, MNRAS, 362, 681
Vassilev, V., Meledin, D., Lapkin, I., et al. 2008, A&A, 490, 1157
Vázquez, R. A. & Baume, G. 2001, A&A, 371, 908
Vázquez, R. A., Giorgi, E. E., Brusasco, M. A., Baume, G., & Solivella, G. R. 2003, Rev. Mexicana Astron. Astrofis., 39, 89
Vig, S., Ghosh, S. K., Kulkarni, V. K., Ojha, D. K., & Verma, R. P. 2006, ApJ, 637, 400
Vig, S., Ghosh, S. K., Ojha, D. K., & Verma, R. P. 2007a, A&A, 463, 175
Vig, S., Testi, L., Walmsley, M., et al. 2007b, A&A, 470, 977
Vrba, F. J., Henden, A. A., Luginbuhl, C. B., et al. 2000, ApJ, 533, L17
Walch, S., Whitworth, A., Bisbas, T., Hubber, D. A., & Wuensch, R. 2011, ApJ, submitted (arXiv:1109.3478)
Walsh, A. J., Burton, M. G., Hyland, A. R., & Robinson, G. 1998, MNRAS, 301, 640
Wang, J., Townsley, L. K., Feigelson, E. D., et al. 2007, ApJS, 168, 100
Watson, C., Corn, T., Churchwell, E. B., et al. 2009, ApJ, 694, 546

Watson, C., Povich, M. S., Churchwell, E. B., et al. 2008, ApJ, 681, 1341
Weaver, R., McCray, R., Castor, J., Shapiro, P., & Moore, R. 1977, ApJ, 218, 377
Weidner, C., Kroupa, P., & Bonnell, I. A. D. 2010, MNRAS, 401, 275
Werner, M. W., Roellig, T. L., Low, F. J., et al. 2004, ApJS, 154, 1
Wienen, M., Wyrowski, F., Schuller, F., et al. 2012, A&A, 544, A146
Williams, J. P., Blitz, L., & McKee, C. F. 2000, Protostars and Planets IV, 97
Williams, J. P., de Geus, E. J., & Blitz, L. 1994, ApJ, 428, 693
Wilson, T. L., Mezger, P. G., Gardner, F. F., & Milne, D. K. 1970, A&A, 6, 364
Wilson, T. L., Rohlfs, K., & Hüttemeister, S. 2009, Tools of Radio Astronomy (Springer-Verlag)
Wilson, T. L. & Rood, R. 1994, ARA&A, 32, 191
Wink, J. E., Altenhoff, W. J., & Mezger, P. G. 1982, A&A, 108, 227
Wolf, J., Martinez, G. D., Bullock, J. S., et al. 2010, MNRAS, 406, 1220
Wolk, S. J., Spitzbart, B. D., Bourke, T. L., et al. 2008, AJ, 135, 693
Wood, D. O. S. & Churchwell, E. 1989, ApJS, 69, 831
Xu, Y., Moscadelli, L., Reid, M. J., et al. 2011, ApJ, 733, 25
Xu, Y., Reid, M. J., Menten, K. M., et al. 2009, ApJ, 693, 413
Zapata, L. A., Leurini, S., Menten, K. M., et al. 2008, AJ, 136, 1455
Zavagno, A., Pomarès, M., Deharveng, L., et al. 2007, A&A, 472, 835
Zhang, B., Zheng, X. W., Reid, M. J., et al. 2009, ApJ, 693, 419

Acknowledgements

I thank Prof. Karl Menten for giving me the opportunity of doing my PhD at the Max-Planck-Institut für Radioastronomie (MPIfR), and Friedrich Wyrowski for supervising me in this thesis. I am grateful to the International Max Planck Research School (IMPRS) for Astronomy and Astrophysics at the Universities of Bonn and Cologne, for its financial support during three years of my PhD. I acknowledge travel support from Prof. Menten and IMPRS, which allowed me to attend schools and conferences, and travel for observations. I thank Prof. Pavel Kroupa from the Argelander-Institut für Astronomie for being part of my IMPRS thesis committee and agreeing to be the second referee of this dissertation. I also thank Prof. Ian Brock from the Physikalisches Institut, and Prof. Reinhard Klein from the Institut für Informatik for being part of the examination board. I am very grateful to Thomas Robitaille from the Max-Planck-Institut für Astronomie (MPIA), for letting me move to Heidelberg in advance and supporting the last months of my PhD work.

I acknowledge the useful discussions and feedback from Maria Messineo about the GLIMPSE search for embedded clusters, and from Marion Wienen about kinematic distances. I also benefited from the email discussions with D. Froebrich (about his catalog of clusters), A. Moisés (about NIR spectrophotometric distances), M. Gieles (about its equation to distinguish bound clusters from associations), and D. Fanning (a.k.a. "Coyote", about image visualization in IDL).

I would like to thank to my family in Chile for their wholehearted support over all these years: Papá y mamá, gracias por su amor y comprensión, y por siempre apoyar mis decisiones. Gracias también a mis hermanos Paulina, Ángela y Marco (gracias Marco por ayudarme cuando murió mi laptop en Chile en plena escritura de tesis), mi sobrina Adalia, y mis abuelos Eliana y Félix, por su valiosa compañía cuando estaba en Chile, en especial las semanas en que escribí parte de mi tesis.

I am also grateful to my colleagues and friends in Bonn, especially to the Latino population: Laura, Felipe, Arturo, Pablo and Yanett, for all the good moments and for making me feel like at home.

Finally, I wish to mention a person without whom it would have been

impossible to finish this thesis: my beloved Denise. In her I found not only the woman of my dreams and the perfect accomplice to all our adventures in life, but also immeasurable support during the whole period of my PhD, despite the long (physical) distance between us in the first three years. I will never forget her help while living together in Granada last year, and when trying to write my thesis and settle in Heidelberg at the same time, as well as her valuable advice in science and life. Her infinite encouragement made me never give up.